A HYDRODYNAMIC INVESTIGATION OF FINE PARTICLE FLOTATION IN A BATCH FLOTATION CELL

By

David Alan Deglon

B.Sc. Chemical Engineering (University of the Witwatersrand)

A thesis submitted to the University of Cape Town in fulfilment of the requirements for the degree of Doctor of Philosophy

Department of Chemical Engineering

University of Cape Town

July 1998

ACKNOWLEDGEMENTS

I should like to express my sincere thanks to my supervisor, Professor Cyril O'Connor, for his enthusiasm, assistance and guidance in this study.

The help of the following people is also gratefully acknowledged:

Mr Joachim Macke and Mr Peter Dobias for their assistance in the construction of the flotation cell.

Mrs Dee Bradshaw and Mr Martin Harris for providing a haven of humour and refuge in the face of the innumerable "thesis plights".

The staff and students of the Mineral Processing Research Unit for their valuable assistance, comments and constructive advice.

My Fiancée, Undere, whose three year extended vacation in Greece afforded me ample opportunity to work on weekends and in the evenings.

My parents, Paul and Avril Deglon, for their encouragement and moral support throughout the years.

The support of the University of Cape Town and the Chamber of Mines over the past five years is gratefully acknowledged.

CERTIFICATION BY SUPERVISOR

In terms of paragraph GP 8 of the rules for the degree of PhD I certify that I approve of the incorporation in this thesis of material that has been published.

Professor CT O'Connor (supervisor)
Department of Chemical Engineering
University of Cape Town
Private Bag
Rondebosch, 7700

LIST OF PUBLICATIONS

Journal Publications

Deglon, D.A. and O'Connor, C.T., 1998. A novel attachment-detachment kinetic model for agitated flotation cells. Int. J. Miner. Process. (submitted for publication).

Deglon, D.A., O'Connor, C.T. and Pandit A.B., 1998. Efficacy of a spinning disc as a bubble breakup device. Chem. Eng. Sci., 53: 59-70.

Harris, M.C., Franzidis, J.P., Breed, A.W. and Deglon D.A., 1994. An on-site evaluation of different flotation technologies for fine coal beneficiation. Miner. Eng., 7: 699-713.

Sawyerr, F., Deglon, D.A. and O'Connor, C.T., 1998. Prediction of bubble size distribution in mechanical flotation cells. J. S. African Inst. Min. Metall. (accepted for publication).

Tucker, J.P., Deglon, D.A., Franzidis, J.P., O'Connor, C.T. and Harris, M.C., 1994. An evaluation of a direct method of bubble size distribution measurement in a laboratory batch flotation cell. Miner. Eng., 7: 667-680.

Conference Papers (Refereed)

Deglon, D.A. and O' Connor, C.T., 1996. A hydrodynamic investigation of fine particle flotation in a conventional flotation cell. Proc. Int. Conf. Miner. Mater. '96, Somerset West, South Africa, pp. 317-325.

Deglon, D.A. and O'Connor, C.T., 1997. The relationship between bubble size and particle size in an agitated flotation cell. Proc. XX Int. Miner. Process. Cong., Aachen, Germany, pp. 167-174.

TABLE OF CONTENTS

LIST OF APPENDICES

Page

APPENDIX A: Hydrodynamic and gas dispersion results.

APPENDIX B: Flotation results.

LIST OF FIGURES

LIST OF TABLES

NOMENCLATURE

A	Tank cross sectional area (m^2)
B	Baffle width (m)
b_m	Vortex Acceleration (m^2s^{-2})
C	Concentration of particles in the pulp - volumetric concentration (kgm^{-3})
C_o	Initial concentration of particles in the pulp (kgm^{-3})
C_s	Concentration of particles on bubble surfaces - surface concentration (kgm^{-2})
D	Impeller diameter (m)
d_{95}	95 Percentile bubble size (m)
d_b	Mean bubble size (m)
d_{bf}	Mean bubble size based on flux (m)
d_{bm}	Maximum stable bubble size (m)
d_p	Mean particle size (m)
d_{pm}	Maximum floatable particle size (m)
d_s	Sauter mean bubble size (m)
d_{sf}	Sauter mean bubble size based on flux (m)
E_1	Energy spectrum function (m^2s^{-1})
$f(d_b)$	Bubble size distribution (Fractional)
$F(d_b)$	Bubble size distribution based on flux (Fractional)
g	Gravitational acceleration (m^2s^{-2})
G	Gibbs free energy (J)
h	Film thickness (m)
H	Tank height (m)
J_g	Superficial gas velocity (ms^{-1})
k	Flotation rate constant (s^{-1})
k_a	Attachment rate constant (s^{-1})
k_d	Detachment rate constant (s^{-1})
L	Blade length (m)
n	Frequency (s^{-1})
n_p	Mean number of times a bubble passes through the impeller zone.
N	Impeller speed (s^{-1})
N_{Af}	Air flow number (Dimensionless)
N_b	Number of bubbles per unit volume (m^{-3})
N_{bf}	Number of bubbles in flux ($m^{-2}s^{-1}$)

N_{Fr}	Froude number (Dimensionless)
N_p	Number of particles per unit volume (m^{-3})
N_{pb}	Number of particle-bubble collisions per unit volume-time ($m^{-3}s^{-1}$)
N_{Pw}	Power number (Dimensionless)
N_{Re}	Reynolds number (Dimensionless)
N_{We}	Weber number (Dimensionless)
P	Power input (W)
P_a	Probability of attachment (Fractional)
P_c	Probability of collision (Fractional)
P_{coll}	Probability of collection (Fractional)
P_d	Probability of detachment (Fractional)
Q	Gas flowrate (m^3s^{-1})
q	Turbulent kinetic energy (Jkg^{-1})
Q_I	Impeller pumping rate (m^3s^{-1})
R	Recovery (Fractional)
r_b	Bubble radius (m)
R_E	Autocorrelation coefficient
r_p	Particle radius (m)
S	Specific bubble surface area (m^2m^{-3})
S_b	Bubble surface area flux (s^{-1})
T	Tank diameter (m)
t	Time (s)
t_i	Induction time (s)
t_{sl}	Sliding time (s)
u'	Fluctuating velocity (ms^{-1})
U	Mean velocity (ms^{-1})
$\bar{u}$	Root mean square (RMS) turbulent velocity (ms^{-1})
U_b	Bubble rise velocity (ms^{-1})
V	Tank volume (m^3)
V_o	Initial tank volume (m^3)
V_I	Impeller region volume (m^3)
W	Blade width (m)
w	Wave number (m^{-1})
x_e	Entrainment fraction (Fractional)
x_g	Gas flow fraction (Fractional)
x_I	Fraction of power dissipated in impeller zone (Fractional)

x_V	Fraction of tank volume occupied by impeller zone (Fractional)

Greek Letters

α	Volume shrinkage factor (s^{-1})
γ	Interfacial tension (Nm^{-1})
ε	Specific power input/turbulent energy dissipation rate (Wkg^{-1})
ε_B	Turbulent energy dissipation rate in bulk tank (Wkg^{-1})
ε_I	Turbulent energy dissipation rate in impeller zone (Wkg^{-1})
ε_n	Normalised turbulent energy dissipation rate (Dimensionless)
η	Kolmogoroff microscale (m)
θ	Static contact angle (°)
λ_f	Eulerian micro length scale (m)
Λ_f	Eulerian macro length scale (m)
Λ_R	Resultant macro length scale (m)
μ	Viscosity (Pa)
ν	Kinematic viscosity (m^2s^{-1})
ρ	Fluid density (kgm^{-3})
ρ_l	Liquid density (kgm^{-3})
ρ_p	Solid/particle density (kgm^{-3})
σ	Surface tension (Nm^{-1})
τ	Lag time (s)
τ_E	Eulerian micro time scale (s)
τ_g	Gas residence time (s)
τ_{gs}	Gas residence time based on surface area (s)
τ_p	Pulp residence time (s)
τ_T	Tank turnover time (s)
T_E	Eulerian macro time scale (s)
ϕ	Gas holdup

Subscripts

B	Bulk tank
I	Impeller zone
i	Size fraction/size class
l	Liquid

s	Solid
v	Vapour

Parameters

c, n	Empirical constants
λ, m	Intermediate variables

#All the units specified in the nomenclature are applicable in this thesis unless otherwise indicated in the text, tables or figures.

SYNOPSIS

This thesis investigates the effects of particle size, bubble size and level of agitation on the flotation of quartz in a laboratory batch flotation cell. The thesis was initiated in order to gain a greater understanding of the influence of agitation on flotation performance with the purpose of improving the rate of fine particle flotation in mechanically agitated cells. The thesis involved a detailed characterisation of hydrodynamic, gas dispersion and flotation parameters in a specially designed batch flotation cell in which it is possible to vary particle size, bubble size and level of agitation independently. The flotation cell was agitated by one of two impellers, a standard Rushton turbine or a high speed spinning disc - a novel impeller used in the field of microbubble generation. The flotation cell was carefully characterised in terms of bubble size, power input and turbulence parameters after which flotation tests were performed on two different samples of fine quartz. Flotation rate constants were then determined for various particle size fractions using the classical first-order batch flotation model. Due to the poor applicability of this model to many of the flotation tests, however, a new kinetic model for flotation in mechanically agitated cells was proposed. This model is termed the *attachment-detachment model* in this thesis and allows for the influence of the gas phase in the flotation cell both in terms of the gas residence time and the attachment/detachment of particles to/from bubbles. Results and conclusions from the characterisation of hydrodynamic, gas dispersion and flotation performance in the flotation cell are summarised individually hereafter, followed by an overview of the attachment-detachment model:

Hydrodynamics: Specific power inputs and characteristic dimensionless numbers for the two impellers were found to be within the range of values observed in industrial mechanical flotation cells. Turbulence parameters and energy spectra for the two impellers were consistent with those obtained by other researchers and found in the turbulence literature. Turbulence in the flotation cell was found to be isotropic but non-homogeneous with the cell being divided into a bulk tank and an impeller zone with uniform, though order of magnitude different, turbulence parameters throughout. For the Rushton turbine a significant percentage of the total power input to the cell was found to be dissipated in the bulk tank while this was minimal for the spinning disc. From this finding it was concluded that the Rushton turbine is a suitable impeller for use in systems where microphenomena are dependent on turbulence in both the bulk tank and the impeller zone while the spinning disc is suitable for use in systems where these microphenomena are controlled by the impeller zone only. In addition, turbulent energy spectra for the spinning disc were found to have significantly less turbulent energy in the intermediate and higher frequency eddy ranges. From this finding it was proposed that the Rushton turbine is a more suitable impeller for use in systems

where microphenomena are dependent on eddies of this size range. Aeration was found to lead to substantial decreases in both mean and turbulent velocities in the bulk tank and, consequently, to an intensification of turbulent velocities and turbulent energy dissipation rates in the impeller zone. Aeration had no effect on the general form of the energy spectrum, however, from which it was concluded that aeration does not affect the mechanism of transmission of energy through the spectrum.

Gas Dispersion: Gas residences times in the flotation cell were found to be significantly longer than those obtained in standard laboratory flotation cells but to be comparable with those observed in industrial mechanical flotation cells. Characteristic bubble sizes were consistent with those obtained by other researchers in similar systems and found in the gas dispersion literature. Two fundamental models for bubble breakup in a turbulent fluid were investigated. The model for bubble breakup based on turbulent pressure fluctuations was found to be applicable to the bubble size data for the Rushton turbine but to be inapplicable to the bubble size data for the spinning disc. The model for bubble breakup based on the collision of a bubble with a turbulent eddy was found to give erratic and opposite trends for the two impellers. The Rushton turbine was found to be a more efficient impeller for bubble breakup than the spinning disc but this was attributed to an inappropriate selection of disc dimensions and impeller speeds. It was proposed that a smaller spinning disc operating at significantly higher impeller speeds to those used in this thesis would be a more efficient impeller for bubble breakup than a standard Rushton turbine.

Flotation Kinetics: The effects of particle size, bubble size and agitation on the flotation rate constant were similar to those obtained by other researchers and presented in the flotation literature. The flotation rate constant was found to be weakly dependent on the particle size and strongly dependent on the bubble size and power input. Agitation was found to have both beneficial and detrimental effects on flotation performance and to result in optima in the flotation rate constant as a function of particle size, bubble size and power input. The beneficial effects of agitation on flotation performance were attributed to increased particle-bubble attachment through improved particle-bubble contacting and the production of smaller bubbles by breakup. The detrimental effects of agitation on flotation performance were attributed to increased particle-bubble detachment through increased turbulence. Increases in particle-bubble attachment were regarded as occurring in both the bulk tank and the impeller zone but were considered to be overridden by particle-bubble detachment in the impeller zone due to the enormously high turbulent energy dissipation rates in this region. Increases in both particle-bubble attachment and detachment were found to be strongly dependent on particle size, though detachment was found to be significant for even ultrafine particles at sufficiently high levels of agitation. For the Rushton turbine agitation was

considered to result in increased particle-bubble attachment through both improved particle-bubble contacting and the production of small bubbles by breakup. For the spinning disc agitation was considered to result in increased particle-bubble attachment through the production of small bubbles by breakup only. For both impellers, however, agitation was considered to result in increased particle-bubble detachment, though this was particularly severe for the Rushton turbine. From these findings it was proposed that the Rushton turbine is a more suitable impeller for promoting particle-bubble contacting than the spinning disc but that the disc is more suitable for the flotation of ultrafine particles as these were unaffected by improved particle-bubble contacting but were prone to significant detachment.

Attachment-Detachment Model: The attachment-detachment model proposed in this thesis was found to be suitable for analysing flotation kinetics in mechanically agitated flotation cells as it decouples the two independent processes of particle-bubble attachment and detachment and allows for the presence of a gas phase in the flotation cell. The model was found to approximate the flotation data for the Rushton turbine impeller reasonably well and empirical correlations for the attachment and detachment rate constants as a function of particle size, bubble size and specific power input were proposed using this data. The attachment-detachment model, used in conjunction with these empirical correlations, predicts experimental phenomena such as the optima in the flotation rate constant as a function of particle size, bubble size and power input observed in this thesis. In addition, the model has important implications for flotation cell scale-up, predicting that small flotation cells have higher flotation rate constants than large flotation cells due to comparatively lower gas residence times. The model also has significant implications for flotation cell design, predicting that mechanical cells which have been sparged with small bubbles using external spargers will outperform conventional cells due to the conflict between the requirements for efficient gas dispersion and flotation in conventional mechanical flotation cells.

CHAPTER 1: INTRODUCTION

Froth flotation as a patented process is over 100 years old (Crabtree and Vincent, 1962) and is the most widely used separation method in the mineral processing industry, responsible for the beneficiation of in excess of two billion tons of over one hundred different mineral species annually. Flotation relies on separating particles of different material composition by rendering their surfaces selectively hydrophobic or hydrophilic through the addition of suitable flotation reagents. Hydrophobic particles become attached to air bubbles and are transported upwards into a froth layer at the top of the flotation cell while hydrophilic particles remain in the slurry in the flotation cell. Consequently, flotation relies on both physical and chemical properties of particles and bubbles and is termed a physico-chemical separation process.

Due to its prevalence in mineral processing, inefficiencies in flotation translate into both an enormous loss of revenue and an unnecessary waste of the world's valuable and steadily declining mineral reserves. These losses are expected to compound in the coming decades as, due to the preferential processing of high quality ores, mining companies are forced to treat more and more complex and finely disseminated ore bodies. In response to this growing problem considerable flotation research has been undertaken in the past two decades, especially in the three major areas of *flotation reagent*, *flotation cell* and *flotation fundamental* research (Schulze, 1984). Research into flotation reagents has focused on the development of new reagents and an understanding of the role of these reagents in the subprocesses of flotation. Research into flotation cells has focused on the development of new flotation cell technologies from a better understanding of the impact of cell hydrodynamics on the subprocesses of flotation. Research into flotation fundamentals impacts on both the aforementioned areas of research and has focused on improving flotation efficiency through an understanding of the fundamental mechanisms of the subprocesses of flotation.

The research presented in this thesis is relevant to the areas of *flotation cell* and *flotation fundamental* research and aims to gain a greater understanding of the influence of agitation on flotation performance by investigating the effects of particle size, bubble size and level of agitation on flotation kinetics in a laboratory batch flotation cell. The emphasis in this thesis is placed on understanding flotation in terms of traditional chemical engineering parameters such as rate constants and residence times, though fundamental mechanisms are explored where appropriate. In

addition, though chemical factors have a significant influence on flotation performance, the focus of the thesis is on investigating the effects of physical factors on flotation kinetics. The scope and objectives of the thesis are outlined in Section 1.7 and are motivated by the literature review presented in Sections 1.1 to 1.6.

1.1 Froth Flotation

Froth flotation is dependent on the successful completion of a large number of interdependent subprocesses, all of which are required for a mineral particle to report to flotation concentrate. Figure 1.1 is a schematic overview of the subprocesses involved in the overall process of froth flotation and will be discussed under the broad terms of conditioning, particle collection and froth removal identified by Schulze (1984).

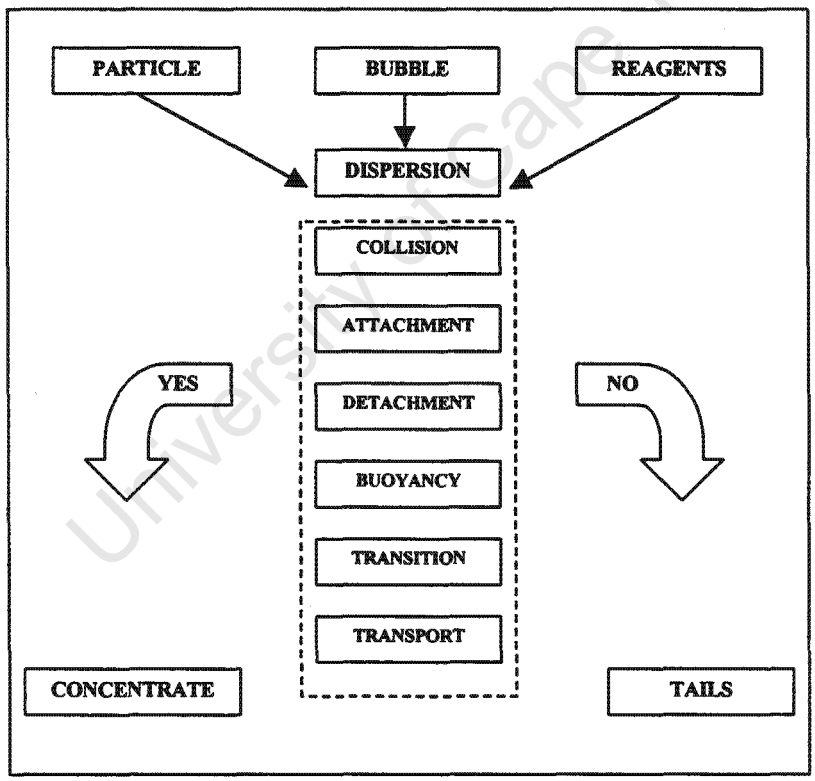

Figure 1.1. Schematic representation of the process of froth flotation.

Conditioning: Solid particles are suspended in the pulp phase in the form of an agitated slurry after which flotation reagents such as collectors, frothers and depressants are added to the flotation cell and dispersed by the impeller. Collectors are responsible for rendering the surface of the valuable

mineral hydrophobic, frothers aid in bubble formation and stabilise the froth while depressants suppress the flotation of naturally hydrophobic gangue material.

Particle Collection: After a suitable conditioning period air is introduced into the flotation cell and dispersed into small bubbles by the impeller. In order to be collected hydrophobic particles have to collide with and become attached to bubbles after which particle-bubble aggregates have to be both sufficiently buoyant to rise through the pulp and sufficiently stable to endure any disturbances in the pulp. On reaching the pulp-froth interface particle-bubble aggregates leave the collection zone of the flotation cell and transition into the froth zone while hydrophilic particles remain in the flotation cell and are removed as flotation tails.

Froth Removal: On entering the froth phase particle-bubble aggregates rise through the froth and are removed from the top of the flotation cell as concentrate. In the froth phase drainage of both hydrophilic particles which have been entrained in the liquid leaving the pulp and hydrophobic particles which have become detached from bubbles occurs, resulting in a flow of mineral and gangue particles back into the pulp phase.

1.2. Flotation Cells

Each of the subprocesses of flotation depicted in Figure 1.1 occur simultaneously in the flotation cell and is affected by different operational variables. Consequently, attaining optimum flotation performance is dependent on optimising each of these subprocess and has resulted in the development of a variety of flotation cells employing different methods of air dispersion, particle-bubble contacting and froth removal. Comprehensive reviews of flotation cell types and technologies have been conducted by researchers such as Miller (1988) and Skillen (1993) and are summarised under the generic classifications of mechanical, column and novel flotation cells below.

Mechanical Flotation Cells: Mechanical flotation cells are the work-horses of the flotation industry and, despite competition from a large variety of alternative flotation technologies, are still responsible for the bulk of world flotation. A mechanical flotation cell consists of square or round tank up to 200 m^3 in volume and agitated by an impeller which is responsible for the processes of solids suspension, gas dispersion and particle-bubble contacting. As high levels of agitation are required for efficient particle suspension and gas dispersion, these flotation cells are thought to be best suited to the flotation of fine and intermediate sized particles due to strong detachment effects

for coarser particles in vigorously agitated systems. Despite the robust and practical nature of mechanical flotation cells, optimum flotation performance cannot be attained in a single unit responsible for all of the processes of solid suspension, gas dispersion and particle-bubble contacting. In addition, the relatively shallow froth depths used in these flotation cells results in high levels of entrainment and comparatively low concentrate grades.

Column Flotation Cells: Despite the fact that column flotation as a patented process is over thirty years old (Wheeler, 1988), column flotation cells have only gained wide application in industry in recent years. A column flotation cell consists of a tall square or round column section up to 3 metres in diameter and 15 metres high. Fresh feed is introduced near the top of the column and flows under gravity in a countercurrent direction to bubbles which are sparged near the base of the column using either internal or external gas spargers. The resultant countercurrent particle-bubble contacting in these cells improves the flotation of fine particles while decoupling the processes of solids suspension, gas dispersion and particle-bubble contacting results in improved flexibility in operation and control. Column flotation cells can operate with very deep froths which can be sprayed with wash water and thus achieve high concentrate grades. Consequently, column flotation cells perform well as cleaners and it is predominately in this capacity that these cells have achieved significant industrial application over mechanical flotation cells.

Novel Flotation Cells: Since the inception of the process of flotation almost 100 years ago, numerous novel flotation cells have been developed in an attempt to exploit or improve the various subprocesses of flotation. The two major thrusts have been on improving gas dispersion through microbubble generation and improving particle-bubble contacting through both high levels of agitation and decoupling the processes of solid suspension and gas dispersion. These improvements have largely been instigated by a better understanding of flotation fundamentals which has led to an appreciation of the micro-environment necessary for optimising flotation performance. This has been complemented by a better understanding of flotation cell hydrodynamics which has led to an improved understanding of the effects of agitation on the micro-environment in the flotation cell. Despite these improvements, however, the influence of agitation on hydrodynamics, gas dispersion and particle-bubble contacting in flotation cells still remains poorly understood (Inoue *et al*, 1986; Ek, 1992).

1.3 Flotation Thermodynamics

Flotation thermodynamics gives information on whether the attachment of a particle to a bubble is at all possible from a thermodynamic perspective, as illustrated in Figure 1.2 which represents the equilibrium state between a bubble and a hydrophobic mineral particle surface.

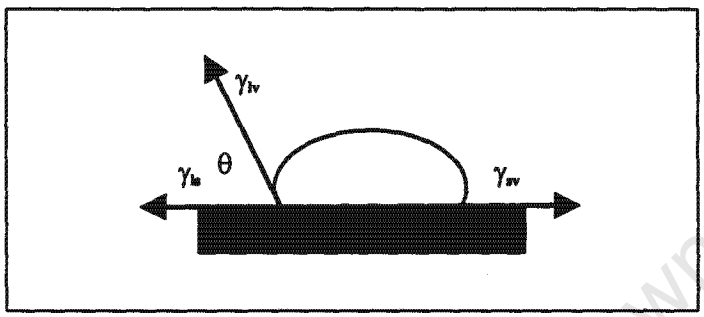

Figure 1.2. Attachment of a bubble to a hydrophobic mineral particle surface.

Flotation thermodynamics has been reviewed extensively in the flotation literature by researchers such as Taggart (1945), Kelly and Spottiswood (1982) and King (1982). The following summary of flotation thermodynamics is based on two more recent review papers by Laskowski (1986, 1989). For the process of particle-bubble attachment to be thermodynamically feasible the Gibbs free energy change on attachment must be negative. As the total surface free energy for the system depicted in Figure 1.2 is equal to the product of the respective solid, liquid and vapour interfacial tensions and interfacial areas, Equation 1.1 can be derived.

$$\Delta G \propto \gamma_{sv} - \gamma_{ls} - \gamma_{lv} \quad (1.1)$$

Consequently, the change in Gibbs free energy on attachment is dependent on the solid, liquid and vapour interfacial tensions. These quantities may be modified through the addition of suitable surfactants such as collectors and frothers, which is generally necessary as most mineral types are naturally hydrophilic due to polar bonding. The details of surfactant adsorption and interactions on mineral and bubble surfaces is outside the scope of this thesis but is reviewed extensively in the literature (King, 1982; Klimpel, 1984). Equation 1.1 can be modified through the introduction of Young's equation to produce the well known thermodynamic criterion for flotation, viz. Equation 1.2.

$$\Delta G \propto \gamma_{lv}(\cos\theta - 1) \quad (1.2)$$

From this relationship it is clear that the process of particle-bubble attachment is only thermodynamically feasible if the angle between the bubble and mineral surface, referred to as the contact angle (θ), is greater than zero. The contact angle is a common thermodynamic parameter used to describe the hydrophobicity of mineral surfaces and is found in many fundamental models of flotation but is difficult to measure and its role in flotation kinetics is still unclear.

Both Equations 1.1 and 1.2 are applicable to the final equilibrium state between a particle and a bubble and overlook the change in free energy of the system in the intermediate states of attachment. Laskowski (1989, 1992) demonstrated that the free energy of the thin liquid film separating a particle and a bubble, referred to as the disjoining film, can change in three ways as the bubble approaches the mineral surface.

1. Stable Wetting Film: When the disjoining film is completely stable, the free energy of the film increases as the bubble approaches the mineral surface and the process of attachment does not occur.
2. Unstable Wetting Film: When the disjoining film is completely unstable, the free energy of the film decreases as the bubble approaches the mineral surface and the film ruptures and forms a stable contact angle.
3. Critical Film Thickness: When the disjoining film is intermediate between the previous two cases, the free energy of the film increases up to some critical film thickness and then starts to decrease.

Laskowski proposed that the net increase in free energy up to the critical film thickness (Scenario 3) is the flotation equivalent of the activation energy in a chemical reaction and considered this to be a direct link between flotation thermodynamics and flotation kinetics.

1.4 Flotation Kinetics

Thermodynamics gives information on whether the process of flotation is feasible without giving any indication as to the rate at which flotation occurs. Though this simple fact is well known it was not until the middle of the 20th century that researchers in flotation began to describe the process by other than purely thermodynamic criteria (Schulze, 1984). Leja (1982) reported the contact angle to be an indicator and not a measure of flotation performance while Laskowski (1986) noted that, although the formation of a stable contact angle is a necessary for flotation, it may be of no

practical significance whatsoever. Consequently, though thermodynamic criteria such as contact angles are necessary prerequisites for flotation, they may have minimal effect on flotation kinetics.

The study of flotation kinetics can be treated from either a macroscopic/phenomenological perspective (macrokinetics) or from a microscopic/mechanistic perspective (microkinetics). Flotation macrokinetics ignores all fundamental interactions and models flotation using classical rate theories and equations while flotation microkinetics attempts to understand flotation from an analysis of the fundamental subprocesses. Flotation macrokinetics has achieved success in the design, modelling and simulation of industrial flotation circuits but there has been a shift to microkinetics in recent years as researchers strive for a more comprehensive understanding of flotation (Inoue *et al*, 1986).

1.4.1 Flotation Macrokinetics

The following overview of flotation macrokinetics is based on review papers by Inoue *et al* (1986), Ek (1992) and Fichera and Chudacek (1992).

1.4.1.1 Flotation Rate Constant

The first attempt at modelling flotation kinetics was by Zuninga (1935) who found that experimental flotation data could be accurately represented by a simple first-order kinetic model. Subsequently, numerous researchers have modelled flotation using the types of kinetic expressions represented by Equation 1.3.

$$\frac{dC}{dt} = -kC^n \quad (1.3)$$

The order of the rate equation (n) has been a subject of active debate over the years and has been found to vary between 0 and 2.8 depending on both the researcher and the system being studied. The arguments for non first-order expressions have been found to be largely empirical and have generally been rejected in favour of the first-order expression (Fichera and Chudacek, 1992). The assumption of a first-order rate process for flotation is reasonable as, in the absence of complex interactions or dependencies in the flotation cell, doubling the concentration of particles should double the rate.

1.4.1.2 Single Parameter Models

The flotation rate expression given in Equation 1.3 is ideally suited to analysing flotation kinetics in systems of particles of uniform size and surface properties. In order to account for differences in particle size and floatability, however, additional parameters have to be included in the rate expression.

1.4.1.2.1 Particle Size Models

Particle size models account for the vast differences in flotation rate constants for particles of different size by assuming a different rate constant for each particle size fraction. Differences in the flotation rate constant as a function of particle size were first discovered by Gaudin *et al* (1942) and were subsequently analysed by Sutherland (1948) who considered the overall flotation rate to be the sum of the rates of the individual size fractions, viz. Equation 1.4.

$$\frac{dC}{dt} = -\sum k_i C_i \qquad (1.4)$$

This methodology has been employed by numerous researchers using discrete particle size fractions and has been extended to continuous particle size distributions. The assumption of independent rate constants for particles of different size for flotation is reasonable as, in the absence of complex interactions or dependencies in the flotation cell, particles should respond as separate and independent species.

1.4.1.2.2 Particle Floatability Models

Particle floatability models account for differences in both particle size and surface properties by combining all possible factors influencing flotation kinetics into a single parameter referred to as the particle floatability. The overall flotation rate is then calculated as the sum over the feed of all particle floatabilities, with the original application being to simple binary systems where the distribution of floatabilities can be represented by two particle floatability classes such as floatable/non-floatable or fast/slow floating. Imaizumi and Inoue (1963) applied a graphical solution to systems with distributions of floatabilities while Woodburn and Loveday (1965) assumed the distribution to be represented by a gamma function. Inoue and Imaizumi (1968) and

Harris and Chakravarti (1970) later considered different forms for the gamma function while Fichera and Chudacek (1992) considered the discrete form to have greater physical significance than either the continuous or gamma functional forms. Particle floatability models allow for flexibility in the analysis of flotation kinetics but are applicable to complex systems where extreme variations in mineralogy and surface properties justify their usage.

1.4.1.3 Double Parameter Models

Double parameter models account for differences in the surface properties of particles of the same size by including both particle size and particle floatability into the flotation rate expression. The earlier models consider each particle size fraction to consist of only floatable and non-floatable fractions (Morris, 1952). Kelsall (1961) later introduced the concept of fast and slow floating fractions as an alternative to floatable/non-floatable particles. Fichera and Chudacek (1992) proposed that the overall flotation rate could be best determined by applying the graphical solution of Imaizumi and Inoue (1963) to each particle size fraction. Double parameter models allow for greater flexibility in the analysis of flotation kinetics than single parameter models but are applicable to very complex systems.

1.4.1.4 Multiphase Models

Multiphase models do not consider the flotation cell to be a single uniform system but divide the cell into a number of components or phases, with the simplest being a pulp and a froth phase. Each phase is then characterised by a separate kinetic expression and the solution to the overall flotation rate is determined by mass transfer between the phases. Arbiter and Harris (1962) were the first to consider multiphase kinetics and multiphase models have subsequently been developed by a number of other researchers (Harris, 1978; Hanumanth and Williams, 1992). Multiphase models are particularly suited to systems where the froth phase has a limiting influence on flotation kinetics.

1.4.2 Flotation Microkinetics

The following overview of flotation microkinetics discusses the fundamental subprocesses of flotation occurring in both quiescent and turbulent systems. The bulk of fundamental flotation research has, however, focused on relatively simple quiescent systems and the overview is largely

derived from these findings. Figure 1.3 depicts the interaction between a particle and a bubble rising through a flotation cell and will be used as a basis for discussion.

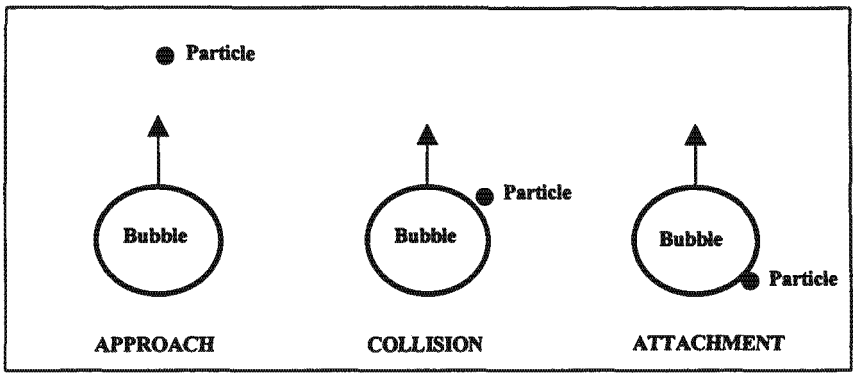

Figure 1.3. Interaction between a particle and a bubble in a flotation cell.

Derjaguin and Dukhin (1961) were the first to distinguish three zones of approach of a particle to a bubble and termed these the hydrodynamic, diffusiophoretic and interparticulate zones of interaction. Though most researchers acknowledge both hydrodynamic and interparticulate forces, there is no unequivocal evidence for the existence of diffusiophoretic forces (Laskowski, 1989). The following brief overview of hydrodynamic and interparticulate forces is based on reviews by Ralston (1983), Schulze (1989), Churaev (1991) and Schimoller *et al* (1993).

Hydrodynamic Forces and Effects: Interceptional effects are caused by fluid streamlines around bubbles and result in particles following streamlines preferentially, thus restricting particle-bubble collision. Interceptional effects are partly countered by gravitational and inertial effects, both of which cause particles to deviate from streamlines and thus promote particle-bubble collision. In the final stages of approach streamline and resistance forces, caused by streamlines near the bubble surface, come into effect. The streamline force tends to drive particles against bubbles while the resistance force resists particle movement towards the bubble surface. In addition to these hydrodynamics forces, more subtle influences such as turbulent wake, diffusional and bubble cloud effects contribute to particle-bubble interactions in certain systems.

Interparticulate Forces and Effects: Interparticulate forces are relatively short range interactions between particles and bubbles and are controlled by largely surface phenomena. Electrostatic forces occur as a result of interaction between the electrical double layers of particles and bubbles and can influence flotation significantly as they are normally repulsive. Dispersion forces are molecular forces occurring as a result of London and Van Der Waal's interactions and can also influence flotation as they too are normally repulsive. Hydrophobic forces occur as a result of the adsorption

of surfactants at bubble and particle interfaces and are considered to have a dramatic influence on flotation. Microrheological forces occur as a result of drainage and rupture of the disjoining film and influence the final stages of the attachment process.

From the above overview it is clear that the interaction between particles and bubbles is affected by a large number of long range and short range hydrodynamic and interparticulate forces. Though these forces tend to control the processes of particle-bubble collision and attachment, for a particle to be collected by a bubble and removed from a flotation cell as concentrate all of the following subprocesses must be satisfied:

1. The particle must collide with the bubble.
2. The disjoining film separating the particle and the bubble must thin, rupture and recede to form a stable contact angle.
3. The particle-bubble aggregate must be sufficiently stable to withstand external stresses in the flotation cell caused by turbulence.
4. The particle-bubble aggregate must transition into the froth layer and be transported through this layer until removed from the flotation cell.

The first three of these subprocesses are termed collision, attachment and detachment respectively (Sutherland, 1948) and apply to collection zone kinetics while the fourth applies to froth zone kinetics. Since Sutherland's pioneering work in this field most researchers consider the probability of particle-bubble collection (P_{coll}) to be the product of the three independent probabilities of collision (P_c), attachment (P_a) and detachment (P_d), viz. Equation 1.5.

$$P_{coll} = P_c P_a (1 - P_d) \quad (1.5)$$

The probabilities of collision, attachment and detachment in Equation 1.5 are central to the analysis of flotation microkinetics and will be reviewed separately in Sections 1.4.2.1 to 1.4.2.3 respectively.

1.4.2.1 Collision

Collision between particles and bubbles is controlled by predominantly hydrodynamic forces and can be predicted by the principles of fluid dynamics (Schimoller *et al*, 1993). Collision is commonly measured in terms of the probability of collision (P_c) which is defined as the ratio of the

number of particles encountering a bubble to the number of particles approaching the bubble in a flow tube of equivalent diameter. As the models and theories for collision in turbulent and quiescent systems are of sufficiently different origin they will be treated separately, though this distinction is seldom identified or considered in the analysis of kinetic data in the flotation literature.

1.4.2.1.1 Quiescent Systems

Over the past half century various attempts at modelling the probability of collision in terms of predominantly hydrodynamic forces have been undertaken. Initial attempts concentrated on including interceptional effects in well defined Stokes and potential flow fields while later attempts included interceptional, gravitational and inertial effects in Stokes, intermediate and potential flow fields. The challenge in this comparatively mature area of research is to develop a unified model for collision including both hydrodynamic and surface forces.

Sutherland (1948) derived an expression for the probability of collision in a potential flow field including interceptional effects only (viz. Equation 1.6) but this expression is limited as it is applicable to bubbles much larger than those used in flotation practice (viz. d_b>>1.0 mm).

$$P_c = 3\frac{d_p}{d_b} \quad (1.6)$$

Gaudin (1957) derived a similar equation to Sutherland's for a Stokes flow field (viz. Equation 1.7) but this expression is also limited as it is applicable to bubbles smaller than those used in flotation practice.

$$P_c = \frac{3}{2}\left(\frac{d_p}{d_b}\right)^2 \quad (1.7)$$

Flint and Howarth (1971) solved the Navier Stokes equations numerically to determine the probability of collision for both Stokes and potential flow fields including interceptional, gravitational and inertial effects. The probability of collision was found to be strongly dependent on inertial forces for large particles and to increase with increasing bubble size but was found to increase with decreasing bubble size for small particles. Flint and Howarth also calculated significantly higher probabilities of collision for particles in a bubble swarm than for single

particle-bubble systems due to streamline straightening effects. Woodburn *et al* (1971) modelled the probability of interception of a particle by a bubble as an exponential function of the particle size, the bubble size and the particle-bubble relative velocity. Reay and Ratcliff (1973) modified the approach of Flint and Howarth (1971) and modelled particle collection for both collision and diffusion including interceptional and gravitational effects. The probability of collection for very fine particles (-20 micron) and very small bubbles (-100 micron) was calculated and an expression of the general form given in Equation 1.8 was proposed.

$$P_c \propto \left(\frac{d_p}{d_b}\right)^n \quad (1.8)$$

The power on this equation (n) was found to be dependent on the particle to fluid density ratio and varied from 1.9 to 2.05 with density ratios from 1.0 to 2.5. Reay and Ratcliff attempted to validate their simulations experimentally through the flotation of glass beads and latex particles in a Hallimond tube but found poor correlations for latex which was ascribed to the influence of electrical or surface forces. Reay and Ratcliff also found the probability of collision to go through a minimum at a particle size of about 1 micron and ascribed this to the transition in the control of the system from hydrodynamic to diffusional forces.

Anfruns and Kitchener (1977) calculated the probability of collision numerically for both Stokes and potential flow fields including interceptional, gravitational and electrostatic effects. The probability of collision was found to be proportional to the particle diameter squared, though it was hypothesised that collision theories based on idealised, smooth particles would always give incorrect predictions as rough or angular particles facilitate film drainage and rupture. Weber and Paddock (1983) derived an expression for the probability of collision for the intermediate flow field including interceptional and gravitational effects. This expression enabled realistic probabilities of collision to be determined for the first time as the intermediate flow field is applicable to bubbles of the size used in flotation practice. Jiang and Holthum (1986) modified the approach of Reay and Ratcliff (1973) and solved the equations of motion numerically for the intermediate flow field including an additional "added mass force" to account for the small mass of fluid associated with a particle. An expression similar to Equation 1.8 was derived and the power on this equation (n) was found to vary from 1.23 to 2.08 for 50 to 80 micron bubbles and to remain approximately constant at 2.0 for 280 to 860 micron bubbles. The probability of collision was found to be insensitive to changes in bubble size for -20 micron particles down to bubbles of approximately 300 microns in size. Luttrell *et al* (1988), Yoon and Luttrell (1989) and Yoon (1991) derived an expression for the

probability of collision for the intermediate flow field including interceptional, gravitational and inertial effects, viz. Equation 1.9.

$$P_c = \left(\frac{3}{2} + \frac{4N_{Re}^{0.72}}{15}\right)\left(\frac{d_p}{d_b}\right)^2 \quad (1.9)$$

This equation reduces to the expressions derived by both Sutherland and Gaudin for the Stokes and potential flow fields and predicts the probability of collision to be inversely proportional to the bubble size and the bubble size squared for very large and small bubbles respectively. Nguyen Van and Kmet (1992) solved the Navier Stokes equations numerically to calculate the probability of collision for the intermediate flow field and found this to be a function of numerous parameters including the particle and bubble sizes, the Galileo and bubble Reynolds numbers, the bubble slip velocity and the particle settling velocity. Schimoller *et al* (1993) solved a dynamic force balance numerically for the particle-bubble system including both hydrodynamic and surface forces and found that collision could be improved by increasing the particle size, increasing the particle hydrophobicity, decreasing the bubble size and decreasing the particle zeta potential.

1.4.2.1.2 Turbulent Systems

While attempts at modelling collision in quiescent systems have focused on the influence of hydrodynamic forces on the probability of collision, the analysis in turbulent systems has focused on determining the number of particle-bubble collisions per unit volume (i.e. rate of collision) from models based on either the kinetic theory of gases or on turbulent diffusion. Over a decade ago Inoue *et al* (1986) considered the analysis of the interactions between particles and bubbles in turbulent systems to be one of the most attractive areas for research in flotation. Despite this bold assertion, however, research into flotation microkinetics in turbulent systems has not developed in recent years and the models and information in the flotation literature remain the same.

Levich (1962) developed a model for collision based on the assumption that streamlines in a turbulent field are completely deformed and predicted the rate of collision to be proportional to the sum of the particle and bubble sizes cubed. As particles are generally significantly smaller than bubbles in flotation cells, this suggests that flotation kinetics is less strongly influenced by particle size in turbulent systems than in quiescent systems. Mika and Fuerstenau (1968) discussed the forms of microkinetic models required for the analysis of flotation in turbulent systems and were the first to suggest the use of the specific power input rather than the impeller speed to describe

turbulence in flotation cells. Koch (1975), Schubert (1977,1979), Schubert and Bischofberger (1978) and Bischofberger and Schubert (1980) derived an expression for the rate of collision based on Abrahamson's theory for the collision between small particles in a vigorously turbulent field (Abrahamson, 1975), viz. Equation 1.10.

$$N_{pb} = 5N_p N_b (r_p + r_b)^2 \sqrt{\bar{u}_p^{\,2} + \bar{u}_b^{\,2}} \qquad (1.10)$$

The RMS relative velocities of the particles and the bubbles ($\bar{u}_p$ and $\bar{u}_b$) in Equation 1.10 can be calculated from the specific power input through an equation derived by Liepe and Mockel (1976), viz. Equation 1.11.

$$\bar{u}_{p/b} = \frac{0.33\varepsilon^{4/9} d_{p/b}^{\,7/9}}{\nu^{1/3}} \left(\frac{\rho_{p/b} - \rho}{\rho} \right) \qquad (1.11)$$

Equations 1.10 and 1.11 predict an increase in the rate of collision with increasing particle size, bubble size and specific power input, which appears to contradict with the theories for collision in quiescent systems as these show the probability of collision to increase with decreasing bubble size. Reducing the bubble size in Equation 1.10, however, leads to a dramatic increase in the number of bubbles per unit volume and in the corresponding rate of collision. Nonaka *et al* (1982) developed a microkinetic model based on turbulent diffusion by considering the flotation cell to be divided into two compartments and assuming the particle and fluid turbulent diffusivities to be equivalent. By substituting the turbulent diffusion coefficient for Kolmogoroff's diffusion coefficient and including the specific power input and air flow number, Nonaka *et al* derived an expression the flotation rate constant based on turbulent collision, viz. Equation 1.12.

$$k \propto \varepsilon^{0.75} N_{Af}^{\,0.50} \qquad (1.12)$$

This expression was confirmed experimentally by flotation of -35 micron quartz in a batch flotation cell and predicts that the specific power input has a stronger influence on collision than models based on Abrahamson's collision theory. Lyman (1983) analysed the method used by Nonaka *et al* more rigorously and concluded that the particle and fluid diffusivities should not be equated but ought to be calculated from the size distribution of eddies larger than the particle. Jordan and Spears (1990) combined Equation 1.10 with suitable expressions for the probability of attachment and detachment and derived a model for fine particle and fine bubble flotation in agitated flotation

cells. The model was verified experimentally by flotation of chalcopyrite and sphalerite in a batch flotation cell and indicated that both increasing power input and decreasing bubble size increase the rate of flotation dramatically.

1.4.2.2 Attachment

Attachment between particles and bubbles is a complex interaction of both hydrodynamic and surface forces and, other than for certain deformation effects, is equivalent for both quiescent and turbulent systems. The probability of attachment is defined as the fraction of particles which remain attached to bubbles after collision has occurred and is commonly modelled in terms of contact and induction times. The contact time is the time for which a particle and a bubble are in contact after collision while the induction time is the time taken for the disjoining film to drain, rupture and form a stable contact angle (Schimmoller *et al*, 1993). Attachment is sometimes modelled using the energy barrier or activation energy to attachment approach postulated by Laskowski (1989) and used by Yoon (1991) in an Arrhenius type equation.

1.4.2.2.1 Induction Time

Research in this field has focused on measuring the effect of parameters such as temperature, collector addition, pH and frother dosage on induction time (Eigles and Volova, 1960; Yoon and Yordan, 1991). Attempts at modelling the induction time have focused on simulating the microhydrodynamics of film drainage through complex models developed by researchers such as Chen and Slattery (1982), Schulze (1989) and Hewitt *et al* (1993). Despite the sophistication of these models reliable estimates of induction times have to be determined experimentally.

Mackenzie and Matheson (1963) demonstrated that film thickness and induction time may be reduced by increasing particle and bubble velocities through intense agitation. Jowett (1980) simulated film drainage by considering the liquid between two solid disks and found the induction time to be constant for quiescent systems and proportional to the particle size to the power of 1.5 for turbulent systems. Schulze (1989) demonstrated that sharp edged particles can promote film drainage and reduce induction time to the order of the contact time in turbulent systems. Jiang (1988) considered attachment to occur if the dynamic energy of a particle colliding with a bubble exceeded the energy barrier of film rupture and proposed that the probability of attachment should increase with increasing agitation. Laskowski (1989, 1993) found frother dosage to have the most

significant influence on induction time with increasing frother dosage leading to dramatic decreases in induction time.

1.4.2.2.2 Contact Time

As particle-bubble contact time is controlled by predominantly hydrodynamic forces, research in this field has focused on calculating contact time through the principles of fluid dynamics. Sutherland (1948) determined the contact time by calculating the sliding time between a particle and a bubble in a potential flow field. Philippoff (1952) and Evans (1954) derived expressions for the contact time based on the elastic deformation of a bubble on collision with a particle and predicted the contact time to be directly proportional to the particle density and proportional to the particle size to the power of 1.5. Dobby and Finch (1986, 1987) derived an expression for the sliding time for the intermediate flow field and predicted an optimum in the probability of collection as a function of particle size, when this was combined with a suitable expression for the probability of collision. This optimum was found to be dependent on the particle density, bubble size and induction time and was attributed to an increase in the probability of collision, and a corresponding decrease in the probability of attachment, with increasing particle size. Luttrell (1986) and Yoon and Luttrell (1989) used an expression for the sliding time in the intermediate flow field to derive the model for the probability of attachment given in Equation 1.13.

$$P_a = \sin^2\left(2\arctan\left(\exp\left(\frac{45+8N_{Re}^{0.72}U_b t_i}{15d_b\frac{d_b}{1+d_p}}\right)\right)\right) \quad (1.13)$$

This expression predicts both a dramatic increase in the probability of attachment with decreasing particle size and an optimum in the probability of attachment as a function of bubble size due to a conflict between the effects of bubble size and rise velocity on the attachment process. Ye and Miller (1989) developed a combined sliding time and bubble deformation model which predicts an increase in contact time with increasing particle size and shows agitation to have minimal effect on contact time. In addition, the model predicts fine particles to have a floatability equal to or better than large particles and demonstrates that fine particle recovery can be improved by imparting greater momentum to the particle through increased agitation. Schulze *et al* (1989) analysed bubble deformation resulting from contact with a particle and found the contact time to be weakly dependent on the particle-bubble relative velocity but found the induction time to be proportional to

this velocity. Schulze *et al* concluded that particle capture occurs mainly by sliding along the bubble surface as the contact time on direct collision was found to be significantly lower. Nguyen Van (1993) derived a numerical model for particle sliding time valid for the Stokes, intermediate and potential flow fields which was found to compare well with experimental data.

Scheludko *et al* (1976) calculated the minimum floatable particle size based on the critical work of expansion required to initiate a primary hole in the bubble surface. This was found to be inversely proportional to the turbulent relative velocity to the power of 2/3 and the particle density to the power of 1/3 suggesting that there is a lower limit to particle floatability which can be improved by imparting greater momentum to a particle through increased agitation. Rulev (1979) derived a model for the probability of collection for the Stokes flow field including both hydrodynamic and surface forces. The model predicts that the Hamaker constant has a weak influence on the probability of collection but requires the constant to be non-zero for flotation to be feasible. Ahmed and Jameson (1989) considered the derivation of a general expression for contact time in turbulent systems to be complicated by bubble pulsations but proposed that thinning and rupturing of the disjoining film could be increased through agitation. Li *et al* (1990) derived an expression for the probability of attachment in terms of the particle and bubble sizes, the specific power input and various solution/surface parameters such as the London-Van Der Waal constant, viscosity and surface tension (viz. Equation 1.14). Here, the various solution and surface parameters have been omitted for reasons of clarity.

$$P_a \propto \exp\left(\frac{r_p^{3.17} r_b^{1.59} \varepsilon^{0.96}}{(r_p + r_b)^{1.76}}\right) \quad (1.14)$$

This expression was incorporated into a kinetic model for flotation which predicts an optimum in the flotation rate constant as a function of both particle size and specific power input and demonstrates that solution and surface forces can inhibit flotation kinetics.

1.4.2.3 Detachment

Detachment between particles and bubbles is controlled by both the stability of particle-bubble aggregates and external shear stresses in the flotation cell. The analysis of detachment is primarily of relevance to turbulent systems as detachment is negligible in quiescent systems due to the appreciably lower external stresses in quiescent environments. The probability of detachment is

defined as the fraction of attached particles which detach from bubbles in the flotation cell and is equal to one minus the probability of stability or retention.

Morris (1952) derived a relationship between particle size, bubble size and surface tension which predicted the probability of retention to increase with decreasing particle size, increasing bubble size and increasing particle hydrophobicity. Mika and Fuerstenau (1968) analysed detachment in an isotropic turbulent field and found the rate of detachment to be proportional to the particle size to the power of 7/3. Woodburn *et al* (1971) considered detachment to occur by sudden acceleration of a particle-bubble aggregate through eddy motion and found the probability of detachment to be proportional to the particle size to the power of 3/2. Schulze (1977, 1982) derived an expression for the maximum floatable particle size by considering compressive, tensile and shear stresses acting on a particle-bubble aggregate in a turbulent field, viz. Equation 1.15.

$$d_{p\max} = \sqrt{\frac{-6\sigma \sin(180 - \frac{\theta}{2}) \sin(180 + \frac{\theta}{2})}{(\rho_p - \rho)g + \rho_p b_m}} \qquad (1.15)$$

The parameter b_m in the denominator of Equation 1.15 is the vortex acceleration and can be calculated from the specific power input and bubble size (viz. $1.9\varepsilon^{2/3}/d_b^{1/3}$). This expression predicts a decrease in the maximum floatable particle size with decreasing bubble size, increasing specific power input and decreasing contact angle. Schulze considered the process of particle-bubble detachment to be controlled by the impeller zone in agitated flotation cells due to the order of magnitude higher turbulent energy dissipation rates in this region. Jowett (1980) developed a model for the rupture of a particle-bubble aggregate in a turbulent eddy in terms of a centrifugal force or "g factor". The maximum floatable particle size was found to be dependent on the eddy rotation, contact angle and particle density and the probability of detachment was shown to increase with increasing particle size and decreasing bubble size. Nishkov and Pugh (1989) developed an experimental centrifuge technique to measure detachment forces for the galena/quartz system and found the force to decrease with increasing particle size. Holtham and Cheng (1991) considered detachment effects in a vibrating particle-bubble system and concluded that the force affecting detachment from small bubbles is greater than from large bubbles.

1.4.3 Integrating Flotation Macrokinetics and Microkinetics

Analysis of flotation kinetics from a macroscopic perspective is useful as it yields models which have practical application in the design of flotation cells and circuits while analysis from a microscopic perspective is intrinsically more powerful as it provides real information on the subprocesses of flotation. The most suitable method of analysing flotation kinetics should, therefore, combine the practicability of macrokinetics with the insight of microkinetics into a unified model for flotation. Jameson *et al* (1977) derived an expression for the first-order flotation rate constant in terms of the bubble size, the superficial gas velocity and the probability of collection, viz. Equation 1.16.

$$k = \frac{3}{2}\frac{J_g P_{coll}}{d_b} \qquad (1.16)$$

This expression relates the macroscopic quantities (k & J_g) to the microscopic quantities (d_b & P_{coll}) and, consequently, allows for comparison of flotation kinetics between cells with similar flotation micro-environments but different dimensions and gas flowrates. Equation 1.16 has been used by numerous researchers (Yoon, 1991; Ralston, 1992) and is one of the first expressions of its kind to link flotation macrokinetics to microkinetics. The challenge in this field is to develop more comprehensive kinetic expressions which relate microscopic quantities to bulk flotation cell parameters such as power input, cell geometry, operating conditions etc.

1.5 Mechanical Agitation

Mechanical flotation cells are characterised by an impeller which is responsible for the processes of solids suspension, gas dispersion and the generation of turbulence through agitation (Schubert *et al*, 1982). The impeller is incorporated in a rotor-stator assembly situated near the bottom of the cell and pumps aerated slurry, in the form of a strong radial jet, which strikes the cell walls and splits into an upper and lower wall jet. The lower wall jet spreads over the bottom of the cell and aids in solids suspension while the upper wall jet almost reaches the surface before spreading into the surrounding fluid. The two wall jets divide the cell into upper and lower eddy spaces which constitute the bulk of the volume of the flotation cell and are considered to be responsible for significant particle-bubble contacting. Air is introduced into the rotor-stator assembly, either by induced air suction or by an external blower, and accumulates in low pressure cavities behind the impeller blades from which bubbles are sheared off by impeller rotation (Tatterson, 1991). Further

bubble breakup occurs in the highly turbulent conditions in the impeller region following which bubbles are dispersed throughout the cell by the impeller pumping action. Here, bubbles may collide and coalesce, recirculate back into the impeller region or rise into the froth phase.

The classical approach to understanding hydrodynamics and gas dispersion in mechanical flotation cells has been to characterise suitable fluid flow regimes in terms of the types of bulk dimensionless numbers given in Table 1.1 (Mavros, 1992).

Table 1.1. Dimensionless numbers used in characterising mechanical flotation cells.

Dimensionless Number	Expression	Physical Interpretation
Power Number (N_{Pw})	$\frac{P}{\rho N^3 D^5}$	Ratio of actual to theoretical power input.
Air Flow Number (N_{Af})	$\frac{Q}{ND^3}$	Ratio of air flowrate to impeller pumping rate.
Froude Number (N_{Fr})	$\frac{N^2 D}{g}$	Ratio of inertial to gravitational forces.
Reynolds Number (N_{Re})	$\frac{\rho N^2 D}{\mu}$	Ratio of inertial to viscous forces.
Weber Number (N_{We})	$\frac{N^2 D^2}{\sigma}$	Ratio of inertial to surface tension forces.

A number of useful empirical relationships for the design and scale-up of flotation cells have been developed using these dimensionless numbers. These relationships do not, however, consider the fundamental subprocesses such as bubble breakup and particle-bubble contacting occurring in the flotation micro-environment. These subprocesses are controlled by the turbulent microstructures in the flotation cell (Inoue *et al*, 1986; Fallenius, 1987) and, consequently, require a detailed knowledge of turbulence and the various turbulence parameters.

1.5.1 Turbulence

Turbulence in mechanical flotation cells has at best been quantified by impeller speed or power input by most researchers and few have considered the types of parameters necessary for a more comprehensive characterisation of turbulence. Exceptions are Nonaka *et al* (1982) and Jordan and

Spears (1990) who measured turbulence parameters such as turbulent fluctuating velocities and energy spectra in batch flotation cells and incorporated these results into microkinetic models for flotation in agitated systems. Both authors considered the turbulent micro-environment in the flotation cell to have a significant impact on both bubble breakup and particle-bubble contacting. Fallenius (1987, 1992) developed an expression for the turbulent fluctuating velocities in terms of parameters such as impeller speed, impeller diameter and tank height and used this as a basis to compare flotation performance in industrial Outokumpu, Wemco, Denver, Minemet and Sala flotation cells. Fallenius considered the turbulent micro-environment in the flotation cell to control particle-bubble contacting and to be applicable to flotation cell scale-up.

1.5.1.1 Turbulent Energy Spectrum

The radial jet of aerated slurry leaving the impeller in a mechanical flotation cell carries energy in the form of kinetic energy into bulk tank which ultimately decays into turbulence in the eddy spaces and is dissipated as heat. The analysis of turbulence from the Navier-Stokes equations is highly complex and is generally limited to computational fluid dynamic (CFD) or direct numerical simulation (DNS) type procedures on simple liquid or gas phase systems. Two more classical approaches to analysing and describing turbulence are the turbulent diffusion and energy spectrum models. The diffusion model measures turbulence in terms of a turbulent diffusivity, analogous to a chemical diffusivity, while the energy spectrum model considers turbulence to be propagated through a continual spectrum of large to small eddies. According to the energy spectrum model large eddies are generated from the bulk flow of fluid and transfer kinetic energy to small eddies by turbulent shear stresses. This process continues progressively from larger to smaller eddies until the initial kinetic energy of the fluid is dissipated in the form of heat in the smallest eddies. The continual flux of energy from larger to smaller eddies results in a turbulent energy spectrum, as illustrated schematically in Figure 1.4.

An energy spectrum may be thought of as a distribution of the energy of turbulence amongst eddies of various frequency or size. The "primary eddies" occur to the extreme left of the spectrum and are the largest eddies, being of a similar scale to the impeller. The "energy containing eddies" occur in the middle of the spectrum and are so named as they incorporate most of the kinetic energy of the system. The "inertial subrange eddies" and "viscous dissipation eddies" constitute the universal equilibrium range which is so termed because the amount of energy transferred by these eddies is large compared to the rate of change of energy of these eddies and consequently they are considered to be statistically independent of the bulk

fluid. The inertial subrange eddies only occur at high levels of turbulence and are sufficiently small to be statistically independent of the bulk fluid and yet sufficiently large to transfer significant kinetic energy through inertial forces. The viscous dissipation range are the smallest eddies in the spectrum and contain the least kinetic energy but dissipate most of the energy of the system as heat.

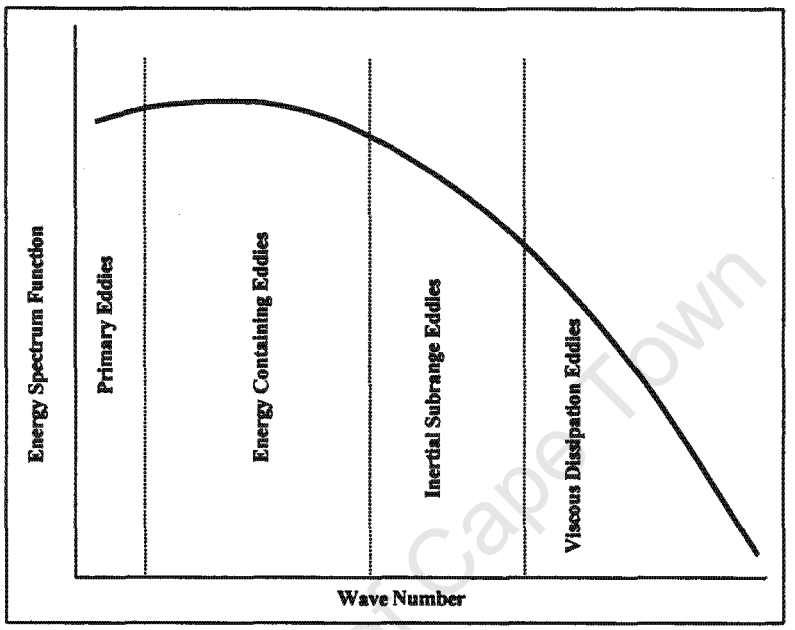

Figure 1.4. Schematic representation of a turbulent energy spectrum.

The determination and analysis of energy spectra is a routine matter for researchers in this field and the following overview is derived from Hinze (1959), Reynolds (1974) and Bradshaw (1978):

The one dimensional energy spectrum in frequency space (E_1) can be obtained from the Fourier transform of the Eulerian autocorrelation coefficient (R_E) of the turbulent velocity fluctuations at a fixed point, viz. Equations 1.17 and 1.18.

$$R_E = \frac{\overline{u'(t)u'(t+\tau)}}{\overline{u}^2} \quad (1.17) \qquad E_1(n) = 2\overline{u}^2 \int_{-\infty}^{+\infty} R_E(\tau) e^{2\pi i n \tau} d\tau \quad (1.18)$$

As the autocorrelation coefficient is a symmetric function, its Fourier transform is a real function and only the cosine part of the integral need be evaluated. Similarly, the autocorrelation coefficient can be obtained from the inverse Fourier transform of the energy spectrum function. The two are therefore Fourier transform pairs and contain equivalent information about the nature of the

turbulent system. The autocorrelation coefficient is commonly used for determining the macro and micro time scales of turbulence and for identifying any large scale periodic fluctuations in the flow.

1.5.1.2 Turbulence Parameters

The turbulent energy spectrum can be used to determine a number of turbulence parameters which are commonly used for comparing and describing the level of turbulence. Employing Equations 1.17 and 1.18 one can demonstrate that the integral over all frequencies of the energy spectrum function gives the mean squared turbulent velocity (viz. Equation 1.19). The square root of this quantity is termed the RMS (root-mean-square) turbulent velocity and is one of the most significant parameters describing turbulence as it appears in both descriptions of turbulent microstructures and theories of particle-particle and particle-bubble collision (Schubert *et al* 1982).

$$\overline{u}^2 = \int_0^\infty E_1(n)dn \qquad (1.19)$$

The Eulerian macro time scale (T_E) and micro time scale (τ_E) can be obtained from the energy spectrum function according to Equations 1.20 and 1.21 respectively.

$$T_E = \frac{E_1(0)}{4\overline{u}^2} \qquad (1.20) \qquad \tau_E{}^2 = \frac{\overline{u}^2}{2\pi^2 \int_0^\infty n^2 E_1(n)dn} \qquad (1.21)$$

Though the energy spectrum in frequency space gives information on the time scale of eddies, it is necessary to have a knowledge of the space scales of eddies in order to determine physical interactions in most systems. This can be achieved through the Fourier transform of the spatial correlation coefficient but this is a difficult process and it is common to transform the energy spectrum in frequency space to that in wave number space by assuming Taylor's "frozen field" hypothesis. Taylor's hypothesis assumes that the autocorrelation may be equated to the spatial correlation through the mean fluid velocity in turbulent systems where the mean fluid velocity is large in comparison to the fluctuating velocity (u/U<0.10). Local convection velocities should, however, be used to transform time scales to length scales in high intensity turbulent shear flows instead of local mean fluid velocities (Wu and Patterson, 1989). Taylor's hypothesis has, however, been applied by a large number of researchers (Sato *et al*, 1967; Mujumdar *et al*, 1970; Rao and Brodkey, 1972; Barthole *et al*, 1983) and mean fluid velocities are used in this study. Under

Taylor's hypothesis the one dimensional energy spectrum in wave number space can be obtained by multiplying the frequency spectrum by $U/2\pi$ and similarly the frequency can be converted to wave number by multiplying by $2\pi/U$.

The Eulerian longitudinal macro length scale (Λ_f) and micro length scale (λ_f) can be obtained from the product of mean fluid velocity (U) and the applicable time scales. The macroscale is a measure of the size of the large energy containing eddies while the microscale is a measure of the smallest (most frequent) eddies in the turbulent field. The turbulent energy dissipation rate (ε) can be determined from either the turbulent microscale or the resultant turbulent macroscale through Equations 1.22 and 1.23 respectively.

$$\varepsilon = \frac{30\nu\overline{u}^2}{\lambda_f^{\,2}} \quad (1.22) \qquad \varepsilon = 0.85\frac{q^{3/2}}{\Lambda_R} \quad (1.23)$$

Equation 1.22 has been used by researchers such as Rao and Brodkey (1972), Komasawa *et al* (1974) and Okamata *et al* (1981) but is limited by inaccuracies and difficulties in determining the turbulent microscale. Equation 1.23 was established by Wu and Patterson (1989) but originated from Townsend (1976) and Tennekes (1977) through a proposal by Batchelor (1953) who considered, on dimensional grounds, that the turbulent energy dissipation rate could be obtained from the product of an empirical constant and the RMS turbulent velocity cubed divided by the turbulent macroscale. Equations of this form avoid the inaccuracies in the measurement of the turbulent microscale and have been used by researchers such as Brodkey (1975) and Laufhütte and Mersmann (1987).

The one dimensional energy spectrum and associated turbulence parameters are useful for describing the nature of turbulence in a specific direction. Turbulence is always three dimensional due to the method of propagation of eddies and a complete characterisation of a system requires the energy spectrum in three dimensional wave number space. However, the one dimensional spectrum is sufficient to describe the system completely for isotropic turbulence as the energy spectrum in all directions is equivalent. Similarly, the one dimensional spectrum is suitable for isotropic turbulence in the wave number range of the physical phenomenon of interest (Ogawa, 1992).

1.5.2 Bubble Breakup and Coalescence

The equilibrium bubble size distribution in a flotation cell is a consequence of the interaction between the processes of bubble breakup and coalescence and the hydrodynamics of the flotation cell. This is a poorly understood area of research in flotation but has been thoroughly investigated in the chemical and bio-chemical industries over the past two decades. The main body of research has been on drop size in stirred liquid-liquid dispersions (Kumar *et al*, 1991), bubble size in bioreactors (Alvarez, 1992), bubble size in bubble column reactors (Prince and Blanch, 1990) and bubble size in stirred, aerated systems (Parthasarathy and Ahmed, 1994). The principles and correlations derived from these areas of research are similar and have common theoretical basis despite the broad variation in processes. The majority of these systems have, however, been modelled on overall vessel average parameters such as power input rather than on measured turbulence parameters and few of the systems have been of the non-coalescing nature found in flotation.

1.5.2.1 Bubble Breakup

Most of the literature on bubble breakup has focused on the prediction of the maximum stable bubble size which is defined as the size below which a bubble will not break if placed in a field of a given turbulent intensity for an infinite time (Hesketh *et al*, 1991). In gas-liquid dispersions bubbles have a comparatively short residence time in the system and the maximum stable bubble size is approached as limiting quantity with increasing gas residence time.

One of the most widely accepted models for bubble breakup is the turbulent pressure fluctuation model proposed by Hinze (1955) who considered breakup to occur due to disruptive inertial stresses caused by dynamic pressure fluctuations. The process of bubble breakup is therefore controlled by relative velocity fluctuations across the drop diameter which, in an isotropic field, are correlated to the turbulent energy dissipation rate. Breakup of the bubble occurs when these disruptive inertial stresses exceed the stabilising elastic stresses due to surface tension through a critical ratio referred to as the critical Weber number (N_{Wec}), viz. Equation 1.24.

$$N_{Wec} = \frac{2\rho\varepsilon^{2/3} d_{bm}^{5/3}}{\sigma} \qquad (1.24)$$

The magnitude of the critical Weber number depends on a particular flow geometry with a value of 1.2 originally obtained by Hinze for droplet breakup in Couette flow while a range of values of between 0.9 and 4.7 were reported by Parthasarthy *et al* (1991). Though this model was originally developed to describe drop breakup in emulsification, it has been modified and/or successively applied to gas-liquid dispersions by a number of researchers (Hesketh *et al*, 1991; Parthasarathy *et al*, 1991).

Another theory for bubble breakup originally proposed by Hinze is that breakup occurs due to the collision of a bubble with a turbulent eddy of comparable dimension to the bubble. The process of bubble breakup is therefore controlled by the turbulent kinetic energy of eddies of similar scale to the bubble. Models for bubble breakup based on this principle have been developed and applied to both liquid-liquid dispersions (Coulaloglou and Tavlarides, 1977; Tsouris and Tavlarides, 1994) and gas-liquid dispersions (Prince and Blanch, 1990). Middleman (1974) proposed that the maximum stable bubble size is related to the ratio of the turbulent kinetic energy of eddies smaller than the bubble size, in a fluid element equal to the bubble volume, to the surface energy of the bubble, viz. Equation 1.25.

$$d_{bm} = f\left(\frac{\rho d_{bm}^{3}\int_{1/d_{bm}}^{\infty} E_1(k)dk}{6\sigma d_{bm}^{2}}\right) \qquad (1.25)$$

This equation can only used in rare instances where the energy spectrum has been measured and there is little experimental data to corroborate its applicability (Clift *et al*, 1992).

1.5.2.2 Bubble Coalescence

When two bubbles coalesce in a turbulent flow they initially collide and trap a small film of liquid which drains until reaching a critical thickness at which point rupture followed by coalescence occurs. Coalescence is therefore affected by a combination of the rate of turbulent collision and the microhydrodynamics of film drainage and rupture. Rates of coalescence and expressions for the minimum bubble size stable against coalescence have been determined by researchers (Prince and Blanch, 1990; Kawase and Moo-Young, 1990) but these are not relevant to most flotation cells as these are considered to be non-coalescing systems due to the addition of surfactants such as frothers.

1.6 Effect of Particle Size, Bubble Size and Agitation on Flotation Kinetics

From the overview of flotation kinetics and mechanical agitation in Sections 1.4 and 1.5 it is evident that the particle and bubble sizes and the level of agitation are three of the most important factors affecting collection zone kinetics in mechanically agitated flotation cells. Though many other chemical and physical factors appear in the various theories and correlations discussed in these sections, the particle and bubble sizes and the level of agitation consistently predominate in their influence on flotation kinetics. Consequently, theoretical and experimental findings applicable to the impact of these parameters on flotation kinetics are reviewed in Sections 1.6.1 and 1.6.2 respectively.

1.6.1 Review of Theoretical Findings

The following section summarises the theoretical effects/influences of particle size, bubble size and agitation on the subprocesses of flotation and is derived predominantly from the discussion of flotation microkinetics in Section 1.4.2.

Collision: Collision is the primary and arguably most important of the subprocesses of flotation and has received considerable theoretical attention for both quiescent and turbulent systems. The analysis of collision in quiescent systems has shown the probability of collision to be proportional to the ratio of the particle and bubble sizes to the power of between 1.0 and 2.0 depending on the flow field. The analysis of collision in turbulent systems has focused on correlating the number of particle-bubble collisions to the sum of the particle and bubble sizes and various parameters describing the level of turbulence. Models that have been derived suggest that the number of collisions is proportional to the sum of the particle and bubble sizes to the power of between 2.0 and 3.0 and to the specific power input to the power of between 0.50 and 0.75.

Attachment: Attachment is considered to be more complex than collision and similar analyses have been applied to both quiescent and turbulent systems. The induction time has been shown to either remain constant or decrease with decreasing particle size. The contact time has been shown to increase with decreasing particle and bubble size for quiescent systems but has yielded conflicting results in turbulent systems. Some researchers have shown the contact time to decrease with decreasing particle size, others have calculated the contact time to be too short for attachment to occur while still others concluded that turbulence does not influence the contact time significantly. The probability of attachment has been shown to increase with decreasing particle and bubble size

in both quiescent and turbulent systems. Several researchers have hypothesised that the probability of attachment increases with increasing agitation due to more efficient rupture of the disjoining film.

Detachment: The analysis of detachment is of relevance to turbulent systems only as buoyancy of the particle-bubble aggregate is of more relevance to quiescent systems than detachment effects. Initial research focused on particle size effects and found the probability of detachment to be proportional to the particle size to the power of between 1.5 and 2.0. Subsequent researched focused on predicting the stability of particle-bubble aggregates in terms of parameters such as particle size, particle density, bubble size, contact angle and level of turbulence. From this analysis the probability of detachment has been shown to increase with increasing particle size and density, decreasing bubble size and increasing level of agitation.

1.6.2 Review of Experimental Findings

The following section summarises the experimental findings of the effects of particle size, bubble size and agitation on flotation kinetics and is derived from a review of the last half century of flotation research in this field.

1.6.2.1 Particle Size

One of the first studies on the effects of particle size on flotation was by Gaudin *et al* (1931) who analysed the recoveries of lead, zinc and copper sulphides and found an optimum particle size range between 10 and 50 microns. In a later study Gaudin *et al* (1942) found the rate of flotation to be independent of particle size for -4 micron galena particles. Morris (1952) conducted batch flotation tests on -250 micron pyrite, pyrrhotite and copper particles and also confirmed the existence of an optimum particle size range. In addition, Morris found the rate of flotation to vary with the natural log of the particle size for particles on the fine side of the optimum range but to be directly proportional to particle size for particles on the coarse side of the range. De Bruyn and Modi (1956) performed batch flotation tests on 5 size fractions of 5 to 254 micron quartz and discovered an optimum particle size range between 10 and 37 microns. The flotation rate constant was found to be proportional to the particle size to the power of between 1.0 and 3.2 for the -65 micron and 79-254 micron size ranges respectively. Eigeles and Volova (1960) measured the induction time of a wide range of minerals and found this to decrease rapidly with decreasing

particle size. In these experiments the -10 micron particles were found to adhere too rapidly to be detected by the experimental apparatus ($t_i<10^{-4}$ s) which suggests that the flotation of fine particles is not limited by attachment.

An exception to the general trend of a strong dependence of the rate of flotation on particle size was evidenced by the work of Bushell (1962) who found this to be independent of particle size. Tomlinson and Fleming (1963) conducted flotation tests on apatite, haematite, galena and quartz in a Hallimond tube and found the rate of flotation to be proportional to the particle size for quartz but to be proportional to the particle size squared for the other minerals. Reay and Ratcliff (1975) investigated the effects of very small bubbles on the flotation of -20 micron glass beads and 5 micron latex particles in a stirred cell and found the flotation rate constant to be proportional to the particle size to the powers of 0.44 and 1.5 for latex and quartz respectively. Collins and Jameson (1976) performed flotation tests on -20 micron polystyrene beads in a dissolved air flotation cell and found the flotation rate constant to be proportional to the particle size to the power of 1.5. In addition the particle and bubble zeta potentials were found to have an enormous effect on the magnitude of the flotation rate constant, but to have minimal effect on the particle size dependence. Anfruns and Kitchener (1977) measured absolute rates of capture of 10 to 50 micron glass beads and quartz particles and found the experimental rate of flotation of quartz to be in close agreement with theoretical collision rates. Jameson *et al* (1977) summarised the work of Collins and Jameson (1976), Reay and Ratcliff (1975) and Anfruns and Kitchener (1977) and concluded that the flotation rate constant was proportional to the particle size to the power of 1.5 for small particles and bubbles and to the power of 2.0 for medium sized particles and bubbles. Crawford and Ralston (1988) conducted flotation tests on 15 to 125 micron methylated quartz in a Hallimond tube and found the flotation rate constant to be approximately proportional to the particle size. Diaz-Penafiel and Dobby (1994) performed flotation tests on -50 micron silica, pyrite and galena in a flotation column and found an optimum in the flotation rate constant as a function of both particle and bubble size. This optimum was shown to shift to larger particle sizes when using small bubbles, indicating that the relationship between the flotation rate constant and the particle size is influenced by the bubble size.

Most of the early fundamental experimental work concentrated on flotation kinetics in idealised, quiescent systems. Researchers investigating flotation kinetics in agitated systems in later years found a weaker dependence of the flotation rate constant on particle size (Cameron *et al*, 1971; Ralston, 1983) which corresponds with results from industrial mechanical flotation cells (Jameson, 1984). Trahar (1981) conducted batch flotation tests on a range of -50 micron base metal sulphides and found the flotation rate constant to vary linearly with particle size. These findings were

supported by Ahmed and Jameson (1985) who measured the flotation rate constant for various size fractions of -50 micron latex, quartz and zircon in an agitated flotation cell and found the flotation rate constant to be less strongly dependent on the particle size than most previous work had suggested. Similar findings were reported by Luttrell (1986) in the flotation of -8 micron quartz, Spears and Jordan (1989) in the flotation of -40 micron galena and Jordan and Spears (1990) in the flotation of -20 micron chalcopyrite.

Although most research on the effect of particle size on flotation kinetics has concentrated on the flotation rate constant, a number of researchers have investigated the actual subprocesses of flotation. Kirchberg and Topfer (1965) photographed particles and bubbles colliding in a mechanical flotation cell and observed the coarse or energetic particles to collide with bubbles and rebound immediately while fine particles were observed to follow the fluid streamlines. Blake and Ralston (1985) investigated the influence of collector surface coverage and contact angle on the flotation response of methylated quartz particles and found a minimum contact angle below which particles did not float and which was found to increase with decreasing particle size. Schulze (1989) considered both theoretical and experimental findings and concluded that the contact time during pure collision followed by deformation of the bubble surface was too short for flotation to occur. Schulze concluded that only collision by the particle followed by sliding along the bubble surface could result in sufficiently long contact times. Bergelt *et al* (1992) confirmed the predictions of Schulze by studying the collision of bubbles with 200 to 900 micron methylated glass and lead spheres and observed no attachment to occur during collision in the normal direction.

1.6.2.2 Bubble Size

In two of the first studies on bubble size, Bennet *et al* (1958) and Brown (1965) found that decreasing the bubble size led to an increase in the flotation rate constant for coal particles. Reay and Ratcliff (1975) found the flotation rate constant to be inversely proportional to the bubble size to the powers of 0.44 and 1.5 for latex and quartz respectively while Anfruns and Kitchener (1977) found this power to be 2.69 for the flotation of glass beads and quartz. Jameson *et al* (1977) found the flotation rate constant to be inversely proportional to the bubble size for small bubbles and to the bubble size to the power of 2.67 for medium sized bubbles. Schubert and Bischofberger (1978) found that decreasing the bubble size led to an increase in the rate of flotation of tin in both laboratory and industrial mechanical flotation cells. Bogdanov *et al* (1980) performed flotation tests on 3 size fractions of -40 micron martite in both quiescent and agitated flotation cells and found an

optimum in the rate of flotation as a function of bubble size for the -20 micron size fraction but not for the coarser fractions.

Ralston (1983) reviewed both theoretical and experimental evidence for the probability of collision and concluded that, though theory predicts this to be proportional to the particle to bubble size ratio to the power of 1.5 to 2.0, industrial results indicate a value closer to unity. Ahmed and Jameson (1985) found poor flotation performance with large or dense particles and small bubbles in a vigorously agitated flotation cell and proposed the existence of an optimum particle to bubble size ratio for agitated systems. Szatkowski and Freyberger (1985) conducted flotation tests on -20 micron quartz using 35 to 100 micron bubbles in both quiescent and agitated flotation cells and found that small bubbles were quickly overloaded with particles. Yoon and Luttrell (1986) found the flotation rate constant to be inversely proportional to the bubble size to the power of 2.1 to 2.3 for the flotation of coal with 300 to 450 micron bubbles and confirmed both the findings and conclusions of a previous study by Ahmed and Jameson (1985). In a later study Yoon and Luttrell (1989) found a dramatic increase in the rate of flotation when using -100 micron bubbles in a quiescent system. Diaz-Penafiel and Dobby (1994) found the rate of flotation to be independent of bubble size for -5 micron particles but to be strongly dependent on bubble size with increasing particle size above this value. The flotation rate constant was found to be inversely proportional to the bubble size to the powers of between 1.15 and 2.08 for the 5 to 40 micron particle size range and an optimum particle to bubble size ratio was observed.

Kirchberg and Topfer (1965) measured a maximum bubble speed of 2 to 10 cm/s above which particles were shown to rebound off the surface of a bubble. Flint and Howarth (1971) found that bubbles in swarms result in higher rates of flotation than single bubbles and proposed this to be due to streamline straightening effects. Holthum and Cheng (1991) postulated that the oscillation and vibration of bubbles in agitated flotation cells could lead to increased detachment. Holtum and Cheng measured the force of detachment experimentally and found the force to increase with increasing bubble size for large particles but to be independent of bubble size for small particles.

1.6.2.3 Agitation

In one of the first studies on agitation Sun and Zimmerman (1950) investigated the effects of impeller speed on the flotation of coal and galena. An optimum in recovery as a function of both impeller speed and particle size was found and observed to move to lower impeller speeds with increasing particle size. Arbiter and Harris (1962) proposed that bubble oscillations and vibrations

in turbulent systems promote both collision and detachment but did not validate this hypothesis experimentally. Mackenzie and Matheson (1963) found an increase in the rate of flotation with increasing impeller speed for individual particle size fractions. Kirchberg and Topfer (1965) confirmed this finding but also observed an optimum in impeller speed after which the rate of flotation began to decrease. Harris and Raja (1970) concluded that high power inputs lead to high rates of flotation. Schubert and Bischofberger (1978) found an increase in the recovery of tin with increasing impeller speed and established optimum power inputs for different particle size fractions. Bogdanov *et al* (1980) found an optimum in the flotation rate constant as a function of both impeller speed and bubble size for -10 micron martite. The optimum was found to occur at the highest impeller speed used in the study for 200 micron bubbles while increasing impeller speed resulted in a continual decrease in the flotation rate constant for 800 micron bubbles. Malhotra *et al* (1980) performed flotation tests on molybdenite in a mechanical flotation cell and found an increase in the rate of flotation with increasing impeller speed for fast floating particles but observed no response for slow floating particles.

Schubert *et al* (1982) postulated that the flotation of fine particles is primarily limited by collision and concluded that fine particle recovery could be improved by agitation. Schubert *et al* considered fine particles to damp turbulence at high percent solids thus limiting the collision process further. Varbanov (1984) performed flotation tests on 4 size fractions of 63 to 500 micron glass spheres in a mechanical flotation cell and found a distinct optimum in recovery as a function of both impeller speed and particle size. Ahmed and Jameson (1985) found an optimum in the flotation rate constant as a function of impeller speed, particle size and density and bubble size. An increase in agitation was found to lead to a decrease in the flotation rate constant for large or dense particles and small bubbles. Ahmed and Jameson hypothesised that the decrease in the flotation rate constant was due to increased particle-bubble detachment through small bubbles being subject to rapid rotation on being caught up in small, high frequency eddies.

Schulze *et al* (1989) suggested that improved flotation performance could be obtained in quiescent environments as the collision in mechanical flotation cells was considered to result in insufficient contact time for attachment. Scheiner and Jordan (1989), Spears and Jordan (1989) and Jordan and Spears (1990) investigated the effects of turbulence on flotation kinetics in a batch flotation cell agitated by a standard impeller and a spinning disc impeller. The flotation rate constant was found to increase with increasing power input for both impellers, though the spinning disc impeller resulted in higher flotation rate constants at a lower power inputs due to the production of very small bubbles. From considerations of the power inputs used in the study it was concluded that agitation leads to an increase in the flotation rate constant for bubbles of constant size. Jordan and

Susko (1992) studied the flotation of coal in a bubble injected hydrocyclone and a mechanical flotation cell and proposed that turbulence should lead to improved flotation performance in mechanical cells. Li *et al* (1993) found an increase in the rate of flotation of both quartz and galena with increasing in impeller speed in a batch flotation cell.

1.7 Scope and Objectives of Thesis

From the reviews presented in Sections 1.1 to 1.6 it should be clear that extensive fundamental research has been conducted into flotation kinetics in quiescent systems but that comparatively little fundamental research has been conducted into flotation kinetics in turbulent/agitated systems. In addition, it should be clear that particle size, bubble size and level of agitation are three of the most important fundamental variables affecting flotation kinetics in turbulent/agitated systems. Consequently, the primary objective of this thesis is to investigate the effects of particle size, bubble size and level of agitation on flotation kinetics in a laboratory batch flotation cell. It is believed that achieving a better understanding of the effects of these variables on flotation performance will lead to improved operation, design and scale-up of mechanically agitated flotation cells. As flotation performance in mechanical flotation cells is dependent on the processes of hydrodynamics, gas dispersion and flotation kinetics, these are investigated separately in the thesis, viz.:

1. *Hydrodynamics:* The flotation cell is agitated by an impeller which is responsible for generating bulk flow patterns and turbulence. In this thesis the influence of agitation on bulk flow properties and turbulence parameters is determined by comparing the hydrodynamic performance of a standard Rushton turbine impeller and a novel high speed spinning disc. In addition, in this thesis the influence of aeration and bubble size on these properties is investigated by comparing the hydrodynamic performance of the two impellers in an unaerated flotation cell and a cell aerated with bubbles of different sizes.
2. *Gas Dispersion:* The impeller disperses gas in the flotation cell through a combination of bulk flow patterns and the generation of turbulence which is responsible for the process of bubble breakup. In this thesis the influence of agitation on bulk gas phase parameters and the process of bubble breakup is investigated by comparing the gas dispersion performance of the standard Rushton turbine impeller and the high speed spinning disc.
3. *Flotation Kinetics:* Particle-bubble contacting in the collection zone of the flotation cell is controlled by turbulence and the bubbles originating from the process of breakup. In this thesis the influence of agitation on particle-bubble contacting is investigated by comparing the

flotation performance of the standard Rushton turbine impeller and the high speed spinning disc using particles and bubbles of different sizes.

The recovery of fine particles in flotation is notoriously poor and represents a major loss of revenue and an unnecessary waste of the world's valuable and steadily declining mineral reserves. These losses are expected to compound in the coming decades as, due to the preferential processing of high quality ores, mining companies are forced to treat more and more complex and finely disseminated ore bodies. Consequently, the focus of this thesis is primarily on the flotation of fine particles (-30 micron) with the aim of determining optimum conditions for fine particle flotation.

CHAPTER 2: EXPERIMENTAL

In order to achieve the objectives outlined in Section 1.7 it was necessary to design, characterise and perform flotation tests in a laboratory flotation cell in which it was possible to determine pure collection zone kinetics and to vary particle size, bubble size and level of agitation independently. The design of the flotation cell is described in Section 2.1, the precharacterisation of hydrodynamics and gas dispersion in the flotation cell is outlined in Section 2.2 and the flotation experiments are discussed in Section 2.3. Results from the characterisation of hydrodynamics and gas dispersion are summarised in Tables A1 to A8 in Appendix A and are discussed in detail in Chapter 4.0. Results from the flotation experiments are summarised in Tables B1 to B12 in Appendix B and are discussed in detail in Chapter 5.0.

2.1 Batch Flotation Cell

The flotation cell chosen for the study was based on that originally used by Ahmed and Jameson (1985) and is depicted in Figure 2.1. The flotation cell specifications are listed in Table 2.1 and are discussed individually thereafter.

Table 2.1. Batch flotation cell specifications.

Tank Specifications	Impeller Specifications	Sintered Disc Specifications	
V = 2.25 litre	Rushton Turbine	Disc	Pore Size (μm)
T = 140 mm	D = 47 mm	Porosity 1	101-160
H:T = 1:1	W:L:D = 4:5:20	Porosity 3	17-40
B:T = 1:10	Spinning Disc	Porosity 4	11-16
	D = 74 mm W = 5 mm		

Tank: The tank was of cylindrical Perspex construction with four equispaced baffles and conformed to the standard stirred-tank geometry used by researchers such as Cutter (1966), Gunkel and Weber (1975) and McManamey (1980). The tank was chosen as it is of well-defined geometry and established hydrodynamics and had been used previously by Ahmed and Jameson (1985). The

tank was agitated by one of two impellers chosen for the study and powered by a 90 W DC permanent magnet motor. The motor was fitted with a variable speed frequency modulated drive and impeller speed was controlled with a micrometer type potentiometer. This system enabled the impeller speed to be controlled to within 1 RPM but this was always confirmed independently using an optical tachometer.

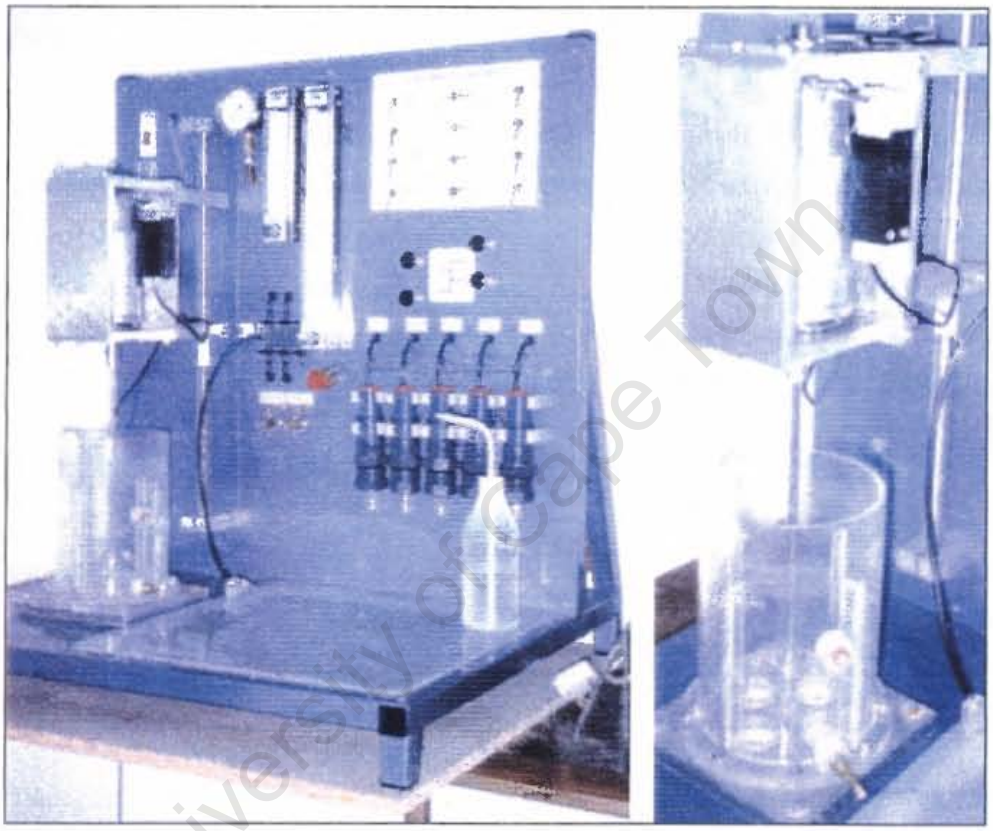

Figure 2.1. Batch flotation cell.

Impellers: A Rushton turbine impeller, conforming to the standard dimensions used by researchers such as Cutter (1966), Wu and Patterson (1989) and Kresta and Wood (1991), was chosen as a primary impeller for the study (cf. Figure 2.2a). Rushton turbines are high shear axial flow impellers with high power numbers and are commonly used in both the mixing and gas dispersion industries. Rushton turbines are similar in both principles and characteristics to the impellers used in industrial mechanical flotation cells as there is a general trend towards the use of high shear axial flow impellers with high power numbers in these cells (Mavros, 1992). A high speed spinning disc, of similar characteristics to that used by Jordan and Spears (1990), was chosen as a secondary impeller for the study (cf. Figure 2.2b). Spinning discs are high shear impellers with low power numbers and are suited to both the generation of microbubbles and colloidal gas aphrons (Solari

and Gochin, 1992). The spinning disc was chosen both for its suitability for gas dispersion and its markedly different hydrodynamic characteristics to the Rushton turbine. Both impellers were located at a standard distance of one Rushton turbine impeller diameter from the bottom of the tank.

(a) Rushton Turbine (b) Spinning Disc

Figure 2.2. Plan view of the Rushton turbine and spinning disc impellers.

Aeration System: The tank was aerated by nitrogen gas which was regulated and passed through a humidifier before being fed to four equispaced sintered glass discs set into the base of the tank. Sintered discs were configured so as to ensure uniform aeration over the base of the tank and were supplied by Corning Laboratory Division (ISO/DIS 4793). Sintered discs of three different porosities were chosen for the study and are referred to as the porosity 1, porosity 3 and porosity 4 spargers in future sections. The gas pressure at each sintered disc was monitored on a pressure gauge and the flowrate was adjusted using a needle valve and a fine rotameter to ensure a fixed nitrogen flowrate at atmospheric pressure. The gas flowrate to the sintered discs was monitored during the course of all experiments, though the aeration system proved extremely stable and adjustments were infrequent.

Froth System: Froth was removed immediately it appeared on the surface of the flotation cell using a specially designed suction nozzle and manifold system. A vacuum pump supplied a constant vacuum of -85 kPa to a manifold connected to five 1 litre sample containers. Each sample container was connected with a separate line to a stopcock valve on a central flow distribution manifold. Froth from the suction nozzle could be routed to any one of the sample containers by changing the appropriate stopcock valves on the flow distribution manifold. Change-over times between sample containers were found to be less than 2 seconds due to the short residence times in the suction nozzle and lines (<1 s). No accumulation of sample in suction lines was observed as lines were flushed with a small quantity of water before changing to a new sample container. The froth suction system was found to be suitable for the rapid and efficient removal of froth for all flotation tests conducted during the study.

2.2 Hydrodynamics and Gas Dispersion

The flotation cell was thoroughly characterised in terms of the effects of impeller type and impeller speed on both hydrodynamics and gas dispersion in the cell before any flotation tests were conducted. The entire characterisation of hydrodynamics and gas dispersion was performed in the absence of solids (i.e. two phase system) to facilitate the turbulence and bubble size measurements. This is not considered a limitation as an extremely low solids concentration of 2% (m/m) was chosen for the flotation tests. The presence of small amounts of solids has been found to have minimal effect on turbulence parameters by researchers such as Levins and Glastonbury (1972) and Komasawa *et al* (1974). The experimental conditions, variables and measurements used in the characterisation of hydrodynamics and gas dispersion are summarised in Table 2.2.

Table 2.2. Experimental conditions, variables and measurements used in the characterisation of hydrodynamics and gas dispersion in the flotation cell.

Conditions	Variables	Measurements
Volume: 2.25 litre	Rushton Turbine	Power Input
Gas Flowrate: 400 ml/min	310, 630, 940, 1260 RPM	Gas Holdup
Frother: MIBC @ 100 ppm	Spinning Disc	Turbulence
	2180, 2490, 2810, 3100 RPM	Bubble Size
	Gas Sparger	
	Porosity 1, 3 & 4	

Experimental Conditions: The tank was filled to just above the top of the baffles with 2.25 litres of deionized water which was decanted from a measuring cylinder. A low gas flowrate of 100 ml/min per sintered disc was chosen for the study so as to reduce rates in the flotation tests and improve the accuracy of recovery-times curves. This flowrate was found to be the minimum required to obtain a steady and uniform stream of bubbles from the porosity 1 sparger and equates to an overall gas flowrate of 400 ml/min for the flotation cell (J_g=0.0433 cm/s). A frother dosage of 100 ppm (m/v) of 4-methyl-2-pentanol (MIBC) was chosen for the study so as to ensure a non-coalescing environment in the flotation cell based on findings from similar studies by both Ahmed and Jameson (1985) and Parthasarathy *et al* (1991). Frother was introduced into the impeller zone of the Rushton turbine (800 RPM) or the spinning disc (2600 RPM) using a micropippette and allowed to disperse for 1 minute. These conditions and procedures were standardised for all experiments and the impeller speeds of 800 RPM for the Rushton turbine and 2600 RPM for the spinning disc were

fixed as the standards for all conditioning periods and/or pre-characterisation experiments for the study.

Experimental Variables: The lowest impeller speed for the Rushton turbine (310 RPM) was established as the minimum required for adequate suspension of solids in the flotation tests while the highest impeller speed (1260 RPM) was established as the maximum prior to the onset of surface aeration. This resulted in a range of specific power inputs between 0.10 and 5.0 W/kg which is comparable to the range of power inputs used in mechanical flotation cells. The corresponding impeller speeds for the spinning disc were chosen so as to overlap with the range of power inputs for the Rushton turbine while still ensuring suspension of solids. Due to the comparatively poor fluid pumping ability of the spinning disc, however, a minimum power input of 3.0 W/kg was required for adequate suspension of solids. This resulted in a range of specific power inputs between 3.0 and 8.0 W/kg which is in the upper end of the range of power inputs used in mechanical flotation cells. The highest power input for the spinning disc (8.0 W/kg) corresponds to an impeller speed of 3100 RPM which was the maximum speed achievable by the DC motor. Three different gas spargers (porosity 1, 3 & 4) were chosen so as to produce a broad range of bubble sizes in the flotation cell and were found to generate bubbles with mean diameters of between 120 and 840 μm. Bubbles generated by the porosity 3 and 4 spargers were too small to be broken-up by impeller action and remained relatively constant in size over the full range of impeller speeds while those generated by the porosity 1 sparger were broken-up by impeller action (cf. Chapter 4.0).

Experimental Measurements: The power input to the flotation cell was calculated from the motor torque and the impeller speed (viz. torque x $2\pi N$). The motor was mounted on a bearing race and was free to rotate but was constrained by a torque arm which impinged on a load cell, thus enabling torque to be measured. This method of power measurement proved both extremely reliable and sensitive and allowed power inputs to be determined to an accuracy of 0.05 Watts. The gas holdup was determined by pumping a fixed flowrate of aerated fluid from the flotation cell using a small peristaltic pump and de-aerating the fluid in an inverse burette before returning the liquid to the flotation cell. The gas holdup was calculated from the pump flowrate and the cumulative volume of gas in the burette and found to be accurate provided sufficiently long sampling periods were used. The gas holdup was determined at a number of points in the flotation cell but found to be similar throughout, suggesting a well-mixed gas phase. The measurement of turbulence and bubble size proved more complex than that of power input and gas holdup and is discussed in Sections 2.2.1 and 2.2.2 respectively.

2.2.1 Turbulence Measurements

The determination of turbulence parameters involved the accurate measurement of fluid mean and fluctuating velocities at various locations in the flotation cell. Measurements of this type are generally performed using sophisticated techniques such as laser-doppler anemometry and particle tracking velocimetry but these were beyond the budgetary constraints of the project. Reasonably accurate velocity measurements can, however, be obtained using simple velocity probes such as hot-wire anemometers, piezo-electric transducers and electrochemical or conductivity probes. It was decided to measure fluid velocity using a small electrochemical probe in the study as this method had been employed successfully by other researchers in flotation due to its suitability for measurements in two and three phase systems (Nonaka *et al*, 1982; Jordan and Spears, 1990). An electrochemical probe based on the oxidation and reduction of the ferro and ferri-cyanide ions was chosen as this has been reported to give equivalent or better responses to a hot-wire anemometer (Ranz, 1958). The conditions and principles of operation of the electrochemical probe were similar to those used by Jordan and Spears (1990) and are discussed below.

Experimental Equipment: The electrochemical probe (cf. Figure 2.3) consisted of a 50 μm diameter platinum wire cathode set into the tip of a 4 mm diameter Perspex rod which was tapered at 30 degrees to a sharp point so as not to perturb flow patterns. The diameter of the wire was chosen so as to be similar to the average Kolmogoroff microscale of turbulence ($\nu^{3/4}/\varepsilon^{1/4}$) in the study. A larger platinum anode was formed by winding several lengths of wire around the untapered section of the rod approximately 5 mm from the tip. By applying a -300 mV potential to the cathode in a solution of 0.2 M potassium chloride and 0.003 M potassium ferric and ferrous cyanide, a diffusion current was generated which was amplified and converted to voltage. The current was limited by the diffusion rate of ferric ions to the small cathode surface area and, consequently, by the fluid velocity over the probe tip. As the resulting diffusion current was only of the order of 1 μA great care had to be taken to eliminate low frequency electrical noise in the probe-amplifier circuits and electrical leads. High frequency noise was eliminated by a first-order analogue low pass filter in the amplifier circuit which was designed to completely eliminate all noise above 10 kHz. No significant attenuation of the signal was observed below 3 kHz which was well above the maximum frequency expected in the measurements of the fluctuating velocity. The voltage signal from the amplifier was digitised by an A/D computer card and saved as an ASCII text file. An A/D card with an on-board clock and a maximum sampling rate of 30 kHz was chosen to ensure accuracy and consistency in the sampling time intervals.

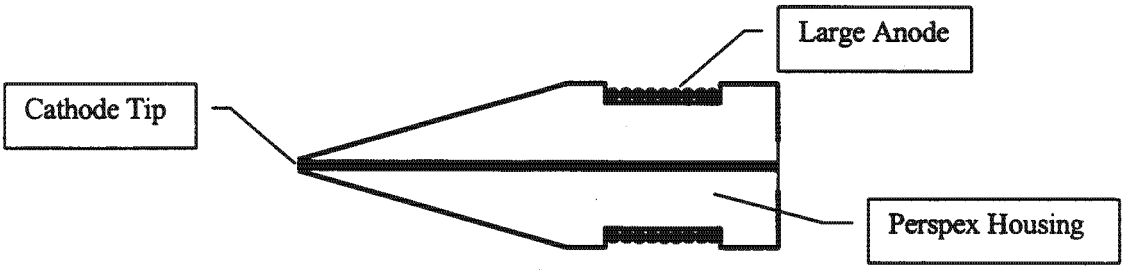

Figure 2.3. Cross-section through the electrochemical probe used in the turbulence measurements.

Experimental Procedure: The electrochemical probe was calibrated in a stream of electrolyte pumped through a 10 mm diameter Perspex pipe at a constant flowrate using a peristaltic pump. Due to the principle of operation and the geometry of the electrochemical probe it responded to a component of the fluid velocity which was not directly normal to the probe tip. Consequently, the calibration involved rotating the probe in 30 degree intervals through 180 degrees of the flow field and determining the mean response of the probe as an average of the response at each angle as per the method of Nonaka *et al* (1982). To ensure consistency the probe was washed in dilute hydrochloric acid and recalibrated every 15 minutes during the turbulence measurements. After calibration the probe was inserted into the flotation cell and fixed into position at one of the measuring points depicted in Figure 2.4. The flotation cell was adjusted to the appropriate experimental conditions and velocity measurements were recorded after allowing the system 5 minutes to equilibrate. Each test involved the sampling of 240 000 velocity data points over a time period of 60 seconds at a sampling frequency of 4 kHz. This gives a Nyquist, or effective maximum, frequency of 2 kHz which is significantly higher than the maximum frequencies observed in other agitated liquid systems (Kim and Manning, 1964; Rao and Brodkey, 1972).

Data Analysis: Velocity data was analysed by a spectral analysis programme developed by Hess (1991) and modified to include the calibration routine for the electrochemical probe. The programme divided each velocity data set into 100 records of 2048 data points which resulted in an effective resolution of 2 Hz in the calculated turbulent energy spectra. The mean velocity was removed from the data set and records were tapered using a Hanning window to eliminate the effects of discontinuities at the end of each time series and a 50% overlap to recover the stability lost due to the tapering operation (Otnes, 1978). A Fast Fourier Transform (FFT) was then performed on the autocorrelation coefficient for each record and results were ensemble averaged over the full set of 100 records to give the turbulent energy spectrum. Turbulence parameters such as RMS turbulent velocities, turbulent macro and micro scales and turbulent energy dissipation rates were then calculated using the velocity measurements, turbulent energy spectra and equations

discussed in Section 1.5.1. Repeatability was found to be extremely good due to the enormous number of velocity measurements and the broad range of measuring points for each test.

Experimental Measurements: Turbulence is always three dimensional and a complete characterisation of turbulence requires the measurement of axial, radial and tangential velocities. Velocities were only measured in the radial and tangential directions, however, as it proved difficult to orientate the electrochemical probe in the axial direction. This proved to be immaterial to the study as turbulence was found to be isotropic and, consequently, measurements in any single direction were sufficient. Radial and tangential velocities were measured in both the unaerated and aerated flotation cells at the points marked 1-6 and 9-11 in Figure 2.4 for both the Rushton turbine and the spinning disc. Equivalent measurements in the impeller zone were in slightly different locations due to the chosen impeller sizes (points 7, 8, 12, 13). Points 1-3, 4-6 and 9-11 were located at one quarter, one half and three quarter tank radii on the central baffle mid-plane and in the upper third, middle third and lower third of the tank respectively. Points 7 and 12 were located within 1 mm of the impeller tip and points 8 and 12 were located in the centre of the impeller discharge stream midway between the impeller tip and the tank wall. Only tangential velocity data and turbulence parameters obtained at one half tank radius in the bulk tank, and at both locations in the impeller zone, are reported in Tables A1 to A8 in Appendix A as turbulence was found to be isotropic throughout the flotation cell.

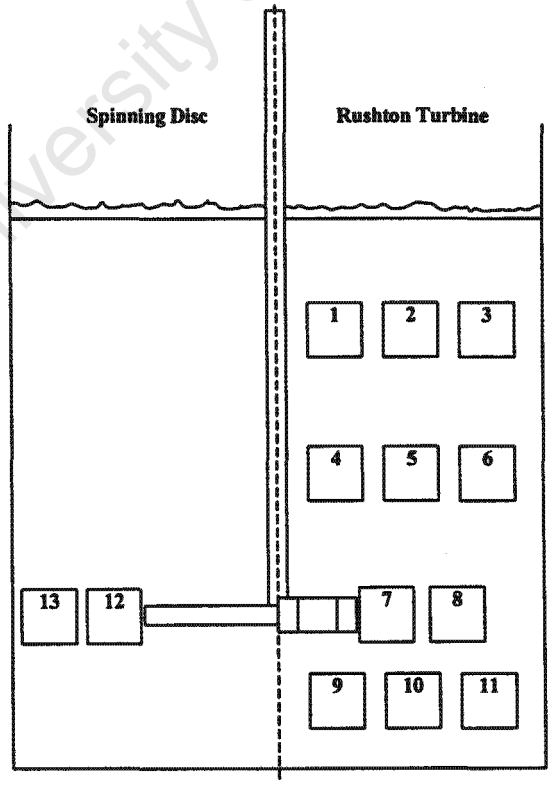

Figure 2.4. Turbulence measuring points in the flotation cell.

2.2.2 Bubble Size Measurements

Bubble size in flotation cells can be measured directly using photographic and capillary suction techniques (Tucker *et al*, 1994) or it can be inferred through techniques such as drift flux analysis (Zhou *et al*, 1993). It was decided to measure the bubble size photographically in this study as it was considered to be the most accurate technique and had been used successfully by Ahmed and Jameson (1985). Bubble size was only measured at a single point in the flotation cell (point 5) as preliminary experiments established that the bubble size was uniform throughout the flotation cell. Similar findings were obtained by both Ahmed and Jameson (1985) and Parthasarathy *et al* (1991) who established that the bubble size distribution in a non-coalescing environment is determined in the impeller region and preserved in the rest of the tank.

Experimental Equipment: The photographic measurement of bubble size involved capturing images of a stream of aerated fluid which was removed from the flotation cell and passed through a custom-built flow-through microscope cell. The design of the flow-through cell was based on that used by Ahmed and Jameson (1985) and consisted of two standard microscope observation slides held at a constant distance of 1 mm apart in a water-tight Perspex frame. Images from the flow-through cell were captured using a Zeiss optical microscope equipped with a video camera which was connected to a computer frame grabber.

Experimental Procedure: A small stream of aerated fluid was sucked from the sampling point (point 5) through the microscope flow-through cell and back to the flotation cell using a peristaltic pump. The pump flowrate was chosen to be sufficiently large so as to prevent bubbles from rising and touching the microscope slide and yet sufficiently small so as to prevent the disruption of bubbles. The residence time of bubbles in the plastic tubing was calculated to be very low (<1 s) as a short distance of 20 cm separated the sampling point from the flow-through cell. The flotation cell was adjusted to the appropriate experimental conditions and, after allowing the system 5 minutes to equilibrate, a total of 20 snapshot images of bubbles in the flow-through cell were taken at intervals of 15 seconds over a period of 5 minutes.

Data Analysis: Bubbles in each image were counted and sized with the aid of an image processing package which was precalibrated with a biological cell-counting graticule. The number of bubbles evaluated for each experimental condition depended on the spread of the bubble size distribution but an average of 300 bubbles were measured per condition. Repeatability of bubble sizes was established at less than 7% based on differences in mean and Sauter mean diameters of duplicate tests from 8 different experimental conditions. Repeatability of the experimental technique was

confirmed by comparing bubble sizes at two additional sampling flowrates but found to be consistent.

2.3 Flotation

The selection of the ore sample for the flotation tests is discussed in Section 2.3.1, the preliminary experiments for establishing conditions and procedures for the flotation tests are discussed in Section 2.3.2 while the final experimental programme is outlined in Section 2.3.3.

2.3.1 Ore Sample

Quartz was chosen for the flotation tests as it has been extensively researched in the literature (Crawford and Ralston, 1988) and is not subject to complications such as chemical oxidation which can lead to the misinterpretation of physical effects. A sample with a relatively fine particle size (95%<32 μm) was chosen as the standard sample for all flotation experiments as a central focus of the study is on fine particle flotation (cf. Section 1.7). In addition, a sample with a more conventional particle size (95%<100 μm) was chosen as an alternative sample as this is typical of the particle size range found in industrial flotation cells.

Sample Preparation: High purity silica (>99.6% SiO_2), supplied by Consol Industrial Minerals and normally used as a raw product for the manufacture of glass, served as the feed material for the generation of the quartz samples. A milling curve was determined and increments of 1 kg were dry milled in a stainless steel rod mill for milling times chosen to suite the generation of either -32 or -100 μm particles. Milled samples were washed in distilled water and magnetics were removed in a laboratory magnetic separator after which samples were cleaned and prepared as per the method of Diggins and Ralston (1993). Samples were first roasted at 550 C for 6 hours, allowed to cool and boiled in concentrated nitric acid for 3 hours. Samples were then filtered, rinsed with distilled water until neutral pH and dispersed in a warm sodium hydroxide solution (10 M) for 1 minute. Samples were again filtered, washed with distilled water until neutral pH and dried in an oven at 120 C for 6 hours. Using this procedure, 2.5 kg each of clean -32 and -100 μm quartz were generated and used in the preparation of the flotation samples.

Fine (-32 μm) Sample: This sample is referred to as the "-32 μm sample" in the study and was prepared by dividing the clean -32 μm quartz directly into increments using a laboratory rotary

splitter and sealing these in glass bottles for use in the flotation tests. The particle size distribution of the -32 μm sample was determined by Malvern Mastersizer and is given in Figure 2.5.

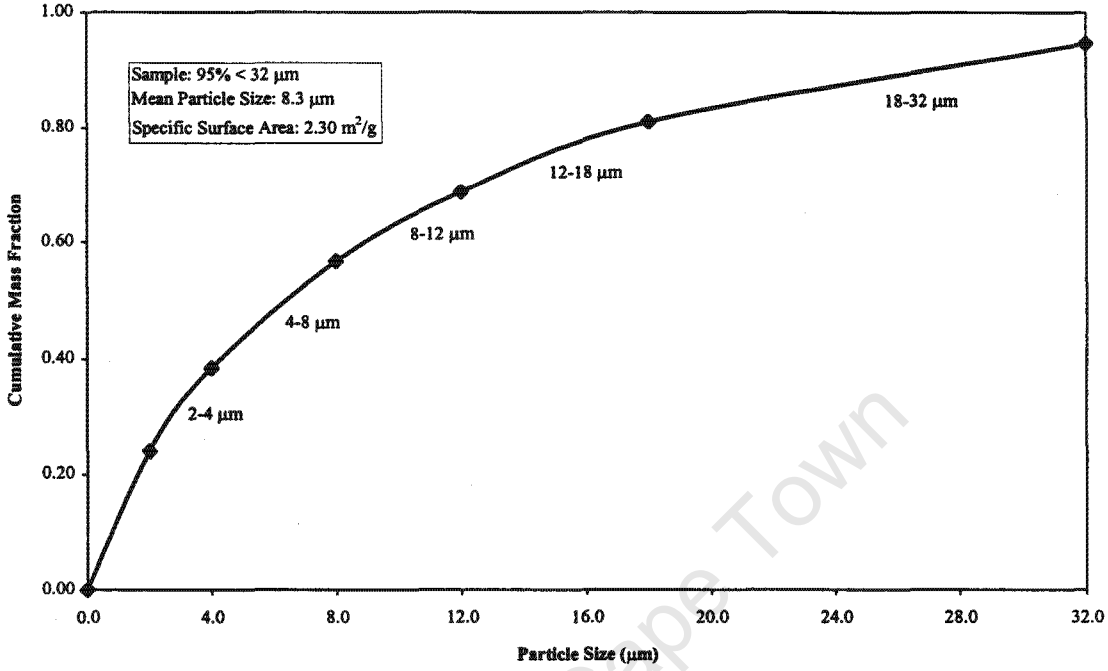

Figure 2.5. Cumulative particle size distribution for the "-32 μm sample".

It is clear from this figure that the -32 μm sample is a standard milled sample as it is biased towards the finer particle sizes, having an arithmetic mean diameter of 8.3 μm and a specific surface area (BET) of 2.30 m^2/g. The particle size distribution in Figure 2.5 has been divided into 5 particle size ranges of approximately equal mass fractions. These particle size ranges were selected as the standard size ranges for comparison in all the flotation tests on the -32 μm sample. The -2 μm material was omitted from the study as particles of this size were considered to be controlled by diffusional effects rather than by turbulent particle-bubble contacting (Gaudin *et al*, 1942).

Conventional (-100 μm) Sample: This sample is referred to as the "-100 μm sample" in the study and was prepared by cyclosizing the clean -100 μm quartz into various size fractions using a Warman cyclosizer and recombining these in suitable amounts to obtain a relatively uniform particle size distribution as per the method of Ahmed and Jameson (1985). The reconstituted sample was divided into increments using a laboratory rotary splitter and sealed in glass bottles for use in the flotation tests. The particle size distribution of the -100 μm sample was determined by Malvern Mastersizer and is given Figure 2.6.

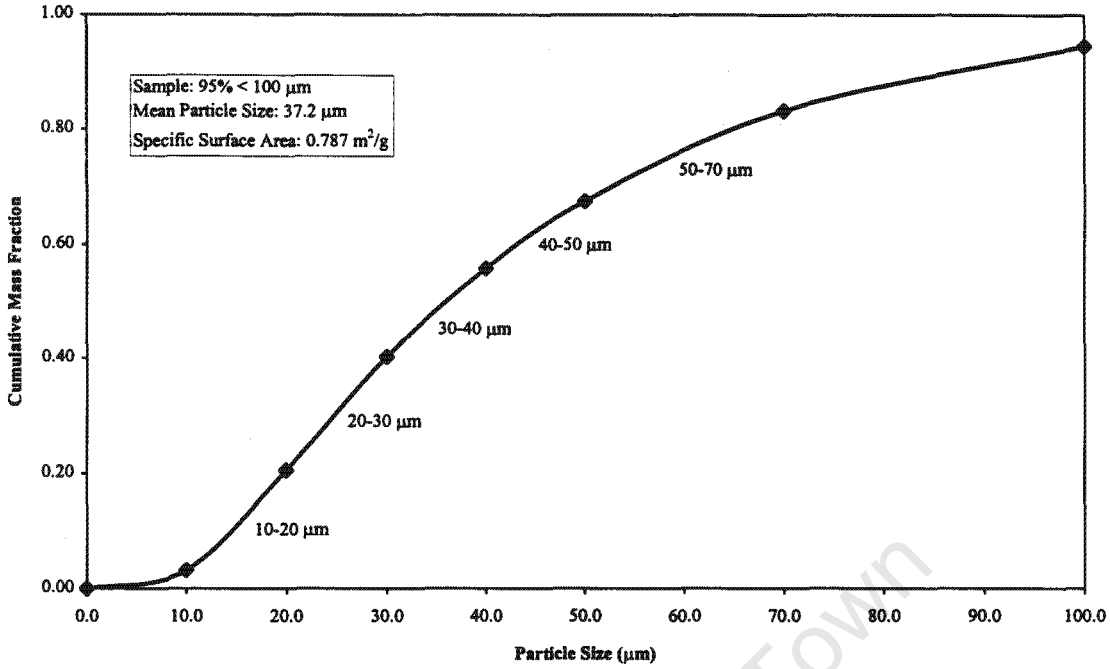

Figure 2.6. Cumulative particle size distribution for the "-100 μm sample".

It is clear from this figure that the -100 μm sample deviates substantially from a standard milled sample as it has almost no ultrafine (-10 μm) particles and approaches linearity between particle sizes of 10 to 50 μm, having an arithmetic mean diameter of 37.2 μm and specific surface area (BET) of 0.787 m^2/g. Ideally, the particle size distribution should have been perfectly linear over the full particle size range but this was the best that could be attained with the cyclosized fractions. The particle size distribution in Figure 2.6 has been divided into 5 particle size ranges of approximately equal mass fractions. These particle size ranges were selected as the standard size ranges for comparison in all the flotation tests on the -100 μm sample. The +70 μm material was omitted from the study as the particle size distribution had begun to level off and extremely broad size ranges were required to obtain equal mass fractions of particles.

2.3.2 Preliminary Experiments

After the -32 μm and -100 μm samples had been generated, suitable experimental conditions for the preliminary flotation tests were chosen based on prior flotation experiments conducted by members of the Flotation Research Group at the University of Cape Town (Stonestreet, 1992; Henwood, 1995). The experimental conditions, variables and measurements used in the preliminary flotation experiments are summarised in Table 2.3 and results are discussed individually in Sections 2.3.2.1 to 2.3.2.3.

Table 2.3. Experimental conditions, variables and measurements used in the preliminary flotation tests.

Conditions#	Variables	Measurements
Solids Mass: 45 g	Collector Dosage	Collector Adsorption
Collector: HPYC	100, 250, 500, 1000 ppm	Particle Zeta Potential
pH: 6.0		Flotation Experiments
pH Modifiers: HCL & NaOH		Particle Entrainment

All experiments: -32 μm sample and Rushton turbine impeller (800 RPM).

Experimental Conditions: A low solids mass of 45 grams was chosen for the flotation tests so as to limit the effects of solids on the turbulence characteristics of the fluid and to reduce the effects of solids on the froth phase. The resulting solids concentration of 2% (m/m) was considered to satisfy these requirements and yet still be sufficiently large to enable appreciable masses of flotation concentrate to be collected. A quaternary amine, hexadecyl pyridinium chloride (HPYC) was chosen as a collector for the flotation tests as it had been used in previous studies and could be detected on a UV spectrophotometer. All flotation tests were conducted at pH 6.0 so as to inhibit the formation of particle-particle aggregates. The Zeta potential of quartz is extremely negative in this pH region (>-30 mV) and particle-particle aggregation is considered to be inhibited at Zeta potentials greater than 30 mV (Collins and Jameson, 1976; King, 1982). Dilute hydrochloric acid (5% m/m) and sodium hydroxide (1 M) were chosen as pH modifiers for the flotation tests as these had been used in previous studies.

Experimental Variables: The primary objective of the preliminary flotation experiments was to determine the effect of collector dosage on factors such as flotation performance and particle Zeta potential in order to establish a suitable collector dosage for the study. Consequently, collector dosage was the only parameter varied in the preliminary flotation experiments. Four collector dosages of between 100 and 1000 ppm (m/m) were chosen as this straddles the range of dosages used in previous studies.

2.3.2.1 Collector Adsorption

Collector adsorption experiments were performed at various collector dosages in order to determine the adsorption behaviour, the appropriate experimental conditioning period and the residual collector concentration in solution at equilibrium. Particle Zeta potentials were measured after each adsorption test so as to ascertain whether particles were sufficiently charged after the adsorption of

collector to inhibit the formation of particle-particle aggregates. Adsorption experiments were conducted in the flotation cell at the experimental conditions shown in Table 2.3 and using the following procedure.

Experimental Procedure: A UV spectrophotometer was set to the characteristic adsorption wavelength for HPYC (258.8 nm) and calibrated over the range of experimental collector dosages. Solids were added to the flotation cell after which the system was adjusted to pH 6.0 using the pH modifiers and allowed to condition for a period of 5 minutes. The appropriate amount of collector was then added to the flotation cell in a solution form and the system was again adjusted to pH 6.0 and controlled for the duration of the adsorption test. Samples of solution were extracted from the flotation cell at intervals of 0.5, 1, 2, 5 and 10 minutes using a syringe fitted with a microfilter and analysed on the UV spectrophotometer. A sample of pulp was taken from the flotation cell after the adsorption test and the Zeta potential of particles was determined using a Malvern Zetasizer. The adsorption isotherm (NTP) for the adsorption of HPYC on the -32 μm sample is shown in Figure 2.7.

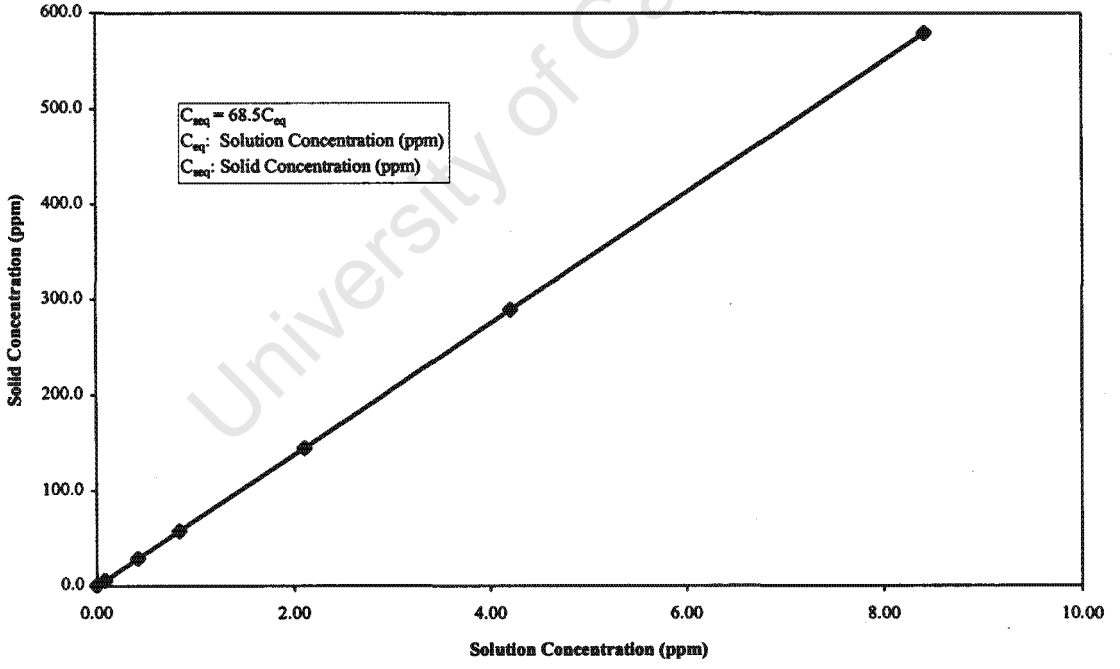

Figure 2.7. Graph of concentration of collector on solids (ppm) versus concentration of collector in solution (ppm) for the adsorption of HPYC on the -32 μm sample.

It is clear from this figure that the system obeys Freundlich adsorption characteristics over the range of experimental collector dosages. The concentration of collector on solids was found to be directly proportional to the concentration of collector in solution with a proportionality constant of

68.5 which implies that 58% of the initial mass of collector is adsorbed. Particle Zeta potentials were found to drop from -42 mV in the pure quartz-water system to -30.5 mV on addition of 500 ppm of collector but to drop to well below -30 mV at higher dosages. Collector adsorption was found to reach equilibrium in under 2 minutes for all collector dosages and, consequently, a conservative conditioning period of 5 minutes was established for the study.

2.3.2.2 Collector Dosage

Preliminary flotation tests were conducted at various collector dosages in order to establish the effect of dosage on flotation performance. Collector dosage experiments were performed in the flotation cell aerated with the porosity 1 sparger, at the experimental conditions shown in Table 2.3 and using the following procedure.

Experimental Procedure: Solids were added to the flotation cell after which the system was adjusted to pH 6.0 using the pH modifiers and allowed to condition for a period of 5 minutes. The appropriate amount of collector was then added to the flotation cell in a solution form and the system was again adjusted to pH 6.0 and allowed to condition for an additional 5 minutes. The gas was then turned on and adjusted to the correct flowrate for a fixed time period of 5 seconds after which the flotation tests was considered to have started. Froth was continually removed as it formed on the surface of the cell using the suction nozzle and a total of 5 flotation concentrates were collected at a range of sampling times chosen to suite the flotation test. On completion of the flotation test, samples were filtered and dried and masses of both dry solids and liquid were determined. Particle size distributions were then determined by Malvern Mastersizer and size by size recovery-time curves were generated for the five standard particle size ranges.

Standard first-order flotation rate constants were determined from the recovery-time curves for the flotation tests (cf. Section 1.4.1.1). Rate constants were found to be similar at collector dosages of 100 and 250 ppm but to increase significantly with increasing collector dosage at the higher dosages of 500 and 1000 ppm. A collector dosage of 500 ppm was chosen for the flotation tests on the -32 μm sample as this was considered to be sufficiently high for collector dosage to have an effect on the flotation rate constant but sufficiently low for the Zeta potential of particles to be greater than –30 mV. A corresponding collector dosage of 171 ppm was calculated for the -100 μm sample on an equivalent collector per surface area (BET) basis of 2.17×10^{-4} g/m^2. Repeatability was determined from 12 flotation tests conducted on the -32 μm sample at two impeller speeds and

using the porosity 1, 3 & 4 spargers. Repeatability was established at 6.1% from these flotation tests based on flotation rate constants calculated from 30 recovery-time curves.

2.3.2.3 Entrainment

Entrainment experiments were performed in order to establish the significance of entrainment on flotation recovery. This was considered necessary as fine particle sizes and shallow froth depths were used in the flotation tests and significant particle entrainment was expected. Consequently, a number of collector-less flotation tests were conducted in the flotation cell on both the -32 μm and -100 μm samples and using a variety of impeller speeds and gas spargers. Figure 2.8 represents the recovery by entrainment as a function of water recovery for four particle size fractions from the -32 μm and -100 μm samples and for impeller speeds of 630 and 940 RPM. Trendlines have been fitted to each data set in this figure and are denoted by the mean particle size fraction values of 3, 25 and 60 μm respectively. As both the 18-32 μm and the 20-30 μm particle size fractions have an equivalent mean particle size of 25 μm, a common trendline has been fitted to the two data sets.

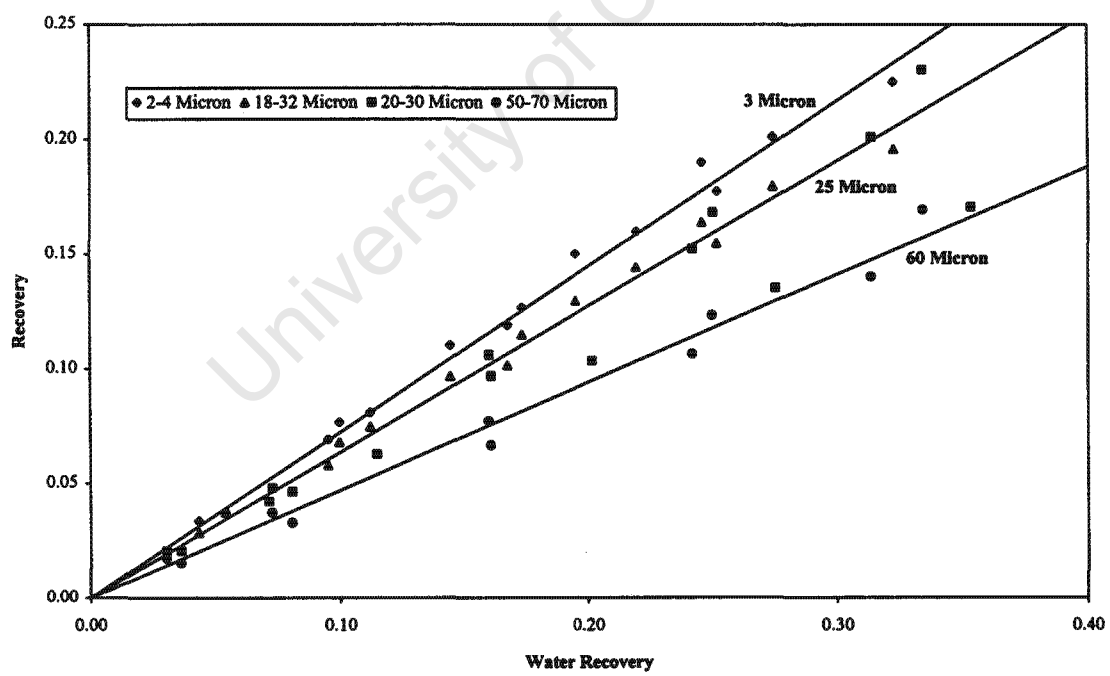

Figure 2.8. Graph of recovery by entrainment versus water recovery for four particle size fractions from the -32 μm and -100 μm samples.

It is clear from this figure that a significant amount of recovery is due to pure particle entrainment and that this is directly proportional to the water recovery and dependent on the particle size but

independent of the impeller speed or the quartz sample. This linear relationship between entrainment and water recovery is commonly found in flotation and the allowance for entrainment in the experimental recovery-time curves will be discussed further in Chapter 3.0.

2.3.3 Experimental Programme

The experimental programme for the flotation tests is summarised in Table 2.4 and was divided into a first phase consisting of 24 flotation tests and a second phase consisting of 30 flotation tests. The first phase investigated the flotation performance of the Rushton turbine and the spinning disc impellers on the -32 μm sample at the impellers speeds used in the characterisation of hydrodynamics and gas dispersion. The second phase investigated the flotation performance of the Rushton turbine on both the -32 μm and -100 μm samples at a more focused range of impeller speeds, derived from findings from the first phase and with divisions based on power input. The experimental conditions and procedures established in the preliminary flotation experiments in Section 2.3.2 were used in all the flotation tests and conditions are summarised in Table 2.5 for convenience.

Table 2.4. Experimental programme for the flotation tests.

Experimental Programme	
PHASE ONE -32 μm Sample Only 24 Flotation Tests	**PHASE TWO** Rushton Turbine Only 30 Flotation Tests
Experimental Variables Rushton Turbine 310, 630, 940, 1260 RPM Spinning Disc 2180, 2490, 2810, 3100 RPM Gas Sparger Porosity 1, Porosity 3, Porosity 4	**Experimental Variables** Rushton Turbine 310, 580, 730, 840, 940 RPM Ore Sample -32 μm, -100 μm Gas Sparger Porosity 1, Porosity 3, Porosity 4

Table 2.5. Experimental conditions used in flotation tests.

Experimental Conditions		
Volume: 2.25 litre	Collector: HPYC @	Zeta Potential: -30.5 mV
Solids Mass: 45 g	500 ppm: -32 μm Sample	d_p = 8.3 μm: -32 μm Sample
Gas Flowrate: 400 ml/min	171 ppm: -100 μm Sample	d_p = 37.2 μm: -100 μm Sample
Frother: MIBC @ 100 ppm	pH: 6.0	

CHAPTER 3: FLOTATION CELL MODELLING

The first-order flotation rate constant for a batch flotation cell is commonly determined from linear regression of experimental recovery data on a ln(1-recovery) versus time curve using Equation 3.1.

$$\ln\left(\frac{C}{C_0}\right) = \ln(1-R) = -kt \qquad (3.1)$$

This classical batch flotation model was found to apply reasonably well to the experimental data and to result in a mean correlation coefficient (r) of 0.98 for the full data set of 270 recovery-time curves. Extremely good fits (r>0.99) were, however, obtained for flotation tests in which the cell was sparged with large bubbles or operated at low impeller speeds while consistently poor fits (r<0.97) were obtained when the cell was sparged with small bubbles or operated at high impeller speeds.

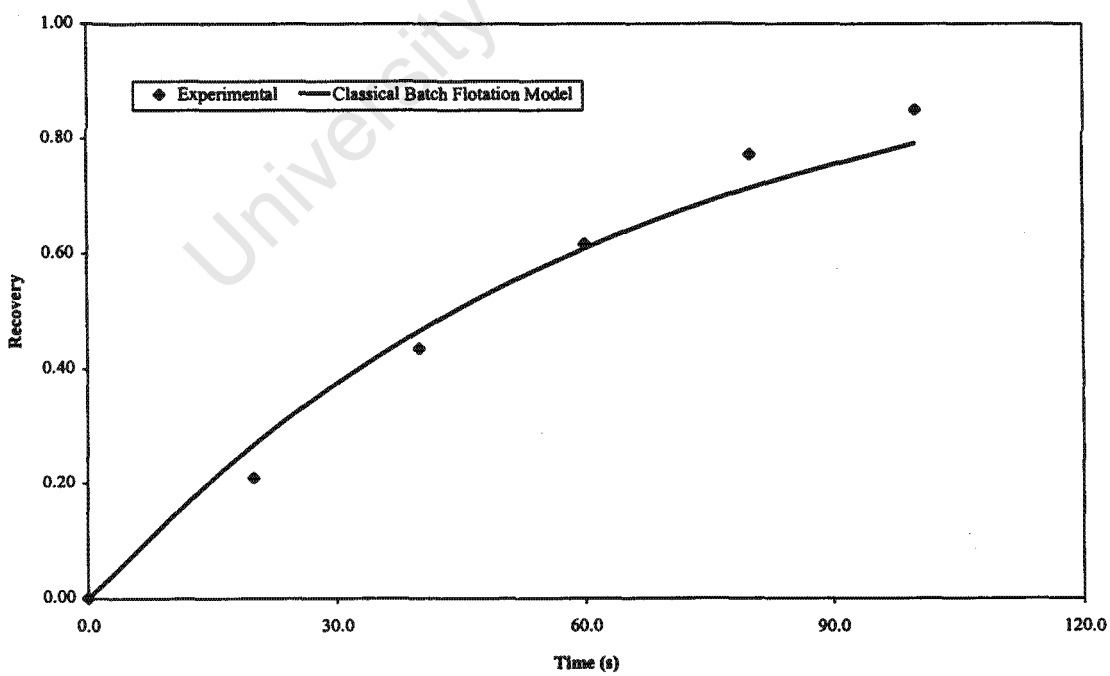

Figure 3.1. The classical batch flotation model applied to an experimental recovery-time curve.

In the latter tests the combination of small bubbles, high levels of agitation and high gas holdups was considered to have a significant influence on flotation kinetics and to result in the poor applicability of Equation 3.1 to the experimental data. For example, Figure 3.1 represents the best-fit of this model to a recovery-time curve from an experiment in which the flotation cell was aerated with small bubbles generated by the porosity 4 sparger and agitated by the Rushton turbine at an intermediate impeller speed of 730 RPM. It is clear from this figure that the classical batch flotation model provides a consistently poor fit and both overpredicts recovery at the start of the curve and underpredicts recovery at later times. The initial lag in the recovery-time curve observed in Figure 3.1 is a characteristic feature of these flotation tests and was attributed to a significant gas residence time in the flotation cell. Analysis of the gas dispersion data (cf. Chapter 4.0) showed gas residence times of between 2 and 50 seconds in some of these experiments. This is substantially higher than the corresponding residence times of between 1 and 4 seconds measured in standard laboratory flotation cells at the University of Cape Town and was attributed to both the high levels of agitation and extremely small bubbles used in the study. Consequently, it was decided to attempt a more detailed analysis of flotation kinetics which allowed for and included the effects of the gas phase in the flotation cell. This analysis is presented in Sections 3.1 and 3.2 and is based on the central assumption that the flotation cell is a well-mixed system, viz. pulp and gas phase properties are equivalent at all points in the flotation cell (cf. Figure 3.2).

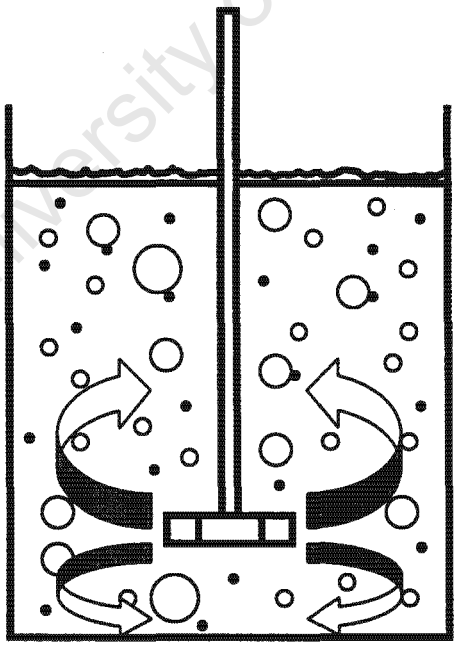

Figure 3.2. Schematic of a well-mixed flotation cell.

The assumption of a well-mixed pulp phase is common and is justified by both the fine particles and high levels of agitation used in the study. The assumption of a well-mixed gas phase has not

been considered or researched in the flotation literature but is motivated in Chapter 4.0. Here it is shown that an average bubble passes through the impeller zone between 1 and 50 times before exiting the flotation cell, depending on the impeller type and the experimental conditions. Consequently, the well-mixed assumption is justified at most of the experimental conditions used in the study. This ultimately proved to be immaterial as the kinetic models discussed in Section 3.2 were only found to be significant when the well-mixed assumption was found to be true, viz. small bubbles & high impeller speeds.

3.1 Gas Phase Modelling

The gas phase in the flotation cell is analysed from both a volumetric and a flux perspective in Sections 3.1.1 to 3.1.3. The volumetric-based and flux-based bubble size and bubble size distributions are defined in Section 3.1.1 and a method by which volumetric-based distributions can be transformed to flux-based distributions is outlined in Section 3.1.2. The gas residence time is defined from a volumetric and a surface area based perspective in Section 3.1.3. The definitions employed and the equations derived in Sections 3.1.1 to 3.1.3 are used in the analysis of flotation kinetics in Section 3.2.

3.1.1 Bubble Size Distributions

Figure 3.3 depicts an idealised flotation cell sparged with single large and small bubbles and will be used to illustrate the difference between bubble size distributions defined from a volumetric and a flux perspective.

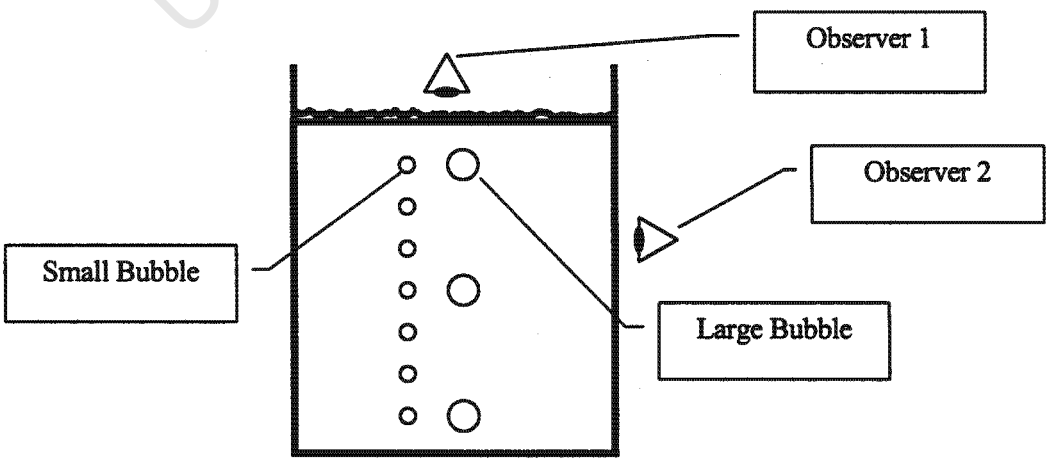

Figure 3.3. Schematic illustrating volumetric-based and flux-based bubble size distributions.

If one large and one small bubble are sparged into the flotation cell every second then at steady state one large and one small bubble will leave the top of the flotation cell every second. Consequently, an observer on top of the flotation cell (observer 1) will measure equal numbers of both large and small bubbles and will derive a bubble size distribution accordingly. Small bubbles have lower rise velocities than large bubbles, however, and an observer in front of the flotation cell (observer 2) will measure a greater number of small bubbles than large bubbles and will derive a different bubble size distribution. The first observer is considered to have measured a distribution based on the flux of bubbles through the flotation cell as would be measured by a capillary probe technique. This is referred to as a flux-based distribution and is defined in terms of the number of bubbles of a specific size class in a state of flux through a plane of unit cross sectional area per unit time (N_{bfi}) in Equation 3.3. The second observer is considered to have measured a distribution based on the spatial variation of bubbles through the flotation cell as would be measured by a photographic technique (cf. Section 2.2.2). This is referred to as volumetric-based distribution and is defined in terms of the number of bubbles of a specific size class per unit volume (N_{bi}) in Equation 3.2. The differences between these two bubble size distributions are seldom considered in the flotation literature and the volumetric-based distribution is generally regarded as the only bubble size distribution in the flotation cell.

$$f(d_{bi}) = \frac{N_{bi}}{\sum N_{bi}} \quad (3.2) \qquad F(d_{bi}) = \frac{N_{bfi}}{\sum N_{bfi}} \quad (3.3)$$

The number of bubbles per unit volume (N_{bi}) and the number of bubbles in flux (N_{bfi}) can be obtained from the gas holdup (ϕ), the superficial gas velocity (J_g) and the relevant bubble size distributions using Equations 3.4 and 3.5 respectively.

$$N_{bi} = \left(\frac{6\phi}{\pi}\right)\frac{f(d_{bi})}{\sum f(d_{bi})d_{bi}^{\,3}} \quad (3.4) \qquad N_{bfi} = \left(\frac{6J_g}{\pi}\right)\frac{F(d_{bi})}{\sum F(d_{bi})d_{bi}^{\,3}} \quad (3.5)$$

Bubble size distributions are accurate representations of bubble size in flotation cells and can facilitate the understanding of phenomena such as bubble breakup and coalescence but bubble size is more conveniently represented by single parameters. The arithmetic mean bubble diameter (d_b) is the most common parameter used in the flotation literature and is defined as the first mode about the bubble size distribution. The Sauter mean bubble diameter (d_s) is more commonly used in the gas and liquid-liquid dispersion literature as it is considered to have more physical significance and is defined for volumetric-based and flux-based distributions in Equations 3.6 and 3.7 respectively.

$$d_s = \frac{\sum f(d_{bi}) d_{bi}^{\ 3}}{\sum f(d_{bi}) d_{bi}^{\ 2}} \quad (3.6) \qquad d_{sf} = \frac{\sum F(d_{bi}) d_{bi}^{\ 3}}{\sum F(d_{bi}) d_{bi}^{\ 2}} \quad (3.7)$$

3.1.2 Transforming Bubble Size Distributions

The volumetric-based bubble size distribution was measured in the study as it proved impractical to measure the flux-based distribution due to limitations of the capillary probe technique in measuring bubbles under 300 μm in diameter. Consequently, the flux-based distribution was estimated by transforming the number of bubbles per unit volume (N_{bi}) to the number of bubbles in flux (N_{bfi}) using the bubble rise velocity through Equation 3.8. Using this equation, in conjunction with the definitions of the bubble size distributions in Section 3.1.1, a volumetric-based distribution can be transformed to a flux-based distribution using Equation 3.9.

$$N_{bfi} = u_{bi} N_{bi} \quad (3.8) \qquad F(d_{bi}) = \frac{u_{bi} f(d_{bi})}{\sum u_{bi} f(d_{bi})} \quad (3.9)$$

The bubble rise velocity can be determined for quiescent flotation cells using the type of relationships developed by Zhou *et al* (1993). No equivalent expressions are available for turbulent flotation cells, however, as agitation affects bulk flow patterns which in turn affect the net velocities with which bubbles rise through the cell. An effective bubble rise velocity (u_{effi}) can, however, be defined as the velocity with which bubbles are required to rise through the cell in order to satisfy the experimentally measured gas holdup and superficial gas velocity, viz. Equation 3.10.

$$u_{effi} = \left(\frac{J_g}{\phi}\right) \frac{F(d_{bi}) \sum f(d_{bi}) d_{bi}^{\ 3}}{f(d_{bi}) \sum F(d_{bi}) d_{bi}^{\ 3}} \quad (3.10)$$

Effective bubble rise velocities have to be determined experimentally as they are not absolute quantities and vary with factors such as agitation, impeller type and frother dosage. In order to transform a volumetric-based to a flux-based distribution using Equation 3.10 one has firstly to estimate the bubble rise velocities using a general correlation for a quiescent flotation cell. These preliminary velocities can then be used to estimate the flux-based distribution through Equation 3.9 after which effective velocities can be obtained from Equation 3.10. Consequently, effective rise velocities have the same functional dependence on bubble size to actual rise velocities but differ in magnitude.

Analysis of the gas dispersion data showed the bubble rise velocity to be proportional to the bubble diameter to the powers of between 1.0 and 0.50 for large bubbles and small bubbles respectively. Consequently, volumetric-based distributions were transformed to flux-based distributions using these simple relationships and effective rise velocities were determined accordingly. For example, a volumetric-based distribution with a Sauter mean diameter of 200 μm transforms to a flux-based distribution with a Sauter mean diameter of 240 μm using these techniques. The flux-based transformation is only an approximation, however, but this ultimately proved to be immaterial as volumetric-based parameters were used throughout the study.

3.1.3 Gas Residence Time

The gas residence time is commonly defined as the ratio of the total volume of dispersed gas in a flotation cell to the gas flowrate ($Q = J_g A$) and can be obtained from the gas holdup and superficial gas velocity using Equation 3.11.

$$\tau_g = \frac{\phi V}{J_g A} \quad (3.11)$$

This expression predicts that the gas residence time increases with increasing cell height ($H = V/A$) for a fixed gas holdup and superficial gas velocity and has significant implications for the kinetic expressions discussed in Section 3.2. The gas residence time for discrete bubble size classes can be determined from Equation 3.11 using the individual gas holdups and superficial gas velocities determined from the bubble size distributions through Equations 3.12 and 3.13.

$$\phi_i = \phi \frac{f(d_{bi}) d_{bi}^{\ 3}}{\sum f(d_{bi}) d_{bi}^{\ 3}} \quad (3.12) \qquad J_{gi} = J_g \frac{F(d_{bi}) d_{bi}^{\ 3}}{\sum F(d_{bi}) d_{bi}^{\ 3}} \quad (3.13)$$

The gas residence times calculated from Equations 3.11 to 3.13 are defined from a volumetric-basis and are commonly used in the gas dispersion literature. In the analysis of flotation kinetics, however, an additional gas residence time, defined as the ratio of the total bubble surface area in the flotation cell to the total flux of bubble surface area through the flotation cell, was required and is proposed in Equation 3.14.

$$\tau_{gs} = \frac{SV}{S_b A} \quad (3.14)$$

The gas residence time in this expression is defined from a surface area-basis (τ_{gs}) rather than a volumetric-basis (τ_g) and is uncommon in the flotation literature. The specific bubble surface area (S), often termed the gas interfacial area, can be obtained from the gas holdup and the volumetric-based Sauter mean diameter using Equation 3.15. The bubble surface area flux (S_b) has been used extensively in recent flotation research (Gorain *et al*, 1997) and can be obtained from the superficial gas velocity and the flux-based Sauter mean diameter using Equation 3.16.

$$S = 6\phi \frac{\sum f(d_{bi}) d_{bi}^{\ 2}}{\sum f(d_{bi}) d_{bi}^{\ 3}} = \frac{6\phi}{d_s} \quad (3.15) \qquad S_b = 6J_g \frac{\sum F(d_{bi}) d_{bi}^{\ 2}}{\sum F(d_{bi}) d_{bi}^{\ 3}} = \frac{6J_g}{d_{sf}} \quad (3.16)$$

The gas residence time for discrete bubble size classes can be determined from Equation 3.14 using the individual specific bubble surface areas and bubble surface area fluxes determined from the bubble size distributions through Equations 3.17 and 3.18.

$$S_i = 6\phi \frac{f(d_{bi}) d_{bi}^{\ 2}}{\sum f(d_{bi}) d_{bi}^{\ 3}} \quad (3.17) \qquad S_{bi} = 6J_g \frac{F(d_{bi}) d_{bi}^{\ 2}}{\sum F(d_{bi}) d_{bi}^{\ 3}} \quad (3.18)$$

Theoretically, identical gas residence times are obtained for single bubble size classes using either the volumetric-based or the surface area-based expressions but these can be different for distributions of bubbles. Surface area-based residence times were, however, approximated using the transformations discussed in Section 3.1.2 but were never found to differ by more than 10% from volumetric-based residence times. Consequently, volumetric-based residence times are substituted for surface area-based residence times throughout the study as these are calculated from robust experimental measurements of gas holdup and superficial gas velocity rather than from approximate transformations.

3.2 Flotation Modelling

As discussed at the start of Chapter 3.0 it was decided to develop a new kinetic model for flotation in agitated flotation cells which incorporates the influence of the gas phase on flotation kinetics.

This kinetic model is discussed in Section 3.2.1 and is based on the assumption that the gas phase and gas phase correlations presented in Section 3.1 are applicable.

3.2.1 Kinetic Analysis

The model proposed here is given in Equations 3.19 and 3.20 and allows for the effects of both the pulp phase (Equation 3.19) and, more significantly, the gas phase (Equation 3.20) on flotation kinetics. These equations are mass balances, incorporating kinetic expressions, and include the processes of particle-bubble attachment, particle-bubble detachment, particle entrainment and the change in volume of pulp in the flotation cell with time.

$$\frac{d(CV)}{dt} = -k_a CV + k_d C_s SV + x_e C\frac{dV}{dt} \quad (3.19)$$

$$\frac{d(C_s SV)}{dt} = k_a CV - k_d C_s SV - S_b C_s A \quad (3.20)$$

The process of particle-bubble attachment is assumed to be first-order with respect to the concentration of particles in the pulp phase (C) and controlled by an attachment rate constant (k_a). This is directly analogous to the definition of the flotation rate constant and the two are equivalent in the absence of significant detachment effects. The process of particle-bubble detachment is assumed to be first-order with respect to the concentration of particles on bubble surfaces (C_s) and controlled by a detachment rate constant (k_d). The argument for the use of first-order kinetics is equivalent to that for the flotation rate constant i.e. elementary "reaction kinetics" in the absence of complex interactions. The specific bubble surface area (S) is used to convert the term to a volumetric basis as a surface concentration (C_s) is employed in the expression.

Particle entrainment is assumed to be proportional to the volumetric flowrate of liquid leaving the pulp phase at concentration (C) and controlled by an entrainment fraction (x_e). The expression for entrainment was selected based on findings from the preliminary collector-less flotation tests for both the -32 and -100 μm samples (cf. Section 2.3.2.3). The entrainment fraction was calculated from the recovery-time curves for these tests and is shown in Figure 3.4 which represents the variation of the entrainment fraction with particle size for the -32 and -100 μm samples. It is clear from this figure that the entrainment fraction is largely independent of the sample and is dependent on the particle size only, decreasing from about 0.75 for 3 μm particles to 0.40 for 60 μm particles.

It is also clear that this relationship is approximately linear over the bulk of the particle size range but decreases slightly for the ultrafine particles. An analysis of the nature of this response is outside the scope of the study, however, as entrainment was merely included in the kinetic models to obtain more accurate rate constants.

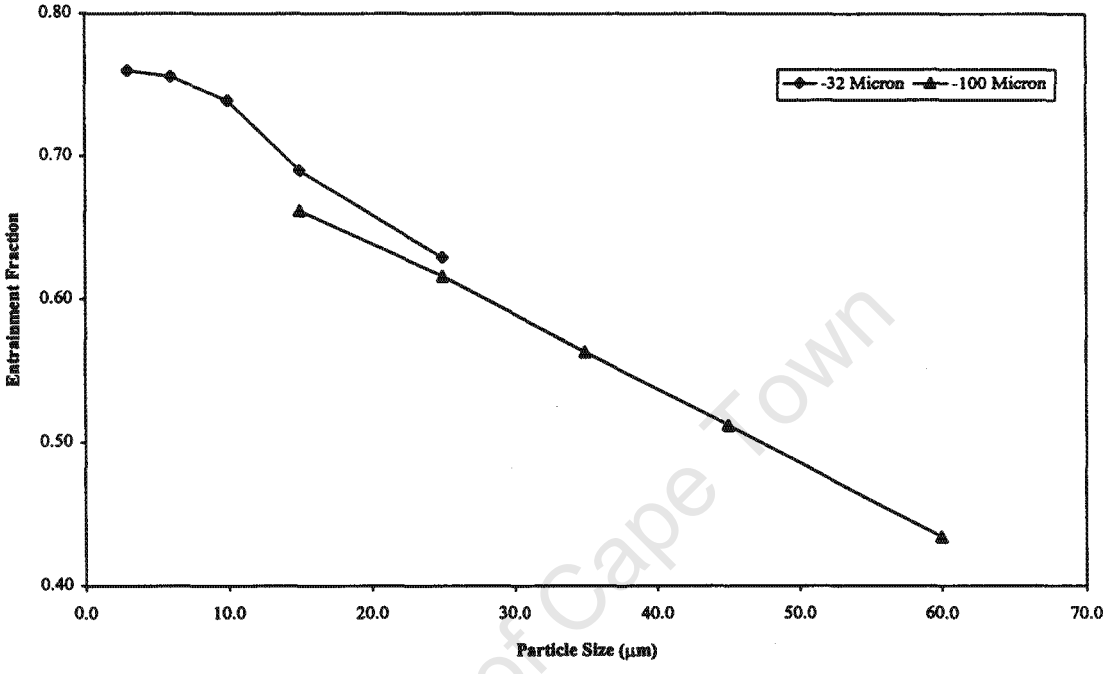

Figure 3.4. Graph of entrainment fraction (x_e) versus particle size (µm) for the -32 and -100 µm samples.

The volume of pulp in the flotation cell is assumed to decrease exponentially with time ($V=V_0e^{-\alpha t}$) and to be controlled by a volume shrinkage factor (α). The expression for volume-time dependence was selected based on observed water-recovery relationships and individual volume shrinkage factors were determined from measured water-recovery data for each flotation test.

Equations 3.19 and 3.20 reduce to Equations 3.21 and 3.22 on substitution of the expressions for the surface area-based gas residence time (Equation 3.14) and the volume-time dependence.

$$\frac{dC}{dt} = (-k_a - x_e\alpha + \alpha)C + k_d C_s S \qquad (3.21)$$

$$\frac{dC_s}{dt} = \frac{k_a C}{S} + (-k_d - \frac{1}{\tau_{gs}} + \alpha)C_s \qquad (3.22)$$

Equations 3.21 and 3.22 are ordinary linear differential equations and can be solved simultaneously using standard techniques to give the kinetic models discussed in Sections 3.2.1.1 to 3.2.1.3. The recovery can be obtained from Equation 3.23 and the expressions for the pulp (C) and surface concentrations (C_s) determined from the relevant kinetic models.

$$R(t) = 1 - \left(\frac{C}{C_o} + \frac{SC_s}{C_o} \right) e^{-\alpha t} \quad (3.23)$$

3.2.1.1 Attachment-Detachment Model

The solution to Equations 3.21 and 3.22 is referred to as the *attachment-detachment model* in this study and is given in Equations 3.24 and 3.25.

$$\frac{C}{C_o} = \left(\frac{1}{\lambda_1 - \lambda_2} \right) \left((\lambda_1 + k_d + \frac{1}{\tau_{gs}} + \alpha) e^{\lambda_1 t} - (\lambda_2 + k_d + \frac{1}{\tau_{gs}} + \alpha) e^{\lambda_2 t} \right) \quad (3.24)$$

$$\frac{C_s S}{C_o} = \left(\frac{k_a}{\lambda_1 - \lambda_2} \right) \left(e^{\lambda_1 t} - e^{\lambda_2 t} \right) \quad (3.25)$$

These equations represent the variation of the pulp and surface concentrations with time as a function of the attachment and detachment rate constants, the gas residence time, the entrainment fraction and the volume shrinkage factor. The pulp and surface concentrations are expressed as dimensionless quantities for comparative purposes and for direct use in Equation 3.23. The additional parameters (λ & m) are intermediate variables originating from the technique used to solve the differential equations and are defined in Equations 3.26 to 3.29.

$$\lambda_1 = \frac{-m_1 + \sqrt{m_1^2 - 4m_2}}{2} \quad (3.26) \qquad \lambda_2 = \frac{-m_1 - \sqrt{m_1^2 - 4m_2}}{2} \quad (3.27)$$

$$m_1 = k_a + k_d + \frac{1}{\tau_{gs}} + \alpha(x_e - 2) \quad (3.28)$$

$$m_2 = k_a \left(\frac{1}{\tau_{gs}} - \alpha \right) + \alpha(x_e - 1) \left(k_d + \left(\frac{1}{\tau_{gs}} - \alpha \right) \right) \quad (3.29)$$

The best-fit of the attachment-detachment model to the experimental data used in Figure 3.1 is given in Figure 3.5 and compared to the classical batch flotation model.

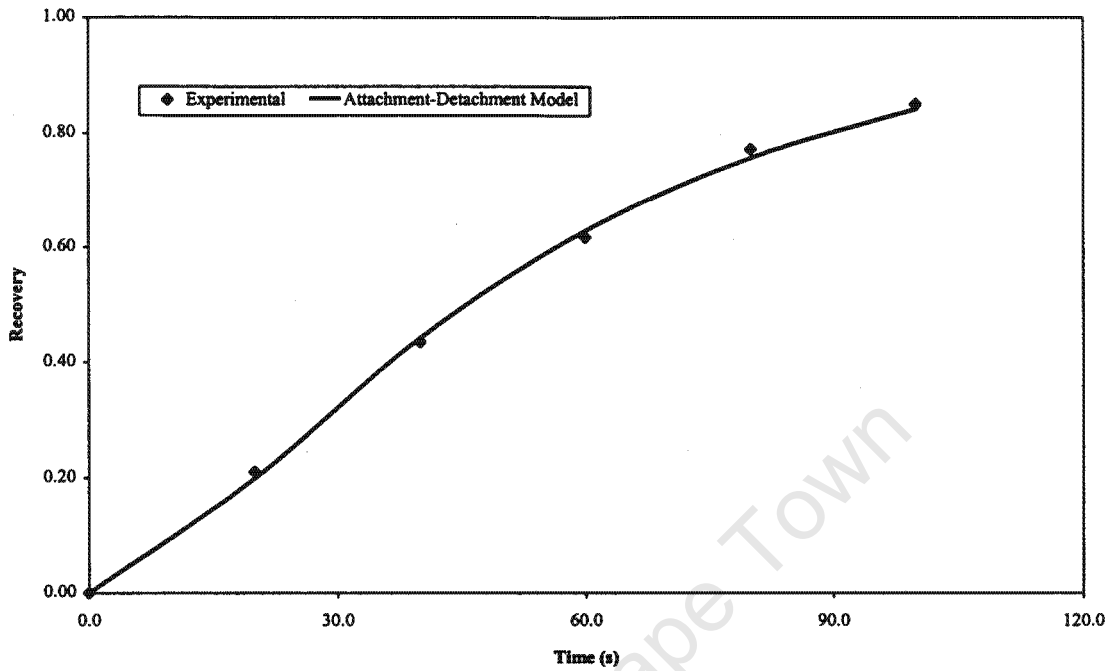

Figure 3.5. The attachment-detachment model applied to an experimental recovery-time curve.

It is clear from this figure that the attachment-detachment model is a better representation of the experimental data than the classical batch flotation model as it allows for the gas residence time in the flotation cell and the subsequent detachment of particles from bubbles. In terms of the classical model recovery is dependent on the concentration of particles in the pulp phase only. In terms of the attachment-detachment model, however, recovery is dependent on individual contributions from particles in the pulp phase, particles on the gas phase and particles entrained into the concentrate. The contributions of these sub-processes to the experimental recovery-time curve given in Figure 3.5 are shown in Figure 3.6.

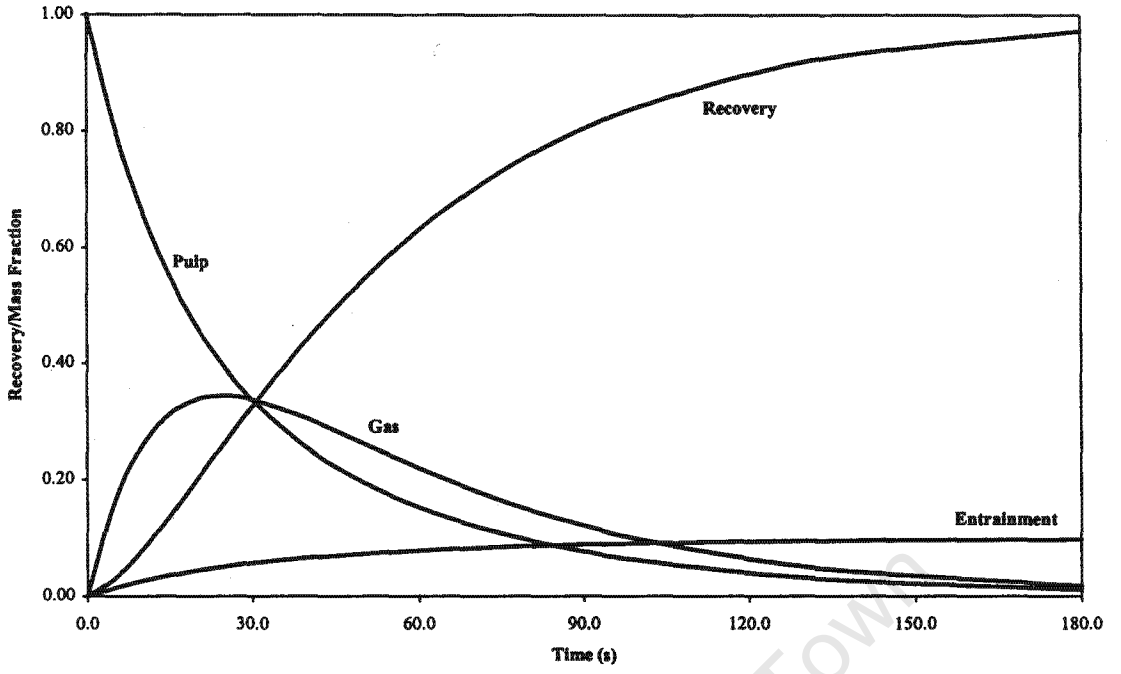

Figure 3.6. Individual contributions of the pulp phase, the gas phase and entrainment to recovery.

In Figure 3.6 the *pulp* and *gas* responses refer to the fraction of the initial mass of particles remaining in the pulp phase and residing on the gas phase respectively while the *entrainment* response represents the cumulative recovery of particles by entrainment. The fraction of particles in the pulp phase decreases rapidly and results in a steep increase in the fraction of particles on the gas phase, though this is not reflected in the recovery until laden bubbles gradually rise out of the pulp phase. Entrainment contributes significantly to the recovery with as much as 10% of the particles being recovered by this process over the course of the flotation test. However, the experimental data used in Figure 3.6 was derived from the flotation of 15 μm particles and the entrainment of coarser particles is less significant.

3.2.1.2 Gas-Residence Model

The attachment-detachment model reduces to what is referred to as the *gas-residence model* in this study by setting the detachment rate constant constant to zero in Equations 3.21 and 3.22, viz. Equations 3.30 and 3.31.

$$\frac{C}{C_o} = e^{(-k-\alpha(x_e-1))t} \qquad (3.30)$$

$$\frac{C_s S}{C_o} = \left(\frac{k}{-k + \frac{1}{\tau_{gs}} - x_e \alpha} \right) \left(e^{(-k-\alpha(x_e-1))t} - e^{\left(\alpha - \frac{1}{\tau_{gs}}\right)t} \right) \quad (3.31)$$

Through this process all attachment and detachment effects are absorbed into the attachment rate constant and, consequently, this quantity reduces to the flotation rate constant. Though the gas-residence model is expressed in terms of the flotation rate constant it differs substantially from the classical batch flotation model and includes the additional effects of gas residence time, entrainment and volume-time dependence on flotation kinetics. The model predicts an initial lag in recovery-time curves due to the gas residence time in the flotation cell and allows for both pulp and surface concentrations to be determined. The gas-residence model predicts meaningful flotation rate constants in cells with appreciable gas residence times as the effects of the gas residence time on the recovery-time response are separated from those due to actual flotation. The classical batch flotation model attributes any initial lag in the recovery-time curve to poor flotation kinetics and, consequently, under-predicts the flotation rate constant in cells with appreciable gas residence times. In standard laboratory flotation cells both kinetic models give similar results as the gas residence time in these cells is very short (1-2 seconds). The best fit of the gas-residence model to the experimental data used in Figure 3.1 is given in Figure 3.7.

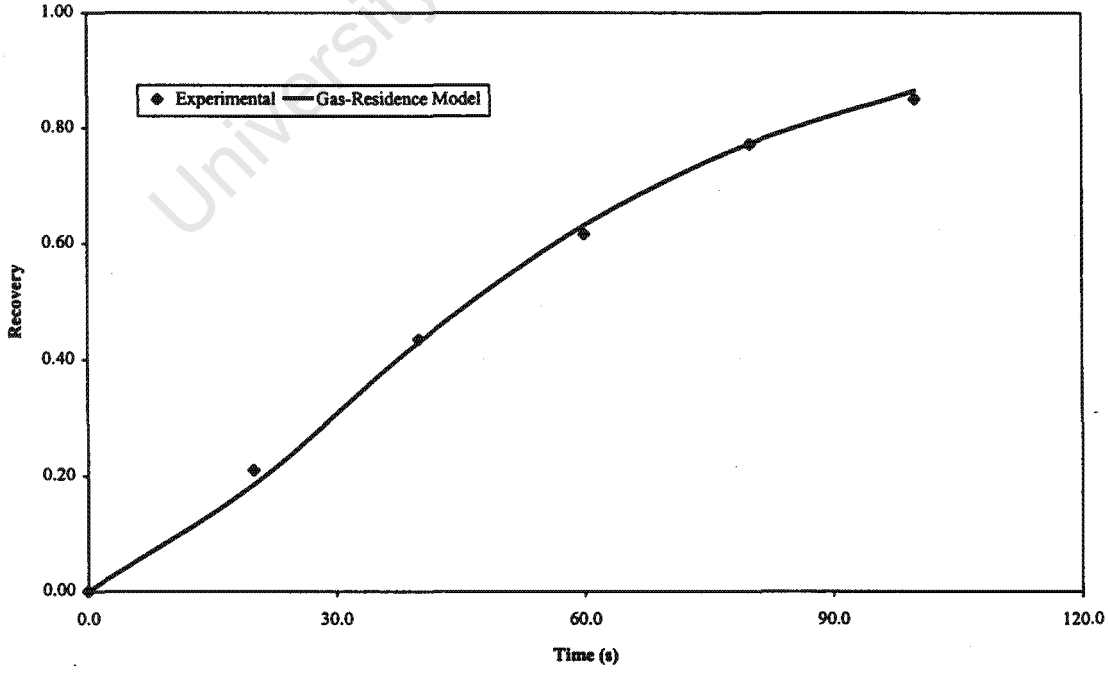

Figure 3.7. The gas-residence model applied to an experimental recovery-time curve.

It is clear from this figure that the gas-residence model is a good representation of the experimental data and compares favourably with the best-fit of the attachment-detachment model. The gas-residence model does, however, deviate slightly from the experimental data near the start of the recovery-time curve due to significant detachment effects caused by high surface concentrations of particles.

3.2.1.3 Standard-Flotation Model

The attachment-detachment model reduces to what is referred to as the *standard-flotation model* in this study by setting both the detachment rate constant and the gas residence time to zero in Equations 3.21 and 3.22, viz. Equation 3.32.

$$\frac{C}{C_o} = e^{(-k-\alpha(x_e-1))t} \qquad (3.32)$$

The standard-flotation model is identical in both form and response to the classical batch flotation model but includes the additional effects of entrainment and volume-time dependence on flotation kinetics. Consequently, the flotation rate constant calculated from the standard-flotation model is a better indicator of true flotation.

3.2.2 Special-Case Relationships

Special-case applications of the kinetic models discussed in Section 3.2.1, required for the analysis of results in Chapters 5.0 and 6.0, are considered in Sections 3.2.2.1 to 3.2.2.3.

3.2.2.1 Distributions of Bubbles

The kinetic models in Section 3.2.1 are applicable to single bubble sizes or to distributions of bubbles characterised by single rate constants and mean bubble diameters. The attachment-detachment model cannot be modified to suit distributions of bubbles due to the large number of variables involved but the gas-residence model can be modified to give Equations 3.33 and 3.34.

$$\frac{C}{C_o} = e^{(-\sum k_i - \alpha(x_e - 1))t} \quad (3.33)$$

$$\frac{S_i C_{si}}{C_o} = \left(\frac{k_i}{-\sum k_i + \frac{1}{\tau_{gsi}} - x_e \alpha} \right) \left(e^{(-\sum k_i - \alpha(x_e - 1))t} - e^{\left(a - \frac{1}{\tau_{gsi}}\right)t} \right) \quad (3.34)$$

These equations are derived on the assumption that the flotation rate constant (k) for a distribution of bubbles can be determined from the sum of the individual flotation rate constants (k_i) for each bubble size class. The contribution to the flotation rate constant from each bubble size class is further assumed to be dependent on the bubble size and proportional to the fraction of the total superficial gas velocity attributed to bubbles of this size class ($x_{gi} = J_{gi}/J_g$). The first assumption considers bubbles to behave independently in the flotation cell and can be justified by similar arguments to those used in the derivation of the expression for the flotation rate constant for distributions of particles (cf. Equation 1.4). The second assumption considers the flotation rate constant to be proportional to the superficial gas velocity and is based on the assumptions used in the derivation of Equation 1.16 in Section 1.4.3. Figure 3.8 represents the surface concentration of particles (C_{si}) on bubbles of different sizes obtained by applying Equations 3.33 and 3.34 to the experimental data used in Figure 3.1. Here, the flotation rate constant for each bubble size class is assumed to be inversely proportional to the bubble size to the power of 1.64 based on findings discussed in Chapter 5.0.

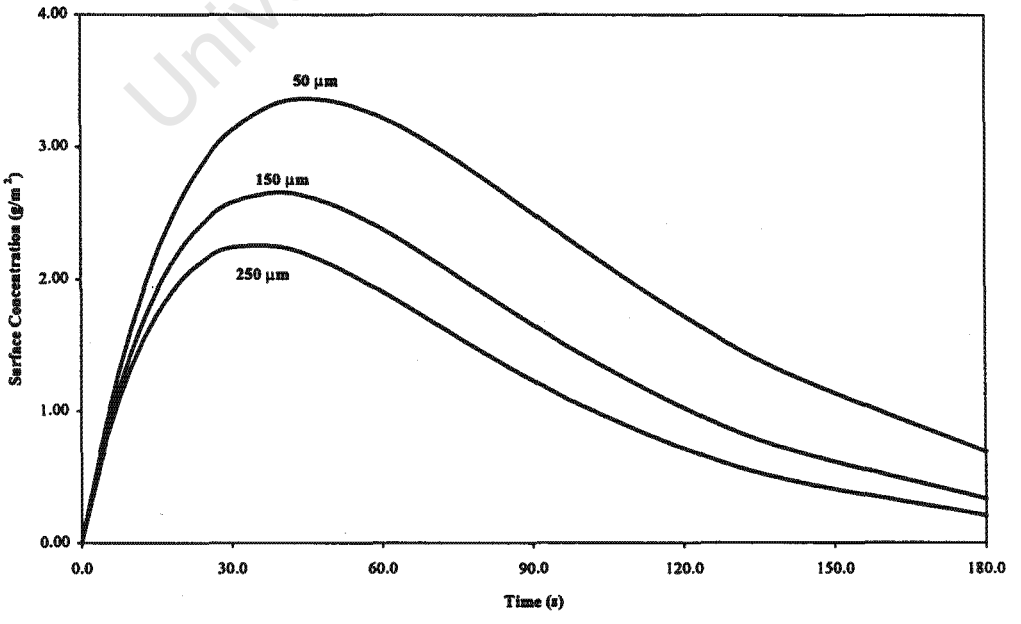

Figure 3.8. Surface concentration of particles on bubbles of different sizes.

It is clear from this figure that small bubbles have both higher surface concentrations than large bubbles and reach maximum surface concentrations after longer times. This can be attributed to a combination of higher flotation rate constants and longer gas residence times, both of which suggest that detachment effects should be more significant for small bubbles.

3.2.2.2 Inferring Detachment

The attachment-detachment model separates flotation into the two independent processes of particle-bubble attachment and particle-bubble detachment. In most instances, however, these two separate processes can be adequately represented through their net outcome/rate using the flotation rate constant in the gas-residence model. Unique attachment and detachment rate constants can only be obtained from recovery-time curves where large variations in pulp and surface concentrations result in the emphasis of attachment or detachment effects in particular regions of the curve. Consequently, attachment and detachment rate constants could seldom be obtained in this study by direct application of the attachment-detachment model to single recovery-time curves. Instead a methodology was devised whereby preliminary estimates of attachment and detachment rate constants were obtained through Equation 3.35.

$$\int_0^t \frac{kC}{C_o} = \int_0^t \frac{k_a C}{C_o} - \int_0^t \frac{k_d C_s S}{C_o} \qquad (3.35)$$

Equation 3.35 is a mass balance relating the cumulative mass of particles recovered by flotation to the difference between the cumulative mass of particles which attach to bubbles and which detach from bubbles over the course of the flotation test. This equation can be applied to experimental data by first determining both flotation rate constants and expressions for the variation of pulp and surface concentrations with time using the gas-residence model. These expressions can then be substituted into Equation 3.35 and integrated to give Equation 3.36.

$$k_a = k + \left(\frac{k}{-k + \frac{1}{\tau_{gs}} - x_e \alpha} \right) \left(1 - \frac{-k - \alpha(x_e - 1)}{\alpha - \frac{1}{\tau_{gs}}} \left(\frac{e^{\left(\alpha - \frac{1}{\tau_{gs}}\right)t} - 1}{e^{(k - \alpha(x_e - 1))t} - 1} \right) \right) k_d \qquad (3.36)$$

This equation provides a relationship between the attachment and detachment rate constants which enables either of the rate constants to be determined provided the other is known. Reasonable

estimates of attachment rate constants can be obtained by extrapolation from the flotation rate constant at low levels of agitation as represented schematically in Figure 3.9.

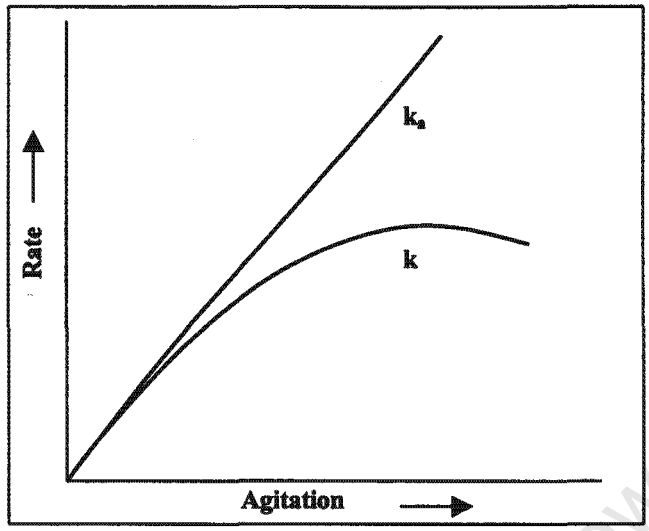

Figure 3.9. Schematic of the relationship between the attachment and flotation rate constants.

Here, the flotation and attachment rate constants are equivalent at low levels of agitation due to the absence of significant detachment effects. As the level of agitation is increased, however, detachment effects become significant and the two rate constant begin to deviate from each other. Consequently, the attachment rate constant can be determined by extrapolation from the curve for the flotation rate constant and substituted into Equation 3.36 to give the detachment rate constant. However, the attachment and detachment rate constants obtained using this technique are only approximations as the technique relies on extrapolation. Accurate attachment and detachment rate constants can be obtained by re-substituting these estimates into the attachment-detachment model, using appropriate constraints, and re-applying the model to the original recovery-time curve.

3.2.2.3 Two-Compartment Model

The models derived in previous sections consider the flotation cell to be a single well-mixed system characterised by single rate constants. Mechanically agitated cells are highly non-uniform with respect to turbulence parameters, however, and are commonly divided into compartments or zones of similar turbulence intensity. The simplest approach is to approximate the cell as being a combination of a bulk tank and an impeller zone as depicted in Figure 3.10. This is referred to as a two-compartment model and has been applied successfully to both flocculation (Koh *et al*, 1984) and flotation (Lu *et al*, 1995) in agitated tanks.

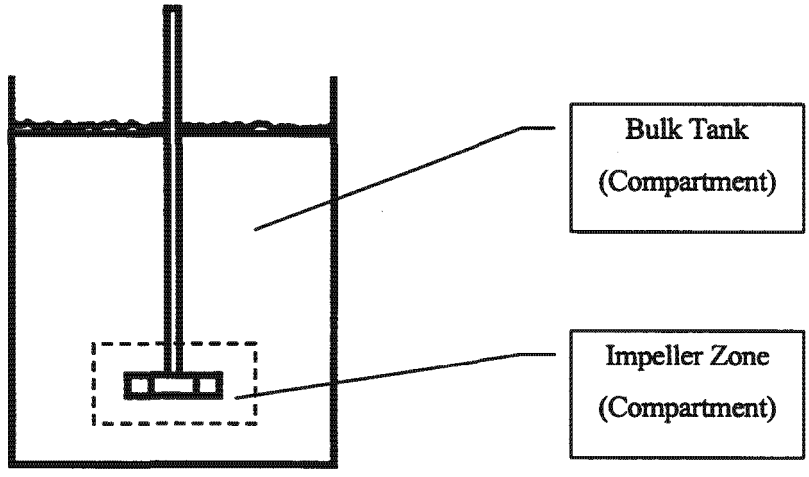

Figure 3.10. Schematic of a two-compartment flotation cell.

By considering a flotation cell to consist of two well-mixed compartments, each characterised by separate attachment and detachment rate constants, expressions for the overall rate constants can be determined using the volumetric fraction occupied by each compartment through Equations 3.37 and 3.38.

$$k_a = x_V k_{aI} + (1 - x_V) k_{aB} \quad (3.37) \qquad k_d = x_V k_{dI} + (1 - x_V) k_{dB} \quad (3.38)$$

3.2.3 Continuous Mechanical Flotation Cell

By applying the attachment-detachment methodology to a continuous mechanical flotation cell the recovery in the absence of entrainment (i.e. true flotation) can be related to the attachment and detachment rate constants, the pulp residence time, (τ_p) and the gas residence time, viz. Equation 3.39.

$$R = \frac{k_a \tau_p}{1 + k_a \tau_p + k_d \tau_{gs}} \quad (3.39)$$

This equation is similar to the expression for recovery in a continuous mechanical flotation cell in terms of the flotation rate constant (viz. Equation 3.40) other than for the detachment term ($k_d\tau_g$) in the denominator.

$$R = \frac{k\tau_p}{1 + k\tau_p} \quad (3.40)$$

The relationship between the flotation rate constant and the attachment and detachment rate constants can be obtained by equating these two models, viz. Equation 3.41.

$$\frac{k}{k_a} = \frac{1}{1 + k_d\tau_{gs}} \quad (3.41)$$

It is clear from this equation that the flotation rate constant is equivalent to the attachment rate constant in the absence of detachment effects but starts to deviate significantly from this quantity through combinations of high detachment rate constants and gas residence times. The gas residence time is strongly dependent on the flotation cell size (cf. Equation 3.10) and, consequently, a large flotation cell is more likely to have a lower flotation rate constant than a small flotation cell. This phenomenon has significant implications for flotation cell design and scale-up and will be explored in detail in Chapter 6.0.

CHAPTER 4: HYDRODYNAMICS AND GAS DISPERSION

The results presented in this chapter are derived from and are applicable to the experimental programme for the characterisation of hydrodynamics and gas dispersion in the flotation cell outlined in Section 2.2. Hydrodynamic data such as turbulence parameters, power inputs and tank turnover times are presented in Tables A1 to A6 in Appendix A. Gas dispersion data such as bubble size, gas holdup and gas residence times are presented in Tables A7 and A8 in Appendix A. Bulk hydrodynamic and gas dispersion parameters and key dimensionless numbers are discussed in Section 4.1. Turbulence and bubble size are discussed individually in Sections 4.2 and 4.3 respectively. Results from Sections 4.1 to 4.3 are used to investigate the validity of theories for bubble breakup in Section 4.4 while findings and conclusions from all of Sections 4.1 to 4.4 are summarised in Section 4.5.

4.1 Bulk Parameters

Hydrodynamic Parameters: As indicated in Section 2.2, specific power inputs in the unaerated flotation cell were found to vary from 0.1 to 5.0 W/kg for the Rushton turbine and from 3.0 to 8.0 W/kg for the spinning disc. Aeration was found to have minimal effect on the power draw for the Rushton turbine at low impeller speeds but to lead to significant decreases (15%) in the power input at high impeller speeds due to appreciably higher gas holdups. The power draw for the spinning disc was found to increase in the aerated flotation cell, especially when the cell was aerated with the porosity 4 sparger. This was an unexpected finding but was confirmed repeatedly and is supported by the measured turbulence parameters discussed in Section 4.2. Tank turnover times (V/Q_I) were calculated for the Rushton turbine using measured fluid velocities at the impeller tip and were found to vary from 0.7 to 5.5 seconds over the range of impeller speeds used in the study (cf. Table 2.2). Corresponding values could not be calculated for the spinning disc, however, as the disc has no characteristic impeller width required for calculating impeller pumping rates. Nonetheless, the spinning disc was inferred to have significantly lower impeller pumping rates than the Rushton turbine as measured turbulence parameters in the bulk tank were found to be orders of magnitude lower (cf. Section 4.2). Aeration was found to lead to significant decreases (20-30%) in impeller

pumping rates for the Rushton turbine and, consequently, to corresponding increases in tank turnover times.

Gas Dispersion Parameters: Gas residence times were calculated using Equation 3.11 and were found to vary from 2 to 53 seconds for the Rushton turbine and from 4 to 41 seconds for the spinning disc over the range of impeller speeds used in the study. The mean gas residence time for all experiments was found to be 26 seconds for the Rushton turbine and 18 seconds for the spinning disc. The significantly higher mean gas residence time for the Rushton turbine is attributed to the higher impeller pumping rates which result in higher gas holdups. The number of times an average bubble passes through the impeller zone before exiting the flotation cell (τ_g/τ_T) was calculated for the Rushton turbine and was found to vary from 1 to 76 passes over the range of impeller speeds used in the study. This suggests that the gas phase in the flotation cell agitated by the Rushton turbine is well-mixed for most of the experiments and supports the assumption of a well-mixed pulp and gas phase used in the derivations in Chapter 3.0. Corresponding conclusions cannot be made for the spinning disc, however, although the significantly lower impeller pumping rates suggest that this assumption is less likely to be true.

Dimensionless Numbers: The power number, impeller Reynolds number, air flow number and Froude number were calculated using the correlations in Table 1.1 and are presented in Table 4.1. The power numbers for the Rushton turbine are consistent with those obtained by Rushton *et al* (1950) while those for the spinning disc are very low but constant. Consequently, the two impellers have power numbers on the extreme sides of the range used in industry and should display vastly different turbulence characteristics. The impeller Reynolds numbers for both impellers are greater than 10 000 for all impeller speeds which indicates that the fluid in the flotation cell is in fully developed turbulent flow (Shinnar and Church, 1960). The Froude numbers are within the range used in industrial flotation cells whereas the air flow numbers are towards the lower end of this range due to the comparatively low gas flowrate chosen for the study (Schubert and Bischofberger, 1978).

Table 4.1. Dimensionless numbers for the Rushton turbine and spinning disc impellers.

	N_{Pw}#	N_{Re}	N_{Af}	N_{Fr}
Rushton Turbine	5.58 – 6.44	12000 – 46000	0.003 - 0.012	0.1 - 2.1
Spinning Disc	0.054 – 0.058	170000 – 280000	0.003 - 0.005	7.50 - 20.2

#Unaerated flotation cell.

4.2 Turbulence

The discussion of turbulence in the flotation cell is divided into an overview of turbulence parameters in Sections 4.2.1 and 4.2.2 and of turbulent energy spectra in Sections 4.2.3 and 4.2.4. The discussion is in the form of both a description and a comparison of turbulence parameters and turbulent energy spectra for the Rushton turbine and spinning disc impellers in both the unaerated and aerated flotation cells. Turbulence parameters and turbulent energy spectra were derived from the experimental measurements discussed in Section 2.2 and using the theory of turbulence discussed in Section 1.5.1.

4.2.1 Turbulence Parameters

Turbulence parameters for the Rushton turbine and the spinning disc in the unaerated flotation cell are presented schematically in Figure 4.1 for the purposes of discussion. The velocity data in this figure refers to the tangential component evaluated at 920 RPM for the Rushton turbine and 2180 RPM for the spinning disc, corresponding to similar power inputs of 2.1 and 2.7 W/kg for the two impellers respectively. Normalised turbulent energy dissipation rates were calculated by averaging over all impeller speeds used in the study.

4.2.1.1 Mean and RMS Turbulent Velocities

Mean Velocities: Mean velocities are up to an order of magnitude higher in the impeller zone than in the bulk tank for both impellers. Mean velocities are, however, up to an order of magnitude lower in the bulk tank for the spinning disc than for the Rushton turbine which suggests that the spinning disc has significantly lower impeller pumping rates. Mean velocities in the impeller zone were found to be directly proportional to the impeller tip velocity for the Rushton turbine. The proportionality constant was found to be 0.86 at the impeller tip and 0.35 midway between the tip and the tank wall which compares well with the findings of other researchers (Wu and Patterson, 1989). Aeration was found to lead to significant decreases (20-30%) in the mean velocity in the impeller zone for the Rushton turbine and to have no significant effect on this quantity for the spinning disc. This was reflected by corresponding reductions (5-18%) in the power input for the Rushton turbine and no change in this quantity for the spinning disc. Aeration was, however, found to lead to significant decreases (20-50%) in the mean velocity in the bulk tank for both impellers.

RMS Turbulent Velocities: As with mean velocities, RMS turbulent velocities are up to an order of magnitude higher in the impeller zone than in the bulk tank for both impellers. Similarly, RMS turbulent velocities are up to an order of magnitude lower in the bulk tank for the spinning disc than for the Rushton turbine. Aeration was found to have minimal effect on the RMS turbulent velocity in the impeller zone for the Rushton turbine but to lead to significant increases (10-30%) in this quantity for the spinning disc. The RMS turbulent velocities in the bulk tank followed similar trends to the mean velocities in both the unaerated and aerated flotation cells, although the decrease in this quantity with aeration was found to be substantially lower (0-20%). The effects of aeration on the mean and RMS turbulent velocities resulted in significant increases (30-100%) in the turbulent intensities throughout the flotation cell.

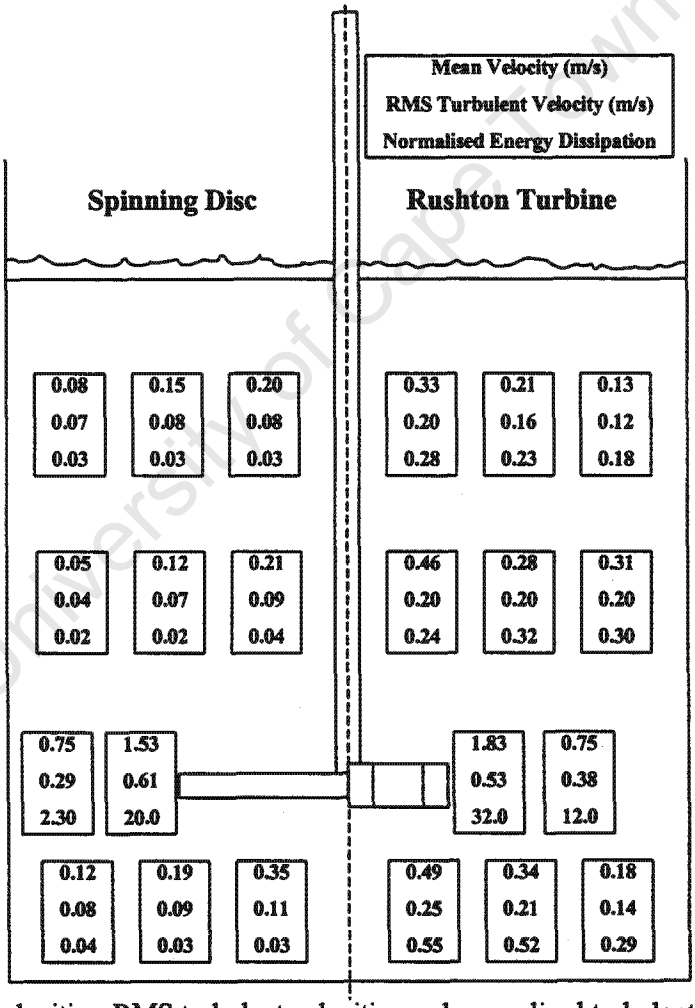

Figure 4.1. Mean velocities, RMS turbulent velocities and normalised turbulent energy dissipation rates for the Rushton turbine (920 RPM) and the spinning disc (2180 RPM) in the unaerated flotation cell.

4.2.1.2 Turbulent Energy Dissipation Rates

For the Rushton turbine turbulent energy dissipation rates are approximately 30 times higher than average (P/ρV) at the impeller tip and fall to 10 to 15 times higher than average in the impeller stream. These values compare well with the findings of other researchers and are exactly in the range of values obtained by Wu and Patterson (1989). For the spinning disc turbulent energy dissipation rates are approximately 20 times higher than average at the impeller tip and fall to 2 to 4 times higher than average in the impeller stream. Turbulent energy dissipation rates in the bulk tank range from 0.20 to 0.50 with an average of 0.32 for the Rushton turbine and remain fairly constant at 0.03 for the spinning disc. Consequently, approximately 30% of the total power input is dissipated in the bulk tank for Rushton turbine which is in good agreement with the findings of Rao and Brodkey (1972), Laufhütte and Mersmann (1987) and Wu and Patterson (1989). Only a few percent of the total power input is dissipated in the bulk tank for the spinning disc, however, and almost all the power is dissipated in the impeller zone. Aeration was found to lead to substantial increases (40-60%) in turbulent energy dissipation rates in the impeller zone for both impellers and to result in corresponding decreases in the bulk tank.

4.2.1.3 Turbulent Macro and Micro Scales

Macroscales: Turbulent macroscales were found to vary from 2 to 3 mm in the impeller zones of both the unaerated and aerated flotation cells for both impellers. This is in the range of values of a quarter to a third of an impeller blade width obtained by both Rao and Brodkey (1972) and Wu and Patterson (1989). Turbulent macroscales were found to vary from 4 to 13 mm with a mean of 7 mm in the bulk tank of the unaerated flotation cell for the Rushton turbine. The mean value of 7 mm is of the order of the impeller blade width which is the characteristic length used in the approximation of the turbulent macroscale (Mujumdar *et al*, 1970). Turbulent macroscales were found to vary from 3 to 10 mm with a mean of 5 mm in the bulk tank of the unaerated flotation cell for the spinning disc. Aeration was found to lead to decreases of up to 50% in turbulent macroscales in the bulk tank for both impellers.

Microscales: Turbulent microscales were found to vary from 0.3 to 1.0 mm in the impeller zone of both the unaerated and aerated flotation cells for both impellers which is in the range of microscales obtained by both Rao and Brodkey (1972) and Wu and Patterson (1989). Turbulent microscales were found to be of the order of 2 mm in the bulk tank of the unaerated flotation cell for both

impellers. Aeration was found to lead to decreases of up to 50% in turbulent microscales in the bulk tank for both impellers.

4.2.2 Discussion of Turbulence Parameters

Comparison of Impellers: An evaluation of the preceding turbulence parameters indicates that, as anticipated, the Rushton turbine and spinning disc vary quite markedly as impellers. The Rushton turbine has a high impeller pumping rate and transfers substantial kinetic energy from the impeller zone to the bulk tank via fluid flow. This results in high mean velocities, RMS turbulent velocities and turbulent energy dissipation rates in the bulk tank and a considerable portion (30%) of the total power input is dissipated in this region. The spinning disc generates comparable RMS turbulent velocities and turbulent energy dissipation rates in the impeller zone to the Rushton turbine. The spinning disc has a lower impeller pumping rate, however, and significantly lower kinetic energy is transferred to the bulk tank via fluid flow. This results in low mean velocities, RMS turbulent velocities and turbulent energy dissipation rates in the bulk tank and only a small portion (2-3%) of the total power input is dissipated in this region.

The Effect of Aeration: Aeration leads to a decrease in the mean velocity at the impeller tip for the Rushton turbine and, consequently, to a reduction in the power input to the flotation cell. This reduction in the mean fluid velocity is further exaggerated in the bulk tank and turbulence parameters such as RMS turbulent velocities and turbulent energy dissipation rates in the impeller zone either remain constant or increase at the expense of these quantities in the bulk tank. Aeration has no effect on the mean velocity at the impeller tip for the spinning disc and, consequently, to the power input to the flotation cell. Aeration does, however, lead to a decrease in the mean velocity in the bulk tank and turbulence parameters such as RMS turbulent velocities and turbulent energy dissipation rates in the impeller zone increase at the expense of these quantities in the bulk tank. The net effect of aeration is a decrease in mean velocities throughout the flotation cell and a corresponding increase in RMS turbulent velocities and turbulent energy dissipation rates in the impeller zone. This general trend was found to be exaggerated when the flotation cell was aerated with progressively smaller bubbles although it is unclear whether this was due to the physical bubble size or to the increased gas holdup.

4.2.3 Turbulent Energy Spectra

Turbulent energy spectra measured at the impeller tip, in the impeller discharge stream and in the bulk tank of the unaerated flotation cell are given for both the Rushton turbine and the spinning disc in Figures 4.2 to 4.4 and are discussed in Sections 4.2.3.1 to 4.2.3.3.

4.2.3.1 Impeller Tip

The turbulent energy spectra obtained at the impeller tip display the characteristic "periodic" component caused by the mechanical pulsation of fluid leaving the impeller blades. The first peaks in both spectra correspond to the impeller speeds of the Rushton turbine (15 Hz) and spinning disc (36 Hz) respectively.

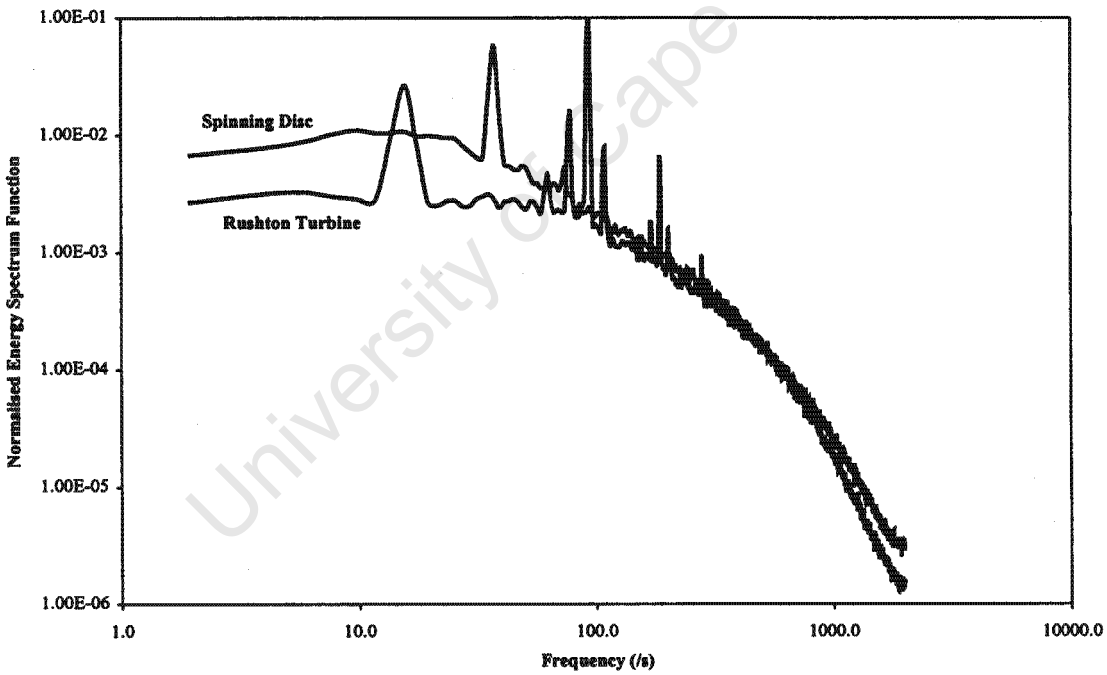

Figure 4.2. Normalised energy spectra for the Rushton turbine (920 RPM) and the spinning disc (2180 RPM) evaluated at the impeller tip.

The peak in the spectrum for the spinning disc is due to the impeller being slightly off-centre and would not be observed in the spectra if the impeller ran perfectly true. The second major peak in the spectrum for the Rushton turbine corresponds to the frequency with which the impeller blades pass the turbulence probe (90 Hz) and is accompanied by several sub-harmonics at integer multiples of

the impeller speed. Peaks at the impeller blade frequency have been observed by Rao and Brodkey (1972) and Komasawa *et al* (1974). Sub-harmonics have been observed by Günkel and Weber (1975) and Van Der Mollen and Van Maanen (1978). The energy spectrum for the spinning disc displays a comparative bias of turbulent kinetic energy toward the lower frequency ranges although this is slightly exaggerated as the spectra were normalised without removing the periodic component. The turbulence parameters listed in Tables A1 to A6 in Appendix A were, however, calculated by integration over the spectrum with the periodic component removed and reflect the true "random" turbulence in the flotation cell. The periodic component of turbulence formed a significant component (40-50%) of the mean square turbulent velocity for the Rushton turbine and a considerably smaller component (5-15%) of this quantity for the spinning disc.

4.2.3.2 Impeller Discharge Stream

The turbulent energy spectra in the impeller discharge stream have been transformed into wave number space under Taylor's hypothesis. The impeller discharge stream is more suitable for the application of Taylor's hypothesis as the mean fluid velocity is high in comparison to the fluctuating velocity and the turbulence is more highly developed than at the impeller tip.

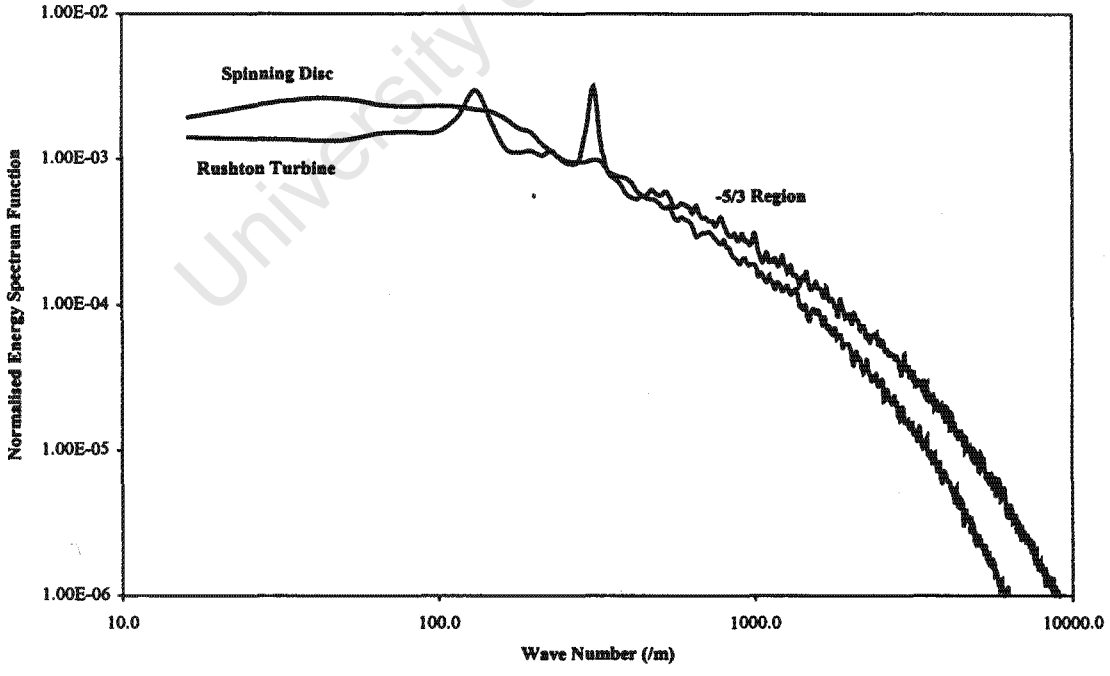

Figure 4.3. Normalised energy spectra for the Rushton turbine (920 RPM) and the spinning disc (2180 RPM) evaluated in the impeller discharge stream.

The energy spectrum for the Rushton turbine goes through the characteristic change in slope from 0 to -1 to -5/3 (log-log axes) as observed by several researchers (Rao and Brodkey, 1972; Günkel and Weber, 1975; Van Der Molen and Van Maanen, 1978; Wu and Patterson, 1989). Beyond the -5/3 region the spectrum reaches a maximum slope of about -5 as opposed to the slope of -7 obtained by Günkel and Weber (1975). The energy spectrum for the spinning disc has a slight positive slope at low wave numbers, then goes through a comparatively rapid change in slope and reaches the -5/3 slope at far lower wavenumbers than the Rushton turbine. The two spectra are similar in form but not in magnitude in the higher wave number ranges although the spectrum for the spinning disc again displays a comparative bias of turbulent kinetic energy toward the lower frequency ranges.

4.2.3.3 Bulk Tank

The turbulent energy spectra in the bulk tank were not found to vary significantly with either impeller speed or location in the flotation cell. This finding is in agreement with the work of Günkel and Weber (1975) who found similar normalised energy spectra throughout the tank for a variety of tanks, impellers and operating conditions.

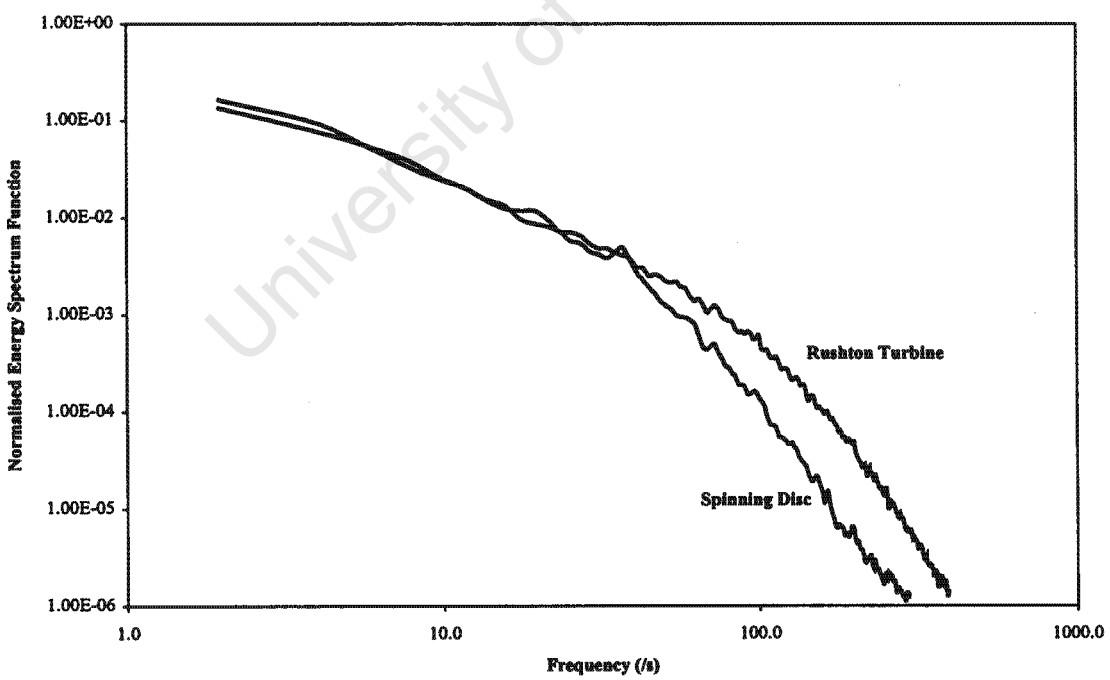

Figure 4.4. Normalised energy spectra for the Rushton turbine (920 RPM) and the spinning disc (2180 RPM) evaluated in the bulk tank.

The energy spectra for the Rushton turbine and the spinning disc display similar characteristics to those discussed in Sections 4.2.3.1 and 4.2.3.2 with the spectrum for the spinning disc again showing a comparative bias of turbulent kinetic energy toward the lower frequency ranges.

4.2.4 Discussion of Turbulent Energy Spectra

Comparison of Impellers: An evaluation of the preceding turbulent energy spectra indicates that, not only do the two impellers differ with respect to turbulence parameters such as RMS turbulent velocities and turbulent energy dissipation rates, but also with respect to the nature of the turbulence generated. The major difference between the energy spectra for the two impellers is the comparative bias of turbulent kinetic energy towards the lower frequency ranges for the spinning disc which results in a corresponding lack of turbulent kinetic energy in the intermediate and high frequency eddies. This is an important difference as it is postulated that it is these intermediate and high frequency eddies which are responsible for effecting microphenomena such as bubble breakup and particle-particle collision. Consequently, even though the spinning disc generates similar turbulence parameters in the impeller zone to the Rushton turbine, the comparative deficiency of appropriate eddies in the energy spectrum might make it a less suitable impeller for effecting microphenomena controlled by this region.

The Effect of Aeration: The turbulent energy spectra discussed in Figures 4.2 to 4.4 were obtained in the unaerated flotation cell but the results and conclusions are directly applicable to the energy spectra for the aerated flotation cell. Aeration was found to have a significant effect on the magnitude of turbulent velocities but to have no effect on the general form of the energy spectra. Consequently, normalised energy spectra in both the unaerated and aerated flotation cells were found to be equivalent which suggests that aeration has an effect on the scale rather than the mechanism of propagation of eddies through the energy spectrum.

4.3 Bubble Size

The discussion of bubble size in the flotation cell is divided into an overview of characteristic bubble sizes and bubble size distributions in Sections 4.3.1 and 4.3.2 respectively. The discussion is in the form of both a description and a comparison of characteristic bubble sizes and bubble size distributions for the Rushton turbine and spinning disc impellers in the flotation cell aerated with the porosity 1, 3 and 4 spargers. Characteristic bubble sizes and bubble size distributions refer to

those obtained on a volumetric-basis and were derived from the experimental measurements discussed in Section 2.2 and using the theory discussed in Section 3.1.

4.3.1 Mean, Sauter Mean and Maximum Stable Bubble Sizes

Mean (d_b), Sauter mean (d_s) and 95 percentile (d_{95}) bubble sizes for the Rushton turbine and the spinning disc and for the flotation cell aerated with the porosity 1, 3 and 4 spargers are summarised in Tables A7 and A8 in Appendix A. The 95 percentile bubble size was obtained graphically from the cumulative bubble size distribution and was chosen as a suitable indicator of the maximum stable (d_{bm}) bubble size as per the method of Takahashi *et al* (1992). Sauter mean bubble sizes are plotted versus specific power input for the Rushton turbine and the spinning disc and for all three spargers in Figures 4.5 and 4.6 respectively.

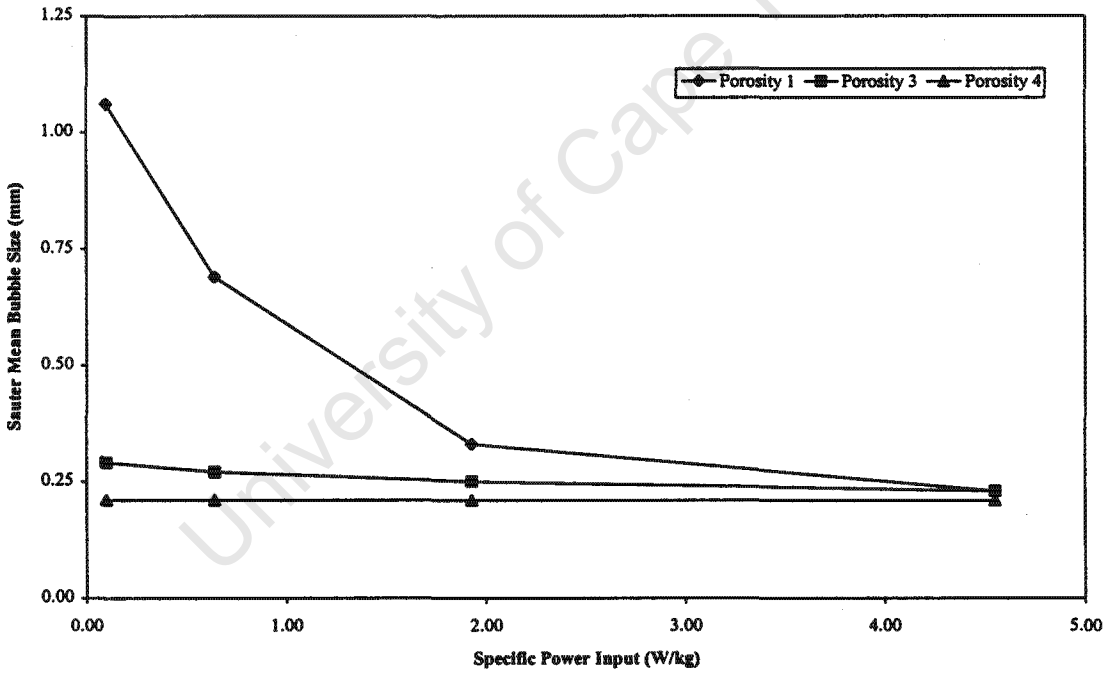

Figure 4.5. Variation of the Sauter mean bubble size (mm) with specific power input (W/kg) for the Rushton turbine (Porosity 1, 3 & 4 spargers).

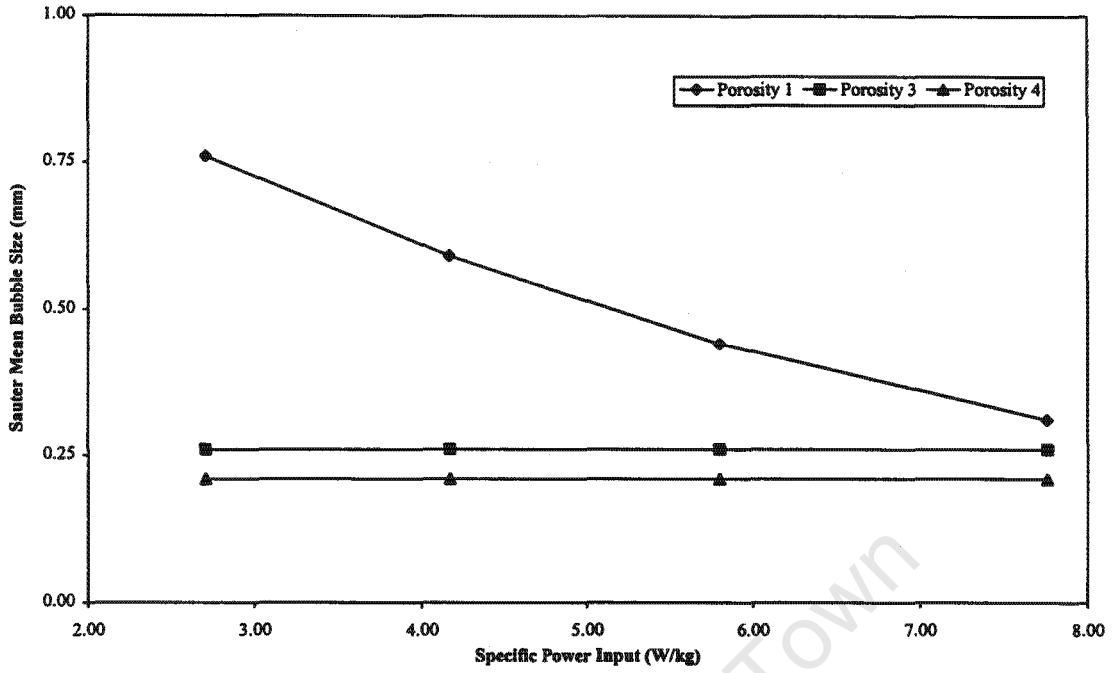

Figure 4.6. Variation of the Sauter mean bubble size (mm) with specific power input (W/kg) for the spinning disc (Porosity 1, 3 & 4 spargers).

It is clear from Figures 4.5 and 4.6 that bubbles generated by the porosity 1 sparger are large and breakup with increasing power input (impeller speed) in a manner analogous to gas dispersion in mechanical flotation cells. It is also clear that bubbles generated by the porosity 3 and 4 spargers are too small to be broken by impeller action and remain reasonably constant in size over the full range of power inputs (impeller speeds) for both impellers. This phenomenon was observed by both Ahmed and Jameson (1985) and Parthasarathy *et al* (1991) in similar systems. Bubbles generated by the porosity 1 sparger asymptote towards those generated by the porosity 3 and 4 spargers and all three spargers would result in equivalent bubble sizes at sufficiently high power inputs. It is interesting to note that the decrease in the Sauter mean bubble size with increasing power input is less severe for the spinning disc than for the Rushton turbine even though the power inputs are somewhat higher. This appears to contradict with the theories for bubble breakup outlined in Section 1.5.2 and will be explored in detail in Section 4.4.

In Section 1.5.2 it was indicated that it is common to assume direct proportionality between the Sauter mean and the maximum stable bubble sizes. The relationship between the mean, Sauter mean and maximum stable bubble sizes was tested by assuming direct proportionality between each of these quantities and performing linear regression over the entire Rushton turbine and spinning disc data sets. The mean bubble size was found to be 0.66 times the Sauter mean bubble size with a poor correlation coefficient of 0.93. The Sauter mean bubble size was, however, found

to be 0.79 times the maximum stable bubble size with an excellent correlation coefficient of 0.995. This is in the range of values obtained by Takahashi *et al* (1992) for agitated gas-liquid dispersions but is significantly higher than the value of 0.62 obtained by Hesketh *et al* (1987) for two-phase pipeline flow.

4.3.2 Bubble Size Distributions

The development of the bubble size distribution with increasing power input (impeller speed) for the Rushton turbine and for the flotation cell aerated with the porosity 1 sparger is represented in Figure 4.7.

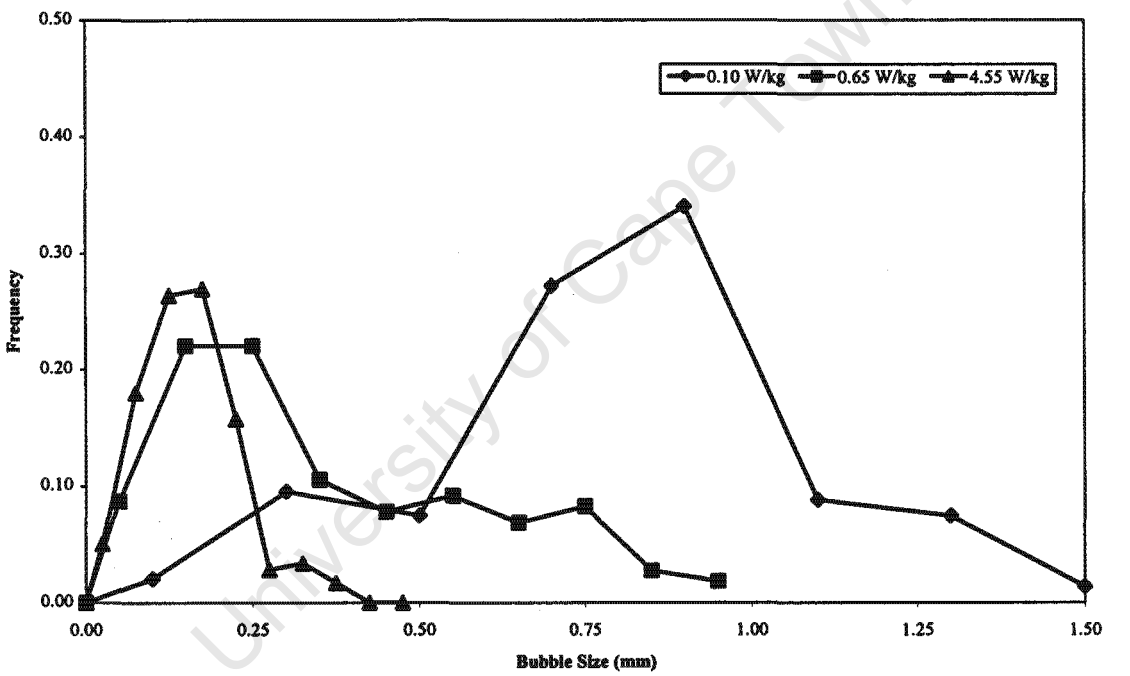

Figure 4.7. Variation of the bubble size distribution for different specific power inputs (W/kg).

It is clear from Figure 4.7 that the porosity 1 sintered glass discs tend to produce irregular, plug-like distributions at low power inputs (0.10 W/kg). Bubble breakup occurs with increasing power input, however, and the initial plug-like distribution becomes bimodal at higher power inputs (0.65 W/kg). With further increases in power input the smaller mode of the bimodal distribution grows at the expense of the larger mode and ultimately (viz. 4.55 W/kg) the bimodal distribution reverts to a typical lognormal distribution. This is a relatively common observation in the gas dispersion literature and has been observed by researchers such as Chatzi and Kiparissides (1992) and Parthasarathy and Ahmed (1994).

4.4 Bubble Breakup

In Section 1.5.2 two theories for predicting the process of bubble breakup in a turbulent fluid were presented. The first theory proposed that bubble breakup occurs due to pressure fluctuations caused by relative velocity fluctuations across the bubble diameter. In the special case of homogeneous isotropic turbulence these relative velocity fluctuations are correlated to the turbulent energy dissipation rate. In the limiting case of equilibrium the maximum stable bubble size is predicted through a critical ratio of the disruptive pressure fluctuations to the stabilising surface tension (viz. N_{Wec} in Equation 1.24). The second theory proposed that bubble breakup occurs due to the collision of the bubble with an eddy of comparable size to the bubble. This means that bubble breakup is controlled by the turbulent kinetic energy of eddies of comparable size to the bubble. In the limiting case of equilibrium the maximum stable bubble size is correlated to the ratio of the disruptive turbulent kinetic energy of eddies smaller than the bubble to the stabilising surface energy of the bubble (viz. Equation 1.25). Though researchers have presented other theories for drop/bubble breakup based on elongational and/or shear stresses (Kumar *et al*, 1991) these are considered to be more relevant to liquid-liquid dispersions. Consequently, the two probable turbulence parameters influencing the process of bubble breakup are the turbulent energy dissipation rate and the turbulent kinetic energy of eddies of comparable size to the bubbles. The relative bubble breakup performance of the Rushton turbine and the spinning disc are discussed in terms of these two turbulence parameters in Sections 4.4.1 and 4.4.2 respectively. Parameters measured in the impeller zone are used for the comparisons as it is generally accepted that the impeller region controls the process of bubble breakup (Parthasarathy *et al*, 1991). The breakup response of bubbles generated by the porosity 1 sparger is used as these bubbles were sufficiently large to undergo breakup over the range of impeller speeds used in the study.

4.4.1 Turbulent Energy Dissipation Rate

Figure 4.8 compares the variation of the maximum stable bubble size with the turbulent energy dissipation rate for the Rushton turbine and the spinning disc. Equation 1.24 has been fitted to the bubble size data for the Rushton turbine as it was found to correlate reasonably well with this data but to correlate poorly with bubble size data for the spinning disc. An average critical Weber number of 1.27 was obtained for the Rushton turbine which compares well with values reported in the literature (cf. Section 1.5.2).

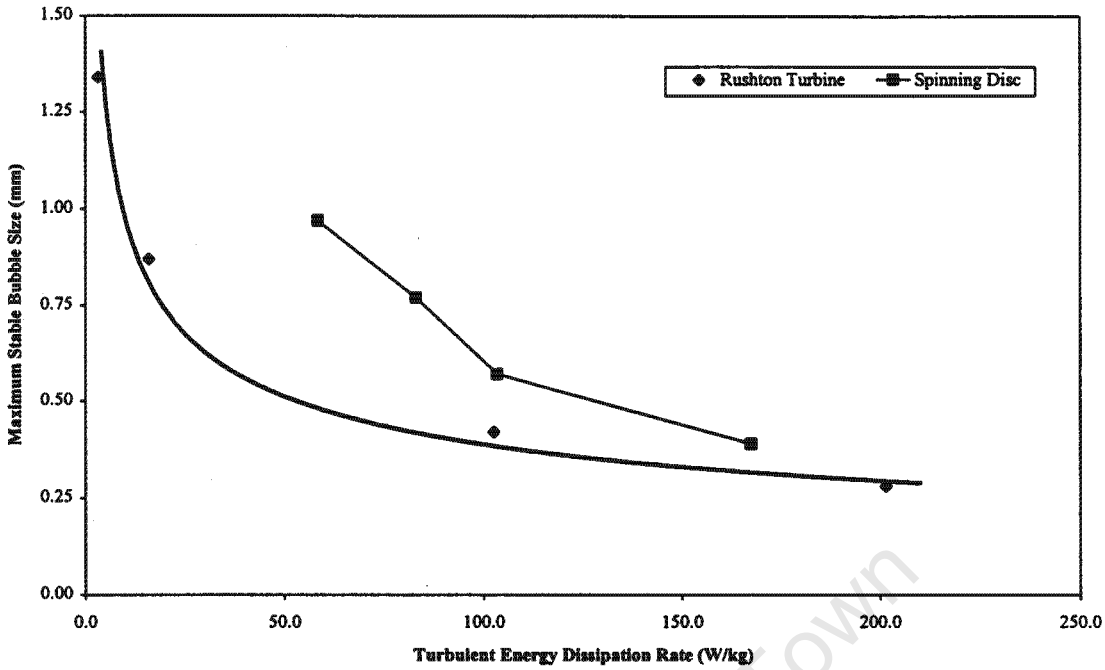

Figure 4.8. Variation of the maximum stable bubble size (mm) with the turbulent energy dissipation rate (W/kg) for the Rushton turbine and the spinning disc.

It is clear from Figure 4.8 that the Rushton turbine achieves significantly smaller bubble sizes than the spinning disc at low turbulent energy dissipation rates but that the bubble sizes for the spinning disc asymptote towards those for the Rushton turbine at higher turbulent energy dissipation rates. According to Equation 1.24, however, both the Rushton turbine and the spinning disc should yield equivalent equilibrium maximum stable bubble sizes at equivalent turbulent energy dissipation rates. Two possible reasons for this discrepancy are that the conditions for the application of Equation 1.24 are not valid or that bubbles in the flotation cell agitated by the spinning disc are not at their equilibrium sizes.

The conditions for the application of Equation 1.24 are that the turbulence is isotropic and that the inertial subrange eddies exist and are of the order of the bubble size. The -5/3 region in Figure 4.3 is an indicator of the existence of the inertial subrange and extends from wave numbers of 1000 to 3000 for the Rushton turbine and from 500 to 2500 for the spinning disc. If the inverse of the wave number is used as an indicator of the scale of eddies then the inertial subrange eddies extend from 0.3 to 1.0 mm for the Rushton turbine and from 0.4 to 2.0 mm for the spinning disc which is exactly in the range of bubbles generated by the porosity 1 sparger (d_s=1.05 mm). The microscale Reynolds numbers (λ_f/ν) in the impeller zone varied from 100 to 500 for the Rushton turbine and from 250 to 700 for the spinning disc which indicates that local isotropic turbulence can be expected for most conditions (Rao and Brodkey, 1972). Consequently, the conditions for the

application of Equation 1.24 are satisfied for both impellers and the poor applicability of the model to the bubble size data for the spinning disc may be attributed to non-equilibrium conditions.

This is considered likely as it was shown in Section 4.1 that the Rushton turbine has both higher impeller pumping rates and results in longer gas residence times than the spinning disc. Consequently, bubbles in the flotation cell agitated by the Rushton turbine pass through the impeller zone more often than bubbles in the flotation cell agitated by the spinning disc. Equilibrium is approached with successive passes through the impeller zone and bubbles in the flotation cell agitated by the Rushton turbine will be closer to equilibrium than those for the spinning disc. Bubbles in the flotation cell agitated by the spinning disc would eventually approach equilibrium with increasing impeller speed due to a combination of successively smaller bubbles, higher gas holdups and higher impeller pumping rates. This explains the gradual asymptotic trend of the bubble size data for the spinning disc towards that for the Rushton turbine and implies that a spinning disc operating at sufficiently high impeller speeds would generate equivalent bubble sizes to a Rushton turbine.

Figure 4.9 represents the variation of the turbulent energy dissipation rate with specific power input for the Rushton turbine and the spinning disc.

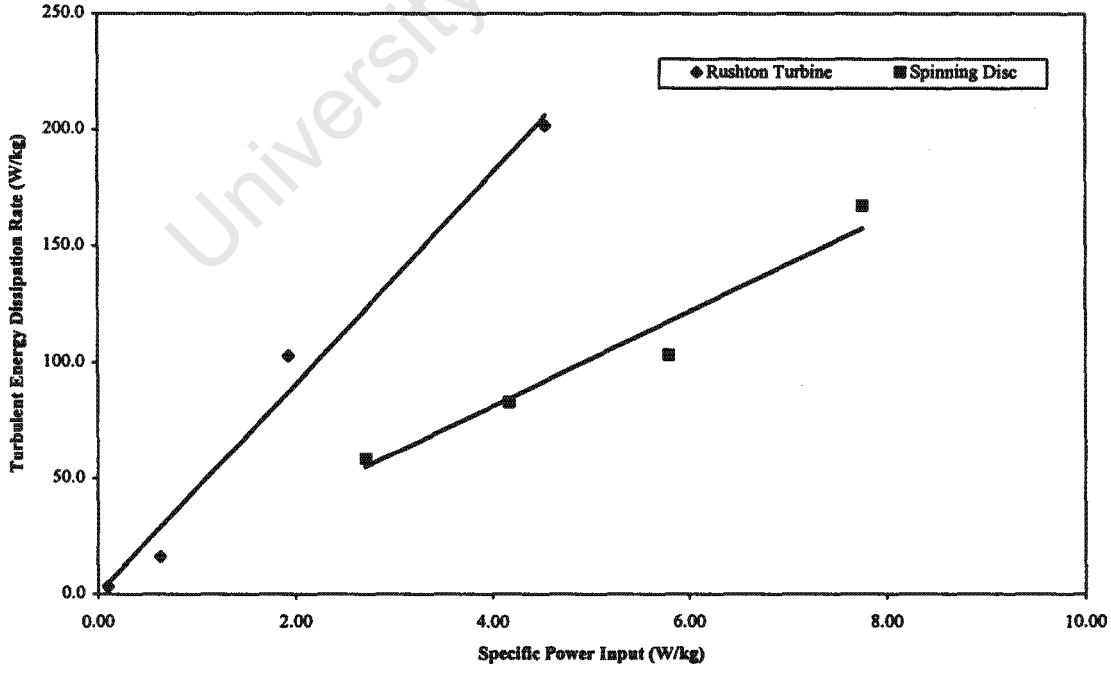

Figure 4.9. Variation of the turbulent energy dissipation rate (W/kg) with specific power input (W/kg) for the Rushton turbine and the spinning disc.

It is clear from Figure 4.9 that the Rushton turbine achieves significantly higher turbulent energy dissipation rates than the spinning disc at equivalent specific power inputs. This appears to conflict with the findings from Section 4.2 in which it was established that almost all the power input to the flotation cell is dissipated in the impeller zone for the spinning disc while only 70% of the power input is dissipated in this region for the Rushton turbine. Consequently, the spinning disc should be able to achieve significantly higher turbulent energy dissipation rates in the impeller zone than the Rushton turbine. A spinning disc with a larger impeller diameter than the Rushton turbine (1.57 times) was chosen for the study for reasons discussed in Section 2.1. This resulted in the spinning disc having a significantly larger impeller swept volume than the Rushton turbine and, consequently, to correspondingly lower turbulent energy dissipation rates in the impeller zone. From Figure 4.9, however, the turbulent energy dissipation rate is approximately proportional to the specific power input which implies that a constant fraction of power is dissipated in the impeller zone at all conditions. Consequently, a small spinning disc operating at high impeller speeds would result in high turbulent energy dissipation rates in the impeller zone and would be a very efficient impeller for bubble breakup.

4.4.2 Turbulent Kinetic Energy

Figure 4.10 compares the variation of the maximum stable bubble size with the turbulent kinetic energy of eddies less than 1 mm in size for the Rushton turbine and the spinning disc. The turbulent kinetic energy was calculated by numerical integration over the energy spectra and represents the total kinetic energy of eddies less than 1 mm in size. This dimension was chosen as it is comparable to the size of bubbles generated by the porosity 1 sparger (d_s=1.05 mm). It is clear from Figure 4.10 that the bubble size data for the Rushton turbine and the spinning disc display completely opposite trends. The Rushton turbine data shows an initial steep decrease in bubble size with increasing turbulent kinetic energy followed by a gradual asymptotic decrease. The spinning disc data shows a steep and continual decrease in bubble size with increasing turbulent kinetic energy, ultimately achieving smaller bubble sizes than the Rushton turbine at equivalent turbulent kinetic energies. The opposite trends for the Rushton turbine and the spinning disc can be explained using Figure 4.11 which represents the variation of the turbulent kinetic energy with specific power input for the two impellers.

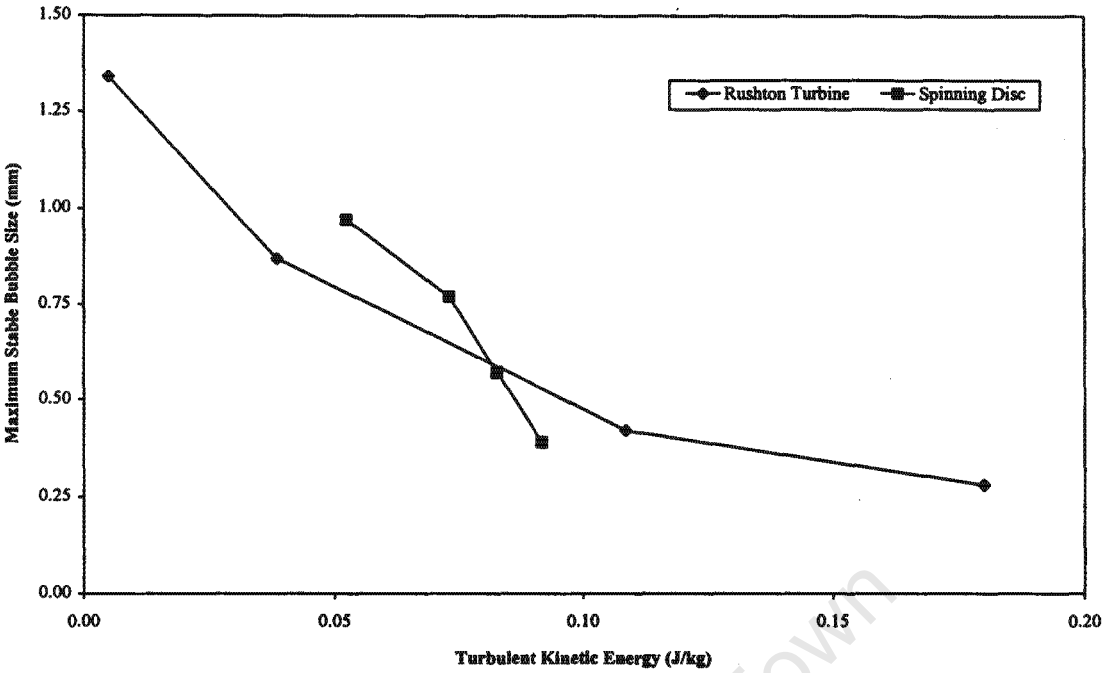

Figure 4.10. Variation of the maximum stable bubble size (mm) with the turbulent kinetic energy of eddies less than 1 mm in size (J/kg) for the Rushton turbine and the spinning disc.

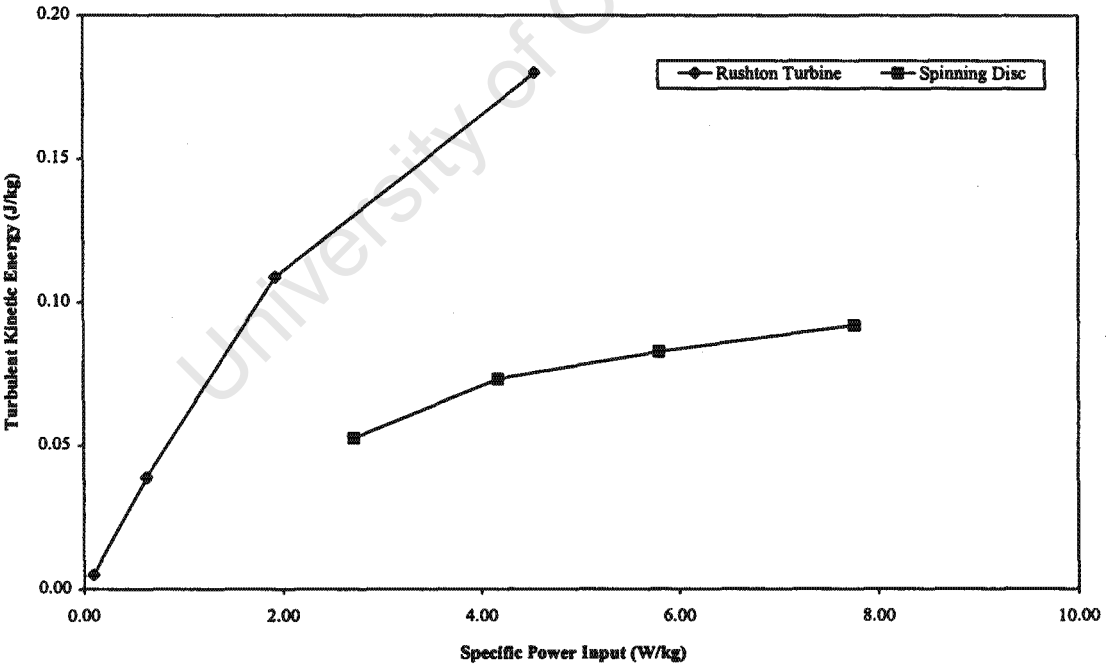

Figure 4.11. Variation of the turbulent kinetic energy (J/kg) with specific power input (W/kg) for the Rushton turbine and the spinning disc.

It is clear from Figure 4.11 that the Rushton turbine displays a steep increase in turbulent kinetic energy with increasing power input while the spinning disc displays a comparatively shallow

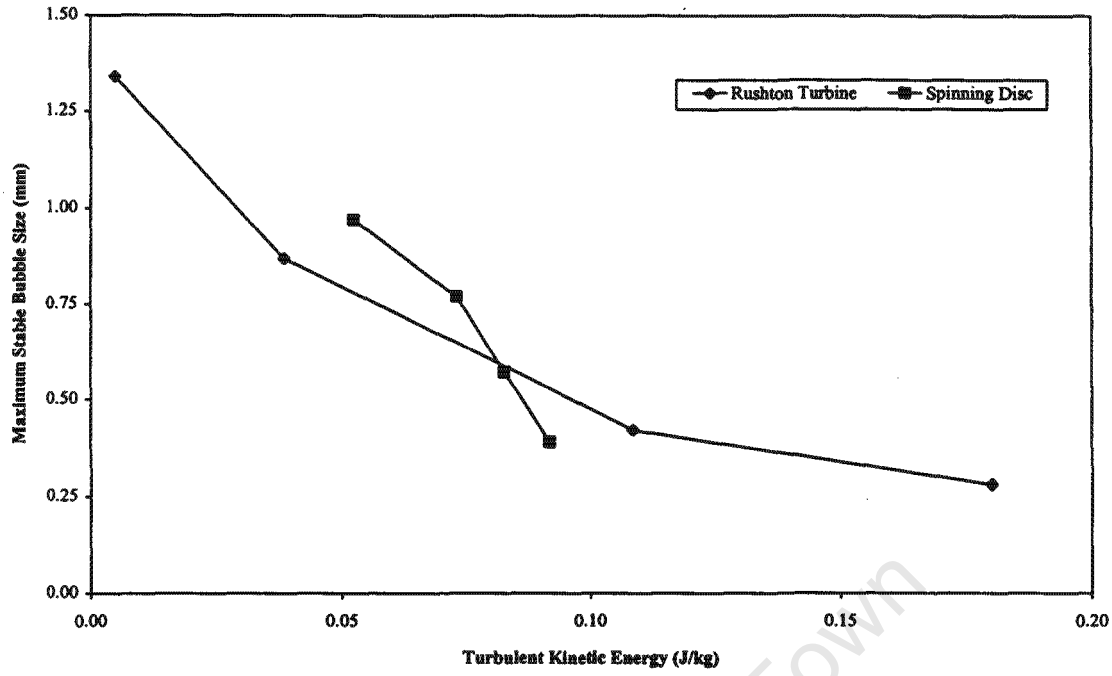

Figure 4.10. Variation of the maximum stable bubble size (mm) with the turbulent kinetic energy of eddies less than 1 mm in size (J/kg) for the Rushton turbine and the spinning disc.

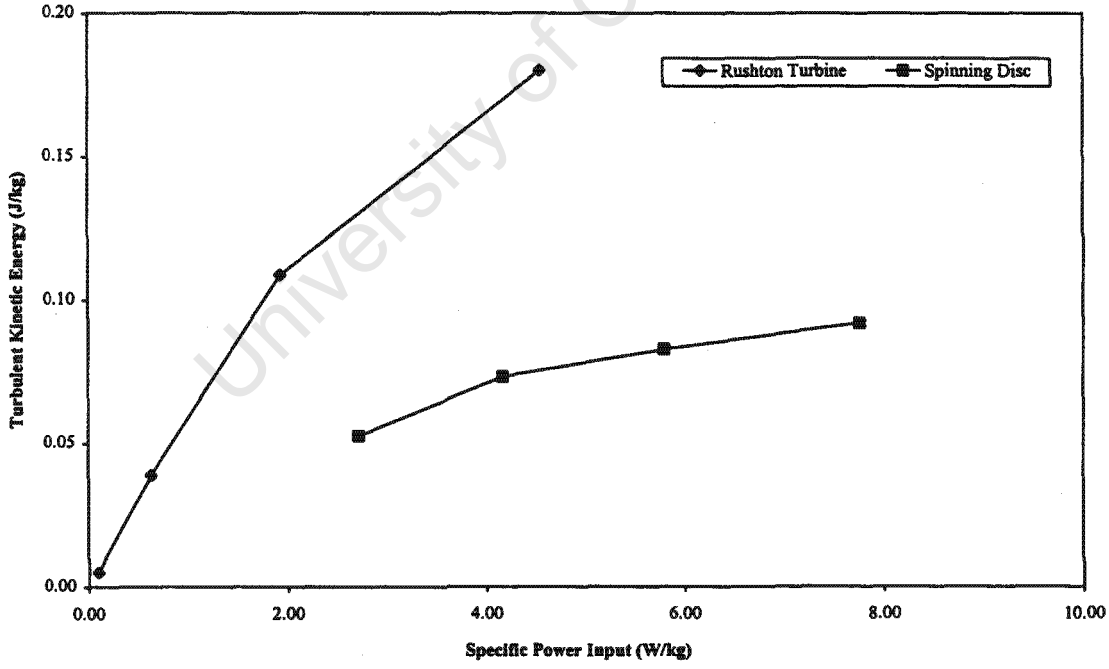

Figure 4.11. Variation of the turbulent kinetic energy (J/kg) with specific power input (W/kg) for the Rushton turbine and the spinning disc.

It is clear from Figure 4.11 that the Rushton turbine displays a steep increase in turbulent kinetic energy with increasing power input while the spinning disc displays a comparatively shallow

asymptotic increase. Consequently, the opposite trends evident in Figure 4.10 are due to the dissimilar nature of the turbulent kinetic energy responses for the two impellers. Similarly, Equation 1.25 was found to result in erratic and contrary trends when applied to the bubble size data for the two impellers. This suggests that the bubble breakup model based on the collision of a bubble with a turbulent eddy is inapplicable to the experimental data.

4.5 Conclusions

Hydrodynamics: The specific power inputs for the Rushton turbine and the spinning disc are within the range of power inputs used in mechanical flotation cells with values for the spinning disc being in the upper end of this range. Characteristic dimensionless numbers for the two impellers are within the range of values typically found in mechanical flotation cells although power numbers are on the extreme sides of this range. Turbulence parameters and energy spectra measured in the flotation cell are consistent with those obtained by other researchers in similar systems and found in the turbulence literature. Turbulence in the flotation cell is isotropic but non-homogeneous and the cell can be regarded as a two-compartment system consisting of a bulk tank and an impeller zone with each compartment having uniform, though order of magnitude different, turbulence parameters throughout. Aeration has a significant influence on the turbulence parameters and leads to a substantial decrease in both mean and turbulent velocities in the bulk tank, especially when the cell is aerated with very small bubbles. Aeration leads to an intensification of both turbulent velocities and local turbulent energy dissipation rates in the impeller zone at the expense of these quantities in the bulk tank. Aeration and bubble size have no effect on the general form of the energy spectrum which suggests that the presence of gas does not affect the mechanism of transmission of energy through the spectrum.

Gas Dispersion: Gas residences times in the flotation cell extend to maximum values of 53 seconds for the Rushton turbine and 41 seconds for the spinning disc which is much longer than those obtained in standard laboratory flotation cells. For the Rushton turbine the gas phase in the flotation cell is considered to be well-mixed due to a combination of high gas residence times and high impeller pumping rates. For the spinning disc, however, a similar conclusion cannot be reached as impeller pumping rates could not be determined. Nonetheless, it is inferred from the measured velocities and gas holdups that the spinning disc has a significantly lower impeller pumping rate than the Rushton turbine. Characteristic bubble sizes such as mean, Sauter mean and maximum stable bubble sizes are consistent with those obtained by other researchers in similar systems and found in the gas dispersion literature. The Sauter mean bubble size is directly proportional to the

maximum stable bubble size with a proportionality constant of 0.79. This is an interesting finding as proportionality between these two characteristic bubble sizes is often assumed in the literature but is seldom verified experimentally. Bubbles generated by the porosity 1 sparger are large and breakup with increasing power input (impeller speed) while bubbles generated by the porosity 3 & 4 spargers are small and remain relatively constant in size over the range of experimental power inputs (impeller speeds). Consequently, the cell aerated with the porosity 1 sparger can be compared to a mechanical flotation cell as the mechanism of gas dispersion is similar while the cell aerated with the porosity 3 & 4 spargers allows for comparisons at fixed bubble sizes. The model for bubble breakup based on turbulent pressure fluctuations is applicable to the bubble size data for the Rushton turbine but is inapplicable to that for the spinning disc. This discrepancy is attributed to the bubbles in the flotation cell agitated by the spinning disc being further from their equilibrium sizes than those for the Rushton turbine due to the lower impeller pumping rate of the spinning disc impeller. The model for bubble breakup based on the collision of a bubble with a turbulent eddy of comparable dimensions to the bubble is erratic and gives opposite trends for the two impellers.

Comparison of Impellers: As anticipated at the outset of this study, the Rushton turbine and the spinning disc differ quite markedly in their behaviour. For the Rushton turbine both turbulent velocities and turbulent energy dissipation rates are considerably higher in the bulk tank than for the spinning disc. Consequently, for the Rushton turbine approximately 30% of the power input is dissipated in the bulk tank and only 2-3% of the power input is dissipated in this region for the spinning disc. This suggests that the Rushton turbine is a suitable impeller for use in systems where microphenomena are dependent on turbulence in the bulk tank, such as the process of particle-bubble collision in flotation. Similarly, this suggests that the spinning disc is a suitable impeller for use in systems where microphenomena are dependent on turbulence in the impeller zone, such as the process of bubble/drop breakup in gas/liquid dispersion. The Rushton turbine was found to be a more efficient impeller for bubble breakup in this study but this is attributed to an inappropriate selection of spinning disc dimensions and impeller speeds. A small spinning disc operating at significantly higher impeller speeds to those used in this study would be a more efficient impeller for bubble breakup. There are, however, distinct differences between the energy spectra for the two impellers. Spectra for the spinning disc display a comparative lack of turbulent energy in the intermediate and higher frequency eddy ranges. This deficiency might limit the suitability of the spinning disc for effecting microphenomena involving eddies of this size range but was not observed in this study.

CHAPTER 5: FLOTATION

The results presented in this chapter are derived from and are applicable to the experimental programme for flotation outlined in Section 2.3.3. Size-by-size recovery-time data for all the flotation tests are presented in Tables B1 to B12 in Appendix B. Rate constants derived from flotation tests on the -32 μm sample for the Rushton turbine and spinning disc impellers are discussed in Section 5.1. Rate constants derived from flotation tests on the -32 and -100 μm samples for the Rushton turbine impeller only are discussed in Sections 5.2 to 5.4. Rate constants presented in Sections 5.1 and 5.2 were calculated using the standard-flotation model only while rate constants presented in Sections 5.3 and 5.4 were calculated using the gas-residence and attachment-detachment models. In this chapter emphasis is placed on the interpretation of results using the standard-flotation model as this is almost exclusively used in the flotation literature and allows for comparison with the review presented in Section 1.6. Similarly, in this chapter, emphasis is placed on the application of the gas-residence and attachment-detachment models to the experimental data while the significance and interpretation thereof are explored in Chapter 6.0. It should be noted that references to "particle-bubble attachment" or "particle-bubble detachment" in the interpretation of results from the standard-flotation model imply the actual physical phenomena occurring and do not refer to quantities calculated using the attachment-detachment model.

5.1 The Rushton Turbine and Spinning Disc Impellers

The results presented in this section are derived from "Phase One" of the experimental programme presented in Table 2.4 and discussed in Section 2.3.3. However, results for the Rushton turbine impeller derived from flotation tests on the -32 μm sample from "Phase Two" of the experimental programme are used in preference to those from "Phase One" as these were found to be equivalent but to cover a more pertinent range of power inputs.

5.1.1 Particle Size

Figure 5.1 represents the variation of the flotation rate constant with particle size for the -32 μm sample and for the flotation cell aerated with the porosity 4 sparger. The responses for the Rushton turbine operating at both low and high impeller speeds (power inputs) have been plotted on this figure for comparative purposes. Equivalent responses for the spinning disc have been omitted from this figure as these are similar to those for the Rushton turbine and do not illustrate any additional principles. Bubbles generated by the porosity 4 sparger remained constant in size over the full range of impeller speeds and, consequently, the responses are applicable to a constant bubble size of 0.21 mm (cf. Section 4.3.1).

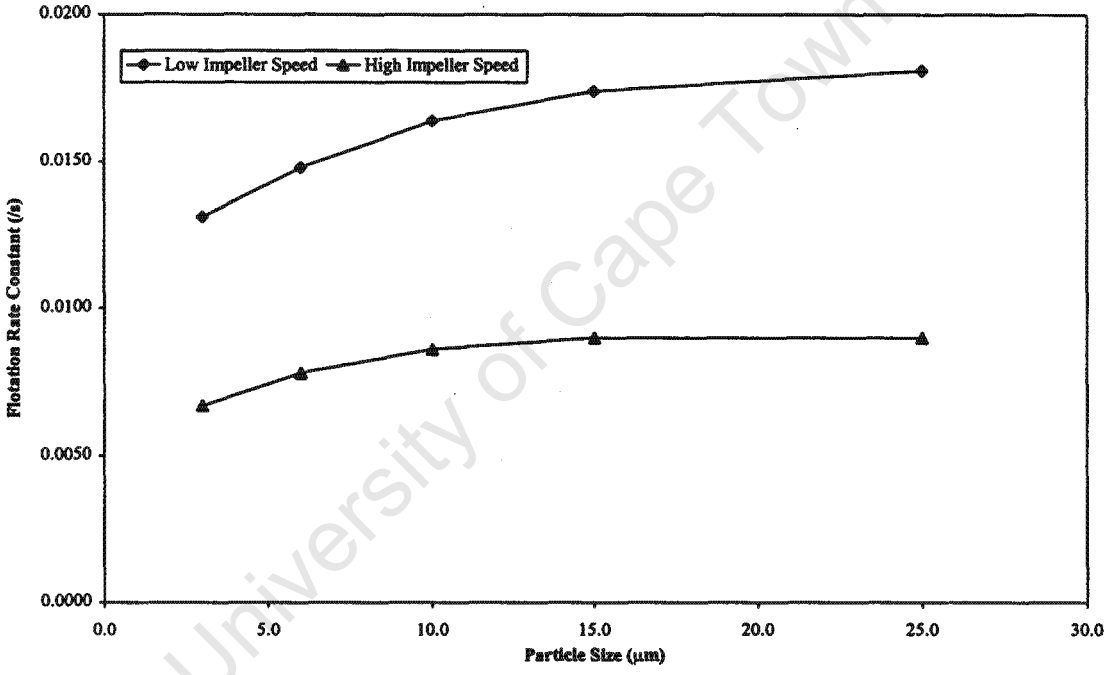

Figure 5.1. Variation of the flotation rate constant (/s) with particle size (μm) for the Rushton turbine.

Low Impeller Speed: Under these comparatively quiescent conditions there is a gradual increase in the flotation rate constant with increasing particle size. The flotation rate constant was found to be proportional to the particle size to the power 0.15 which is substantially lower than the value of about 1.0 commonly quoted for quartz in the flotation literature (cf. Section 1.6.2.1). Most of the results quoted in the literature were, however, derived from flotation tests on narrow size ranges of considerably coarser particles than the -32 μm sample used in this study (d_p=8.3 μm). The rate of flotation of fine particles is known to be less dependent on particle size than that for coarse particles and, for very fine particles, is considered to be independent of particle size (Gaudin *et al*, 1942).

5.1.1 Particle Size

Figure 5.1 represents the variation of the flotation rate constant with particle size for the -32 μm sample and for the flotation cell aerated with the porosity 4 sparger. The responses for the Rushton turbine operating at both low and high impeller speeds (power inputs) have been plotted on this figure for comparative purposes. Equivalent responses for the spinning disc have been omitted from this figure as these are similar to those for the Rushton turbine and do not illustrate any additional principles. Bubbles generated by the porosity 4 sparger remained constant in size over the full range of impeller speeds and, consequently, the responses are applicable to a constant bubble size of 0.21 mm (cf. Section 4.3.1).

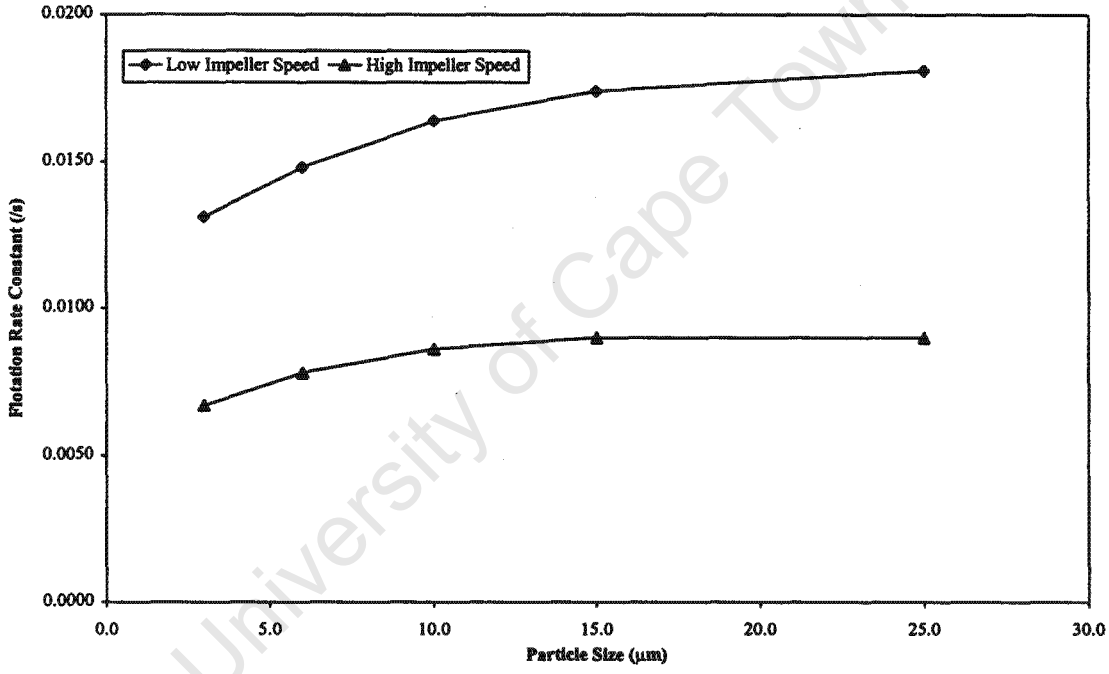

Figure 5.1. Variation of the flotation rate constant (/s) with particle size (μm) for the Rushton turbine.

Low Impeller Speed: Under these comparatively quiescent conditions there is a gradual increase in the flotation rate constant with increasing particle size. The flotation rate constant was found to be proportional to the particle size to the power 0.15 which is substantially lower than the value of about 1.0 commonly quoted for quartz in the flotation literature (cf. Section 1.6.2.1). Most of the results quoted in the literature were, however, derived from flotation tests on narrow size ranges of considerably coarser particles than the -32 μm sample used in this study (d_p=8.3 μm). The rate of flotation of fine particles is known to be less dependent on particle size than that for coarse particles and, for very fine particles, is considered to be independent of particle size (Gaudin *et al*, 1942).

Only responses for the Rushton turbine have been plotted on this figure as the responses for the spinning disc were found to be similar to those for the Rushton turbine and do not illustrate any additional principles. The response indicated as "Porosity 1" on this figure refers to the flotation cell aerated with the porosity 1 sparger only. Here, the successively smaller bubble sizes were obtained by the process of bubble breakup with increasing impeller speed (cf. Section 4.3.1). The response indicated as "Porosity 1, 3 & 4" on this figure refers to the flotation cell aerated with either the porosity 1, 3 or 4 spargers and operated at a low impeller speed. Here, the successively smaller bubble sizes were obtained artificially by sparging bubbles into the flotation cell using either the porosity 1, 3 or 4 spargers.

Porosity 1 Sparger: As the smaller bubble sizes in this response were obtained by the process of bubble breakup with agitation the results can be compared to those which would be obtained in a mechanically agitated flotation cell. The flotation rate constant was found to be inversely proportional to the bubble size to the power 0.77 which is somewhat lower than the values of between about 1.0 and 3.0 commonly quoted in the flotation literature (cf. Section 1.6.2.2). Most of the results quoted in the literature were, however, derived from flotation tests in relatively quiescent systems where smaller bubble sizes were obtained artificially through sparging. In mechanically agitated flotation cells, however, the beneficial effects of agitation on flotation performance are eventually offset by increased particle-bubble detachment at high impeller speeds. This results in a weaker dependence of the flotation rate constant on the bubble size in these cells, as observed by researchers such as Ahmed and Jameson (1989) and Gorain *et al* (1997).

Porosity 1, 3 & 4 Spargers: As the smaller bubble sizes in this response were obtained artificially using different spargers in a comparatively quiescent flotation cell the results can be compared to those commonly reported in the flotation literature. The flotation rate constant was found to be inversely proportional to the bubble size to the power 2.2 which is exactly in the range of values quoted in the literature. This finding supports the argument for the observation of a weaker dependence of the flotation rate constant on bubble size in mechanically agitated flotation cells, viz. increased particle-bubble detachment at high impeller speeds.

5.1.3 Agitation

Figure 5.3 represents the variation of the flotation rate constant with specific power input for the finest size range (2-4 μm) from the -32 μm sample and for the flotation cell aerated with the porosity 1 and 4 spargers. The results from the porosity 3 sparger are not plotted on this figure as

these were found to be equivalent in form, though different in magnitude, to those for the porosity 4 sparger and do not illustrate any additional principles.

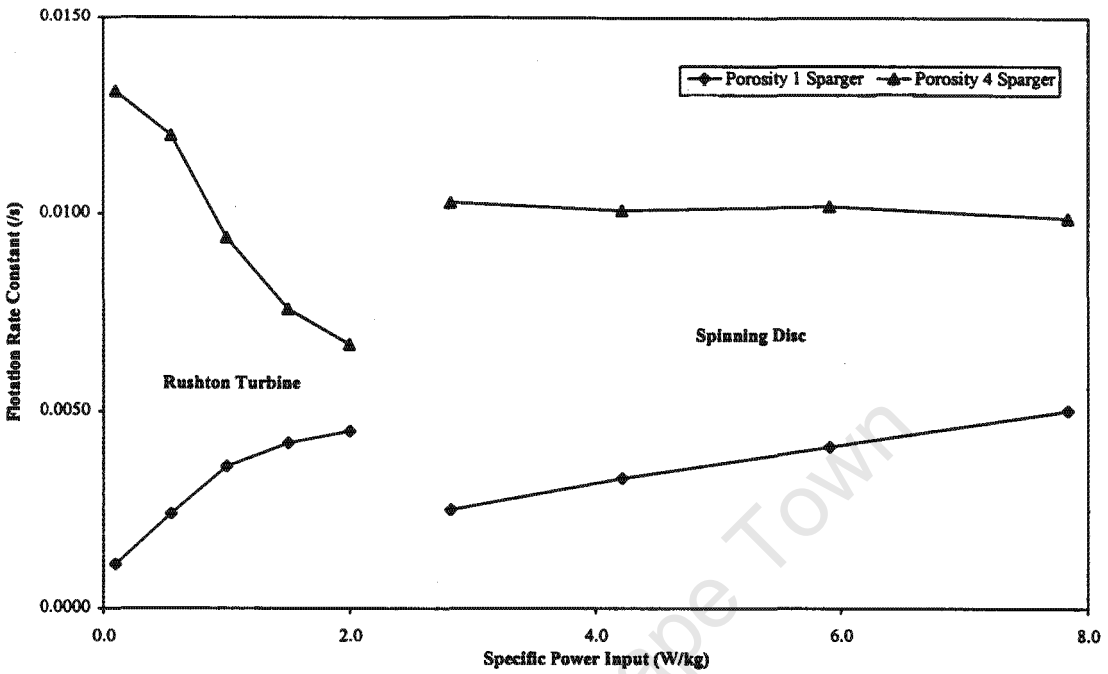

Figure 5.3. Variation of the flotation rate constant (/s) with specific power input (W/kg) for the Rushton turbine and the spinning disc.

Porosity 1 Sparger: The most immediate and notable difference between the responses for the Rushton turbine and the spinning disc is that the two impellers operate in completely different power input regimes. This extreme difference in power input is considered to be misleading, however, and may be attributed to the inappropriate selection of disc dimensions discussed in Section 4.5 where it was concluded that a smaller disc operating at higher impeller speeds would be more efficient. The differences in the nature of the responses for the two impellers are regarded as being more significant. For the Rushton turbine increasing power input leads to a rapid increase in the flotation rate constant, though this appears to reach an optimum at relatively high power inputs. For the spinning disc increasing power input leads to a more gradual increase in the flotation rate constant, though this appears to increase steadily with increasing power input. These results suggest that increasing power input has a beneficial effect on flotation performance for both impellers but that for the Rushton turbine this is eventually offset by greater particle-bubble detachment at high power inputs. This increased detachment is attributed to the significantly higher turbulent energy dissipation rates, impeller pumping rates and gas holdups for the Rushton turbine impeller.

Porosity 4 Sparger: Increasing power input leads to a steep decrease in the flotation rate constant for the Rushton turbine and a shallow decrease in the rate constant for the spinning disc. This confirms the conclusion that increasing power input leads to greater particle-bubble detachment for the Rushton turbine. More significantly, however, this suggests that agitation does not have a beneficial effect on particle-bubble contacting through increased turbulence for these ultrafine particles as bubbles remained constant in size for this sparger. This observation is not consistent with the theories and hypotheses discussed in Sections 1.4.2.1.2 and 1.6.2.3 where it was proposed that the flotation performance of ultrafine particles could be improved by highly turbulent particle-bubble contacting. Consequently, the increase in the flotation rate constant with increasing power input for the porosity 1 sparger is attributed entirely to improved flotation performance through the production of smaller bubbles by breakup and not to any improvement in particle-bubble contacting.

Figure 5.4 represents the variation of the flotation rate constant with specific power input for the coarsest size range (18-32 μm) from the -32 μm sample and for the flotation cell aerated with the porosity 1 and 4 spargers. The results from the porosity 3 sparger are not plotted on this figure as these were found to be equivalent in form, though different in magnitude, to those for the porosity 4 sparger and do not illustrate any additional principles.

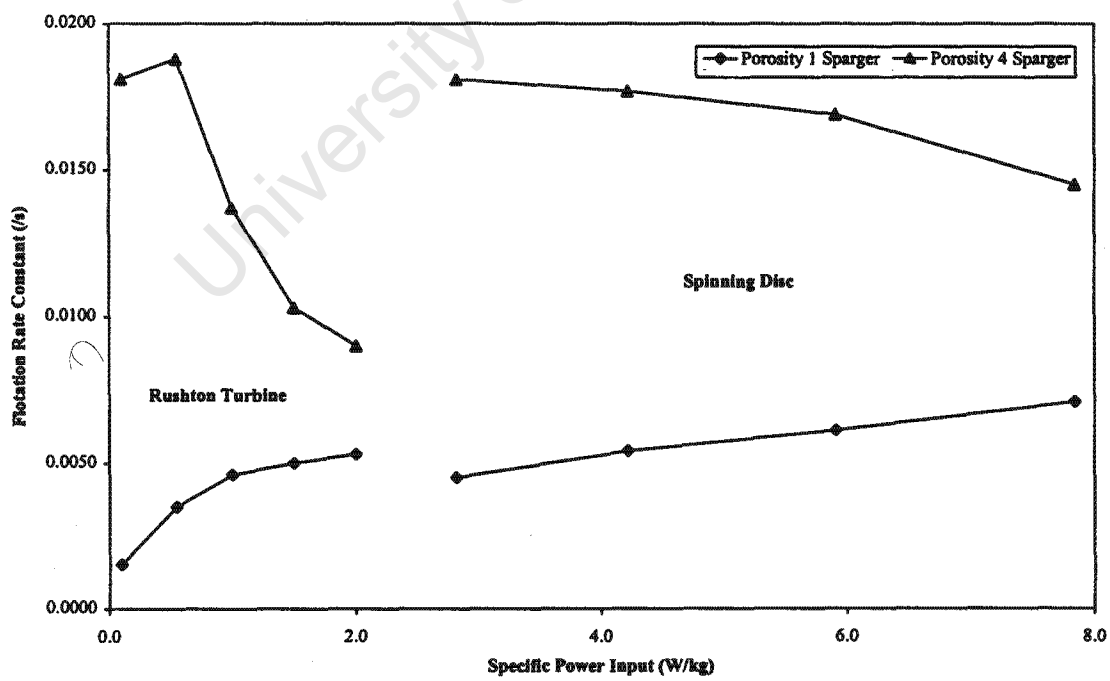

Figure 5.4. Variation of the flotation rate constant (/s) with specific power input (W/kg) for the Rushton turbine and the spinning disc.

For the porosity 1 sparger the responses shown in Figure 5.4 are similar to those in Figure 5.3 except for the observation of slightly poorer flotation performance for the coarse particles at high power inputs. For the porosity 4 sparger, however, the responses shown in Figure 5.4 differ significantly from those in Figure 5.3. For the Rushton turbine increasing power input leads to an initial increase in the flotation rate constant followed by a rapid decrease in the rate constant at high power inputs. For the spinning disc, however, increasing power input leads to a decrease in the flotation rate constant for all power inputs. The observed increase in the flotation rate constant for the Rushton turbine is attributed to improved particle-bubble contacting through increased turbulence as bubbles remained constant in size for this sparger. As no such increase was observed for the ultrafine particles it must be concluded that increases in particle-bubble contacting through increased turbulence are strongly dependent on particle size and increase with increasing particle size. No such increase is observed in the response for the spinning disc, however, which suggests that agitation does not improve particle-bubble contacting for this impeller due to the nature of the turbulence generated rather than to the particle size. For both impellers, however, it is clear that increasing power input leads to increased particle-bubble detachment for coarse particles which results in a significant decrease in the flotation rate constant at high power inputs. It is interesting to note from Figure 5.4 that optimum flotation performance occurs at significantly lower power inputs than those required to produce very small bubbles by agitation. This suggests that a combination of gas dispersion and flotation in mechanically agitated flotation cells is not optimal and has been noted by researchers such as Ahmed and Jameson (1985).

5.1.4 Comparison of Impellers

An evaluation of the preceding flotation results indicates that the Rushton turbine and the spinning disc differ quite markedly with respect to their flotation performance. For the Rushton turbine agitation has a beneficial effect on flotation performance through both increased particle-bubble contacting and the production of smaller bubbles by breakup, though the extent of this increase is dependent on the particle size. For the spinning disc agitation has a beneficial effect on flotation kinetics through the production of smaller bubbles by breakup only and no increase in particle-bubble contacting is observed. For both impellers, however, agitation leads to increased particle-bubble detachment and these effects dominate at high power inputs, especially for coarse particles. The differences in the flotation performance of the Rushton turbine and the spinning disc relate to the fundamentally different nature of the turbulence generated by these impellers (cf. Section 4.2.2). For the Rushton turbine a significant percentage of the power input is dissipated in the bulk tank and, consequently, agitation leads to increased particle-bubble contacting through increased

turbulence in this region. For the spinning disc almost no power input is dissipated in the bulk tank and, consequently, agitation has no effect on particle-bubble contacting in this region. For both impellers a significant percentage of the power input is dissipated in the impeller zone and turbulent energy dissipation rates are orders of magnitude higher in this region than in the bulk tank. These high turbulent energy dissipation rates lead to increased particle-bubble contacting but these beneficial effects are clearly dominated and overridden by dramatically increased particle-bubble detachment in this region.

5.2 The -32 and -100 Micron Samples

The results presented in this section are derived from "Phase Two" of the experimental programme presented in Table 2.4 and discussed in Section 2.3.3. The spinning disc impeller was not used in "Phase Two" of the experimental programme as results from "Phase One" showed that increasing the level of agitation did not lead to any increases in particle-bubble contacting for this impeller.

5.2.1 Particle Size

Figure 5.5 represents the variation of the flotation rate constant with particle size for the -32 and -100 μm samples and for the flotation cell aerated with the porosity 4 sparger. Only the responses for the Rushton turbine operating at a low impeller speed have been plotted on this figure as responses for the high impeller speed displayed similar tendencies to those discussed in Section 5.1.1. It is clear from Figure 5.5 that both the magnitude of the flotation rate constant and the dependence of the rate constant on particle size are significantly greater for the -100 μm sample than for the -32 μm sample. As collector dosage was the only parameter varied between the flotation tests for the -32 and -100 μm samples, the increase in the magnitude of the flotation rate constant is attributed to increased flotation kinetics through increased particle hydrophobicity. The collector dosages for the two samples were, however, calculated on an equivalent (BET) surface area basis (cf. Section 2.3.2.2). This suggests that equating collector dosage on a surface area basis might be misleading or that sample preparation by cyclosizing, and the subsequent removal of ultrafine material, may have a beneficial effect on flotation performance.

turbulence in this region. For the spinning disc almost no power input is dissipated in the bulk tank and, consequently, agitation has no effect on particle-bubble contacting in this region. For both impellers a significant percentage of the power input is dissipated in the impeller zone and turbulent energy dissipation rates are orders of magnitude higher in this region than in the bulk tank. These high turbulent energy dissipation rates lead to increased particle-bubble contacting but these beneficial effects are clearly dominated and overridden by dramatically increased particle-bubble detachment in this region.

5.2 The -32 and -100 Micron Samples

The results presented in this section are derived from "Phase Two" of the experimental programme presented in Table 2.4 and discussed in Section 2.3.3. The spinning disc impeller was not used in "Phase Two" of the experimental programme as results from "Phase One" showed that increasing the level of agitation did not lead to any increases in particle-bubble contacting for this impeller.

5.2.1 Particle Size

Figure 5.5 represents the variation of the flotation rate constant with particle size for the -32 and -100 μm samples and for the flotation cell aerated with the porosity 4 sparger. Only the responses for the Rushton turbine operating at a low impeller speed have been plotted on this figure as responses for the high impeller speed displayed similar tendencies to those discussed in Section 5.1.1. It is clear from Figure 5.5 that both the magnitude of the flotation rate constant and the dependence of the rate constant on particle size are significantly greater for the -100 μm sample than for the -32 μm sample. As collector dosage was the only parameter varied between the flotation tests for the -32 and -100 μm samples, the increase in the magnitude of the flotation rate constant is attributed to increased flotation kinetics through increased particle hydrophobicity. The collector dosages for the two samples were, however, calculated on an equivalent (BET) surface area basis (cf. Section 2.3.2.2). This suggests that equating collector dosage on a surface area basis might be misleading or that sample preparation by cyclosizing, and the subsequent removal of ultrafine material, may have a beneficial effect on flotation performance.

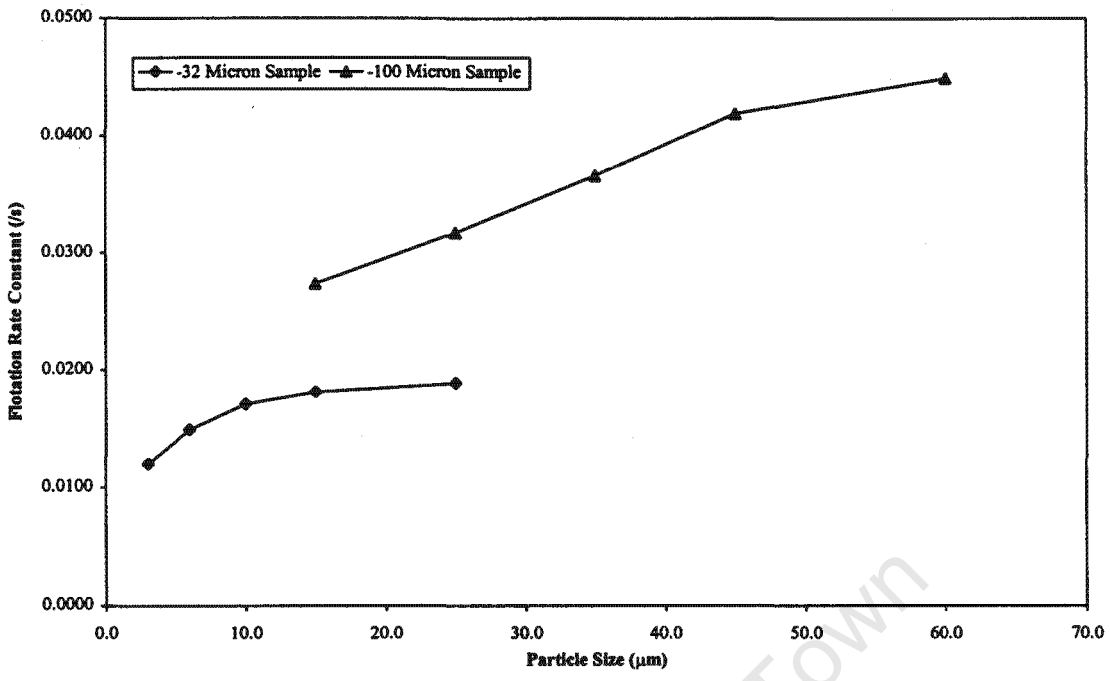

Figure 5.5. Variation of the flotation rate constant (/s) with particle size (μm) for the -32 and -100 μm samples.

Although this is an interesting observation and is worth further investigation it is beyond the scope of this study to critique methodologies for equating collector dosage between different samples. It is sufficient to note that in this study the -100 μm sample appeared more hydrophobic. Nonetheless, the flotation results for the -100 μm sample were found to be equivalent in tendency, though greater in magnitude, to those for the -32 μm sample and serve to confirm and emphasise these results. The increase in the dependence of the flotation rate constant on the particle size is attributed to either increased particle hydrophobicity or, most likely, to the coarser nature of the -100 μm sample (d_p=37.2 μm). The flotation rate constant was found to be proportional to the particle size to the power 0.38 which is substantially higher than the value of 0.15 for the -32 μm sample but is still somewhat lower than the value of 1.0 commonly quoted for quartz in the flotation literature. However, the dependence of the flotation rate constant on the particle size was confirmed with results from flotation tests at other operating conditions.

5.2.2 Bubble Size

Figure 5.6 represents the variation of the flotation rate constant with bubble size for the 12-18 and 10-20 μm size ranges from the -32 and -100 μm samples respectively and for the flotation cell aerated with the porosity 1 sparger. It should be re-emphasised that responses for this sparger are

Figure 5.8 represents the variation of the flotation rate constant with specific power input for the 10-20 and 50-70 μm size ranges from the -100 μm sample and for the flotation cell aerated with the porosity 4 sparger.

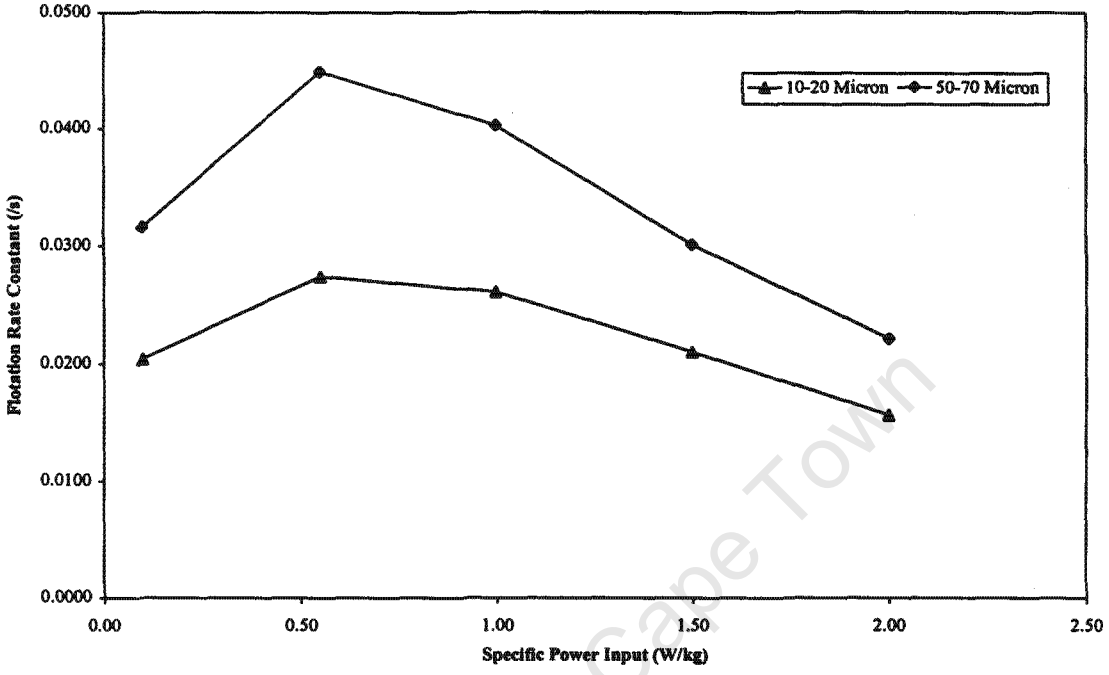

Figure 5.8. Variation of the flotation rate constant (/s) with specific power input (W/kg) for the -100 μm sample.

It is clear from Figure 5.8 that there is a more significant increase in the flotation rate constant with increasing power input for coarse particles than for fine particles. This confirms the observation in Section 5.1.3 that increases in particle-bubble contacting through increased turbulence are more significant for coarse particles. It is, however, again clear that at sufficiently high power inputs the dramatic increases in particle-bubble detachment dominate and override all other factors and the responses for both particle size ranges tend towards similar values.

5.2.4 Comparison of Samples

An evaluation of the preceding flotation results indicates that the flotation responses for the -32 and -100 μm samples are different in magnitude but very similar in terms of observed trends. The increase in the magnitude of the flotation rate constant is attributed to either increased particle hydrophobicity through an inappropriate selection of collector dosage or to effects resulting from differences in the method of sample preparation. A more significant difference between the two

samples is that the flotation rate constant displays a stronger dependence on the particle size for the -100 μm sample. This increased dependence is attributed to either increased particle hydrophobicity or, most likely, to the coarser nature of the -100 μm sample. The effects of agitation and bubble size on the flotation rate constant are very similar for both samples, though these are again more pronounced for the -100 μm sample. Agitation leads to more dramatic increases in particle-bubble attachment for the -100 μm sample which is complemented by a possible reduction in particle-bubble detachment. A combination of these two factors results in the formation of very distinct optima in the flotation rate constant as a function of power input for the -100 μm sample. For both samples, however, increases in particle-bubble attachment and detachment are strongly dependent on the particle size, though particle-bubble detachment clearly dominates and overrides all other factors at high levels of agitation.

5.3 The Gas-Residence Model

In Section 3.2.1.2 it was indicated that the gas-residence model predicts more meaningful flotation rate constants than the standard-flotation model in cells with appreciable gas residence times as the effects of the gas residence time on the recovery-time response are separated from those due to actual flotation. Consequently, the gas-residence model is useful for comparing flotation rate constants in cells with appreciable gas residence times to those in standard laboratory flotation cells where the gas residence time is relatively short. Figure 5.9 compares the differences in the flotation rate constant calculated using the gas-residence and standard-flotation models for the 12-18 μm size range from the -32 μm sample. Here, the flotation cell was aerated with the porosity 1 sparger and agitated by the Rushton turbine which resulted in a broad range of gas residence times (2-25 s).

It is clear from Figure 5.9 that the flotation rate constants calculated using the gas-residence and standard-flotation models correspond closely at low power inputs but start to deviate substantially at high power inputs due to increases in the gas residence time in the flotation cell. Consequently, the gas-residence model predicts higher flotation rate constants than the standard-flotation model in tests where the flotation cell was aerated with small bubbles or operated at high power inputs. The results for the gas-residence model are therefore equivalent to those for the standard-flotation model discussed in Sections 5.1 and 5.2 except that certain tendencies are either emphasised or de-emphasised depending on the test conditions.

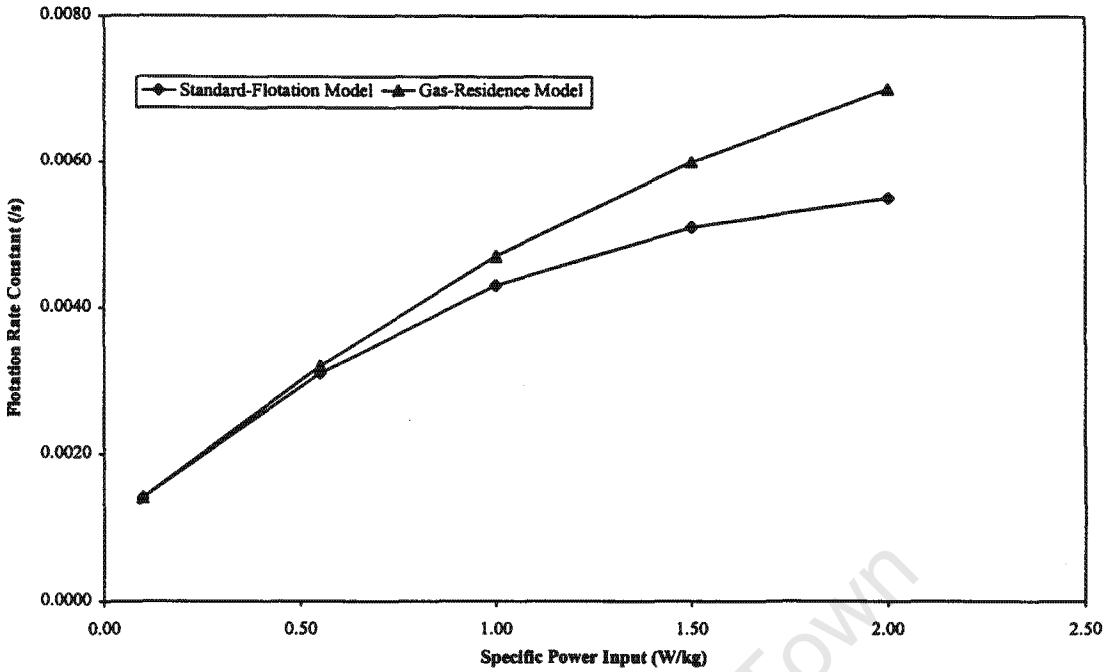

Figure 5.9. Variation of the flotation rate constant (/s) with specific power input (W/kg) for the standard-flotation and gas-residence models.

The dependence of the flotation rate constant on the particle size is identical for both models as the comparisons were made at a fixed gas residence time. The dependence of the flotation rate constant on the bubble size is slightly lower for the flotation cell sparged with the porosity 1, 3 & 4 spargers but slightly higher for the flotation cell sparged with the porosity 1 sparger. The dependence of the flotation rate constant on the power input is emphasised significantly and the optima in the rate constants are increased in magnitude and moved to higher power inputs due to increases in gas holdup with increasing impeller speed. The gas-residence model therefore emphasises the trends discussed in Sections 5.1 and 5.2 and conclusions are equivalent to those for the standard-flotation model. Detailed results for the gas-residence model are not presented in this thesis, however, as these are superseded by results from the attachment-detachment model which also includes the effects of the gas residence time.

5.4 The Attachment-Detachment Model

In Section 3.2.1.1 it was indicated that the attachment-detachment model allows for the presence of a gas phase in the flotation cell, both in terms of a gas residence time and the attachment/detachment of mineral particles to/from from bubbles. Consequently, the attachment-detachment model not only allows for the gas residence time in the cell but also separates flotation

into the two independent processes of particle-bubble attachment and detachment. However, the application of the attachment-detachment model to the experimental data was not as straightforward as that for the standard-flotation and gas-residence models and is discussed in Section 5.4.1 and 5.4.2. None of the flotation tests for the spinning disc were analysed using the attachment-detachment model as no increases in particle-bubble contacting through increased turbulence were observed for this impeller. In addition, the condition of a well-mixed gas phase necessary for the application of this model is considered questionable for the spinning disc impeller (cf. Section 4.1).

5.4.1 Application of the Attachment-Detachment Model

In Section 3.2.2.2 it was indicated that unique attachment and detachment rate constants could seldom be obtained by direct application of the attachment-detachment model to single recovery-time curves due to sensitivities in fitting two rate constants to a single response. Consequently, the methodology for obtaining preliminary estimates of attachment and detachment rate constants outlined in Section 3.2.2.2 was employed. Using this procedure, robust estimates of attachment and detachment rate constants were obtained for the entire -32 μm sample data set but this was not possible for the entire -100 μm sample data set due to sensitivities in flotation tests with small bubbles and large particles. Here, the extremely fast kinetics resulted in rapid decreases in the pulp concentration (C) with time and values of near zero were obtained by the 2nd or 3rd sampling period. The accuracy of the pulp concentration-time responses affects the application of Equation 3.36 and, consequently, reliable estimates of rate constants could not be obtained for many of the flotation tests. Therefore only examples of the variation of the estimated attachment and detachment rate constants with specific power input for the -32 μm sample are shown in Figure 5.10. The rate constants presented in this figure are for the 12-18 μm size range and were obtained from flotation tests where the cell was aerated with the porosity 1 and 4 spargers.

Attachment Rate Constant: For the porosity 1 sparger the estimated attachment rate constant increases steeply with increasing power input. This is attributed to increased particle-bubble attachment through both increased particle-bubble contacting and the production of smaller bubbles by breakup. For the porosity 4 sparger, however, the estimated attachment rate constant increases almost linearly with increasing power input. This is attributed entirely to increased particle-bubble attachment through increased particle-bubble contacting as bubbles remained constant in size for this sparger. These findings support the observations and conclusions made in Sections 5.1.3 and 5.2.3 and demonstrate that, for particles of this size, agitation has a significant influence on particle-

bubble attachment through both improved particle-bubble contacting and the production of smaller bubbles by breakup.

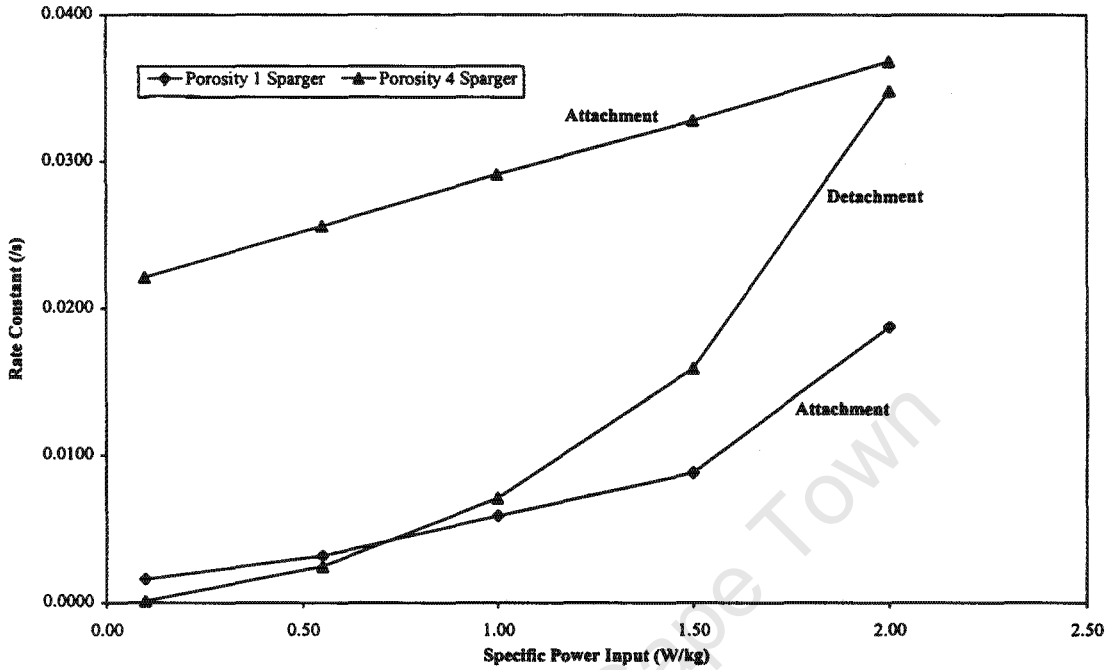

Figure 5.10. Variation of the estimated attachment and detachment rate constants with specific power input (W/kg) for the porosity 1 and 4 spargers.

Detachment Rate Constant: Only the response for the porosity 4 sparger is plotted in Figure 5.10 as this was found to be similar in form, though different in magnitude, to that for the porosity 1 sparger. It is clear from this response that the estimated detachment rate constant increases dramatically with increasing power input. This is attributed entirely to increased particle-bubble detachment through increased turbulence as bubbles remained constant in size for this sparger. The response for the porosity 1 sparger was, however, found to differ only slightly in magnitude to that for the porosity 4 sparger which suggests that particle-bubble detachment is more strongly influenced by agitation than by bubble size.

As all the estimated attachment and detachment rate constants displayed the types of consistent trends shown in Figure 5.10 it was decided to propose general empirical correlations for the variation of these rate constants with particle size, bubble size and specific power input. These general correlations could then be re-applied to the entire flotation data set so as to determine values for the empirical constants and, consequently, to determine actual rather than estimated attachment and detachment rate constants. Using the variation of the estimated attachment and

detachment rate constants for the entire -32 μm sample data set, the general empirical correlations shown in Equations 5.1 and 5.2 were proposed.

$$k_a = \frac{d_p^{n_1}(c_1 + c_2\varepsilon^{n_3})}{d_b^{n_2}} \quad (5.1) \qquad k_d = (c_3 + c_4 d_p^{n_4}) d_b^{n_5} \varepsilon^{n_6} \quad (5.2)$$

Equations 5.1 and 5.2 were incorporated into the attachment-detachment model and re-applied to the entire -32 μm sample data set of 75 recovery-time curves to give a best-fit with a mean error of 5.1% for the empirical constants shown in Table 5.1.

Table 5.1. Empirical constants for the -32 μm sample.

Attachment Rate Constant#		Detachment Rate Constant#	
c_1	0.00093	c_3	0.0188
c_2	0.00026	c_4	0.00066
n_1	0.20	n_4	1.00
n_2	1.60	n_5	0.48
n_3	0.91	n_6	1.64

#Valid for d_p (μm), d_b (mm), ε (W/kg).

Figure 5.11 compares the experimental recovery for the -32 μm sample data set (375 points) to the recovery predicted by the attachment-detachment model and the empirical correlations.

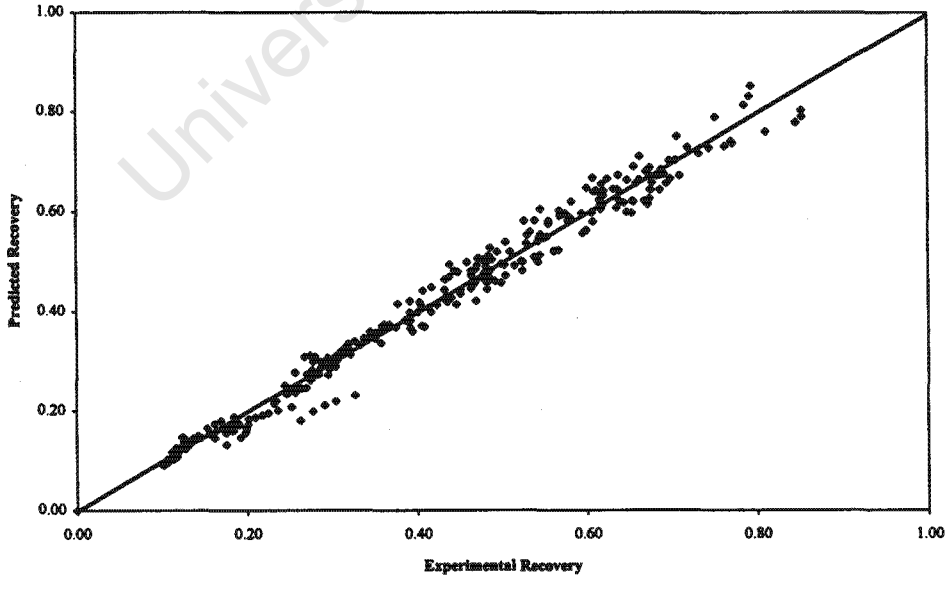

Figure 5.11. Graph of predicted recovery versus experimental recovery for the -32 μm sample data set.

model (Equation 1.12). It is interesting to note that the increase in the attachment rate constant with increasing power input is dependent on the particle size and that no increase in this quantity would be observed for very small particles, as found in Section 5.1.3. It is also interesting to note that the constant c_1 is the flotation rate constant for a 1 μm particle and a 1 mm bubble in a quiescent environment and could have been obtained directly by interpolation from the experimental data.

Detachment rate constant: Models for particle-bubble detachment generally predict the maximum stable aggregate/particle size rather than the rate of detachment (cf. Section 1.4.2.3). Consequently, it is difficult to comment on the form of the detachment expression other than to indicate that it is dominated by the robust value of n_6=1.64 for the specific power input. This supports the observations and conclusions made in Sections 5.1.3 and 5.2.3 where it was found that agitation controlled particle-bubble detachment and that particle size and bubble size had a lesser influence. It is, however, interesting to note that the detachment rate constant increases with increasing bubble size as this conflicts with the theoretical models for detachment based on the centrifugal forces experienced by a particle-bubble aggregate caught up in the energetic inertial sub-range eddies (cf. Section 1.4.2.3). From the measured turbulent energy spectra, however, these eddies were found to extended from about 300 to 1000 μm in size (cf. Section 4.4.1). This is appreciably larger than the majority of bubble sizes in the study and might explain the discrepancy from the flotation theory. It is also interesting to note that, at sufficiently high power inputs, the detachment expression predicts an appreciable detachment rate constant for even ultrafine particles, as observed in the response for the 2-4 μm size range in Figure 5.3.

Using the attachment-detachment model, the empirical correlations and constants for the -32 μm sample and the model for bubble breakup discussed in Section 4.4 (viz. Equation 1.24) the recovery-time responses for the flotation cell aerated with the porosity 1 sparger were simulated. Flotation rate constants were then back-calculated from these simulated recovery-time curves using the standard-flotation model and are shown in Figures 5.12 and 5.13. These figures compare the simulated flotation, attachment and detachment rate constants for the 12-18 μm size range with the experimental flotation rate constants discussed in Section 5.1. It should be noted that the trends in the flotation, attachment and detachment rate constants presented in these figures include the effects of both agitation and bubble size and, consequently, can be compared to those that would be obtained in a mechanically agitated flotation cell.

model (Equation 1.12). It is interesting to note that the increase in the attachment rate constant with increasing power input is dependent on the particle size and that no increase in this quantity would be observed for very small particles, as found in Section 5.1.3. It is also interesting to note that the constant c_1 is the flotation rate constant for a 1 μm particle and a 1 mm bubble in a quiescent environment and could have been obtained directly by interpolation from the experimental data.

Detachment rate constant: Models for particle-bubble detachment generally predict the maximum stable aggregate/particle size rather than the rate of detachment (cf. Section 1.4.2.3). Consequently, it is difficult to comment on the form of the detachment expression other than to indicate that it is dominated by the robust value of n_6=1.64 for the specific power input. This supports the observations and conclusions made in Sections 5.1.3 and 5.2.3 where it was found that agitation controlled particle-bubble detachment and that particle size and bubble size had a lesser influence. It is, however, interesting to note that the detachment rate constant increases with increasing bubble size as this conflicts with the theoretical models for detachment based on the centrifugal forces experienced by a particle-bubble aggregate caught up in the energetic inertial sub-range eddies (cf. Section 1.4.2.3). From the measured turbulent energy spectra, however, these eddies were found to extended from about 300 to 1000 μm in size (cf. Section 4.4.1). This is appreciably larger than the majority of bubble sizes in the study and might explain the discrepancy from the flotation theory. It is also interesting to note that, at sufficiently high power inputs, the detachment expression predicts an appreciable detachment rate constant for even ultrafine particles, as observed in the response for the 2-4 μm size range in Figure 5.3.

Using the attachment-detachment model, the empirical correlations and constants for the -32 μm sample and the model for bubble breakup discussed in Section 4.4 (viz. Equation 1.24) the recovery-time responses for the flotation cell aerated with the porosity 1 sparger were simulated. Flotation rate constants were then back-calculated from these simulated recovery-time curves using the standard-flotation model and are shown in Figures 5.12 and 5.13. These figures compare the simulated flotation, attachment and detachment rate constants for the 12-18 μm size range with the experimental flotation rate constants discussed in Section 5.1. It should be noted that the trends in the flotation, attachment and detachment rate constants presented in these figures include the effects of both agitation and bubble size and, consequently, can be compared to those that would be obtained in a mechanically agitated flotation cell.

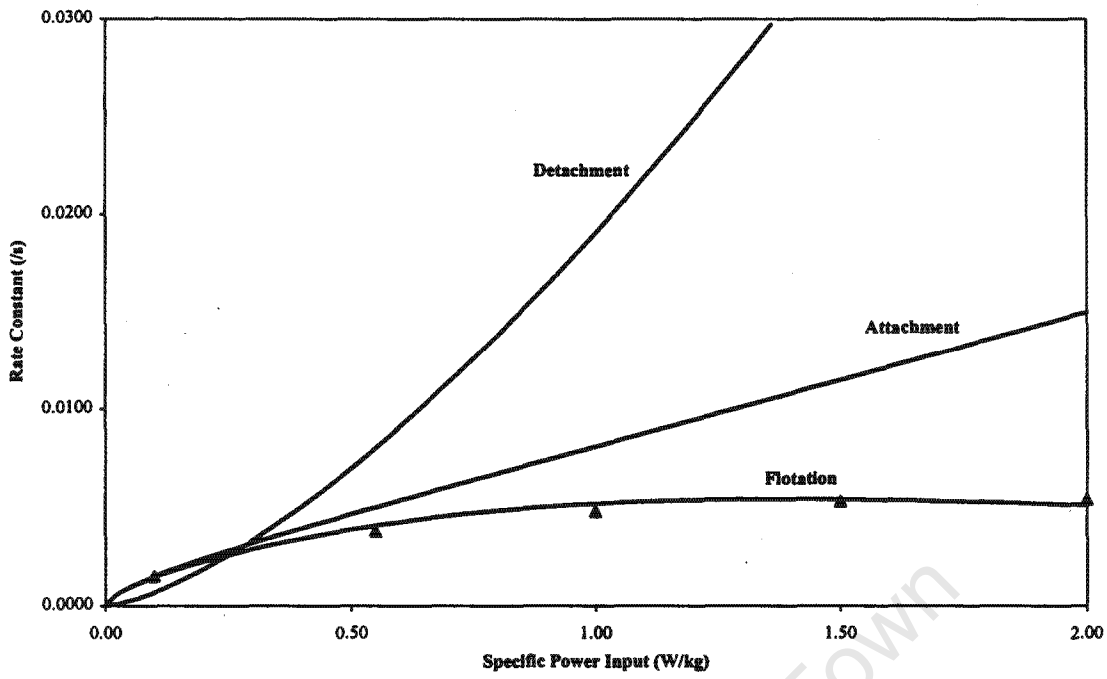

Figure 5.12. Variation of the flotation, attachment and detachment rate constants (/s) with specific power input (W/kg) for the porosity 1 sparger.

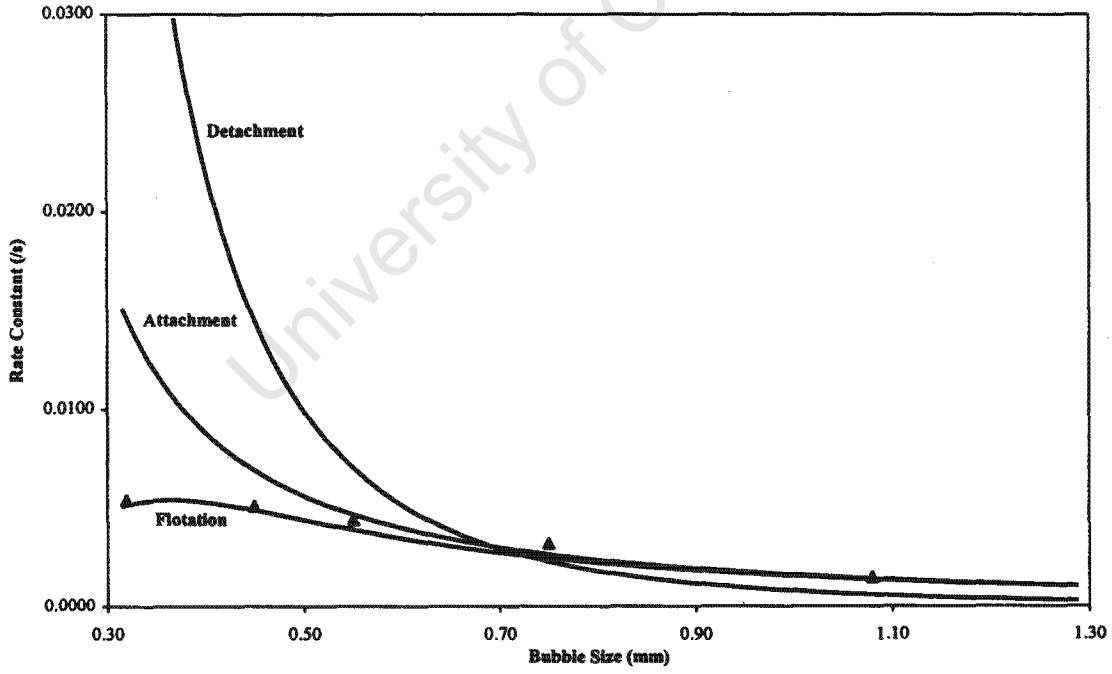

Figure 5.13. Variation of the flotation, attachment and detachment rate constants (/s) with bubble size (mm) for the porosity 1 sparger.

It is clear from Figure 5.12 that both the attachment and detachment rate constants increase rapidly with increasing power input but result in a flotation rate constant which approximates the

experimental data reasonably accurately. It is also clear from this figure that the flotation rate constant and the attachment rate constant correspond very closely at low power inputs but start to deviate substantially at high power inputs due to the dramatic increase in the detachment rate constant. The net effect of the conflict between the processes of attachment and detachment is therefore that the flotation rate constant goes through an optimum as a function of power input, as found in Sections 5.1.3 and 5.2.3. It is clear from Figure 5.13 that the attachment and detachment rate constants both increase rapidly with decreasing bubble size but result in a flotation rate constant which approximates the experimental data reasonably accurately. It is interesting to note that the simulation predicts an optimum in the flotation rate constant as a function of bubble size. This optimum is only alluded to as a tendency in the experimental data for the -32 μm sample but is supported by the optimum observed in the experimental data for the -100 μm sample in Figure 5.5. Consequently, it is clear from Figures 5.12 and 5.13 that the attachment-detachment model and the empirical correlations and constants provide an accurate representation of both the experimental data and the trends and tendencies observed in Sections 5.1 and 5.2.

5.5 Conclusions

Particle Size, Bubble Size and Agitation: The effects of particle size, bubble size and agitation on the flotation rate constant are similar to those presented in the flotation literature and discussed in Section 1.6. The flotation rate constant is less strongly dependent on the particle size than suggested in the literature (viz. d_p^{1-2}) and this dependence decreases even further with increasing agitation until an optimum in the flotation rate constant as a function of particle size is observed. The flotation rate constant is as strongly dependent on the bubble size as suggested in the literature (viz. $1/d_b^{1-3}$) but this dependence also decreases dramatically with increasing agitation until an optimum in the flotation rate constant as a function of bubble size is observed. Agitation has both beneficial and detrimental effects on flotation performance and, consequently, results in an optimum in the flotation rate constant as a function of power input (impeller speed). The beneficial effects of agitation on flotation performance are attributed to increased particle-bubble attachment through increased particle-bubble contacting and the production of smaller bubbles by breakup. The detrimental effects of agitation on flotation performance are attributed to increased particle-bubble detachment through increased turbulence. Increases in particle-bubble attachment are regarded as occurring in both the bulk tank and the impeller zone but are considered to be overridden by particle-bubble detachment in the impeller zone due to the enormously high turbulent energy dissipation rates in this region. Increases in both particle-bubble attachment and detachment are

strongly dependent on particle size, though particle-bubble detachment is significant for even ultrafine particles at sufficiently high levels of agitation.

Comparison of Impellers: The Rushton turbine and spinning disc impellers differ quite markedly with respect to their flotation performance and this is attributed to the fundamentally different nature of the turbulence generated by each impeller. The Rushton turbine generates turbulence in both the bulk tank and the impeller zone which results in increased particle-bubble attachment through both increased particle-bubble contacting and the production of small bubbles by breakup but also results in increased particle-bubble detachment. The spinning disc generates turbulence in the impeller zone only, however, which results in increased particle-bubble attachment through the production of small bubbles by breakup but also results in increased particle-bubble detachment. The Rushton turbine is therefore a more suitable impeller for promoting particle-bubble contacting than the spinning disc but also results in more significant particle-bubble detachment due to high turbulent energy dissipation rates, impeller pumping rates and gas holdups. The spinning disc might therefore be a more suitable impeller for the flotation of ultrafine particles as these are unaffected by improved particle-bubble contacting through increased turbulence but are prone to significant particle-bubble detachment.

The Attachment-Detachment Model: The attachment-detachment model is suitable for analysing flotation kinetics in mechanically agitated flotation cells as it decouples the two independent processes of particle-bubble attachment and detachment and allows for the presence of a gas phase in the flotation cell. Using separate rate constants improves the flexibility and insight in the analysis of flotation kinetics but can lead to the misinterpretation of simple kinetics. Allowing for a gas phase in the flotation cell is important for cells with appreciable gas residence times but not for standard laboratory cells where the gas residence time is relatively short. The empirical correlations for the attachment and detachment rate constants in terms of particle size, bubble size and specific power input have no mechanistic basis but appear to follow the general trends observed in the experimental data and reflected in the flotation literature. The attachment-detachment model, used in conjunction with the empirical correlations and constants, provides an accurate representation of both the experimental data and the trends and tendencies discussed in Sections 5.1 and 5.2. The implications of the attachment-detachment model and the empirical correlations and constants will be discussed further in Chapter 6.0.

CHAPTER 6: CONCLUSIONS

The primary objective of this thesis was to investigate the effects of particle size, bubble size and level of agitation on flotation kinetics in a laboratory batch flotation cell. The thesis was initiated in order to gain a greater understanding of the influence of agitation on flotation performance with the purpose of improving the rate of fine particle flotation. As flotation in mechanical flotation cells involves a complex interaction between the subprocesses of turbulence, bubble breakup and particle-bubble contacting, the thesis involved a detailed characterisation of hydrodynamic, gas dispersion and flotation parameters. This characterisation was conducted by way of an evaluation of those parameters generated by two markedly different impellers, the Rushton turbine and the spinning disc. The conclusions from the characterisation of hydrodynamic, gas dispersion and flotation performance in the flotation cell are reviewed in Sections 6.1.1 to 6.1.3 and are used in Section 6.1.4 to propose fundamental principles for impeller design.

In this thesis a new kinetic model for flotation in mechanically agitated flotation cells, termed the attachment-detachment model, was developed in order to describe certain consistent trends in the flotation data. The attachment-detachment model requires a knowledge of the hydrodynamic, gas dispersion and flotation parameters measured in this study. Consequently, the model represents a more comprehensive kinetic model for flotation in mechanically agitated flotation cells than the classical first-order flotation model. The scope and application of the attachment-detachment model are discussed in Section 6.2 and are used, together with the empirical correlations and constants for the -32 μm sample, to demonstrate some important findings with regard to the optimum operation, scale-up and design of mechanical flotation cells.

6.1 The Rushton Turbine and Spinning Disc Impellers

Results and conclusions from the characterisation of hydrodynamics, gas dispersion and flotation for both the Rushton turbine and the spinning disc are discussed in Sections 6.1.1 to 6.1.3 and are incorporated into a discussion of principles for impeller design in Section 6.1.4.

6.1.1 Hydrodynamics

The specific power inputs for the Rushton turbine and the spinning disc were found to be within the range of power inputs used in mechanical flotation cells with values for the spinning disc being in the upper end of this range. Power, airflow and Froude dimensionless numbers for the two impellers were found to be within the range of values typically found in mechanical flotation cells, although power numbers were at the extreme ends of this range. Turbulence parameters and energy spectra for the two impellers were consistent with those obtained by other researchers (Wu and Patterson, 1989) and found in the turbulence literature. Turbulence in the flotation cell was found to be isotropic but non-homogeneous with the cell being divided into a bulk tank and an impeller zone with uniform, though order of magnitude different, turbulence parameters throughout. For the Rushton turbine approximately 30% of the total power input to the cell was found to be dissipated in the bulk tank while this value was only 2-3% for the spinning disc. This finding suggests that the Rushton turbine is a suitable impeller for use in systems where interrelated microphenomena such as particle-bubble collision and bubble breakup are dependent on turbulence in both the bulk tank and the impeller zone. Similarly this finding suggests that the spinning disc is a suitable impeller for use in systems where these microphenomena are limited to the impeller zone only, such as the process of bubble breakup. In addition to the difference in the distribution of energy throughout the flotation cell, distinct differences were found between the turbulent energy spectra for the two impellers. Turbulent energy spectra for the spinning disc were found to have significantly less turbulent energy in the intermediate and higher frequency eddy ranges than equivalent spectra for the Rushton turbine. This finding suggests that the Rushton turbine is a more suitable impeller for effecting microphenomena such as particle-bubble collision and bubble breakup than the spinning disc as these are reputed to be dependent on the intermediate and higher frequency eddies. Aeration was found to have a significant influence on turbulence parameters and to lead to substantial decreases in both mean and turbulent velocities in the bulk tank, especially when the cell was aerated with very small bubbles. Aeration was found to lead to an intensification of both turbulent velocities and turbulent energy dissipation rates in the impeller zone at the expense of these quantities in the bulk tank. Aeration and bubble size were, however, found to have no effect on the general form of the energy spectrum. These findings suggests that aeration alters the distribution of energy throughout the flotation cell, by influencing bulk velocities, but does not affect the mechanism of transmission of energy through the spectrum.

6.1.2 Gas Dispersion

Gas residences times in the flotation cell were found to extend to maximum values of 53 seconds for the Rushton turbine and 41 seconds for the spinning disc which is significantly longer than those obtained in standard laboratory flotation cells. For the Rushton turbine the gas phase in the flotation cell was found to be well-mixed due to a combination of high gas residence times and high impeller pumping rates. For the spinning disc, however, the well-mixed criterion could not be established as impeller pumping rates could not be quantified but the gas phase was not considered to be well-mixed due to the low gas holdups and fluid velocities. Characteristic bubble sizes such as mean, Sauter mean and maximum stable bubble sizes were consistent with those obtained by other researchers in similar systems (Parthasarathy *et al*, 1991) and found in the gas dispersion literature. The Sauter mean bubble size was found to be directly proportional to the maximum stable bubble size which is often assumed in the literature but is seldom verified experimentally. Bubbles generated by the porosity 1 sparger were found to breakup with increasing impeller speed while bubbles generated by the porosity 3 & 4 spargers were found to remain constant in size over the full range of impeller speeds. Consequently, the flotation cell aerated with the porosity 1 sparger was considered to be comparable to a mechanical flotation cell due to similarities in the mechanism of gas dispersion. The model for bubble breakup based on turbulent pressure fluctuations was found to be applicable to the bubble size data for the Rushton turbine but to be inapplicable to the bubble size data for the spinning disc. This discrepancy was attributed to the bubbles in the flotation cell agitated by the spinning disc being further from their equilibrium size than those for the Rushton turbine due to the lower impeller pumping rate of the spinning disc impeller. The model for bubble breakup based on the collision of a bubble with a turbulent eddy of comparable dimensions to the bubble was found to give erratic and opposite trends for the two impellers. The Rushton turbine was, however, found to be a more efficient impeller for bubble breakup than the spinning disc but this was attributed to an inappropriate selection of spinning disc dimensions and impeller speeds. It was proposed that a smaller spinning disc operating at significantly higher impeller speeds to those used in this study would be a more efficient impeller for bubble breakup than a standard Rushton turbine.

6.1.3 Flotation Kinetics

The effects of particle size, bubble size and agitation on the flotation rate constant were similar to those obtained by other researchers (Ahmed and Jameson, 1985) and presented in the flotation literature. The flotation rate constant was found to be less strongly dependent on the particle size

than suggested in the literature and this dependence was found to decrease with increasing agitation until an optimum in the flotation rate constant as a function of particle size was observed. The flotation rate constant was found to be as strongly dependent on the bubble size as suggested in the literature but this dependence was also found to decrease dramatically with increasing agitation until an optimum in the flotation rate constant as a function of bubble size was observed. Agitation was found to have both beneficial and detrimental effects on flotation performance and to result in an optimum in the flotation rate constant as a function of power input (impeller speed). The beneficial effects of agitation on flotation performance were attributed to increased particle-bubble attachment through improved particle-bubble contacting and the production of smaller bubbles by breakup. The detrimental effects of agitation on flotation performance were attributed to increased particle-bubble detachment through increased turbulence. Increases in particle-bubble attachment were regarded as occurring in both the bulk tank and the impeller zone but were considered to be overridden by particle-bubble detachment in the impeller zone due to the enormously high turbulent energy dissipation rates in this region. Increases in both particle-bubble attachment and detachment were found to be strongly dependent on particle size, though particle-bubble detachment was found to be significant for even ultrafine particles at sufficiently high levels of agitation. The Rushton turbine and spinning disc impellers were found to differ quite markedly with respect to their flotation performance and this was attributed to the fundamentally different nature of the turbulence generated by each impeller. As the Rushton turbine was found to generate turbulence in both the bulk tank and the impeller zone, this was considered to result in increased particle-bubble attachment through both improved particle-bubble contacting and the production of small bubbles by breakup but also to result in increased particle-bubble detachment. As the spinning disc was found to generate turbulence in the impeller zone only, this was considered to result in increased particle-bubble attachment through the production of small bubbles by breakup but also to result in increased particle-bubble detachment. These findings suggest that the Rushton turbine is a more suitable impeller for promoting particle-bubble contacting than the spinning disc but that the consequent improvement in flotation performance could be countered by significant particle-bubble detachment due to the comparatively higher turbulent energy dissipation rates, impeller pumping rates and gas holdups for the Rushton turbine impeller. Similarly, these findings suggest that the spinning disc is a more suitable impeller for the flotation of ultrafine particles as these were unaffected by improved particle-bubble contacting but were prone to significant particle-bubble detachment which is substantially lower for the spinning disc impeller.

6.1.4 Implications for Impeller Design

In a mechanical flotation cell the impeller is responsible for the processes of solids suspension, gas dispersion and the generation of turbulence through agitation. As the research presented in this thesis is of a fundamental nature, recommendations cannot be made concerning the mechanical aspects of impeller design and must be confined to a consideration of the subprocesses affected by impeller action. From the hydrodynamic results it is clear that, not only can different impellers affect the distribution and intensity of turbulent energy through the flotation cell, but they can also affect the spectrum of turbulent energy. In this study it is unclear whether differences in the spectrum of turbulent energy affects subprocesses such as particle-bubble contacting and bubble breakup but it is clear that differences in the distribution and intensity of turbulent energy throughout the flotation cell have a significant influence. From the gas dispersion results it is clear that extremely high turbulent energy dissipation rates in the impeller zone promote the process of bubble breakup which suggests that a small impeller operating at high impeller speeds is suitable for gas dispersion. These turbulent energy dissipation rates can be further increased by restricting the flow of fluid leaving the impeller zone, either through an appropriate impeller design or through the addition of a stator. This limits the flow of kinetic energy into the bulk tank and confines turbulent energy to the impeller zone but reduces the impeller pumping rate which impacts dramatically on the suspension of solids. A sensible compromise would appear to be the use of a small radial-flow impeller with a high power number as this would generate high turbulent energy dissipation rates in the impeller zone and would still have an appreciable impeller pumping rate. These are the characteristics of the types of impellers currently being used in industrial mechanical flotation cells which suggests that impeller design is developing along appropriate lines for efficient gas dispersion.

From the flotation results it is clear that the impeller has a significant influence on flotation performance, both through the production of small bubbles by efficient gas dispersion and through promoting particle-bubble contacting. For very fine particles, however, improvements in flotation performance are exclusively due to the production of small bubbles, though the conditions necessary for the generation of these bubbles by impeller action also result in high rates of particle-bubble detachment. This suggests that, for ultrafine particles, flotation should occur in relatively quiescent environments with bubbles introduced by external sparging. Here, the impeller should be responsible for the suspension of solids only and a low power input impeller with a high pumping rate, such as an axial flow impeller, would be suitable. For coarser particles, however, improvements in flotation performance are due to a combination of both the production of small bubbles and improved particle-bubble contacting through turbulence. Unfortunately, for these

particles, the conditions necessary for the generation of small bubbles by impeller action result in even higher rates of particle-bubble detachment. This suggests that, for coarser particles, flotation should occur in mildly turbulent environments with bubbles again introduced by external sparging. Here, in addition to the suspension of solids, the impeller should be responsible for generating turbulence and a moderate power input impeller with a large diameter should be used as this would generate low, though uniform, turbulent energy dissipation rates throughout the cell. This would lead to increased particle-bubble attachment through improved turbulent contacting but would have minimal effect on particle-bubble detachment. Both of these scenarios suggest that the processes of gas dispersion and flotation should not occur in a single flotation cell and this will be discussed further in Section 6.2.3.

6.2 The Attachment-Detachment Model

The attachment-detachment model has been found suitable in this study for analysing flotation kinetics in mechanically agitated flotation cells as it decouples the two independent processes of particle-bubble attachment and detachment and allows for the presence of a gas phase in the flotation cell. Using separate rate constants improves the flexibility and insight into the analysis of flotation kinetics but can lead to the misinterpretation of simple kinetics. Allowing for a gas phase in the flotation cell is important for cells with appreciable gas residence times but is irrelevant for standard laboratory cells where the gas residence time is very short. The empirical correlations for the attachment and detachment rate constants in terms of particle size, bubble size and specific power input were developed without any mechanistic basis but appear to follow the general trends observed in the experimental data and reflected in the flotation literature. However, both the attachment-detachment model and the empirical correlations for the rate constants were found to be applicable to the flotation cell used in this study and the principles outlined in Section 6.2.1 should be considered before applying the methodology to other flotation cells.

6.2.1 Application to Other Flotation Cells

The empirical correlations and constants are valid for the flotation of a sample of -32 μm quartz in a laboratory flotation cell of fixed geometry and operating at fixed chemical conditions. When applying the attachment-detachment methodology to other systems new constants for the empirical correlations would have to be determined, either through inference from the flotation literature, or by performing flotation tests over an equally broad range of particle sizes, bubble sizes, specific

power inputs and gas residence times to those used in this study. In addition, the following considerations should be noted before attempting to apply the attachment-detachment methodology to other flotation cells.

Assumptions: The attachment-detachment model was derived on the assumption of a well-mixed pulp and gas phase. This is certainly true in this study as an average bubble was shown to pass through the impeller zone several times before exiting the flotation cell (cf. Section 4.1). The assumption of a well-mixed gas phase is only an approximation in industrial flotation cells, however, but is likely to hold true for very small bubbles as these tend to follow the bulk fluid flow. These small bubbles are more relevant to the attachment-detachment model as they tend to dominate both flotation kinetics and the gas residence time in the flotation cell. Large flotation cells cannot be regarded as single well-mixed systems, however, and the model is applicable to the "reaction" zone in the impeller region than to the upper "separation" zone. Nonetheless, the well-mixed assumption must become true in all flotation cells at sufficiently high impeller speeds due to the production of small bubbles, high impeller pumping rates and high gas residence times.

Gas Flowrate: The attachment rate constant was defined so as to correspond directly to the flotation rate constant. Consequently, the attachment rate constant is affected by changes in the gas flowrate and the values calculated from the empirical correlation are only applicable to the superficial gas velocity used in this study (0.043 cm/s). The attachment rate constant can, however, be scaled-up to any new superficial gas velocity (J_g) using (J_g/0.043) as a scale-up factor based on the derivation by Jameson *et al* (1977) who derived a simple proportional relationship between the superficial gas velocity and the flotation rate constant. The detachment rate constant was defined so as to be independent of the gas phase, however, and changes in the gas flowrate are reflected in proportional changes in the specific bubble surface area (S) rather than the detachment rate constant.

Cell Geometry: The empirical correlations for the rate constants are defined in terms of the specific power input rather than the turbulent energy dissipation rate which is a comparable "micro-level" quantity for agitation to the particle and bubble sizes. This proved immaterial as it was found that the measured turbulent energy dissipation rates were all directly proportional to the specific power input (cf. Figure 4.9) but does limit the empirical correlations to flotation cells and impellers with identical geometry to those used in this study. As discussed in Section 6.1.1, however, it was found that the flotation cell could be divided into a bulk tank and impeller zone which enabled the general empirical correlations for the rate constants to be modified to suit flotation cells of two-compartment geometry. Using the two-compartment methodology outlined in Section 3.2.2.3 a set

of expressions for transforming the constants (c_1 to c_4) in Table 5.1 to general constants (c_{1g} to c_{4g}) were derived and are given in Table 6.1. These general constants can be used, in conjunction with the relevant equations in Section 3.2.2.3 and Table 6.1, to determine the overall attachment and detachment rate constant for any two-compartment flotation cell as a weighted volumetric sum of the separate rate constants for the bulk tank and the impeller zone.

Table 6.1. Two-compartment transformations.

c_{1g}	c_1	c_{3g}	$\frac{c_3}{x_V^{(1-n_6)} x_I^{n_6} + (1-x_V)^{(1-n_6)}(1-x_I)^{n_6}}$
c_{2g}	$\frac{c_2}{x_V^{(1-n_3)} x_I^{n_3} + (1-x_V)^{(1-n_3)}(1-x_I)^{n_3}}$	c_{4g}	$\frac{c_4}{x_V^{(1-n_6)} x_I^{n_6} + (1-x_V)^{(1-n_6)}(1-x_I)^{n_6}}$
$\varepsilon_I = \frac{x_I \varepsilon}{x_V}$		$\varepsilon_B = \frac{(1-x_I)\varepsilon}{(1-x_V)}$	
$k_{aB/I} = \frac{d_p^{n_1}(c_{1g} + c_{2g}\varepsilon_{B/I}^{n_3})}{d_b^{n_2}}$		$k_{dB/I} = (c_{3g} + c_{4g} d_p^{n_4}) d_b^{n_5} \varepsilon_{B/I}^{n_6}$	

#Parameters applicable to this study: $x_V = 0.0074$ and $x_I = 0.65$.

It should be noted that the overall rate constant calculated using this procedure is independent of changes in tank or impeller geometry and is dependent only on the particle size, bubble size and specific power input. This is due to the continuous nature of the empirical correlations which result in increases/decreases in the rate constant for the impeller zone being complemented by corresponding decreases/increases in the rate constant for the bulk tank. However, the magnitude of the separate rate constants affords a better reflection of the probability of the physical processes of attachment and/or detachment occurring in each zone which allows one to modify or omit the appropriate rate constant accordingly.

For example, using the general empirical correlations and constants for the -32 μm sample and the characteristic dimensions of a typical mechanical flotation cell (10 m^3), one can demonstrate that the detachment rate constant for the impeller zone is several orders of magnitude higher than the detachment rate constant for the bulk tank. In Section 1.4.2.3 it was indicated that particle-bubble aggregates are stable below certain critical sizes and/or levels of agitation which implies that there is some critical detachment rate constant below which the physical process of particle-bubble detachment will not occur. This critical detachment rate constant was not considered in this thesis as the impeller zone was found to control the entire process of particle-bubble detachment. Consequently, for the flotation cell and impeller used in this study the inclusion or omission of

model (Equation 1.12). It is interesting to note that the increase in the attachment rate constant with increasing power input is dependent on the particle size and that no increase in this quantity would be observed for very small particles, as found in Section 5.1.3. It is also interesting to note that the constant c_1 is the flotation rate constant for a 1 μm particle and a 1 mm bubble in a quiescent environment and could have been obtained directly by interpolation from the experimental data.

Detachment rate constant: Models for particle-bubble detachment generally predict the maximum stable aggregate/particle size rather than the rate of detachment (cf. Section 1.4.2.3). Consequently, it is difficult to comment on the form of the detachment expression other than to indicate that it is dominated by the robust value of n_6=1.64 for the specific power input. This supports the observations and conclusions made in Sections 5.1.3 and 5.2.3 where it was found that agitation controlled particle-bubble detachment and that particle size and bubble size had a lesser influence. It is, however, interesting to note that the detachment rate constant increases with increasing bubble size as this conflicts with the theoretical models for detachment based on the centrifugal forces experienced by a particle-bubble aggregate caught up in the energetic inertial sub-range eddies (cf. Section 1.4.2.3). From the measured turbulent energy spectra, however, these eddies were found to extended from about 300 to 1000 μm in size (cf. Section 4.4.1). This is appreciably larger than the majority of bubble sizes in the study and might explain the discrepancy from the flotation theory. It is also interesting to note that, at sufficiently high power inputs, the detachment expression predicts an appreciable detachment rate constant for even ultrafine particles, as observed in the response for the 2-4 μm size range in Figure 5.3.

Using the attachment-detachment model, the empirical correlations and constants for the -32 μm sample and the model for bubble breakup discussed in Section 4.4 (viz. Equation 1.24) the recovery-time responses for the flotation cell aerated with the porosity 1 sparger were simulated. Flotation rate constants were then back-calculated from these simulated recovery-time curves using the standard-flotation model and are shown in Figures 5.12 and 5.13. These figures compare the simulated flotation, attachment and detachment rate constants for the 12-18 μm size range with the experimental flotation rate constants discussed in Section 5.1. It should be noted that the trends in the flotation, attachment and detachment rate constants presented in these figures include the effects of both agitation and bubble size and, consequently, can be compared to those that would be obtained in a mechanically agitated flotation cell.

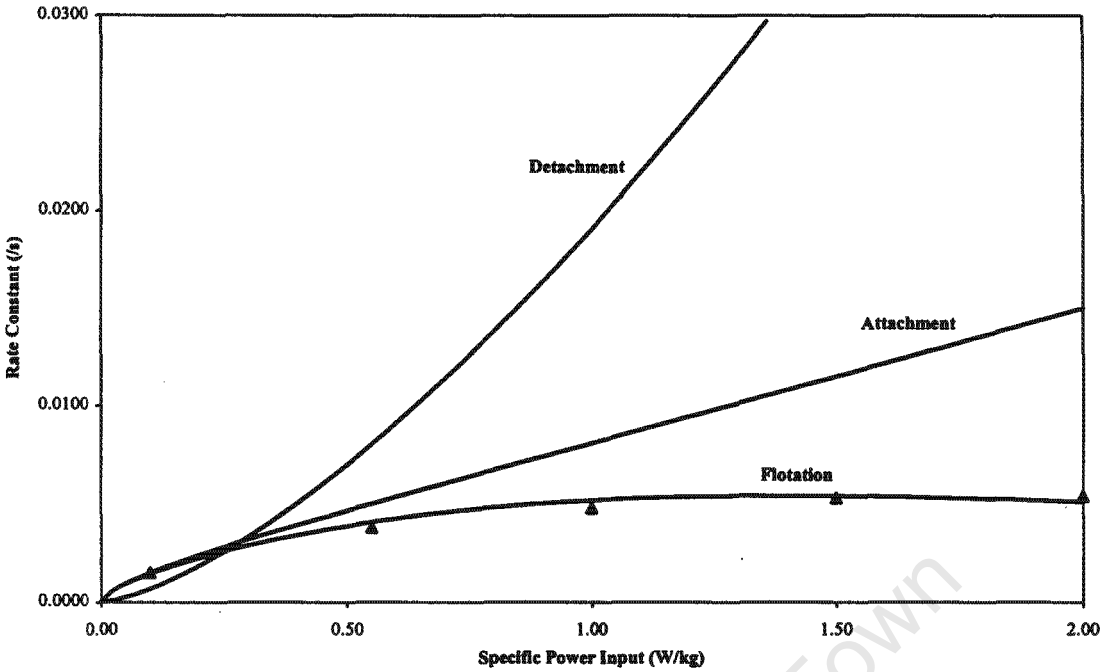

Figure 5.12. Variation of the flotation, attachment and detachment rate constants (/s) with specific power input (W/kg) for the porosity 1 sparger.

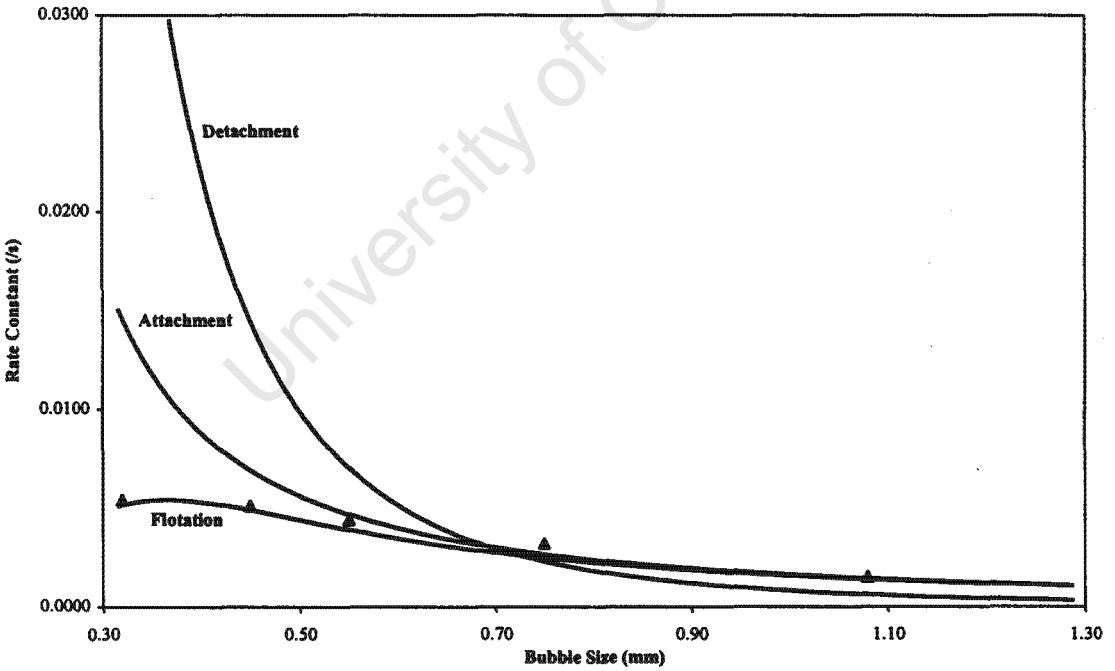

Figure 5.13. Variation of the flotation, attachment and detachment rate constants (/s) with bubble size (mm) for the porosity 1 sparger.

It is clear from Figure 5.12 that both the attachment and detachment rate constants increase rapidly with increasing power input but result in a flotation rate constant which approximates the

experimental data reasonably accurately. It is also clear from this figure that the flotation rate constant and the attachment rate constant correspond very closely at low power inputs but start to deviate substantially at high power inputs due to the dramatic increase in the detachment rate constant. The net effect of the conflict between the processes of attachment and detachment is therefore that the flotation rate constant goes through an optimum as a function of power input, as found in Sections 5.1.3 and 5.2.3. It is clear from Figure 5.13 that the attachment and detachment rate constants both increase rapidly with decreasing bubble size but result in a flotation rate constant which approximates the experimental data reasonably accurately. It is interesting to note that the simulation predicts an optimum in the flotation rate constant as a function of bubble size. This optimum is only alluded to as a tendency in the experimental data for the -32 μm sample but is supported by the optimum observed in the experimental data for the -100 μm sample in Figure 5.5. Consequently, it is clear from Figures 5.12 and 5.13 that the attachment-detachment model and the empirical correlations and constants provide an accurate representation of both the experimental data and the trends and tendencies observed in Sections 5.1 and 5.2.

5.5 Conclusions

Particle Size, Bubble Size and Agitation: The effects of particle size, bubble size and agitation on the flotation rate constant are similar to those presented in the flotation literature and discussed in Section 1.6. The flotation rate constant is less strongly dependent on the particle size than suggested in the literature (viz. d_p^{1-2}) and this dependence decreases even further with increasing agitation until an optimum in the flotation rate constant as a function of particle size is observed. The flotation rate constant is as strongly dependent on the bubble size as suggested in the literature (viz. $1/d_b^{1-3}$) but this dependence also decreases dramatically with increasing agitation until an optimum in the flotation rate constant as a function of bubble size is observed. Agitation has both beneficial and detrimental effects on flotation performance and, consequently, results in an optimum in the flotation rate constant as a function of power input (impeller speed). The beneficial effects of agitation on flotation performance are attributed to increased particle-bubble attachment through increased particle-bubble contacting and the production of smaller bubbles by breakup. The detrimental effects of agitation on flotation performance are attributed to increased particle-bubble detachment through increased turbulence. Increases in particle-bubble attachment are regarded as occurring in both the bulk tank and the impeller zone but are considered to be overridden by particle-bubble detachment in the impeller zone due to the enormously high turbulent energy dissipation rates in this region. Increases in both particle-bubble attachment and detachment are

strongly dependent on particle size, though particle-bubble detachment is significant for even ultrafine particles at sufficiently high levels of agitation.

Comparison of Impellers: The Rushton turbine and spinning disc impellers differ quite markedly with respect to their flotation performance and this is attributed to the fundamentally different nature of the turbulence generated by each impeller. The Rushton turbine generates turbulence in both the bulk tank and the impeller zone which results in increased particle-bubble attachment through both increased particle-bubble contacting and the production of small bubbles by breakup but also results in increased particle-bubble detachment. The spinning disc generates turbulence in the impeller zone only, however, which results in increased particle-bubble attachment through the production of small bubbles by breakup but also results in increased particle-bubble detachment. The Rushton turbine is therefore a more suitable impeller for promoting particle-bubble contacting than the spinning disc but also results in more significant particle-bubble detachment due to high turbulent energy dissipation rates, impeller pumping rates and gas holdups. The spinning disc might therefore be a more suitable impeller for the flotation of ultrafine particles as these are unaffected by improved particle-bubble contacting through increased turbulence but are prone to significant particle-bubble detachment.

The Attachment-Detachment Model: The attachment-detachment model is suitable for analysing flotation kinetics in mechanically agitated flotation cells as it decouples the two independent processes of particle-bubble attachment and detachment and allows for the presence of a gas phase in the flotation cell. Using separate rate constants improves the flexibility and insight in the analysis of flotation kinetics but can lead to the misinterpretation of simple kinetics. Allowing for a gas phase in the flotation cell is important for cells with appreciable gas residence times but not for standard laboratory cells where the gas residence time is relatively short. The empirical correlations for the attachment and detachment rate constants in terms of particle size, bubble size and specific power input have no mechanistic basis but appear to follow the general trends observed in the experimental data and reflected in the flotation literature. The attachment-detachment model, used in conjunction with the empirical correlations and constants, provides an accurate representation of both the experimental data and the trends and tendencies discussed in Sections 5.1 and 5.2. The implications of the attachment-detachment model and the empirical correlations and constants will be discussed further in Chapter 6.0.

CHAPTER 6: CONCLUSIONS

The primary objective of this thesis was to investigate the effects of particle size, bubble size and level of agitation on flotation kinetics in a laboratory batch flotation cell. The thesis was initiated in order to gain a greater understanding of the influence of agitation on flotation performance with the purpose of improving the rate of fine particle flotation. As flotation in mechanical flotation cells involves a complex interaction between the subprocesses of turbulence, bubble breakup and particle-bubble contacting, the thesis involved a detailed characterisation of hydrodynamic, gas dispersion and flotation parameters. This characterisation was conducted by way of an evaluation of those parameters generated by two markedly different impellers, the Rushton turbine and the spinning disc. The conclusions from the characterisation of hydrodynamic, gas dispersion and flotation performance in the flotation cell are reviewed in Sections 6.1.1 to 6.1.3 and are used in Section 6.1.4 to propose fundamental principles for impeller design.

In this thesis a new kinetic model for flotation in mechanically agitated flotation cells, termed the attachment-detachment model, was developed in order to describe certain consistent trends in the flotation data. The attachment-detachment model requires a knowledge of the hydrodynamic, gas dispersion and flotation parameters measured in this study. Consequently, the model represents a more comprehensive kinetic model for flotation in mechanically agitated flotation cells than the classical first-order flotation model. The scope and application of the attachment-detachment model are discussed in Section 6.2 and are used, together with the empirical correlations and constants for the -32 μm sample, to demonstrate some important findings with regard to the optimum operation, scale-up and design of mechanical flotation cells.

6.1 The Rushton Turbine and Spinning Disc Impellers

Results and conclusions from the characterisation of hydrodynamics, gas dispersion and flotation for both the Rushton turbine and the spinning disc are discussed in Sections 6.1.1 to 6.1.3 and are incorporated into a discussion of principles for impeller design in Section 6.1.4.

6.1.1 Hydrodynamics

The specific power inputs for the Rushton turbine and the spinning disc were found to be within the range of power inputs used in mechanical flotation cells with values for the spinning disc being in the upper end of this range. Power, airflow and Froude dimensionless numbers for the two impellers were found to be within the range of values typically found in mechanical flotation cells, although power numbers were at the extreme ends of this range. Turbulence parameters and energy spectra for the two impellers were consistent with those obtained by other researchers (Wu and Patterson, 1989) and found in the turbulence literature. Turbulence in the flotation cell was found to be isotropic but non-homogeneous with the cell being divided into a bulk tank and an impeller zone with uniform, though order of magnitude different, turbulence parameters throughout. For the Rushton turbine approximately 30% of the total power input to the cell was found to be dissipated in the bulk tank while this value was only 2-3% for the spinning disc. This finding suggests that the Rushton turbine is a suitable impeller for use in systems where interrelated microphenomena such as particle-bubble collision and bubble breakup are dependent on turbulence in both the bulk tank and the impeller zone. Similarly this finding suggests that the spinning disc is a suitable impeller for use in systems where these microphenomena are limited to the impeller zone only, such as the process of bubble breakup. In addition to the difference in the distribution of energy throughout the flotation cell, distinct differences were found between the turbulent energy spectra for the two impellers. Turbulent energy spectra for the spinning disc were found to have significantly less turbulent energy in the intermediate and higher frequency eddy ranges than equivalent spectra for the Rushton turbine. This finding suggests that the Rushton turbine is a more suitable impeller for effecting microphenomena such as particle-bubble collision and bubble breakup than the spinning disc as these are reputed to be dependent on the intermediate and higher frequency eddies. Aeration was found to have a significant influence on turbulence parameters and to lead to substantial decreases in both mean and turbulent velocities in the bulk tank, especially when the cell was aerated with very small bubbles. Aeration was found to lead to an intensification of both turbulent velocities and turbulent energy dissipation rates in the impeller zone at the expense of these quantities in the bulk tank. Aeration and bubble size were, however, found to have no effect on the general form of the energy spectrum. These findings suggests that aeration alters the distribution of energy throughout the flotation cell, by influencing bulk velocities, but does not affect the mechanism of transmission of energy through the spectrum.

6.1.2 Gas Dispersion

Gas residences times in the flotation cell were found to extend to maximum values of 53 seconds for the Rushton turbine and 41 seconds for the spinning disc which is significantly longer than those obtained in standard laboratory flotation cells. For the Rushton turbine the gas phase in the flotation cell was found to be well-mixed due to a combination of high gas residence times and high impeller pumping rates. For the spinning disc, however, the well-mixed criterion could not be established as impeller pumping rates could not be quantified but the gas phase was not considered to be well-mixed due to the low gas holdups and fluid velocities. Characteristic bubble sizes such as mean, Sauter mean and maximum stable bubble sizes were consistent with those obtained by other researchers in similar systems (Parthasarathy *et al*, 1991) and found in the gas dispersion literature. The Sauter mean bubble size was found to be directly proportional to the maximum stable bubble size which is often assumed in the literature but is seldom verified experimentally. Bubbles generated by the porosity 1 sparger were found to breakup with increasing impeller speed while bubbles generated by the porosity 3 & 4 spargers were found to remain constant in size over the full range of impeller speeds. Consequently, the flotation cell aerated with the porosity 1 sparger was considered to be comparable to a mechanical flotation cell due to similarities in the mechanism of gas dispersion. The model for bubble breakup based on turbulent pressure fluctuations was found to be applicable to the bubble size data for the Rushton turbine but to be inapplicable to the bubble size data for the spinning disc. This discrepancy was attributed to the bubbles in the flotation cell agitated by the spinning disc being further from their equilibrium size than those for the Rushton turbine due to the lower impeller pumping rate of the spinning disc impeller. The model for bubble breakup based on the collision of a bubble with a turbulent eddy of comparable dimensions to the bubble was found to give erratic and opposite trends for the two impellers. The Rushton turbine was, however, found to be a more efficient impeller for bubble breakup than the spinning disc but this was attributed to an inappropriate selection of spinning disc dimensions and impeller speeds. It was proposed that a smaller spinning disc operating at significantly higher impeller speeds to those used in this study would be a more efficient impeller for bubble breakup than a standard Rushton turbine.

6.1.3 Flotation Kinetics

The effects of particle size, bubble size and agitation on the flotation rate constant were similar to those obtained by other researchers (Ahmed and Jameson, 1985) and presented in the flotation literature. The flotation rate constant was found to be less strongly dependent on the particle size

than suggested in the literature and this dependence was found to decrease with increasing agitation until an optimum in the flotation rate constant as a function of particle size was observed. The flotation rate constant was found to be as strongly dependent on the bubble size as suggested in the literature but this dependence was also found to decrease dramatically with increasing agitation until an optimum in the flotation rate constant as a function of bubble size was observed. Agitation was found to have both beneficial and detrimental effects on flotation performance and to result in an optimum in the flotation rate constant as a function of power input (impeller speed). The beneficial effects of agitation on flotation performance were attributed to increased particle-bubble attachment through improved particle-bubble contacting and the production of smaller bubbles by breakup. The detrimental effects of agitation on flotation performance were attributed to increased particle-bubble detachment through increased turbulence. Increases in particle-bubble attachment were regarded as occurring in both the bulk tank and the impeller zone but were considered to be overridden by particle-bubble detachment in the impeller zone due to the enormously high turbulent energy dissipation rates in this region. Increases in both particle-bubble attachment and detachment were found to be strongly dependent on particle size, though particle-bubble detachment was found to be significant for even ultrafine particles at sufficiently high levels of agitation. The Rushton turbine and spinning disc impellers were found to differ quite markedly with respect to their flotation performance and this was attributed to the fundamentally different nature of the turbulence generated by each impeller. As the Rushton turbine was found to generate turbulence in both the bulk tank and the impeller zone, this was considered to result in increased particle-bubble attachment through both improved particle-bubble contacting and the production of small bubbles by breakup but also to result in increased particle-bubble detachment. As the spinning disc was found to generate turbulence in the impeller zone only, this was considered to result in increased particle-bubble attachment through the production of small bubbles by breakup but also to result in increased particle-bubble detachment. These findings suggest that the Rushton turbine is a more suitable impeller for promoting particle-bubble contacting than the spinning disc but that the consequent improvement in flotation performance could be countered by significant particle-bubble detachment due to the comparatively higher turbulent energy dissipation rates, impeller pumping rates and gas holdups for the Rushton turbine impeller. Similarly, these findings suggest that the spinning disc is a more suitable impeller for the flotation of ultrafine particles as these were unaffected by improved particle-bubble contacting but were prone to significant particle-bubble detachment which is substantially lower for the spinning disc impeller.

6.1.4 Implications for Impeller Design

In a mechanical flotation cell the impeller is responsible for the processes of solids suspension, gas dispersion and the generation of turbulence through agitation. As the research presented in this thesis is of a fundamental nature, recommendations cannot be made concerning the mechanical aspects of impeller design and must be confined to a consideration of the subprocesses affected by impeller action. From the hydrodynamic results it is clear that, not only can different impellers affect the distribution and intensity of turbulent energy through the flotation cell, but they can also affect the spectrum of turbulent energy. In this study it is unclear whether differences in the spectrum of turbulent energy affects subprocesses such as particle-bubble contacting and bubble breakup but it is clear that differences in the distribution and intensity of turbulent energy throughout the flotation cell have a significant influence. From the gas dispersion results it is clear that extremely high turbulent energy dissipation rates in the impeller zone promote the process of bubble breakup which suggests that a small impeller operating at high impeller speeds is suitable for gas dispersion. These turbulent energy dissipation rates can be further increased by restricting the flow of fluid leaving the impeller zone, either through an appropriate impeller design or through the addition of a stator. This limits the flow of kinetic energy into the bulk tank and confines turbulent energy to the impeller zone but reduces the impeller pumping rate which impacts dramatically on the suspension of solids. A sensible compromise would appear to be the use of a small radial-flow impeller with a high power number as this would generate high turbulent energy dissipation rates in the impeller zone and would still have an appreciable impeller pumping rate. These are the characteristics of the types of impellers currently being used in industrial mechanical flotation cells which suggests that impeller design is developing along appropriate lines for efficient gas dispersion.

From the flotation results it is clear that the impeller has a significant influence on flotation performance, both through the production of small bubbles by efficient gas dispersion and through promoting particle-bubble contacting. For very fine particles, however, improvements in flotation performance are exclusively due to the production of small bubbles, though the conditions necessary for the generation of these bubbles by impeller action also result in high rates of particle-bubble detachment. This suggests that, for ultrafine particles, flotation should occur in relatively quiescent environments with bubbles introduced by external sparging. Here, the impeller should be responsible for the suspension of solids only and a low power input impeller with a high pumping rate, such as an axial flow impeller, would be suitable. For coarser particles, however, improvements in flotation performance are due to a combination of both the production of small bubbles and improved particle-bubble contacting through turbulence. Unfortunately, for these

particles, the conditions necessary for the generation of small bubbles by impeller action result in even higher rates of particle-bubble detachment. This suggests that, for coarser particles, flotation should occur in mildly turbulent environments with bubbles again introduced by external sparging. Here, in addition to the suspension of solids, the impeller should be responsible for generating turbulence and a moderate power input impeller with a large diameter should be used as this would generate low, though uniform, turbulent energy dissipation rates throughout the cell. This would lead to increased particle-bubble attachment through improved turbulent contacting but would have minimal effect on particle-bubble detachment. Both of these scenarios suggest that the processes of gas dispersion and flotation should not occur in a single flotation cell and this will be discussed further in Section 6.2.3.

6.2 The Attachment-Detachment Model

The attachment-detachment model has been found suitable in this study for analysing flotation kinetics in mechanically agitated flotation cells as it decouples the two independent processes of particle-bubble attachment and detachment and allows for the presence of a gas phase in the flotation cell. Using separate rate constants improves the flexibility and insight into the analysis of flotation kinetics but can lead to the misinterpretation of simple kinetics. Allowing for a gas phase in the flotation cell is important for cells with appreciable gas residence times but is irrelevant for standard laboratory cells where the gas residence time is very short. The empirical correlations for the attachment and detachment rate constants in terms of particle size, bubble size and specific power input were developed without any mechanistic basis but appear to follow the general trends observed in the experimental data and reflected in the flotation literature. However, both the attachment-detachment model and the empirical correlations for the rate constants were found to be applicable to the flotation cell used in this study and the principles outlined in Section 6.2.1 should be considered before applying the methodology to other flotation cells.

6.2.1 Application to Other Flotation Cells

The empirical correlations and constants are valid for the flotation of a sample of -32 μm quartz in a laboratory flotation cell of fixed geometry and operating at fixed chemical conditions. When applying the attachment-detachment methodology to other systems new constants for the empirical correlations would have to be determined, either through inference from the flotation literature, or by performing flotation tests over an equally broad range of particle sizes, bubble sizes, specific

power inputs and gas residence times to those used in this study. In addition, the following considerations should be noted before attempting to apply the attachment-detachment methodology to other flotation cells.

Assumptions: The attachment-detachment model was derived on the assumption of a well-mixed pulp and gas phase. This is certainly true in this study as an average bubble was shown to pass through the impeller zone several times before exiting the flotation cell (cf. Section 4.1). The assumption of a well-mixed gas phase is only an approximation in industrial flotation cells, however, but is likely to hold true for very small bubbles as these tend to follow the bulk fluid flow. These small bubbles are more relevant to the attachment-detachment model as they tend to dominate both flotation kinetics and the gas residence time in the flotation cell. Large flotation cells cannot be regarded as single well-mixed systems, however, and the model is applicable to the "reaction" zone in the impeller region than to the upper "separation" zone. Nonetheless, the well-mixed assumption must become true in all flotation cells at sufficiently high impeller speeds due to the production of small bubbles, high impeller pumping rates and high gas residence times.

Gas Flowrate: The attachment rate constant was defined so as to correspond directly to the flotation rate constant. Consequently, the attachment rate constant is affected by changes in the gas flowrate and the values calculated from the empirical correlation are only applicable to the superficial gas velocity used in this study (0.043 cm/s). The attachment rate constant can, however, be scaled-up to any new superficial gas velocity (J_g) using (J_g/0.043) as a scale-up factor based on the derivation by Jameson *et al* (1977) who derived a simple proportional relationship between the superficial gas velocity and the flotation rate constant. The detachment rate constant was defined so as to be independent of the gas phase, however, and changes in the gas flowrate are reflected in proportional changes in the specific bubble surface area (S) rather than the detachment rate constant.

Cell Geometry: The empirical correlations for the rate constants are defined in terms of the specific power input rather than the turbulent energy dissipation rate which is a comparable "micro-level" quantity for agitation to the particle and bubble sizes. This proved immaterial as it was found that the measured turbulent energy dissipation rates were all directly proportional to the specific power input (cf. Figure 4.9) but does limit the empirical correlations to flotation cells and impellers with identical geometry to those used in this study. As discussed in Section 6.1.1, however, it was found that the flotation cell could be divided into a bulk tank and impeller zone which enabled the general empirical correlations for the rate constants to be modified to suit flotation cells of two-compartment geometry. Using the two-compartment methodology outlined in Section 3.2.2.3 a set

of expressions for transforming the constants (c_1 to c_4) in Table 5.1 to general constants (c_{1g} to c_{4g}) were derived and are given in Table 6.1. These general constants can be used, in conjunction with the relevant equations in Section 3.2.2.3 and Table 6.1, to determine the overall attachment and detachment rate constant for any two-compartment flotation cell as a weighted volumetric sum of the separate rate constants for the bulk tank and the impeller zone.

Table 6.1. Two-compartment transformations.

c_{1g}	c_1	c_{3g}	$\frac{c_3}{x_V^{(1-n_6)} x_I^{n_6} + (1-x_V)^{(1-n_6)}(1-x_I)^{n_6}}$
c_{2g}	$\frac{c_2}{x_V^{(1-n_3)} x_I^{n_3} + (1-x_V)^{(1-n_3)}(1-x_I)^{n_3}}$	c_{4g}	$\frac{c_4}{x_V^{(1-n_6)} x_I^{n_6} + (1-x_V)^{(1-n_6)}(1-x_I)^{n_6}}$
$\varepsilon_I = \frac{x_I \varepsilon}{x_V}$		$\varepsilon_B = \frac{(1-x_I)\varepsilon}{(1-x_V)}$	
$k_{aB/I} = \frac{d_p^{n_1}(c_{1g} + c_{2g}\varepsilon_{B/I}^{n_3})}{d_b^{n_2}}$		$k_{dB/I} = (c_{3g} + c_{4g} d_p^{n_4}) d_b^{n_5} \varepsilon_{B/I}^{n_6}$	

#Parameters applicable to this study: $x_V = 0.0074$ and $x_I = 0.65$.

It should be noted that the overall rate constant calculated using this procedure is independent of changes in tank or impeller geometry and is dependent only on the particle size, bubble size and specific power input. This is due to the continuous nature of the empirical correlations which result in increases/decreases in the rate constant for the impeller zone being complemented by corresponding decreases/increases in the rate constant for the bulk tank. However, the magnitude of the separate rate constants affords a better reflection of the probability of the physical processes of attachment and/or detachment occurring in each zone which allows one to modify or omit the appropriate rate constant accordingly.

For example, using the general empirical correlations and constants for the -32 μm sample and the characteristic dimensions of a typical mechanical flotation cell (10 m^3), one can demonstrate that the detachment rate constant for the impeller zone is several orders of magnitude higher than the detachment rate constant for the bulk tank. In Section 1.4.2.3 it was indicated that particle-bubble aggregates are stable below certain critical sizes and/or levels of agitation which implies that there is some critical detachment rate constant below which the physical process of particle-bubble detachment will not occur. This critical detachment rate constant was not considered in this thesis as the impeller zone was found to control the entire process of particle-bubble detachment. Consequently, for the flotation cell and impeller used in this study the inclusion or omission of

detachment effects in the bulk tank would have no influence on the overall detachment rate constant. For a flotation cell and/or impeller with a different geometry, however, the detachment rate constant for the bulk tank, calculated using the empirical correlations, could be below this critical value and yet could still contribute significantly to the overall detachment rate constant. In this flotation cell the omission of detachment effects in the bulk tank, through setting the detachment rate constant for the bulk tank to zero, could have a significant impact on the re-calculated overall detachment rate constant for the flotation cell.

Another advantage of using separate rate constants is that one can determine the relative contributions of the impeller zone and the bulk tank to the overall attachment and detachment rate constants. For example, using the general empirical correlations and constants for the -32 μm sample and the characteristic dimensions of a typical mechanical flotation cell (10 m^3), one can demonstrate that the impeller zone contributes significantly to the overall attachment rate constant (10-30%) but entirely controls the overall detachment rate constant (>95%). This supports the findings in Chapter 5.0 in which it was concluded that the impeller zone controls the process of particle-bubble detachment and demonstrates that the impeller zone could play a major role in promoting particle-bubble attachment if detachment effects could be restricted.

6.2.2 Implications for Flotation Cell Scale-Up

In Section 3.2.3 the relationship between the flotation rate constant and the attachment and detachment rate constants was determined using the attachment-detachment model and the standard-flotation model for a continuous mechanical flotation cell (cf. Equations 3.39 & 3.40). Here, it was shown that the flotation rate constant is equivalent to the attachment rate constant in the absence of detachment effects but starts to deviate significantly from this quantity through combinations of high detachment rate constants and gas residence times (cf. Equation 3.41). The gas residence time is strongly dependent on the flotation cell size (cf. Equation 3.11) and, consequently, a large flotation cell is more likely to have a lower flotation rate constant than a small flotation cell. This phenomenon is illustrated in Figure 6.1 which represents the variation (simulated) of the flotation rate constant with specific power input for five flotation cells of identical geometry but different volumes. The simulation was generated using Equation 3.41, a fixed superficial gas velocity of 1.0 cm/s, the characteristic dimensions of an industrial mechanical flotation cell (10 m^3), the empirical constants for the -32 μm sample and fixed particle size of 15 μm. In addition, correlations for the bubble size and gas holdup in terms of the specific power input, obtained from the gas dispersion literature, were used in the simulation. These expressions

are not relevant to the thesis and it is sufficient to note that the attachment and detachment rate constants, bubble size, gas holdup and superficial gas velocity are identical at each value of specific power input for all five flotation cells in this figure. For example, however, the gas phase correlations used in the simulation predict Sauter mean bubble sizes of 1.32, 1.00 & 0.85 mm, with corresponding gas holdups of 5.6, 10.0 & 14.1%, for specific power inputs of 1.0, 2.0 & 3.0 W/kg respectively.

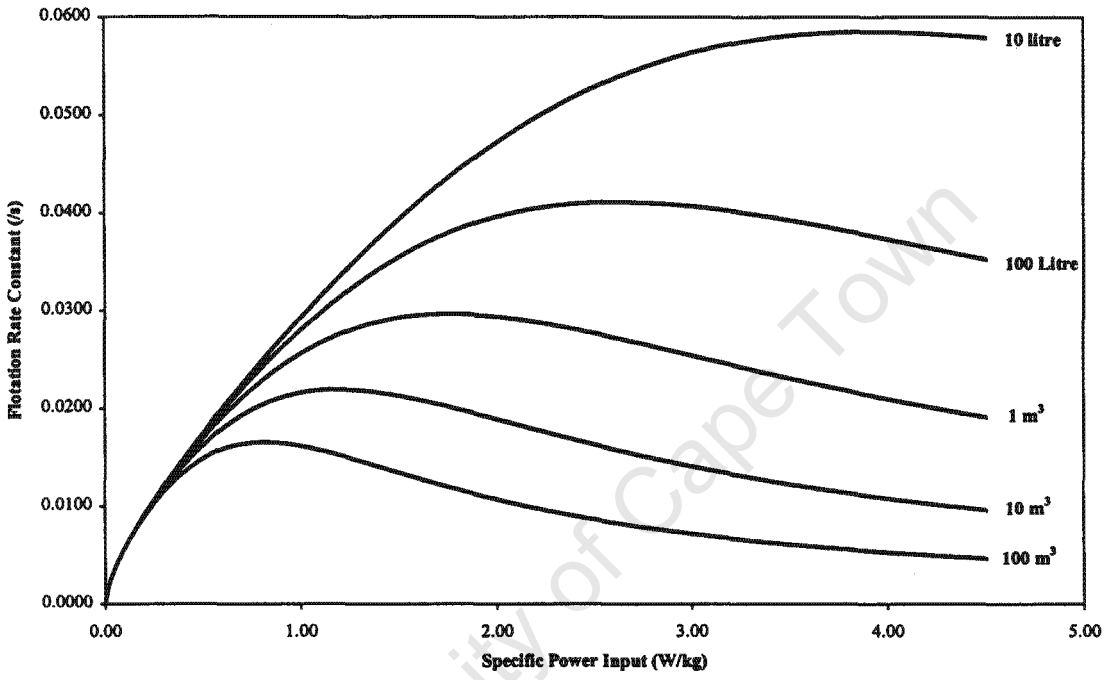

Figure 6.1. Graph of flotation rate constant (/s) versus specific power input (W/kg) for continuous mechanical flotation cells of different volume.

The comparison between the flotation cells in Figure 6.1 is based on the assumption that the attachment and detachment rate constants, the gas holdup and the superficial gas velocity are the "micro-level" quantities controlling kinetics in the flotation micro-environment and applicable to flotation cell scale-up. This is regarded as a reasonable assumption as it implies that, under constant chemical conditions, the particle size, bubble size, specific power input/turbulent energy dissipation rate, gas holdup and superficial gas velocity control the flotation micro-environment. It is clear from Figure 6.1 that there is an optimum in the flotation rate constant as a function of power input for each flotation cell and that this optimum is at a far higher power input for a small flotation cell than for a large flotation cell. It is also clear from this figure that a small flotation cell has a higher flotation rate constant than a large flotation cell and that the difference between these rate constants increases dramatically with increasing specific power input, though all rate constants ultimately tend to zero at very high power inputs. The trends shown in this figure provide a sensible basis for

determining scale-up factors between flotation cells as they show that scale-up is strongly dependent on both the cell size and specific power input. For example, the simulation used in generating Figure 6.1 predicts a scale-up factor of 2.7 when comparing kinetic data from a 10 litre and a 10 m^3 flotation cell, with both cells operating at their optimum power inputs of 4.0 and 1.2 W/kg respectively. In addition, though not immediately clear from Figure 6.1, Equation 3.41 predicts a "hyperbolic" relationship between the flotation rate constant and the cell size which suggests that "errors" in scale-up would be largest when using rate constants from very small flotation cells. This implies that there is some critical cell size at which the "hyperbolic" relationship has levelled off sufficiently for direct scale-up between flotation cells to be feasible. For example, the simulation used in generating Figure 6.1 predicts a critical cell size of at least 2-3 m^3 for direct scale-up to flotation cells of 10 m^3 to be possible (<20% error).

The simulation used in generating Figure 6.1 also predicts experimentally observed phenomena such as the classical optimum particle size range found in flotation (cf. Section 1.6.2.1). This phenomenon has been observed by numerous researchers and a less common finding is illustrated in Figure 6.2 which represents the variation (simulated) of the flotation rate constant with bubble size for the same five flotation cells.

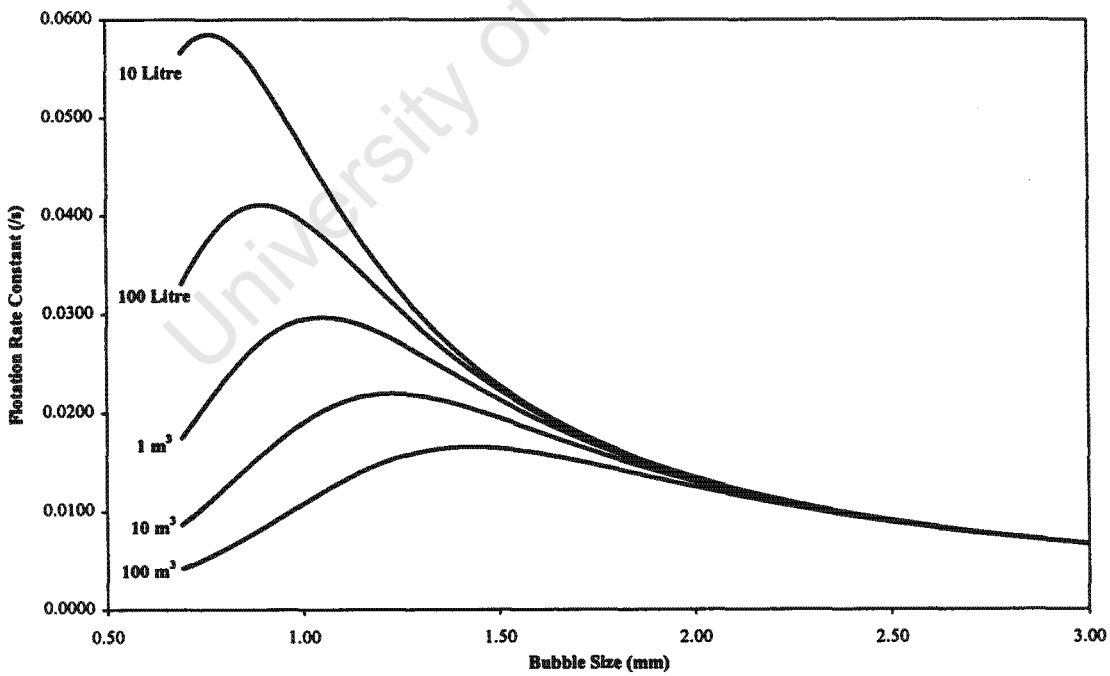

Figure 6.2. Graph of flotation rate constant (/s) versus bubble size (mm) for continuous mechanical flotation cells of different volume.

It is clear from Figure 6.2 that there is an optimum in the flotation rate constant as a function of bubble size for each flotation cell and that this optimum is at a far smaller bubble size for a small flotation cell than for a large flotation cell. It is again clear from this figure that a small flotation cell has a higher flotation rate constant than a large flotation cell and that the difference between these rate constants increases dramatically with decreasing bubble size, though all rate constants ultimately tend to zero at very small bubble sizes. The responses shown in Figure 6.2 essentially mirror those in Figure 6.1 from the perspective of bubble size rather than power input and highlight the conflict between the processes of gas dispersion and flotation in mechanical flotation cells.

6.2.3 Implications for Flotation Cell Design

From the discussion of the attachment-detachment model and the results presented in the previous section it is clear that the attachment-detachment methodology indicates some important conclusions regarding the design of flotation cells. The first, and most obvious conclusion, is that small flotation cells are more efficient than large flotation cells as they have lower gas residence times and, consequently, achieve both higher flotation rate constants and optimum performance at higher specific power inputs. This is a reasonable, though not unusual, conclusion from a metallurgical perspective but in practice it is common to use large flotation cells as these are more economical from an installed and operational cost basis. The gas residence time is, however, proportional to the cell volume through the cell height (cf. Equation 3.11) and a flotation cell with a low height to diameter (aspect) ratio will have a lower gas residence time than a cell with a high aspect ratio. A second conclusion is therefore that large flotation cells with low aspects ratios should outperform similar cells with high aspect ratios due to comparatively lower gas residence times. This conclusion is, however, based on the assumption of a constant superficial gas velocity which implies that cells with low aspect ratios would require comparatively higher aeration rates due to greater cell cross-sectional areas.

Though these are interesting findings perhaps the most significant conclusion, emphasised in both Chapter 5.0 and Section 6.1, is that a combination of gas dispersion and flotation in a mechanical flotation cell is inefficient. This is because the extremely high turbulent energy dissipation rates required for the production of small bubbles also result in high rates of particle-bubble detachment which implies that there is a conflict between the requirements for high rates of attachment and low rates of detachment in mechanical flotation cells. This conflict dictates the optimum in the flotation rate constant as a function of power input but also implies that the high power inputs required for the generation of small bubbles are far removed from the low power inputs required for optimum

flotation with these bubbles. This phenomenon is illustrated in Figure 6.3 which represents the variation (simulated) of the flotation rate constant with specific power input for two mechanical flotation cells, a conventional cell and a cell which has been sparged with bubbles of two different sizes using an external sparger.

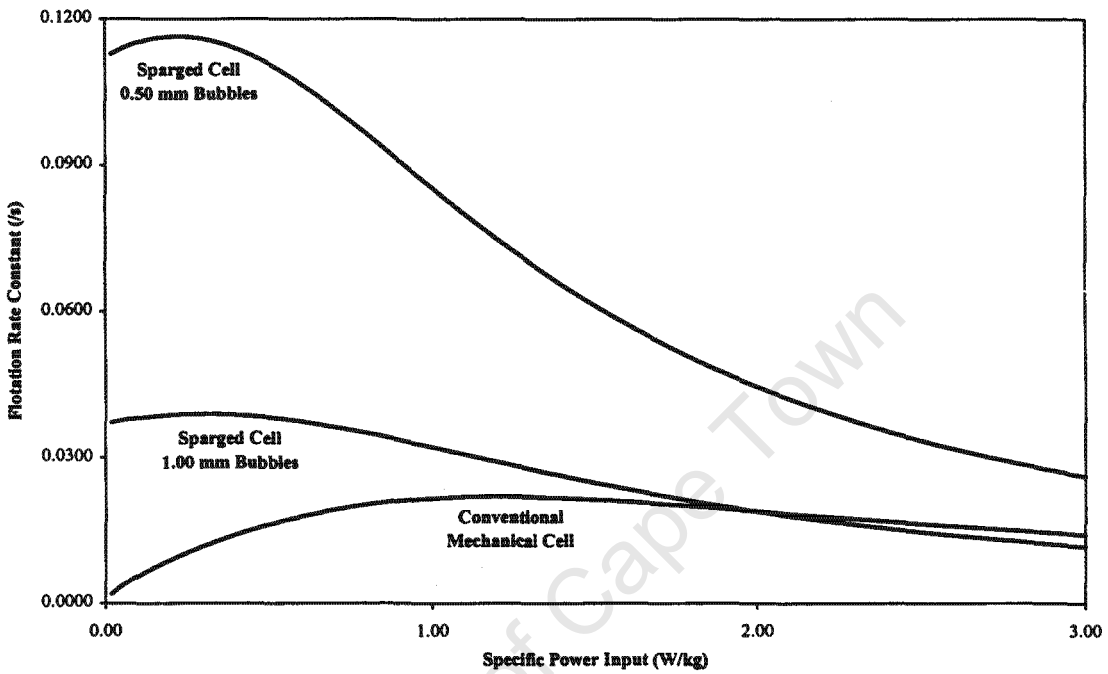

Figure 6.3. Graph of flotation rate constant (/s) versus specific power input (W/kg) for a conventional and a sparged mechanical flotation cell.

It is clear from Figure 6.3 that the sparged mechanical cell outperforms the conventional mechanical cell and achieves optimum performance at far lower power inputs. This is because the high specific power inputs of 2.0 and 10.0 W/kg required for the generation of 1.0 and 0.5 mm bubbles in the conventional mechanical cell are far higher than the comparatively low specific power inputs of 0.35 and 0.20 W/kg required for optimum flotation with these bubbles. It is also clear from this figure that optimum performance for the sparged mechanical cell is achieved at lower power inputs for small bubbles than for large bubbles, suggesting that flotation with microbubbles should occur in relatively quiescent environments. It should be noted that the sparged mechanical cell is operating at an optimum power input for a particular bubble size but that significant particle-bubble detachment is still occurring in the cell. Consequently, the sparged mechanical cell represents a more efficient flotation cell rather than the "ideal flotation cell" which would respond favourably to agitation without the influence of any detachment effects. This "ideal flotation cell" would be sparged with very small bubbles and operated at low, though uniform, turbulent energy dissipation rates throughout the cell. These low turbulent energy dissipation rates

LIST OF REFERENCES

Abrahamson, J., 1975. Collision rates of small particles in a vigorously turbulent fluid. Chem. Eng. Sci., 30: 1371-1379.

Ahmed, N. and Jameson, G.J., 1985. The effect of bubble size on the rate of flotation of fine particles. Int. J. Miner. Process., 14: 195-215.

Ahmed, N. and Jameson, G.J., 1989. Flotation kinetics. Miner. Process. Extract. Metall. Rev., 5: 77-99.

Alvarez, J., 1992. Gas-liquid bioreactors - Maximum stable bubble size. Chem. Eng. J., 49: B13-B16.

Anfruns, J.F. and Kitchener, J.A., 1977. The rate of capture of small particles in flotation. Trans. Inst. Min. Metall., 86: C9-C15.

Arbiter, N. and Harris, C.C., 1962. Flotation kinetics. In: D.W. Fuerstenau (Editor), Froth Flotation. A.I.M.E., New York, pp. 215-246.

Barthole, J.P., Maisonneuve, J., Gence, J.N., David, R., Mathieu, J. and Villermaux, J., 1983. Measurement of mass transfer rates, velocity and concentration fluctuations in an industrial stirred tank. Chem. Eng. Fundam., 1: 17-26.

Batchelor, G.K., 1953. The Theory of Homogeneous Turbulence. Cambridge University Press, Cambridge.

Bennett, A.J.R., Chapman, W.R. and Dell, C.C., 1958. Studies in froth flotation of coal. Proc. 3rd Int. Coal Prep. Cong., Liege, pp. 452-462.

Bergelt, H., Stechemesser, H. and Weber, K., 1992. Experimental investigation of collision time of a spherical particle colliding with a liquid/gas interface. Int. J. Miner. Process., 34: 321-331.

Bischofberger, C. and Schubert, H., 1980. Untersuchungen zur hydrodynamischen optimierung des flotationsprozesses bei der kalisalz-flotation. Neue Bergbautechnik, 10: 58-62, in Inoue, Nonaka and Imaizumi, 1986. *op cit.*

Blake, P. and Ralston, J., 1985. Particle size, surface coverage and flotation response. Coll. Surf., 16: 41-53.

Bogdanov, O.S., Emelyanov, M.F., Maximov, I.I. and Otrozhdennova, L.A., 1980. Influence of some factors on fine particle flotation. In: P. Somasundran (Editor), Fine Particle Processing. S.M.E., New York, pp. 706-719.

Bradshaw, P., 1978. Turbulence: Topics in Applied Physics. Springer-Verlag, Berlin.

Brodkey, R.S., 1975. Turbulence in Mixing Operations. Academic Press, New York.

Brown, D.J., 1965. A photographic study of froth flotation. Fuel Soc. J., 16: 22-34, in Jameson, Nam and Moo Young, 1977. *op cit.*

Bushell, C.H.G., 1962. Kinetics of flotation. Trans. Soc. Min. Eng., 223: 266-278, in Jameson, Nam and Moo Young, 1977. *op cit.*

Cameron, A.W., Kelsall, D.F., Restarick, C.J. and Stewart, P.S.B., 1971. A detailed assessment of concentrator performance at Broken Hill South Ltd. Proc. Australas. Inst. Min. Metall., 240: 53-67, in Trahar and Warren, 1976. *op cit.*

Chatzi, E.G. and Kiparissides, C., 1992. Dynamic simulation of bimodal drop size distributions in low-coalescence batch dispersion systems. Chem. Eng. Sci. 47: 445-456.

Chen, J.D. and Slattery, J.C., 1982. Effects of London-Van der Waals forces on the thinning of a dimpled liquid film as a small drop or bubble approaches a horizontal solid plane. A.I.Ch.E.J., 28: 955-963, in Hewitt, Fornasiero and Ralston, 1993. *op cit.*

Churaev, N.V., 1991. Surface forces and their role in mineral processing. Proc. XVII Int. Miner. Process. Cong., Dresden, pp. 1-16.

Clift, R., Grace, J.R. and Weber, M.E., 1992. Bubbles, Drops and Particles. Academic Press, London.

Collins, G.L. and Jameson, G.J., 1976. Experiments on the flotation of fine particles - The influence of particle size and charge. Chem. Eng. Sci., 31: 985-991.

Coulaloglou, C.A. and Tavlarides, L.L., 1977. Description of interaction processes in agitated liquid-liquid dispersions. Chem. Eng. Sci., 32: 1289-1297.

Crabtree, E.H. and Vincent, J.D., 1962. Historical outline of major flotation developments. In: D.W. Fuerstenau (Editor), Froth Flotation. A.I.M.E., New York, pp. 39-54.

Crawford, R. and Ralston, J., 1988. The influence of particle size and contact angle in mineral flotation. Int. J. Miner. Process., 23: 1-24.

Cutter, L.A., 1966. Flow and turbulence in a stirred tank. A.I.Ch.E.J., 12: 35-44.

De Bruyn, P.L. and Modi, H.J., 1956. Particle size and the flotation rate of quartz. Min. Eng., 8: 415-419.

Derjaguin, B.V. and Dukhin, S.S.,1961. Theory of flotation of small and medium sized particles. Trans. Inst. Min. Metall., 70: 221-245.

Diaz-Penafiel, P. and Dobby, G.S., 1994. Kinetic studies in flotation columns - Bubble size effects. Miner. Eng., 7: 465-478.

Diggins, D. and Ralston, R., 1993. Particle wettability equilibrium capillary pressure measurements. Coal Prep., 13: 1-19.

Dobby, G.S. and Finch, J.A., 1986. A model of particle sliding time for flotation size bubbles. J. Coll. Int. Sci., 109: 493-498.

Dobby, G.S. and Finch, J.A., 1987. Particle size dependence in flotation derived from a fundamental model of the capture process. Int. J. Miner. Process., 21: 241-260.

Eigles, M.A. and Volova, M.L., 1960. Kinetic investigation of effect of contact time, temperature and surface condition on the adhesion of bubbles to mineral surfaces. Proc. V Int. Miner. Process. Cong., London, pp. 271-284.

Ek, C., 1992. Flotation kinetics. In: P. Mavros and K.A. Matis (Editors), Innovations in Flotation Technology. Kluwer Academic Publishers, Netherlands, pp. 183-210.

Evans, L.F., 1954. Bubble-mineral attachment in flotation. Ind. Eng. Chem., 46: 2420-2424.

Fallenius, K., 1987. Turbulence in flotation cells. Int. J. Miner. Process., 21: 1-23.

Fallenius, K., 1992. Turbulence in flotation cells - A simplified approach. Int. J. Miner. Process., 34: 133-135.

Fichera, M.A. and Chudacek, M.W., 1992. Batch cell flotation models - A review. Miner. Eng., 5: 41-55.

Flint, L.R. and Howarth, W.J., 1971. Collision efficiency of small particles with spherical air bubbles. Chem. Eng. Sci., 26: 1155-1168.

Gaudin, A.M., 1957. Flotation (2nd Edition), McGraw-Hill, New York.

Gaudin, A.M., Groh, J.O., and Henderson, H.B., 1931. The effect of particle size on flotation. A.I.M.E. Tech. Pub., 414: 3-23, in Trahar, 1981. *op cit.*

Gaudin, A.M., Schuhmann, R. and Schlecten, W., 1942. The effect of size on the behaviour of galena particles. J. Phys. Chem., 46: 902-910.

Gorain, BK, Franzidis, JP and Manlapig, EV, 1997. Studies on impeller type, impeller speed and air flow rate in an industrial scale flotation cell. Part 4: Effect of bubble surface area flux on flotation kinetics. Miner. Eng., 10: 367-379.

Günkel, A.A. and Weber, M.E., 1975. Flow phenomena in stirred tanks. A.I.Ch.E.J., 21: 931-949.

Hanumanth, G.S. and Williams, D.J.A., 1992. A three phase model of froth flotation. Int. J. Miner. Process., 34: 261-273.

Harris, C.C., 1978. Multiphase models of flotation machine behaviour. Int. J. Miner. Process., 5: 107-129.

Harris, C.C. and Chakravarti, A., 1970. Semi-batch froth flotation kinetics - Species distribution analysis. Trans. Soc. Min. Eng., 247: 162-172.

Harris, C.C. and Raja, A., 1970. Flotation machine impeller speed and air rate as scale-up criteria. Trans. Inst. Min. Metall., 79: C295-C297.

Henwood, D.V., 1995. Analysis of the conditioning step in flotation. M.Sc. Thesis, University of Cape Town, South Africa.

Hesketh, R.P., Etchells, A.W. and Russel, T.W.F., 1991. Bubble breakage in pipeline flow. Chem. Eng. Sci., 46: 1-9.

Hesketh, R.P., Fraser Russel, T.W. and Etchells, A.W., 1987. Bubble size in horizontal pipelines. A.I.Ch.E.J., 33: 663-667.

Hess, D.E., 1991. Spectral Analysis on a PC. National Institute of Standards and Technology, Gaithersburg.

Hewitt, D., Fornasiero, D. and Ralston, J., 1993. Aqueous film drainage at the quartz/water/air interface. J. Chem. Soc. Faraday Trans., 89: 817-822.

Hinze, J.O., 1955. Fundamentals of the hydrodynamic mechanism of splitting in dispersion processes. A.I.Ch.E.J., 1: 289-295.

Hinze, J.O., 1959. Turbulence. McGraw-Hill, New York.

Holtham, P.N. and Cheng, T.W., 1991. Study of the probability of detachment of particles from bubbles in flotation. Trans. Inst. Min. Metall., 100: C147-C153.

Imaizumi, T. and Inoue, T., 1963. Kinetic consideration of froth flotation. Proc. VI Int. Miner. Process. Cong., Cannes, pp. 581-593, in Fichera and Chudacek, 1992. *op cit.*

Inoue, T. and Imaizumi, T., 1968. Some aspects of flotation kinetics. Proc. VIII Int. Miner. Process. Cong., Leningrad, Paper S-15, in Fichera and Chudacek, 1992. *op cit.*

Inoue, T., Nonaka, M. and Imaizumi, T., 1986. Flotation kinetics - Its macro and micro structure. In: P. Somasundran (Editor), Advances in Mineral Processing. S.M.E., Colorado, pp. 209-228.

Jameson, G.J., 1984. Physical aspects of fine particle flotation. In: R. Moore (Editor), Principles of Mineral Flotation (The Wark Symposium). Australas. Inst. Min. Metall., pp. 215-232.

Jameson, G.J., Nam, S. and Moo Young, M., 1977. Physical factors affecting recovery rates in flotation. Miner. Sci. Eng., 9: 103-118.

Jiang, Z.W., 1988. Modelling of flotation process by quantitative analysis of the collision and adhesion between particles and bubbles. Proc. XVII Int. Miner. Process. Cong., Dresden, pp. 429-440.

Jiang, Z.W. and Holtham, P.N., 1986. Theoretical model of collision between particles and bubbles in flotation. Trans. Inst. Min. Metall., 95: C187-C193.

Jordan, C.E. and Spears, D.R., 1990. Evaluation of a turbulent flow model for fine-bubble and fine-particle flotation. Miner. Metall. Process., 7: 65-73.

Jordan, C.E. and Susko, F.J., 1992. Rapid flotation using a modified bubble-injected hydrocyclone and a shallow-depth froth separator for improved flotation kinetics. Miner. Eng., 5: 1239-1257.

Jowett, A., 1980. Formation and disruption of particle-bubble aggregates in flotation. In: P. Somasundran (Editor), Fine Particle Processing. S.M.E., New York, pp. 720-754.

Kawase, Y. and Moo-Young, M., 1990. Mathematical models for design of bioreactors - Applications of Kolmogoroff's theory of isotropic turbulence. Chem. Eng. J., 43: B19-B41.

Kelly, E.G. and Spottiswood, D.J., 1982. Introduction to Mineral Processing. John Wiley and Sons, New York.

Kelsall, D.F., 1961. Application of probability in the assessment of flotation systems. Trans. Inst. Min. Metall., 70: C191-C204, in Fichera and Chudacek, 1992. *op cit.*

Kim, W.J. and Manning, F.S., 1964. Turbulence energy and intensity spectra in a baffled, stirred vessel. A.I.Ch.E.J., 10: 747-752.

King, R.P., 1982. Principles of Flotation. S.A.I.M.M., Johannesburg.

Kirchberg, H and Topfer, E., 1965. The mineralization of air bubbles in flotation. Proc. VII Int. Miner. Process. Cong., New York, pp. 157-168

Klimpel, R.R., 1984. The effect of chemical reagents on the flotation recovery of minerals. Chem. Eng., 91: 75-79.

Koch, P., 1975. Die einflusse der konstruktion und betriebsweise von ruhrern in mechanischen flotationsapparaten auf die hydrodynamik des dreiphasensystem und den flotationserfolg. Freiberg Forschunghefte, 546: 5-80, in Inoue, Nonaka and Imaizumi, 1986. *op cit.*

Koh, P.T.L., Andrews, J.R.G. and Uhlherr, P.H.T., 1984. Flocculation in stirred tanks. Chem. Eng. Sci., 39: 975-985.

Kolmogoroff, A.N., 1941. The local structure of turbulence in incompressible viscous fluid for very large Reynolds numbers. Dokl. Akad. Nauk. SSSR 32, in Mavros, 1992. *op cit.*

Komasawa, I., Kuboi, R. and Otake, T., 1974. Fluid and particle motion in turbulent dispersion. Chem. Eng. Sci., 29: 641-650.

Kresta, S.M. and Wood, P.E., 1991. Prediction of the three dimensional turbulent flow in stirred tanks. A.I.Ch.E.J., 37: 448-460.

Kumar, S., Kumar, R. and Gandhi, K.S., 1991. Alternative mechanisms of drop breakage in stirred vessels. Chem. Eng. Sci., 46: 2483-2489.

Laskowski, J.S., 1986. The relationship between floatability and hydrophobicity. In: P. Somasundran (Editor), Advances in Mineral Processing., S.M.E., Littleton, pp. 189-208.

Laskowski, J.S., 1989. Thermodynamic and kinetic flotation criteria. Miner. Process. Extract. Metall. Rev., 5: 25-41.

Laskowski, J.S., 1992. Introduction to physicochemical separation methods. In: J.S. Laskowski and J. Ralston (Editors), Colloidal Chemistry in Mineral Processing. Elsevier, Oxford, pp. 225-241.

Laskowski, J.S., 1993. Frothers and flotation froths. Miner. Process. Extract. Metall. Rev., 12: 61-89.

Laufhütte, H.D. and Mersmann, A., 1987. Local energy dissipation in agitated turbulent fluids and its significance for the design of stirring equipment. Chem. Eng. Techn., 10: 56-63.

Leja, J., 1982. Surface Chemistry of Froth Flotation. Plenum Press, New York.

Levich, V.G., 1962. Physicochemical Hydrodynamics. Prentice Hall, New Jersey, in Ahmed and Jameson, 1989. *op cit.*

Levins, D.M. and Glastonbury, J.R., 1972. Particle-liquid hydrodynamics and mass transfer in a stirred vessel. Trans. Inst. Chem. Eng., 50: 32-41.

Li, D., FitzPatrick, J.A. and Slattery, C., 1990. Rate of collection of particles by flotation. Ind. Eng. Chem. Res., 29: 955-967.

Li, R., Hoberg, H. and Schneider, F.U., 1993. Investigation on the influence of particle size in flotation. Proc. XVIII Int. Miner. Process. Cong., Sydney, pp. 689-697.

Liepe, F. and Mockel, O.H., 1976. Untersuchungen zum stoffvereinigen in flussiger phase. Chem. Techn., 28: 205-209, in Schulze, 1994. *op cit.*

Lu, S., Song, S., Pan, S. and Gou, J., 1995. An approach to mineral particle air bubble interaction in turbulent flow of flotation cell. Proc. XIX Int. Miner. Process. Cong., San Fransisco, pp. 87-93.

Luttrell, G.H., 1986. Hydrodynamic studies and mathematical modelling of fine coal flotation. Ph.D. Thesis, Virginia Polytechnic Institute and State University, USA, in Luttrell, Adel and Yoon, 1988. *op cit.*

Luttrell, G.H., Adel, G.T. and Yoon, R.H., 1988. Hydrodynamics and mathematical modelling of fine coal flotation. Proc. XVI Int. Miner. Process. Cong., Amsterdam, pp. 1791-1802.

Lyman ,G.J., 1983. Enhancement of coarse particle recovery in froth flotation of coal. J.K.M.R.C. Report, in Nicholson, 1985. *op cit.*

Mackenzie, J.M.W. and Matheson, G.H., 1963. Kinetic and dynamic relationships in coal flotation. Trans. Soc. Min. Eng., 226: 68-75, in Jameson, Nam and Moo Young, 1977. *op cit.*

Malhotra, D., Hoover, R.M. and Bender, F.N., 1980. Effect of agitation and aeration on flotation of Molybdenite. Min. Eng., September, pp. 1392-1397.

Mavros, P., 1992. Mixing and hydrodynamics in flotation cells. In: P.Mavros and K.A. Matis (Editors), Innovations in Flotation Technology. Kluwer Academic Publishers, Netherlands, pp. 211-234.

McManamey, W.J., 1980. A circulation model for batch mixing in agitated baffled vessels. Trans. Inst. Chem. Eng., 58: 271-276.

Middleman, S., 1974. Drop size distributions produced by turbulent pipe flow of immiscible fluids through a static mixer. Ind. Eng. Chem. Process Des. Develop., 13: 78-83.

Mika, T.S. and Fuerstenau, D.W., 1968. A microscopic model of the flotation process. Proc. VIII Int. Miner. Process. Cong., Leningrad, pp. 246-269, in Ahmed and Jameson, 1989. *op cit.*

Miller, K.J., 1988. Novel flotation technology - A survey of equipment and processes. S.M.E. Conf., Hidden Valley, Somerset, pp. 347-363.

Morris, T.M., 1952. Measurement and evaluation of the rate of flotation as a function of particle size. Min. Eng., 4: 794-798.

Mujumdar, A.S., Huang, B., Wolf, D., Weber, M.E. and Douglas, W.J.M., 1970. Turbulence parameters in a stirred tank. Can. J. Chem. Eng., 48: 475-483.

Nguyen Van, A., 1993. On the sliding time in flotation. Int. J. Miner. Process., 37: 1-25.

Nguyen Van, A. and Kmet, S., 1992. Collision efficiency for fine particles with single bubble in a countercurrent flow regime. Int. J. Miner. Process., 35: 205-223.

Nicholson, T.A., 1985. A study of the role of turbulence in the flotation process. M.Sc. Thesis, University of Queensland, Australia.

Nishkov, I. and Pugh, R.J., 1989. The relationship between flotation and adhesion of galena particles to the air-solution interface. Int. J. Miner. Proc., 25: 275-288.

Nonaka, M., Inoue, T. and Imaizumi, T., 1982. A micro-hydrodynamic flotation model and its application to the flotation process. Proc. XIV Int. Miner. Process. Cong., Toronto, pp. III-9.1-III-9.18.

Ogawa, K., 1992. Evaluation of common scaling-up rules for a stirred vessel from the viewpoint of energy spectrum function. J. Chem. Eng. Japan, 25: 750-752.

Okamoto, Y., Nishikawa, M. and Hashimoto, K., 1981. Energy dissipation rate distribution in mixing vessels and its effect on liquid-liquid dispersion and solid-liquid mass transfer. Int. Chem. Eng., 21: 88-94, in Wu and Patterson, 1989. *op cit.*

Otnes, R.K., 1978. Applied Time Series Analysis. Wiley, New York, pp. 336-359.

Parthasarathy, R. and Ahmed, N., 1994. Bubble size distribution in a gas sparged vessel agitated by a Rushton turbine. Ind. Eng. Chem. Res., 33: 703-711.

Parthasarathy, R., Jameson, G.J. and Ahmed, N., 1991. Bubble breakup in stirred vessels - Predicting the Sauter mean diameter. Trans. Inst. Chem. Eng., 69: 295-301.

Philippoff, W., 1952. Some dynamic phenomena in flotation. Min. Eng., 4: 386-390.

Prince, M.J. and Blanch, H.W., 1990. Bubble coalescence and break-up in air sparged bubble columns. A.I.Ch.E.J., 36: 1485-1499.

Ralston, J., 1983. Thin films and froth flotation. Advan. Coll. Int. Sci., 19: 1-26.

Ralston, J., 1992. The influence of particle size and contact angle in flotation. In: J.S. Laskowski and J. Ralston (Editors), Colloidal Chemistry in Mineral Processing. Elsevier, Oxford, pp. 203-224.

Ranz, W.E., 1958. Electrolytic methods for measuring water velocities. A.I.Ch.E.J., 4: 338-342.

Rao, M.A. and Brodkey, R.S., 1972. Continuous flow stirred tank turbulence parameters in the impeller stream. Chem. Eng. Sci., 27: 137-156.

Reay, D. and Ratcliff, G.A., 1973. Removal of fine particles from water by dispersed air flotation - Effects of bubble size and particle size on collection efficiency. Can. J. Chem. Eng., 51: 178-185.

Reay, D. and Ratcliff, G.A., 1975. Experimental testing of the hydrodynamic collision model of fine particle flotation. Can. J. Chem. Eng., 53: 481-486.

Reynolds, A.J., 1974. Turbulent Flows in Engineering. Wiley, London.

Rulev, N.N., 1979. Coll. J. U.S.S.R., 40: 747-756, in Solari and Gochin, 1992. *op cit.*

Rushton, J.H., Costich, E.W. and Everett, H.J., 1950. Power characteristics of mixing impellers. Chem. Eng. Prog., 46: 395-404.

Sato, Y., Ishii, K., Horie, Y., Kamiwano, M. and Yamamoto, K., 1967. Turbulent flow in a stirred vessel. Kagaku Kogaku, 31: 275-281, in Wu and Patterson, 1989. *op cit.*

Scheiner, B.J. and Jordan, C.E., 1989. Hydrodynamic effects in flotation of ores. In S. Chander and R.R. Klimpel (Eds). Advances in Coal and Mineral Processing Using Flotation, S.M.E., Littleton, pp. 219-224.

Scheludko, A., Toshev, B. and Bogadiev, B., 1976. Attachment of particles to a liquid surface. J. Chem. Soc. Faraday Trans., 72: 2815-2828.

Schimmoller, B.K., Luttrell, G.H. and Yoon, R.H., 1993. A combined hydrodynamic-surface force model for bubble-particle collection. Proc. XVIII Int. Miner. Process. Cong., Sydney, pp. 751-756.

Schubert, H., 1977. Die modellierung des flotationsprozesses auf hydro-dynamischer grundlage. Neue Bergbautechnik, 7: 446-456, in Inoue, Nonaka and Imaizumi, 1986. *op cit.*

Schubert, H., 1979. Über die hydrodynamik von flotationsprozessen. Aufbereitungs-Technik, 20: 252-260, in Inoue, Nonaka and Imaizumi, 1986. *op cit.*

Schubert, H. and Bischofberger, C., 1978. On the hydrodynamics of flotation machines. Int. J. Miner. Process., 5: 132-142.

Schubert, H., Bischofberger, G. and Koch, P., 1982. Über den einfluss der hydrodynamik auf flotationsprozesse. Aufbereitungs-Technik, 23: 306-315.

Schulze, H.J., 1977. New theoretical and experimental investigations on stability of bubble/particle aggregates in flotation - A theory on the upper particle size of floatability. Int. J. Miner. Process., 4: 241-259.

Schulze, H.J., 1982. Dimensionless number and approximate calculation of the upper particle size of floatability in flotation machines. Int. J. Miner. Process., 9: 321-328.

Schulze, H.J., 1984. Physico-Chemical Elementary Processes in Flotation. Elsevier, Amsterdam.

Schulze, H.J., 1989. Hydrodynamics of bubble-mineral particle collisions. Miner. Process. Extract. Metall. Rev., 5: 43-76.

Schulze, H.J., 1994. Comparison of the elementary steps of particle/bubble interaction in mineral and deinking flotation. Proc. 8th Int. Coll. Surf. Sci. Cong., Adelaide.

Schulze, H.J., Radoev, B., Geidel, T., Stechmesser, H. and Topfer, E., 1989. Investigations of the collision process between particles and gas bubbles in flotation. Int. J. Miner. Process., 27: 263-278.

Shinnar, R. and Church, J.M., 1960. Predicting particle size in agitated dispersions. Ind. Eng. Chem. 52: 253-256.

Sivamohan, R. 1990. The problem of recovering very fine particles in mineral processing – A review. Int. J. Miner. Process., 28: 247-288.

Skillen, A., 1993. Froth flotation - New technologies bubbling under. Ind. Miner., February, pp. 48-54.

Solari, J.A and Gochin, R.J., 1992. Fundamental aspects of microbubble flotation process. In: J.S. Laskowski and J. Ralston (Editors), Colloidal Chemistry in Mineral Processing. Elsevier, Oxford, pp. 395-416.

Spears, D.R. and Jordan, C.E., 1989. The effect of turbulence on the flotation rate of galena when using fine bubbles. In S. Chander and R.R. Klimpel (Eds). Advances in Coal and Mineral Processing Using Flotation, S.M.E., Littleton, pp. 77-84.

Spetl, F. and Dedek, F., 1964. New ideas on the kinetics of the flotation process. Proc. 5th Int. Coal Prep. Cong., pp. 25-35.

Stonestreet, P., 1992. Reverse flotation - A novel process for the beneficiation of fine coal. Ph.D. Thesis, University of Cape Town, South Africa.

Sun, S.C. and Zimmerman, R.E., 1950. The mechanism of coarse coal and mineral froth flotation. Trans. Soc. Min. Eng., 187: 616-622.

Sutherland, K.L., 1948. Kinetics of the flotation process. J. Phys. Coll., 52: 394-425.

Szatkowski, M. and Freyberger, W.L., 1985. Kinetics of flotation with fine bubbles. Trans. Inst. Min. Metall., 94: C61-C70.

Taggart, A.F., 1945. Handbook of Mineral Dressing, Ores and Industrial Minerals (2nd Edition). Wiley, New York.

Takahashi, K., Mcmanamey, W.J. and Nienow, A.W., 1992. Bubble size distributions in impeller region in a gas-sparged vessel agitated by a Rushton turbine. J. Chem. Eng. Japan, 25: 427-432.

Tatterson, G.B., 1991. Fluid Mixing and Gas Dispersion in Agitated Tanks. McGraw-Hill, New York.

Tennekes, H., 1977. Turbulence: diffusion statistics, special dynamics. In: W. Frost and T.M. Moulden (Editors), Handbook of Turbulence. Plenum Press, New York.

Tomlinson, H.S. and Fleming, M.G., 1963. Flotation rate studies. Proc. VI Int. Miner. Process. Cong., Cannes, pp. 563-579, in Szatkowski and Freyberger, 1985. *op cit.*

Townsend, A.A., 1976. The Structure of Turbulent Shear Flow (2nd Edition). Cambridge University Press, Cambridge.

Trahar, W.J., 1981. A rational interpretation of the role of particle size in flotation. Int. J. Miner. Process., 8: 289-327.

Trahar, W.J. and Warren, L.J., 1976. The floatability of very fine particles. Int. J. Miner. Process., 3: 103-131.

Tsouris, C. and Tavlarides, L.L., 1994. Breakage and coalescence models for drops in turbulent dispersions. A.I.Ch.E.J., 40: 395-406.

Tucker, J.P., Deglon, D.A., Franzidis, J.P., O'Connor, C.T. and Harris, M.C., 1994. An evaluation of a direct method of bubble size distribution measurement in a laboratory batch flotation cell. Miner. Eng., 7: 667-680.

Van Der Molen, K. and Van Maanen, H.R.E., 1978. Laser-doppler measurements of the turbulent flow in stirred vessels to establish scaling rules. Chem. Eng. Sci., 33: 1161-1168.

Varbanov, R., 1984. Flotation of spherical particles. Trans. Inst. Min. Metall., 93: C6-C8.

Weber, M.E. and Paddock, D., 1983. Interceptional and gravitational collision efficiencies for single collectors at intermediate Reynolds numbers. J. Coll. Inter. Sci., 94: 328-335.

Wheeler, D.A., 1988. Historical view of column flotation development. Column 88 - Proc. Int. Conf., S.M.E., Phoenix, pp. 3-4.

Woodburn, E.T., King, R.P. and Colborn, R.P., 1971. The effect of particle size distribution on the performance of a phosphate flotation process. Metall. Trans., 2: 3163-3174.

Woodburn, E.T. and Loveday, B.K., 1965. The effect of variable residence time on the performance of a flotation system. J.S.A.I.M.M, 65: 612-628.

Wu, H. and Patterson, G.K., 1989. Laser-doppler measurements of turbulent-flow parameters in a stirred mixer. Chem. Eng. Sci., 44: 2207-2221.

Ye, Y. and Miller, J.D., 1989. The significance of bubble/particle contact time during collision in the analysis of flotation phenomena. Int. J. Miner. Process., 25: 199-219.

Yoon, R.H., 1991. Hydrodynamic and surface forces in bubble-particle interaction. Aufbereitungs Technik, 32: 474.

Yoon, R.H., 1993. Microbubble flotation. Miner. Eng., 6: 619-630.

Yoon, R.J. and Luttrell, G.H., 1986. The effect of bubble size on fine coal flotation. Coal Prep., 2: 179-192.

Yoon, R.H. and Luttrell, G.H., 1989. The effect of bubble size on fine particle flotation. Miner. Process. Extract. Metall. Rev., 5: 101-122.

Yoon, R.H. and Yordan, J.L., 1991. Induction time measurements for a quartz-amine flotation system. J. Coll. Inter. Sci., 141: 374-383.

Zhou, Z.A., Egiebor, N.O. and Plitt, L.R., 1993. Frother effects on bubble size estimation in a flotation column. Miner. Eng., 6: 55-67.

Zuniga, H.G., 1935. Flotation recovery is an exponential function of its rate. Boln. Soc. Nac. Min. Santiago, 47: 83-86.

APPENDIX A: HYDRODYNAMIC AND GAS DISPERSION DATA

1. Tables A1 to A6 present hydrodynamic data for the Rushton turbine and the spinning disc and for the flotation cell aerated with the porosity 1, 3 & 4 spargers. Turbulence parameters listed in these tables refer to the tangential component of the measured turbulence velocities only. Equivalent parameters for the radial component of the measured turbulence velocities are not presented as turbulence was found to be isotropic throughout the flotation cell.

2. Tables A7 and A8 present gas dispersion data for the Rushton turbine and the spinning disc and for the flotation cell aerated with the porosity 1, 3 & 4 spargers. Most of the parameters listed in these tables were derived from a volumetric-basis as these were predominantly used in this study.

Table A1. Hydrodynamic parameters for the Rushton turbine (unaerated).

RUSHTON TURBINE UNAERATED FLOTATION CELL					
Bulk Parameters					
N (RPM)	**310**	**630**	**940**	**1260**	
P (W/kg)	0.10	0.65	2.10	5.25	
τ_T (s)	3.7	1.6	0.9	0.6	
Turbulence Parameters					
N (RPM)	**310**	**630**	**940**	**1260**	
U (m/s)	0.06	0.17	0.28	0.39	**Bulk Tank**
ū (m/s)	0.04	0.12	0.19	0.26	
Λ_f (mm)	2.50	5.73	8.10	10.3	
λ_f (mm)	1.14	1.73	2.10	2.37	
ε (W/kg)	0.03	0.26	0.83	1.70	
ε_n	0.31	0.40	0.40	0.32	
U (m/s)	0.15	0.43	0.75	1.21	**Impeller Stream**
ū (m/s)	0.11	0.24	0.38	0.59	
Λ_f (mm)	1.10	1.90	2.20	2.70	
λ_f (mm)	0.25	0.66	0.95	1.20	
ε (W/kg)	1.16	6.99	22.3	68.6	
ε_n	11.9	10.6	10.7	13.1	
U (m/s)	0.44	1.04	1.83	2.96	**Impeller Tip**
ū (m/s)	0.19	0.33	0.53	0.81	
Λ_f (mm)	1.40	2.10	2.30	3.10	
λ_f (mm)	0.58	0.98	1.30	1.60	
ε (W/kg)	4.42	15.6	58.8	154.5	
ε_n	45.2	23.6	28.3	29.6	

Table A2. Hydrodynamic parameters for the spinning disc (unaerated).

SPINNING DISC UNAERATED FLOTATION CELL					
Bulk Parameters					
N (RPM)	**2180**	**2490**	**2810**	**3100**	
P (W/kg)	2.70	4.05	5.70	7.65	
τ_T **(s)**	n/a	n/a	n/a	n/a	
Turbulence Parameters					
N (RPM)	**2180**	**2490**	**2810**	**3100**	
U (m/s)	0.15	0.17	0.18	0.18	**Bulk Tank**
ū (m/s)	0.08	0.09	0.09	0.09	
Λ_f **(mm)**	5.30	5.20	5.07	5.10	
λ_f **(mm)**	1.70	1.63	1.57	1.60	
ε **(W/kg)**	0.09	0.11	0.14	0.14	
ε_n	0.03	0.03	0.02	0.02	
U (m/s)	0.75	0.86	0.98	1.10	**Impeller Stream**
ū (m/s)	0.29	0.31	0.35	0.38	
Λ_f **(mm)**	3.00	2.80	3.00	3.80	
λ_f **(mm)**	1.50	1.50	1.60	1.70	
ε **(W/kg)**	7.22	9.76	13.0	13.5	
ε_n	2.68	2.41	2.27	1.76	
U (m/s)	1.53	1.82	2.07	2.33	**Impeller Tip**
ū (m/s)	0.61	0.67	0.67	0.67	
Λ_f **(mm)**	3.00	3.00	2.50	2.30	
λ_f **(mm)**	1.60	1.70	1.50	1.70	
ε **(W/kg)**	68.0	90.2	107.1	120.1	
ε_n	25.2	22.3	18.8	15.7	

Table A5. Hydrodynamic parameters for the Rushton turbine (porosity 4 sparger).

RUSHTON TURBINE POROSITY 4 SPARGER					
Bulk Parameters					
N (RPM)	**310**	**630**	**940**	**1260**	
P (W/kg)	0.10	0.65	1.90	4.40	
τ_T **(s)**	4.7	1.5	0.9	0.7	
Turbulence Parameters					
N (RPM)	**310**	**630**	**940**	**1260**	
U (m/s)	0.03	0.10	0.20	0.30	**Bulk Tank**
ū (m/s)	0.02	0.09	0.15	0.22	
Λ_f **(mm)**	1.04	3.17	5.37	7.90	
λ_f **(mm)**	0.36	1.00	1.42	1.73	
ε **(W/kg)**	0.01	0.20	0.69	1.23	
ε_n	0.13	0.31	0.36	0.28	
U (m/s)	0.09	0.37	0.68	0.98	**Impeller Stream**
ū (m/s)	0.09	0.25	0.40	0.53	
Λ_f **(mm)**	0.57	1.30	1.80	2.00	
λ_f **(mm)**	0.26	0.51	0.77	0.87	
ε **(W/kg)**	1.03	11.1	32.3	68.1	
ε_n	10.1	17.0	16.8	15.6	
U (m/s)	0.35	1.08	1.82	2.45	**Impeller Tip**
ū (m/s)	0.21	0.49	0.72	0.92	
Λ_f **(mm)**	1.50	3.10	3.20	3.00	
λ_f **(mm)**	0.67	0.97	1.20	1.30	
ε **(W/kg)**	5.64	34.0	106.5	236.2	
ε_n	55.1	52.1	55.5	53.9	

Table A6. Hydrodynamic parameters for the spinning disc (porosity 4 sparger).

SPINNING DISC POROSITY 4 SPARGER					
Bulk Parameters					
N (RPM)	**2180**	**2490**	**2810**	**3100**	
P (W/kg)	2.95	4.30	6.00	7.90	
τ_T **(s)**	n/a	n/a	n/a	n/a	
Turbulence Parameters					
N (RPM)	**2180**	**2490**	**2810**	**3100**	
U (m/s)	0.07	0.08	0.09	0.11	**Bulk Tank**
ū (m/s)	0.05	0.06	0.08	0.08	
Λ_f **(mm)**	2.17	2.10	2.43	2.67	
λ_f **(mm)**	0.71	0.66	0.75	0.81	
ε (W/kg)	0.07	0.11	0.17	0.19	
ε_n	0.02	0.03	0.03	0.03	
U (m/s)	0.64	0.80	0.94	1.14	**Impeller Stream**
ū (m/s)	0.32	0.40	0.45	0.53	
Λ_f **(mm)**	3.00	4.00	3.60	4.30	
λ_f **(mm)**	1.20	1.40	1.40	1.60	
ε (W/kg)	9.55	14.5	22.1	32.1	
ε_n	3.26	3.39	3.66	4.05	
U (m/s)	1.50	1.82	2.16	2.25	**Impeller Tip**
ū (m/s)	0.61	0.70	0.82	0.86	
Λ_f **(mm)**	2.60	3.10	2.80	2.40	
λ_f **(mm)**	1.40	1.40	1.60	1.60	
ε (W/kg)	77.5	100.2	176.7	242.0	
ε_n	26.4	23.5	29.3	30.6	

Table A7. Gas dispersion parameters for the Rushton turbine.

RUSHTON TURBINE					
N (RPM)	**310**	**630**	**940**	**1260**	
ε (W/kg)	0.10	0.65	1.95	4.50	
ϕ	0.0062	0.0232	0.0752	0.1324	**Porosity 1 Sparger**
d_b (mm)	0.82	0.38	0.20	0.16	
d_s (mm)	1.05	0.69	0.33	0.23	
d_{95} (mm)	1.34	0.87	0.42	0.28	
d_{sf} (mm)	1.16	0.80	0.37	0.26	
S (/cm)	0.35	2.00	13.9	35.4	
S_b (/s)	2.23	3.26	7.00	10.3	
τ_g (s)	2.1	7.8	25.4	44.7	
τ_{gs} (s)	2.3	9.0	29.1	50.4	
n_p	0.4	3.3	25.4	63.9	
ϕ	0.0204	0.0388	0.0791	0.1324	**Porosity 3 Sparger**
d_b (mm)	0.24	0.20	0.18	0.16	
d_s (mm)	0.29	0.27	0.25	0.23	
d_{95} (mm)	0.35	0.34	0.32	0.31	
d_{sf} (mm)	0.32	0.29	0.28	0.26	
S (/cm)	4.21	8.73	19.0	35.4	
S_b (/s)	8.20	8.82	9.40	10.3	
τ_g (s)	6.9	13.1	26.7	44.7	
τ_{gs} (s)	7.5	14.5	29.5	50.4	
n_p	n/a	n/a	n/a	n/a	
ϕ	0.0523	0.0787	0.1159	0.1575	**Porosity 4 Sparger**
d_b (mm)	0.13	0.13	0.13	0.13	
d_s (mm)	0.21	0.21	0.21	0.21	
d_{95} (mm)	0.28	0.28	0.28	0.28	
d_{sf} (mm)	0.24	0.24	0.24	0.24	
S (/cm)	14.6	22.0	32.4	44.0	
S_b (/s)	10.7	10.7	10.7	10.7	
τ_g (s)	17.7	26.6	39.1	53.2	
τ_{gs} (s)	19.9	30.0	44.2	60.0	
n_p	3.8	17.7	43.4	76.0	

Table A8. Gas dispersion parameters for the spinning disc.

SPINNING DISC					
N (RPM)	**2180**	**2490**	**2810**	**3100**	
ε (W/kg)	2.80	4.20	5.90	7.85	
ϕ	0.0129	0.0168	0.0204	0.0304	**Porosity 1 Sparger**
d_b (mm)	0.48	0.29	0.22	0.20	
d_s (mm)	0.76	0.59	0.44	0.31	
d_{95} (mm)	0.97	0.77	0.57	0.39	
d_{sf} (mm)	0.86	0.70	0.55	0.37	
S (/cm)	1.02	1.70	2.80	5.88	
S_b (/s)	3.03	3.71	4.69	7.05	
τ_g (s)	4.4	5.7	6.9	10.3	
τ_{gs} (s)	4.9	6.7	8.7	12.2	
n_p	n/a	n/a	n/a	n/a	
ϕ	0.0301	0.0392	0.0487	0.0661	**Porosity 3 Sparger**
d_b (mm)	0.19	0.19	0.19	0.19	
d_s (mm)	0.26	0.26	0.26	0.26	
d_{95} (mm)	0.32	0.32	0.32	0.32	
d_{sf} (mm)	0.28	0.28	0.28	0.28	
S (/cm)	6.88	8.97	11.1	15.1	
S_b (/s)	9.17	9.17	9.17	9.17	
τ_g (s)	10.2	13.2	16.4	22.3	
τ_{gs} (s)	11.0	14.3	17.8	24.1	
n_p	n/a	n/a	n/a	n/a	
ϕ	0.0711	0.0911	0.0989	0.1220	**Porosity 4 Sparger**
d_b (mm)	0.13	0.13	0.13	0.13	
d_s (mm)	0.21	0.21	0.21	0.21	
d_{95} (mm)	0.28	0.28	0.28	0.28	
d_{sf} (mm)	0.24	0.24	0.24	0.24	
S (/cm)	19.9	25.5	27.6	34.1	
S_b (/s)	10.7	10.7	10.7	10.7	
τ_g (s)	24.0	30.7	33.4	41.2	
τ_{gs} (s)	27.1	34.7	37.7	46.5	
n_p	n/a	n/a	n/a	n/a	

APPENDIX B: FLOTATION DATA

1. Tables B1 to B6 present recovery-time data for the -32 μm sample and for the Rushton turbine and spinning disc impellers.

2. Tables B7 to B12 present recovery-time data for the -32 μm and -100 μm samples and for the Rushton turbine impeller.

Table B3. Recovery-time data for the Rushton turbine impeller (porosity 4 sparger).

POROSITY 4 SPARGER					
310 RPM					
Time (s)	**2-4 μm**	**4-8 μm**	**8-12 μm**	**12-18 μm**	**18-32 μm**
30	0.3477	0.3710	0.3869	0.4041	0.4383
60	0.5876	0.6256	0.6474	0.6644	0.6887
90	0.7579	0.8049	0.8229	0.8262	0.8306
120	0.8502	0.8984	0.9093	0.9021	0.8956
180	0.8837	0.9279	0.9325	0.9197	0.9102
630 RPM					
Time (s)	**2-4 μm**	**4-8 μm**	**8-12 μm**	**12-18 μm**	**18-32 μm**
30	0.2892	0.3256	0.3522	0.3722	0.3979
60	0.5780	0.6459	0.6840	0.7040	0.7224
90	0.7385	0.8154	0.8491	0.8567	0.8602
120	0.7951	0.8703	0.8966	0.8960	0.8929
180	0.8471	0.9125	0.9275	0.9195	0.9123
940 RPM					
Time (s)	**2-4 μm**	**4-8 μm**	**8-12 μm**	**12-18 μm**	**18-32 μm**
30	0.2351	0.2650	0.2756	0.2743	0.2665
60	0.4831	0.5433	0.5707	0.5727	0.5624
90	0.6428	0.7214	0.7548	0.7591	0.7488
120	0.7459	0.8284	0.8596	0.8611	0.8497
180	0.8443	0.9187	0.9381	0.9324	0.9183
1260 RPM					
Time (s)	**2-4 μm**	**4-8 μm**	**8-12 μm**	**12-18 μm**	**18-32 μm**
30	0.1472	0.1592	0.1662	0.1617	0.1529
60	0.3738	0.4155	0.4368	0.4345	0.4208
90	0.5626	0.6208	0.6484	0.6487	0.6362
120	0.6634	0.7242	0.7507	0.7497	0.7370
180	0.7945	0.8522	0.8711	0.8654	0.8518

Table B4. Recovery-time data for the spinning disc impeller (porosity 1 sparger).

POROSITY 1 SPARGER					
2180 RPM					
Time (s)	**2-4 μm**	**4-8 μm**	**8-12 μm**	**12-18 μm**	**18-32 μm**
60	0.1675	0.1816	0.1992	0.2176	0.2396
120	0.3055	0.3307	0.3614	0.3920	0.4266
195	0.4605	0.4990	0.5405	0.5789	0.6202
300	0.6142	0.6643	0.7117	0.7509	0.7874
480	0.7773	0.8331	0.8742	0.8973	0.9130
2490 RPM					
Time (s)	**2-4 μm**	**4-8 μm**	**8-12 μm**	**12-18 μm**	**18-32 μm**
45	0.1584	0.1722	0.1899	0.2070	0.2249
105	0.3369	0.3660	0.3990	0.4281	0.4558
180	0.5258	0.5712	0.6158	0.6504	0.6777
225	0.6677	0.7226	0.7680	0.7981	0.8165
390	0.7992	0.8548	0.8891	0.9037	0.9072
2810 RPM					
Time (s)	**2-4 μm**	**4-8 μm**	**8-12 μm**	**12-18 μm**	**18-32 μm**
30	0.1361	0.1499	0.1640	0.1753	0.1835
60	0.2525	0.2780	0.3017	0.3187	0.3296
105	0.4140	0.4537	0.4873	0.5092	0.5198
165	0.5850	0.6388	0.6768	0.6974	0.7031
255	0.7566	0.8176	0.8492	0.8607	0.8581
3100 RPM					
Time (s)	**2-4 μm**	**4-8 μm**	**8-12 μm**	**12-18 μm**	**18-32 μm**
30	0.1420	0.1559	0.1706	0.1816	0.1886
60	0.2961	0.3247	0.3502	0.3660	0.3708
90	0.4392	0.4807	0.5134	0.5309	0.5330
150	0.6282	0.6848	0.7205	0.7349	0.7301
210	0.7577	0.8161	0.8449	0.8524	0.8433

Table B5. Recovery-time data for the spinning disc impeller (porosity 3 sparger).

POROSITY 3 SPARGER					
2180 RPM					
Time (s)	**2-4 μm**	**4-8 μm**	**8-12 μm**	**12-18 μm**	**18-32 μm**
30	0.2093	0.2361	0.2624	0.2836	0.3044
60	0.4096	0.4601	0.5048	0.5373	0.5663
90	0.5824	0.6507	0.7051	0.7397	0.7654
135	0.7614	0.8432	0.8948	0.9189	0.9286
210	0.8978	0.9758	1.0000	1.0000	0.9981
2490 RPM					
Time (s)	**2-4 μm**	**4-8 μm**	**8-12 μm**	**12-18 μm**	**18-32 μm**
30	0.2413	0.2758	0.3038	0.3238	0.3390
60	0.4518	0.5120	0.5553	0.5806	0.5968
90	0.6130	0.6890	0.7358	0.7577	0.7668
135	0.7646	0.8488	0.8866	0.8936	0.8904
210	0.8686	0.9384	0.9524	0.9424	0.9324
2810 RPM					
Time (s)	**2-4 μm**	**4-8 μm**	**8-12 μm**	**12-18 μm**	**18-32 μm**
30	0.2281	0.2576	0.2792	0.2916	0.2981
60	0.4371	0.4896	0.5242	0.5404	0.5430
90	0.5983	0.6652	0.7033	0.7164	0.7129
135	0.7680	0.8406	0.8702	0.8731	0.8623
210	0.8666	0.9271	0.9389	0.9303	0.9170
3100 RPM					
Time (s)	**2-4 μm**	**4-8 μm**	**8-12 μm**	**12-18 μm**	**18-32 μm**
30	0.2229	0.2533	0.2758	0.2871	0.2908
60	0.4375	0.4937	0.5288	0.5422	0.5404
90	0.6053	0.6738	0.7120	0.7228	0.7150
135	0.7735	0.8450	0.8726	0.8729	0.8592
210	0.8636	0.9226	0.9344	0.9260	0.9113

Table B6. Recovery-time data for the spinning disc impeller (porosity 4 sparger).

POROSITY 4 SPARGER					
2180 RPM					
Time (s)	**2-4 μm**	**4-8 μm**	**8-12 μm**	**12-18 μm**	**18-32 μm**
20	0.1896	0.2146	0.2388	0.2603	0.2860
40	0.3866	0.4382	0.4823	0.5165	0.5529
60	0.5529	0.6226	0.6744	0.7089	0.7403
90	0.7064	0.7848	0.8288	0.8478	0.8627
150	0.8345	0.9002	0.9188	0.9166	0.9194
2490 RPM					
Time (s)	**2-4 μm**	**4-8 μm**	**8-12 μm**	**12-18 μm**	**18-32 μm**
20	0.1799	0.1997	0.2232	0.2442	0.2667
40	0.4003	0.4460	0.4880	0.5190	0.5486
60	0.5511	0.6114	0.6599	0.6910	0.7151
90	0.6961	0.7638	0.8067	0.8265	0.8394
150	0.8632	0.9172	0.9335	0.9319	0.9324
2810 RPM					
Time (s)	**2-4 μm**	**4-8 μm**	**8-12 μm**	**12-18 μm**	**18-32 μm**
30	0.2961	0.3430	0.3764	0.3938	0.4065
60	0.5478	0.6268	0.6715	0.6878	0.6928
90	0.7131	0.8044	0.8429	0.8482	0.8417
120	0.8039	0.8918	0.9173	0.9118	0.8994
180	0.8656	0.9397	0.9498	0.9364	0.9216
3100 RPM					
Time (s)	**2-4 μm**	**4-8 μm**	**8-12 μm**	**12-18 μm**	**18-32 μm**
30	0.2821	0.3231	0.3494	0.3606	0.3664
60	0.5187	0.5856	0.6206	0.6310	0.6319
90	0.7012	0.7791	0.8092	0.8112	0.8048
120	0.7878	0.8625	0.8827	0.8769	0.8670
180	0.8600	0.9203	0.9264	0.9140	0.9029

Table B6. Recovery-time data for the spinning disc impeller (porosity 4 sparger).

POROSITY 4 SPARGER					
2180 RPM					
Time (s)	**2-4 μm**	**4-8 μm**	**8-12 μm**	**12-18 μm**	**18-32 μm**
20	0.1896	0.2146	0.2388	0.2603	0.2860
40	0.3866	0.4382	0.4823	0.5165	0.5529
60	0.5529	0.6226	0.6744	0.7089	0.7403
90	0.7064	0.7848	0.8288	0.8478	0.8627
150	0.8345	0.9002	0.9188	0.9166	0.9194
2490 RPM					
Time (s)	**2-4 μm**	**4-8 μm**	**8-12 μm**	**12-18 μm**	**18-32 μm**
20	0.1799	0.1997	0.2232	0.2442	0.2667
40	0.4003	0.4460	0.4880	0.5190	0.5486
60	0.5511	0.6114	0.6599	0.6910	0.7151
90	0.6961	0.7638	0.8067	0.8265	0.8394
150	0.8632	0.9172	0.9335	0.9319	0.9324
2810 RPM					
Time (s)	**2-4 μm**	**4-8 μm**	**8-12 μm**	**12-18 μm**	**18-32 μm**
30	0.2961	0.3430	0.3764	0.3938	0.4065
60	0.5478	0.6268	0.6715	0.6878	0.6928
90	0.7131	0.8044	0.8429	0.8482	0.8417
120	0.8039	0.8918	0.9173	0.9118	0.8994
180	0.8656	0.9397	0.9498	0.9364	0.9216
3100 RPM					
Time (s)	**2-4 μm**	**4-8 μm**	**8-12 μm**	**12-18 μm**	**18-32 μm**
30	0.2821	0.3231	0.3494	0.3606	0.3664
60	0.5187	0.5856	0.6206	0.6310	0.6319
90	0.7012	0.7791	0.8092	0.8112	0.8048
120	0.7878	0.8625	0.8827	0.8769	0.8670
180	0.8600	0.9203	0.9264	0.9140	0.9029

Table B7. Recovery-time data for the -32 μm sample (porosity 1 sparger).

POROSITY 1 SPARGER					
310 RPM					
Time (s)	**2-4 μm**	**4-8 μm**	**8-12 μm**	**12-18 μm**	**18-32 μm**
90	0.1757	0.1925	0.1982	0.1992	0.2016
180	0.2700	0.2951	0.3042	0.3061	0.3097
330	0.4136	0.4515	0.4662	0.4694	0.4727
510	0.5458	0.5940	0.6144	0.6198	0.6239
780	0.6666	0.7257	0.7519	0.7592	0.7598
580 RPM					
Time (s)	**2-4 μm**	**4-8 μm**	**8-12 μm**	**12-18 μm**	**18-32 μm**
45	0.1175	0.1272	0.1319	0.1347	0.1415
120	0.2969	0.3215	0.3333	0.3409	0.3581
180	0.4166	0.4513	0.4690	0.4796	0.4996
285	0.5958	0.6469	0.6736	0.6860	0.6982
420	0.7456	0.8093	0.8400	0.8478	0.8460
730 RPM					
Time (s)	**2-4 μm**	**4-8 μm**	**8-12 μm**	**12-18 μm**	**18-32 μm**
30	0.1014	0.1091	0.1119	0.1133	0.1177
75	0.2624	0.2807	0.2867	0.2881	0.2945
135	0.4363	0.4678	0.4794	0.4810	0.4846
210	0.6076	0.6546	0.6745	0.6769	0.6746
330	0.7753	0.8312	0.8547	0.8550	0.8454
840 RPM					
Time (s)	**2-4 μm**	**4-8 μm**	**8-12 μm**	**12-18 μm**	**18-32 μm**
30	0.1063	0.1132	0.1149	0.1147	0.1161
60	0.2319	0.2470	0.2497	0.2467	0.2449
120	0.4465	0.4828	0.4922	0.4864	0.4766
180	0.6001	0.6525	0.6717	0.6679	0.6536
270	0.7526	0.8139	0.8383	0.8359	0.8199
940 RPM					
Time (s)	**2-4 μm**	**4-8 μm**	**8-12 μm**	**12-18 μm**	**18-32 μm**
30	0.1163	0.1254	0.1266	0.1251	0.1238
60	0.2562	0.2777	0.2797	0.2741	0.2675
105	0.4331	0.4708	0.4790	0.4717	0.4589
150	0.5677	0.6196	0.6361	0.6311	0.6158
225	0.7266	0.7913	0.8128	0.8073	0.7874

Table B8. Recovery-time data for the -32 μm sample (porosity 3 sparger).

POROSITY 3 SPARGER					
310 RPM					
Time (s)	**2-4 μm**	**4-8 μm**	**8-12 μm**	**12-18 μm**	**18-32 μm**
20	0.1422	0.1533	0.1616	0.1693	0.1847
40	0.3042	0.3267	0.3449	0.3613	0.3909
60	0.4327	0.4639	0.4888	0.5098	0.5430
90	0.5744	0.6161	0.6474	0.6697	0.6974
120	0.6557	0.7029	0.7364	0.7567	0.7765
580 RPM					
Time (s)	**2-4 μm**	**4-8 μm**	**8-12 μm**	**12-18 μm**	**18-32 μm**
20	0.1325	0.1460	0.1563	0.1634	0.1713
40	0.2868	0.3155	0.3373	0.3512	0.3615
60	0.4072	0.4480	0.4775	0.4946	0.5048
90	0.5453	0.5999	0.6370	0.6555	0.6623
120	0.6496	0.7139	0.7548	0.7722	0.7745
730 RPM					
Time (s)	**2-4 μm**	**4-8 μm**	**8-12 μm**	**12-18 μm**	**18-32 μm**
20	0.1116	0.1230	0.1304	0.1343	0.1363
40	0.2701	0.2983	0.3144	0.3203	0.3189
60	0.3775	0.4171	0.4384	0.4443	0.4388
90	0.5267	0.5816	0.6106	0.6174	0.6070
150	0.7175	0.7895	0.8268	0.8347	0.8223
840 RPM					
Time (s)	**2-4 μm**	**4-8 μm**	**8-12 μm**	**12-18 μm**	**18-32 μm**
20	0.1057	0.1145	0.1188	0.1198	0.1191
40	0.2532	0.2753	0.2840	0.2832	0.2761
60	0.3588	0.3914	0.4046	0.4032	0.3915
90	0.4865	0.5338	0.5554	0.5556	0.5393
150	0.6934	0.7592	0.7924	0.7974	0.7827
940 RPM					
Time (s)	**2-4 μm**	**4-8 μm**	**8-12 μm**	**12-18 μm**	**18-32 μm**
20	0.1032	0.1131	0.1173	0.1177	0.1158
40	0.2343	0.2572	0.2652	0.2629	0.2544
60	0.3576	0.3949	0.4088	0.4059	0.3924
90	0.4873	0.5384	0.5616	0.5614	0.5447
150	0.6778	0.7472	0.7828	0.7892	0.7742

Table B9. Recovery-time data for the -32 μm sample (porosity 4 sparger).

POROSITY 4 SPARGER					
310 RPM					
Time (s)	**2-4 μm**	**4-8 μm**	**8-12 μm**	**12-18 μm**	**18-32 μm**
20	0.2630	0.2777	0.2916	0.3047	0.3273
40	0.4697	0.4994	0.5242	0.5429	0.5673
60	0.6189	0.6581	0.6872	0.7043	0.7187
80	0.7063	0.7513	0.7861	0.7920	0.7941
100	0.7504	0.7970	0.8243	0.8286	0.8231
580 RPM					
Time (s)	**2-4 μm**	**4-8 μm**	**8-12 μm**	**12-18 μm**	**18-32 μm**
20	0.1909	0.2097	0.2251	0.2365	0.2527
40	0.3915	0.4329	0.4636	0.4825	0.5046
60	0.5802	0.6376	0.6751	0.6937	0.7091
80	0.7442	0.8115	0.8472	0.8543	0.8538
100	0.8603	0.9280	0.9541	0.9479	0.9341
730 RPM					
Time (s)	**2-4 μm**	**4-8 μm**	**8-12 μm**	**12-18 μm**	**18-32 μm**
20	0.1740	0.1894	0.2020	0.2101	0.2181
40	0.3676	0.4014	0.4237	0.4350	0.4409
60	0.5303	0.5781	0.6058	0.6163	0.6180
80	0.6742	0.7319	0.7627	0.7718	0.7703
100	0.7548	0.8149	0.8437	0.8499	0.8462
840 RPM					
Time (s)	**2-4 μm**	**4-8 μm**	**8-12 μm**	**12-18 μm**	**18-32 μm**
20	0.1559	0.1707	0.1791	0.1823	0.1827
40	0.3436	0.3752	0.3902	0.3923	0.3861
60	0.4845	0.5290	0.5502	0.5534	0.5445
80	0.6083	0.6617	0.6868	0.6908	0.6821
100	0.6845	0.7416	0.7672	0.7707	0.7626
940 RPM					
Time (s)	**2-4 μm**	**4-8 μm**	**8-12 μm**	**12-18 μm**	**18-32 μm**
20	0.1618	0.1754	0.1828	0.1843	0.1820
40	0.3123	0.3382	0.3503	0.3506	0.3426
60	0.4640	0.5035	0.5229	0.5248	0.5149
80	0.5683	0.6152	0.6395	0.6436	0.6349
100	0.6611	0.7115	0.7364	0.7401	0.7301

Table B10. Recovery-time data for the -100 μm sample (porosity 1 sparger).

POROSITY 1 SPARGER					
310 RPM					
Time (s)	**10-20 μm**	**20-30 μm**	**30-40 μm**	**40-50 μm**	**50-70 μm**
30	0.1954	0.2202	0.2541	0.2836	0.3252
60	0.3389	0.3782	0.4251	0.4634	0.5099
120	0.5216	0.5729	0.6258	0.6686	0.6986
180	0.6616	0.7123	0.7565	0.7893	0.7992
240	0.7389	0.7855	0.8207	0.8457	0.8452
580 RPM					
Time (s)	**10-20 μm**	**20-30 μm**	**30-40 μm**	**40-50 μm**	**50-70 μm**
20	0.1749	0.2028	0.2388	0.2707	0.3164
40	0.3597	0.4071	0.4637	0.5127	0.5760
60	0.4955	0.5535	0.6159	0.6675	0.7310
90	0.6518	0.7115	0.7680	0.8139	0.8584
120	0.7657	0.8169	0.8614	0.8931	0.9190
730 RPM					
Time (s)	**10-20 μm**	**20-30 μm**	**30-40 μm**	**40-50 μm**	**50-70 μm**
20	0.2324	0.2656	0.3050	0.3372	0.3820
40	0.4425	0.4961	0.5525	0.5973	0.6533
60	0.5972	0.6521	0.7055	0.7483	0.7863
90	0.7582	0.8010	0.8412	0.8685	0.8850
120	0.8487	0.8786	0.9069	0.9226	0.9259
840 RPM					
Time (s)	**10-20 μm**	**20-30 μm**	**30-40 μm**	**40-50 μm**	**50-70 μm**
20	0.3320	0.3693	0.4098	0.4462	0.4863
40	0.5295	0.5740	0.6169	0.6532	0.6910
60	0.6761	0.7156	0.7509	0.7819	0.8061
90	0.8090	0.8365	0.8596	0.8817	0.8916
120	0.8701	0.8914	0.9094	0.9268	0.9301
940 RPM					
Time (s)	**10-20 μm**	**20-30 μm**	**30-40 μm**	**40-50 μm**	**50-70 μm**
20	0.2684	0.2936	0.3213	0.3460	0.3726
40	0.4742	0.5044	0.5347	0.5606	0.5875
60	0.6091	0.6353	0.6614	0.6855	0.7037
90	0.7321	0.7538	0.7749	0.7961	0.8044
120	0.8227	0.8388	0.8553	0.8737	0.8750

Table B11. Recovery-time data for the -100 μm sample (porosity 3 sparger).

POROSITY 3 SPARGER					
310 RPM					
Time (s)	**10-20 μm**	**20-30 μm**	**30-40 μm**	**40-50 μm**	**50-70 μm**
20	0.3053	0.3432	0.3951	0.4401	0.5041
40	0.5295	0.5795	0.6365	0.6846	0.7258
60	0.6835	0.7321	0.7821	0.8154	0.8307
90	0.7982	0.8347	0.8689	0.8858	0.8823
120	0.8470	0.8728	0.8983	0.9089	0.9005
580 RPM					
Time (s)	**10-20 μm**	**20-30 μm**	**30-40 μm**	**40-50 μm**	**50-70 μm**
20	0.3431	0.3942	0.4535	0.5011	0.5670
40	0.6330	0.6985	0.7546	0.8036	0.8464
60	0.8066	0.8580	0.8977	0.9276	0.9450
90	0.8948	0.9280	0.9501	0.9648	0.9688
120	0.9162	0.9436	0.9610	0.9720	0.9731
730 RPM					
Time (s)	**10-20 μm**	**20-30 μm**	**30-40 μm**	**40-50 μm**	**50-70 μm**
20	0.3435	0.3849	0.4308	0.4721	0.5197
40	0.6742	0.7224	0.7696	0.8154	0.8452
60	0.8058	0.8407	0.8766	0.9101	0.9239
90	0.8897	0.9103	0.9344	0.9575	0.9599
120	0.9166	0.9324	0.9528	0.9726	0.9715
840 RPM					
Time (s)	**10-20 μm**	**20-30 μm**	**30-40 μm**	**40-50 μm**	**50-70 μm**
20	0.3435	0.3812	0.4219	0.4580	0.4993
40	0.6483	0.6867	0.7250	0.7623	0.7862
60	0.7875	0.8153	0.8434	0.8736	0.8844
90	0.8767	0.8936	0.9143	0.9370	0.9384
120	0.9082	0.9222	0.9403	0.9607	0.9584
940 RPM					
Time (s)	**10-20 μm**	**20-30 μm**	**30-40 μm**	**40-50 μm**	**50-70 μm**
20	0.3196	0.3494	0.3824	0.4123	0.4461
40	0.5875	0.6168	0.6495	0.6826	0.7044
60	0.7154	0.7386	0.7655	0.7951	0.8070
90	0.8244	0.8389	0.8586	0.8835	0.8861
120	0.8776	0.8835	0.9052	0.9283	0.9266

Table B12. Recovery-time data for the -100 μm sample (porosity 4 sparger).

POROSITY 4 SPARGER					
310 RPM					
Time (s)	**10-20 μm**	**20-30 μm**	**30-40 μm**	**40-50 μm**	**50-70 μm**
15	0.2345	0.2628	0.3031	0.3385	0.3901
30	0.4684	0.5131	0.5656	0.6116	0.6485
45	0.6555	0.7018	0.7786	0.7849	0.7977
60	0.7537	0.7909	0.8573	0.8522	0.8512
75	0.8172	0.8452	0.9031	0.8908	0.8827
580 RPM					
Time (s)	**10-20 μm**	**20-30 μm**	**30-40 μm**	**40-50 μm**	**50-70 μm**
15	0.2817	0.3223	0.3695	0.4078	0.4617
30	0.5810	0.6367	0.6909	0.7369	0.7746
45	0.7493	0.7949	0.8352	0.8706	0.8887
60	0.8435	0.8752	0.9038	0.9284	0.9346
75	0.8873	0.9110	0.9335	0.9530	0.9540
730 RPM					
Time (s)	**10-20 μm**	**20-30 μm**	**30-40 μm**	**40-50 μm**	**50-70 μm**
15	0.2810	0.3142	0.3531	0.3882	0.4276
30	0.5628	0.6068	0.6496	0.6854	0.7224
45	0.7353	0.7704	0.8028	0.8317	0.8542
60	0.8327	0.8591	0.8836	0.9071	0.9205
75	0.8688	0.8909	0.9118	0.9320	0.9414
840 RPM					
Time (s)	**10-20 μm**	**20-30 μm**	**30-40 μm**	**40-50 μm**	**50-70 μm**
15	0.2652	0.2937	0.3250	0.3533	0.3853
30	0.5312	0.5659	0.5980	0.6247	0.6533
45	0.6813	0.7111	0.7382	0.7628	0.7819
60	0.7635	0.7876	0.8094	0.8309	0.8435
75	0.7985	0.8204	0.8403	0.8606	0.8706
940 RPM					
Time (s)	**10-20 μm**	**20-30 μm**	**30-40 μm**	**40-50 μm**	**50-70 μm**
15	0.2446	0.2687	0.2947	0.3176	0.3423
30	0.4595	0.4867	0.5131	0.5354	0.5584
45	0.5895	0.6137	0.6377	0.6600	0.6767
60	0.6693	0.6916	0.7140	0.7362	0.7487
75	0.7209	0.7422	0.7638	0.7860	0.7960